The Hong Kong Polytechnic University

Department of Mechanical Engineering

Stability and Thermal Characteristics of Rod-Stabilized Premixed Flame Jets

Miroslav Drkos

A thesis submitted in partial fulfilment of the requirements for the Degree of Doctor of Philosophy

August 2008

CERTIFICATE OF ORIGINALITY

I hereby declare that this thesis is my own work and that, to the best of my knowledge and belief, it reproduces no material previously published or written, nor material that has been accepted for the award of any other degree or diploma, except where due acknowledgement has been made in the text.

Miroslav Drkos

Dedicated to my late Father, Jaroslav Drkos

ABSTRACT

A comprehensive study of rod-stabilized butane / air flames has been carried out to provide more information on flammability limits, thermal characteristics of free-jet flames and heat transfer of impinging flames. An experimental setup, consisting of round flame jet with axially mounted solid rod had been designed and there were two non-dimensional parameters proposed to represent the variation of geometrical configurations of the nozzle: rod protrusion B_R and rod-to-tube ratio B_T.

Primarily, regions of flame stability had been obtained experimentally for low Reynolds numbers (<3600). Equivalence ratio ranged between 0.4 - 3.0, variable rod protrusion B_R (0 – 2) and rod-to-tube ratio B_T (0.51 to 0.8) have been applied. Inverted, partially-inverted and regular (Bunsen) flames were fundamental flame types identified across the stable regions. Inter-regions were characterized by the existence of more than one stable flame type, primarily depended on the axial and radial distances of the ignition source from the burner port. Size of the unstable region extended with increasing B_R and the effect of B_T showed a similar trend. Smaller rod diameters extended the flashback region. Blow-off limits were found to be less dependent on the geometrical parameters. It has been also shown that the rod-stabilized method enabled the premixed flame to operate at very fuel-lean mixtures.

Structure and temperature profiles of free-jet inverted and partially-inverted flames have been further studied separately. Inverted flames at equivalence ratio equals to 0.9 and partially-inverted flames equivalent to 1.4 were chosen representatives from

respective regions. Temperature profiles, obtained experimentally at *Re* = 2000, demonstrate very uniform distribution over the central area with increasing height. Partially-inverted flames, characterized by occurrence of inner and outer reaction zone, further widen the area with uniform temperature distribution, in comparison with inverted flames with single reaction zone.

An experimental investigation was conducted to deal with the inverted flame impinging vertically onto a flat water-cooled plate. Local and area-averaged distributions of heat flux and *Nu* for various *Re* and geometrical configurations were obtained together with flame temperature profiles for better understanding of impinging process. It has been proved that for nozzle-to-plate ratio equal to 3 and higher, heat flux distribution is nearly uniform over a large area around the stagnation and impingement region. This is predominately due to the convex shape of inverted flame that creates central core of burned gas with high temperatures. For very small *H* (1.0 to 2.5), the maximum local heat flux increased. Decreasing of *Re* lowered these maximums and shifted them slightly away from the stagnation point. Increasing of B_T showed opposite trend. Impact of B_R was negligible.

Similarly, identical experiments were carried out to understand the heat transfer characteristics of impinging partially-inverted flames. Local and area-averaged distributions of heat flux and *Nu* for various geometrical configurations and *Re* and temperature profiles have been obtained. The presence of outer reaction zone is more significant in further nozzle-to-plate distances as it further elongates plateaus with high heat flux and *Nu*. Increasing of *Re* shifted the peaks slightly inwards for higher *H* values, while for small *H* the trend was opposite.

Thermal efficiency is generally lower in partially-inverted flames than in inverted flames and is in the range of 36 - 63 % for inverted flames and 30 - 51 % for partially-inverted flames.

Comparison of both inverted and partially-inverted flames with regular Bunsen flame and Bunsen flame with induced swirl, confirmed the major advantage of rod-stabilized flames, i.e. very uniform heat transfer characteristics over large area of the impinging plate.

Semi-analytical approach has been used to predict convective heat transfer without TCHR from impinging inverted flames onto a target plate using extensive experimental data. Based on boundary layer theory, empirical correlations had been derived for local and area-averaged *Nu* as a function of Reynolds number, nozzle-to-plate ratio and non-dimensional geometrical parameters of the jet.

LIST OF PUBLICATIONS BASED ON THE PRESENT THESIS

Drkos, M., Leung, C. W. and Cheung, C.S (2004) Flammable Characteristics of the Rod-stabilized Laminar Premixed Flame, Proceedings of the seventh Asia-Pacific International Symposium on Combustion and Energy Utilization (7th APISCEU), Hong Kong.

Drkos, M., Leung, C. W. and Cheung, C.S (2007) Flammability Characteristics of the Rod-stabilized Laminar Premixed Flame, Clean Air, Vol. 8, pp. 171-182.

Drkos, M., Leung, C. W. and Cheung, C.S (2008) Flame Stability and Flame Type of Rod-stabilized Premixed Flames, Journal of the Energy Institute, (paper accepted).

ACKNOWLEDGEMENTS

I would like to express my sincere appreciation to my supervisors, Prof. C.W. Leung and Dr. C.S. Cheung for giving me the opportunity to pursuit my postgraduate studies at the Hong Kong Polytechnic University, and also for their guidance and especially patience throughout my study. Their valuable advices on this research topic are appreciated.

Special thanks should be given particularly to Prof. C.W. Leung, who was very patient with me and was helpful when I had to overcome many difficulties in my personal life.

TABLE OF CONTENTS

LIST OF FIGURES

LIST OF TABLES

NOMENCLATURE

A	Lagrangian area
b	distance between rod tip and tube rim (mm)
B_R	rod protrusion, $B_R = b / d_e$
B_T	rod-to-tube ratio, $B_T = D / d_e$
d	rod diameter (mm)
d_e	effective diameter of the burner exit area (mm)
D	bore diameter of the tube (mm)
h	heat transfer coefficient (kW/m^2K)
h	axial distance between tube rim and plate (mm)
h’	axial distance between rod tip and impingement plate (mm)
H	nozzle-to-plate ratio, $H = h/(D- d_e)$
k	thermal conductivity (kW/mK)
LHV	low heating value (kJ / kg)

Nu	Nusselt number
$\dot{q}$	heat flux density (kW / m^2)
$\dot{Q}$	flow rate (m^3 / s)
r	radial distance from stagnation point (mm)
R	dimensionless radial distance from stagnation point, R = r/ d_e
Re	Reynolds number
S	burning velocity (m / s)
T	temperature (K)
u	velocity of butane / air mixture (m / s)
U	flow velocity (m / s)

Greek symbols

α	angle between the reaction zone and the gas flow direction (^{o})
κ	Karlovitz number
η	thermal efficiency (%)
ν	gas mixture kinematic viscosity (m^2 / s)
ϕ	equivalence ratio, stoichiometric to actual air-to-fuel ratio
γ	spread angle (^{o})

ρ	fuel density (kg / m^2)
λ	thermal conductivity (W / mK)
σ	Stefan-Boltzmann constant (W / m^2K^2)
ε	emissivity

Subscripts

bead	of bead diameter
e	effective
exit	at exit position
f	flame
fuel	of fuel
fl	flashback occurs
impgregion	impingement region
max	maximum value
min	minimum value
mix	air / fuel mixture
opt	optimal value
T	tube

Total	total value
R	rim
s	surface
Stagpoint	stagnation point
Stagcircle	stagnation circle
Stagregion	stagnation region
u	of burning velocity
Wallregion	wall-jet region

Superscripts

–	Area-averaged value
~	Weighted mean value

1. INTRODUCTION

1.1. Background and literature review

1.1.1. Flame impingement and its major disadvantage

Flame impingement is more used in comparison with radiative burners due to much higher efficiency of heat transfer distribution. According to Viskanta (1996), forced convection produces up to 98% of total heat transfer; Beer and Chigier (1968) reported that convection contributed 80% to the total heat transferred. It also occurs very rapidly so heat losses are effectively minimized. Moreover, in case of premixed burners, emissions are assumed to be environment friendly. Recently, researchers focus to optimize impinging flame jet design and operating range to achieve the most uniform heat transfer distribution while still using very high efficiency of forced convection to provide rapid heating.

The radiative burners, in which the whole combustion process occurs inside the porous media have a steady, nearly homogenous combustion in quasi-thermal equilibrium. The reaction zone is elongated (internal feedback of the heat occurs), which leads to higher burning velocities and leaner flammability limits. Emission results of NO_x, and partially also CO_x are characteristically low and burner produces

radiative heat that results in uniform heat fluxes along the target surface (Trimis et al., 1999).

In comparison, flame impinging heating can not produce such uniform heat flux and temperature distributions over a large target surface (i.e. flat plate). This turns to be its major disadvantage (Viskanta, 1996).

Uniform heat transfer is significant characteristics in applications where the uniform heating distribution over a large area is required and the efficiency of flame impingement is not the major concern.

The source of this disadvantage might be partly due to negative curvature of regular (Bunsen) type of flame. Hydrodynamic parameters (i.e. velocity and pressure profiles) of round or slot flame jets are similar to isothermal jet. The air / fuel, which exits from the nozzle, creates conically shaped combustion wave in the free jet beyond the tube rim. The conical shape is due to the thermal expansion to the ambient atmosphere that causes a deflection of the gas flow (Lewis and von Elbe, 1987). As the distance from tube rim increases, momentum exchange between the jet flow and the ambient atmosphere causes enlargement of free boundary at the expense of potential core, where hydrodynamic parameters remain the same. Isotherms are convergent and reaction zones merge to create tip of the flame. By summarizing, two main points might be observed as a result:

- Regular flame (i.e. flame stabilized on the rim) has large negative curvature of the reaction zone.

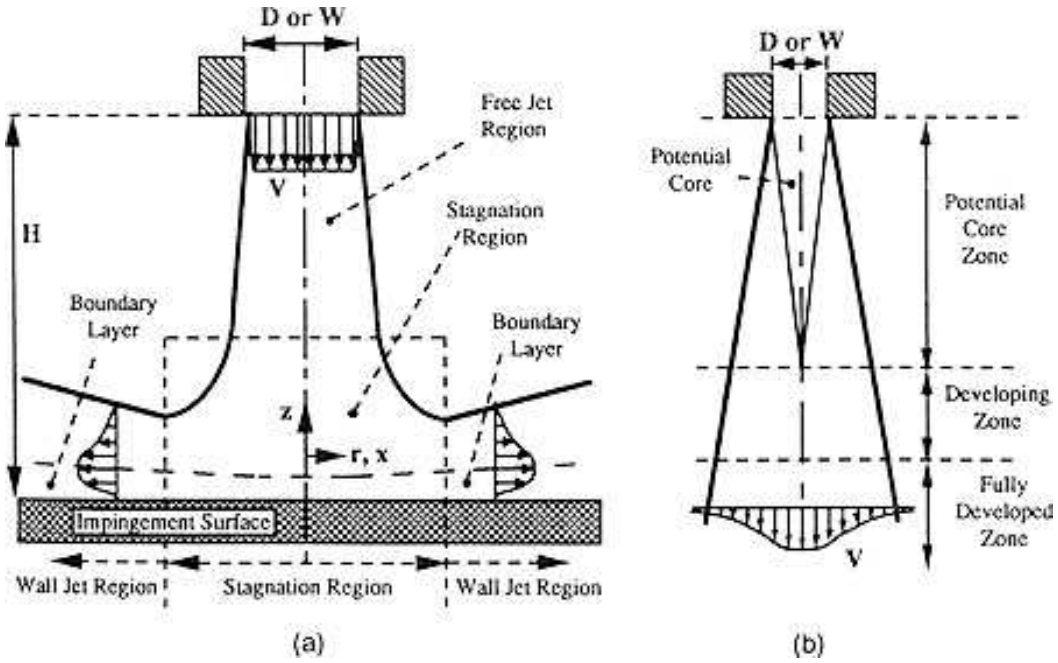

Figure 1.1. a) flow regions for an impinging free-surface jet; b) flow zones of a free jet (Viskanta, 1993).

- Topography to the unburned mixture is concave.

The flame, which impinges on a flat plate, follows free jet dynamics as shown in Figure 1.1. Fully developed free jet flow is established in a short transition zone and is deflected in the stagnation zone while impinging onto the surface. Radial flow is accelerated due to negative gradients of surface pressure. After the pressure gradients disappear, wall-jet region is formed downstream as it has been observed by Kataoka et al. (1984). Due to the presence of reaction zone (in free, stagnation and wall-jet zones), heat transfer occurs between the deflected flow and the surface of the flat plate.

Assuming that type of the burner is the premixed one, target surface is a large flat plate and the specific air / fuel (e.g. LPG / air) is used, impinging heat transfer distribution will strongly depend on the following parameters:

- Reaction zone curvature (defined by nozzle geometry)
- Reynolds number *Re*
- Equivalence ratio ϕ
- Separation distance (nozzle-to-plate-distance *h*)

Influence of last three parameters on heat transfer and their reciprocal dependence has been experimentally and numerically investigated in many previous studies. However, fundamental research of an impact of the combustion wave curvature to the stagnation and radial heat flux distribution, temperature distribution and flame structure has been limited only to regular (Bunsen) flames with negative curvature.

Maximum average heat transfer to the flat plate occurs for:

- Small values of separation distance, if *Re* serves as a reference parameter.
- High values of *Re*, if *H/d* is a reference parameter.

Apparently both cases lack from non-uniformity of heat flux due to existence of a cool central core. This core is directly linked to the potential core.

As investigated by Milson and Chigier (1973) and Baukal and Gebhard (1995), for small values of *H*, nozzle-to-plate distance is smaller than the length of potential

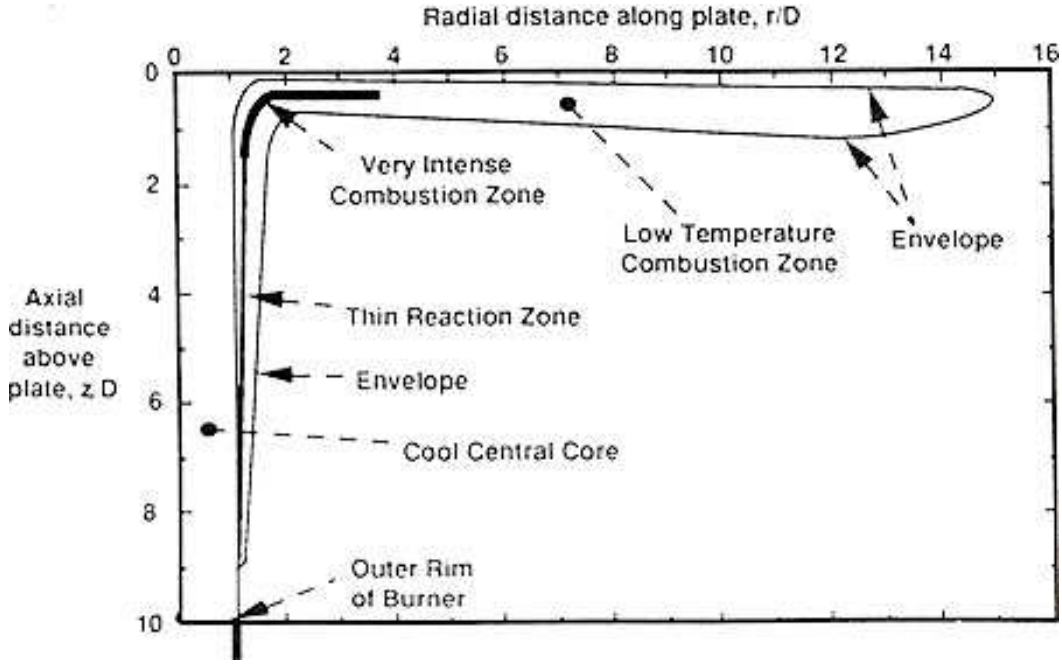

Figure 1.2. Regions of an impinging methane/air flame for *Re* = 7000, *H* = 10 and *Φ* = 2 (Milson and Chigier, 1973).

core, so the hydrodynamic parameters remain unchanged until it is deflected by the impingement plate. Deflection of gas flow is more significant along the entire nozzle-to-plate distance and isotherms tend to be less convergent (parallel) and for very small *H* they diverge from the streamline. Therefore inner reaction zone is being shifted away from the stagnation point and central cool core is widened (Figure 1.1). This has a negative impact on uniformity of heat distribution on the plate. The region around the stagnation point is not burning and maximum heat flux occurs at some distance away from the point. (Figure 1.2).

Increase or decrease of equivalence ratio towards flammability limits of the air / fuel slightly widens the central inner core of cool temperatures by delaying complete

reaction process until positions at larger values of *r/R*, as observed by Posillico and Lederman, (1989). In fact there is negligible influence to the nature of flame.

As previously observed (e.g. Dong, et al. 2001), variations of separation distance *H/d* and *Re* produce either slight improvement or even negative influence to the uniformity of impinging heat transfer. An approach to improve the heat flux distribution has been made by Mohr et al. (1997). Specially designed radial jet, i.e. Radial Reattachment Combustion (RJRC) nozzle, has been used to generate highly turbulent recirculation region between the nozzle and the impinging surface. Such nozzle produces so called reattachment flame. Relatively better results in terms of temperature distribution have been reported.

1.1.2. Rod stabilized flames

Feasible solution to this problem is based on transformation of reaction zone curvature. Promising results in terms of heat flux distribution might be achieved if flame curvature would be changed from negative (concave shape) to positive (convex shape). An axially-mounted solid rod or wire, introduced into a flow, creates such flame. The reaction zone stabilizes above the tip of the rod where burning velocity finds equilibrium with flow velocity, which is reduced by frictional drug inside the boundary layer. Such flame type is often called inverted flame or V-flame. In case the reaction zone stabilizes on the tip as well as on the flame holder rim, flame becomes partially-inverted. Stabilizing rod makes the exit cross-sectional area to be an annulus and instead of a cold central zone of unburned mixture, the

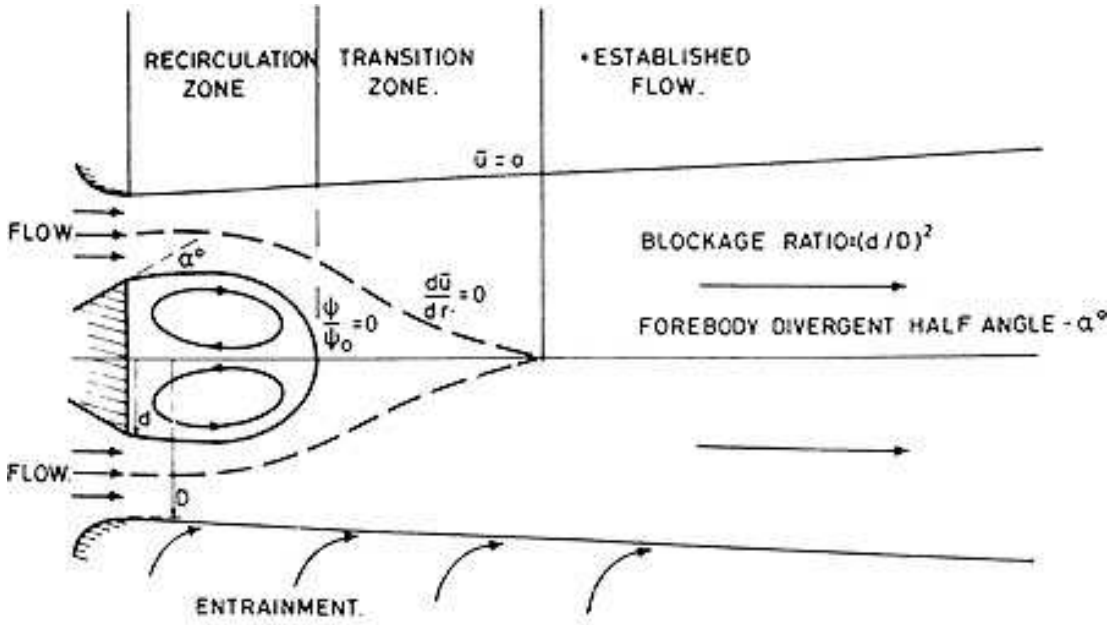

Figure 1.3. Flow system for flow in the wake of a bluff body (Beer and Chigier, 1974).

positively curved and convex inverted or partially-inverted flame creates a zone of burned gas with high temperatures.

Inverted and partially-inverted flames, stabilized on axially mounted rod, are special cases of flames stabilized by bluff bodies. Flow system for the wake of a bluff body inserted into a uniform air is shown in Figure 1.3. It is characterized by the presence of torodial vortex, which is formed within the recirculation zone. The vortex is considered to be a closed loop and its center is the point where static pressure has its minimum. The reaction zone attaches itself to an obstruction (i.e. bluff-body) in the stream, where a decrease of stagnation pressure occurs as a result of pressure drop across the zone. The stagnation pressure is highly reduced and stable vortex pair is formed (Lewis and von Elbe, 1987), as shown in Figure 1.4. The reduction of vortex

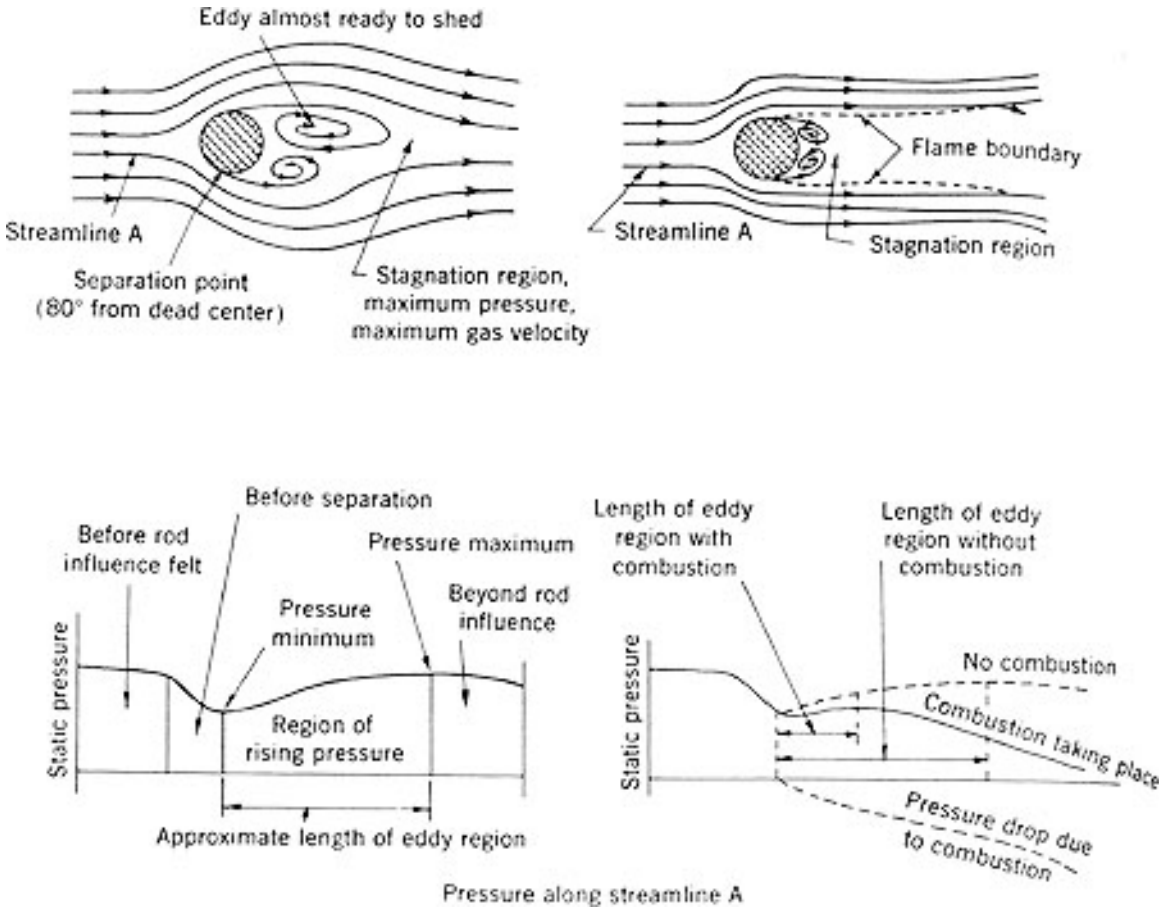

Figure 1.4. Flow around a cross-wise mounted rod; left: no combustion; right: combustion (Lewis and von Elbe, 1987).

size might be also affected by increased viscosity of air / fuel, which helps to transfer the momentum from external flow to the boundary layer.

The most comprehensive source on topic of inverted flames comes from Lewis and von Elbe (1942, 1987). They dealt with boundary velocity gradient theory of flame stability for both inverted and regular flames and carried out experimentally flashback and blow-off limits of inverted flames stabilized above centrally-mounted thin wires (0.643 - 5.36 mm). It has been reported that critical velocity gradients for blow-off are independent of the diameter of wire. They also experimented with flow

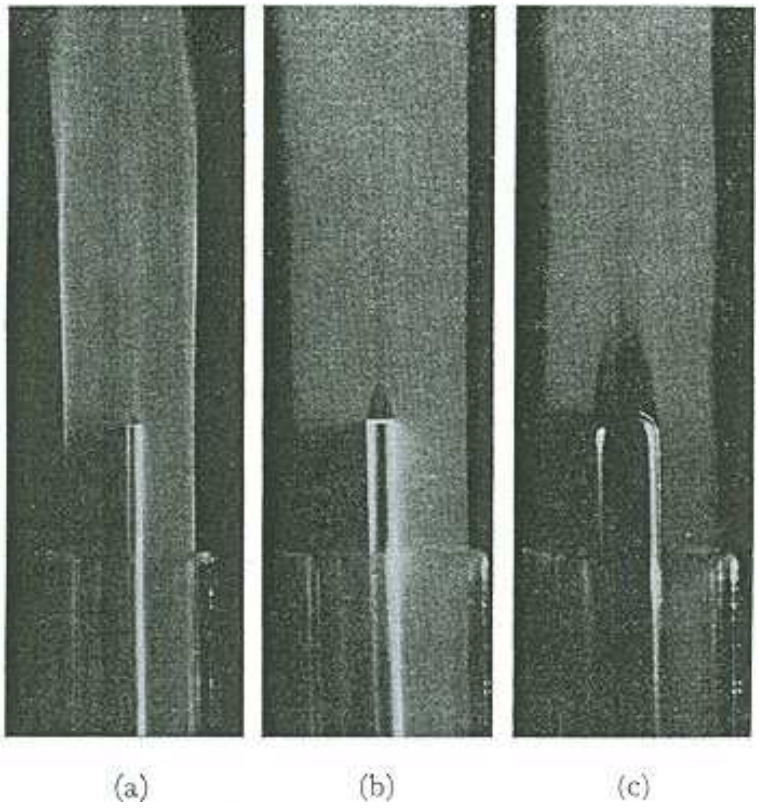

Figure 1.5. Air streams with smoke from tubes with centrally mounted wires, showing annular vortex above wires ((Lewis and von Elbe, 1987).

visualization and reported that the torodial vortices remains stagnant for low Reynolds numbers above the wires as shown in Figures 1.5 and 1.6a. Comparison of ignited and unignited air / fuel flow revealed that torodial eddies in the recirculation zone become very small after reaction zone stabilizes above the wire, as shown in Figure 1.6b. The velocity profile of an air jet with annulus exit area is presented in Figure 1.8.

The concept of flame stretch to describe flame quenching had been introduced by Karlovitz et al. (1953). The flame stretch κ describes flame quenching by strong

velocity gradients. The stretch is represented as the fractional rate change of a Lagrangian flame surface element *A*:

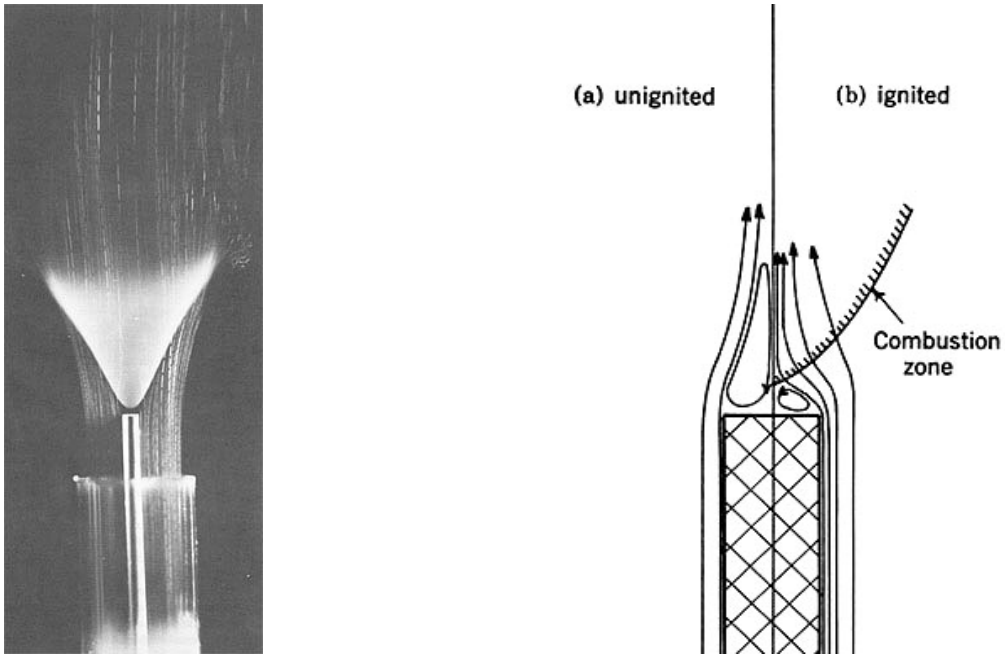

Figure 1.6. a) inverted flame cone with particle tracks; b) streamlines above wire with flat end showing vortex (Lewis and von Elbe, 1987).

$$\kappa = \frac{1}{A} \cdot \frac{dA}{dt} \tag{1.1}$$

The stretch effects are burner dependent and it can be addressed as the regular flame has a negative curvature and negative flame stretch, the positive curvature of inverted flame shows positive stretch rate.

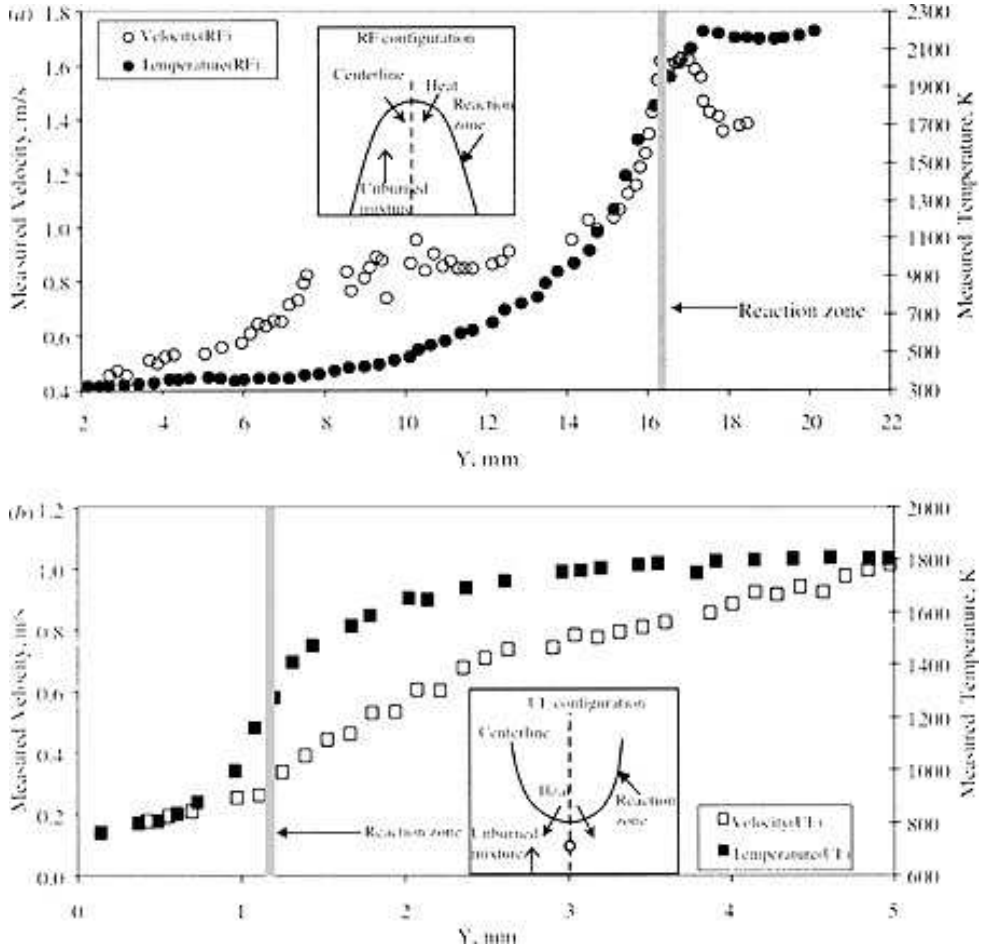

Figure 1.7. Comparison of the centerline temperatures and velocities for methane/air a) regular flame established at Φ = 1.7 and b) inverted flame with 10% nitrogen dilution at Φ = 1.7 (Choi and Puri, 2003).

Recent studies of Choi and Puri (2003) compared flame velocites of positively curved and negatively curved flames burning methane / air and propane / air mixtures. It has been reported that positive curvature of inverted flames is found to induce positive stretch rate, which reduces flame propagation speed by lowering local reaction and generation rates. They also observed that curved inverted flame behaves as a lens that defocuses heat from the burned to the unburned side, but

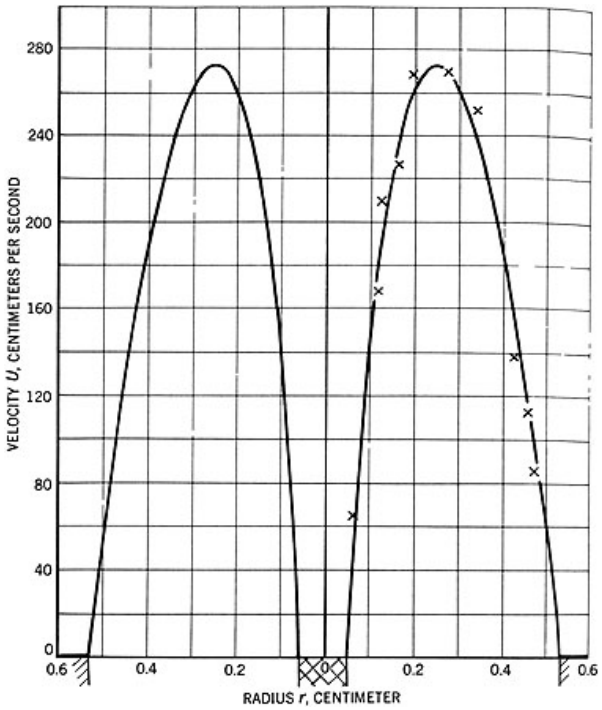

Figure 1.8. Velocity distribution in a laminar stream of air at the orifice of a cylindrical tube in whose axis a wire is mounted. – calculated velocity; x experimental velocity. (Lewis and von Elbe, 1987).

focuses concentration of the deficient reactant (i.e. fuel or air) from the unburned side into the premixed reaction zone. In contrast with regular (Bunsen) flame, which shows opposite behavior: the focusing of heat in the unburned side of negatively curved regular flames raises local temperature in the unburned region and increases upstream flame velocity as seen in Figure 1.7.

Among other studies that focused on investigation of inverted premixed flames, there is a notable study of blow-off limits of inverted flames conducted by Edmondson and Heap (1970). They found out in correlation with Lewis and von Elbe (1987) that the blow-off limits are undependable on diameters of the rod. In

another study, Coghe et al. (2002) experimentally characterized multiple adjacent inverted flames for different equivalence ratios.

1.1.3. Pros and cons of rod-stabilized flames

Convex shape and presence of recirculation zone in inverted flames seem to meet the requirements for heat flux uniformity. Using impinging heat transfer reference parameters (i.e. *Re* and Φ) it might be suggested that:

- For small values of nozzle-to-plate distance *h*, positive curvature of the flame should create nearly uniform heat flux distribution, mainly due to the fact that the space between the reaction zone and the impinging plate is filled with burned gas. That also means the central cool core does not occur and instead the recirculation zone may affect the impinging heat transfer.

- Same effect of increase and decrease of the equivalence ratio towards flammability limits might be observed.

Assuming the pros and cons, impinging flame jet using rod-stabilized configuration may benefit from:

- Nearly uniform heat flux distribution over large area of a target surface.

- Nearly uniform heat flux distribution for small *H* values.

- Optimization of heat flux distribution with accordance to maximum average heat transfer to the flat plate (and vice-versa) by changing geometrical

parameters of the stabilizing rod while keeping values of H, Re and ϕ unchanged.

- Better flame stabilization due to deceleration of flame speed caused by positive flame curvature.

Hence the configuration might cause following potential problems:

- Lower overall efficiency of the burner due to higher minimum value of nozzle-to-plate distance, i.e. in case the rod protrudes over the tube rim.

- Design problems – higher H_{min}, rod asymmetry relative to the tube rim that can cause asymmetrical flow field and flame.

According to the extensive reviews conducted by Baukal & Gebhart (1995) and Viskanta (1993), a study of inverted or partially-inverted flame impinging has not been reported. Hence the study of an impinging air jet, whose exit area is annular has not been reported. Thus this research study is the first one to initiate the investigation in this area.

In recent years, premixed butane / air impinging flame jets, round and slot one, have been extensively studied by Dong et al. (2001, 2002 and 2003) and Kwok et al. (2003). Both studies proved the above mentioned heat transfer dependence on various parameters (i.e. Reynolds numbers, equivalence ratio and nozzle-to-plate distance). These reports can be used to compare experimentally obtained distributions of heat flux, Nusselt number and flame temperature of the rod-

stabilized flame jets with round and slot flame jets as the experiments had been performed using the identical laboratory setup and similar air / fuel mixture.

1.2. Summary

Fundamentals of impinging heat transfer characteristics of round and slot premixed flame jets has been extensively documented by many researchers and these types of burners are widely used in the industry. Flame impingement is very effective but the major drawback is the non-uniformity over the target surface. The reattachment nozzle is one of the attempts to solve this problem. The other one is to use a nozzle with an axially-mounted stabilizing rod, which can produce inverted and partially-inverted flames. However, a few publications about inverted and partially-inverted rod-stabilized premixed flames, which have been published, dealt only with the fundamental research of the free-jet flames and no research studies concerning the impinging rod-stabilized premixed flames has been reported. The present investigation is carried out to fill this gap.

Table 1.1 summarizes main features of rod-stabilized flames that should be able to produce uniform heat transfer distribution when impinged onto a flat plate. Comparison with regular Bunsen type is included.

Inverted / Partially-inverted flames	**Regular (Bunsen) flames**
Axially-mounted rod in the tube – the exit area of the nozzle is annulus.	**The tube only** - the exit area is circular.
Convex topography – the flame front stabilizes itself above the rod tip (and above the tube rim), creating the shape that is convex and opens up towards the impingement plate, avoiding shifting of the reaction zone from the central core.	**Concave topography** – the flame front stabilizes itself above the tube rim, creating concave shape. The tip faces the impingement plate. At small nozzle-to-plate distances, the tip interferes with the plate and the reaction zone is shifted away.
Positive curvature of reaction zone – the products of combustion of high temperature faces the impingement plate along the entire radial distance.	**Negative curvature of reaction zone** – the reactants are situated in the central section. At small nozzle to plate distances, it creates so called cool central core of unburned gas.

Table 1.1. Comparison of main features of rod-stabilized and Bunsen flames.

1.3. Objectives

The aim of the present investigation is to find out the solution of major drawback of flame impingement, i.e. the non-uniformity of heat flux and temperature distributions over a target surface, especially for small nozzle-to-plate distances, where the presence of cool central core is the key negative factor. Thus rod-stabilized flames, whose convex shape, positive flame stretch and positive curvature might provide clear impact on the uniformity of impinging heat transfer distribution, will be used in the present study.

The thesis will provide a comprehensive investigation of rod-stabilized flames. A flame jet with replaceable and exchangeable stabilizing rods will be designed and various geometrical configurations will be used to fully understand flame stability and thermal characteristics. Two principal tasks will be conducted:

Free-jet flames investigation

Flammable and stability characteristics of free-jet flames will be determined and regions of stability will be classified as the function of Reynolds number and equivalence ratio. Effects of the geometrical parameters of the nozzle will be investigated. An analysis of structure and flame shape of rod-stabilized flames will be also performed.

Impinging flames investigation

Study of thermal and flame characteristics of impinging rod-stabilized flames will be carried out. Quantitative effect of impinging parameters (i.e. nozzle-to-plate distance, equivalence, ratio, Reynolds number and geometrical parameters of the nozzle) on stability and uniformity of heat transfer characteristics will be investigated experimentally. Prediction models for impingement heat transfer of rod-stabilized flames that include local and area-averaged characteristics will be developed.

1.4. Thesis organization

The thesis is divided into eight chapters.

Introduction on the topic of rod-stabilized premixed flame is presented in Chapter 1, which contains relevant literature sources on inverted flames and provides background materials for the present study.

Chapter 2 describes experimental setups and instrumentation and procedures for both free-jet and impinging flames. Calculation procedures and analysis of experimental uncertainty are also presented.

Investigation on flammability characteristics of rod-stabilized flames is presented in Chapter 3. Core flame types of rod-stabilized flames are identified, stability characteristics are determined and the effects of various geometrical configurations are investigated.

Chapter 4 provides deeper understanding of flame structure for both inverted and partially-inverted flames, including driving forces of flame stabilization and analysis of flame temperature profiles.

Chapter 5 and 6 deal with heat transfer characteristics of impinging flames. Chapter 5 covers inverted flames and partially-inverted flames are presented in Chapter 6. Obtained experimental data are analyzed and the effects of various parameters on heat transfer are evaluated.

Empirical correlations of impinging heat transfer for inverted and partially-inverted flames are presented in Chapter 7.

Overall discussion and conclusions of the current work are presented in Chapter 8. Ideas and recommendation for future research are provided.

2. EXPERIMENTAL APPARATUS AND PROCEDURES

An experimental apparatus is described individually for both free-jet flame and impinging flame experiments together with detailed overview of burner geometry. Measurement procedures of flammability characteristics, flame temperature profiles of free-jet flames as well as local heat flux and surface temperature measurements of impinging flame are presented. Calculation procedures of local heat transfer and area-averaged heat transfer are determined and correlations have been derived for non-dimensional geometrical parameters. The results of uncertainty analysis confirm practical usability of obtained experimental data.

2.1. Apparatus overview

2.1.1. Free-jet flame setup

Figure 2.1 shows schematically the burner setup used to obtain the regions of flame stability of a free-jet flame. Both fuel, which is supplied from a pressurized fuel tank, and compressed air are metered before mixing. The fuel was a liquefied petroleum gas (LPG), containing 70% of propane (C_3H_8) of butane (C_4H_{10}) and 30% of butane (C_4H_{10}). The measuring system consists of two pressure gauges, and two rotameters, which are calibrated by a piston calibrator to an accuracy of ± 2%. The

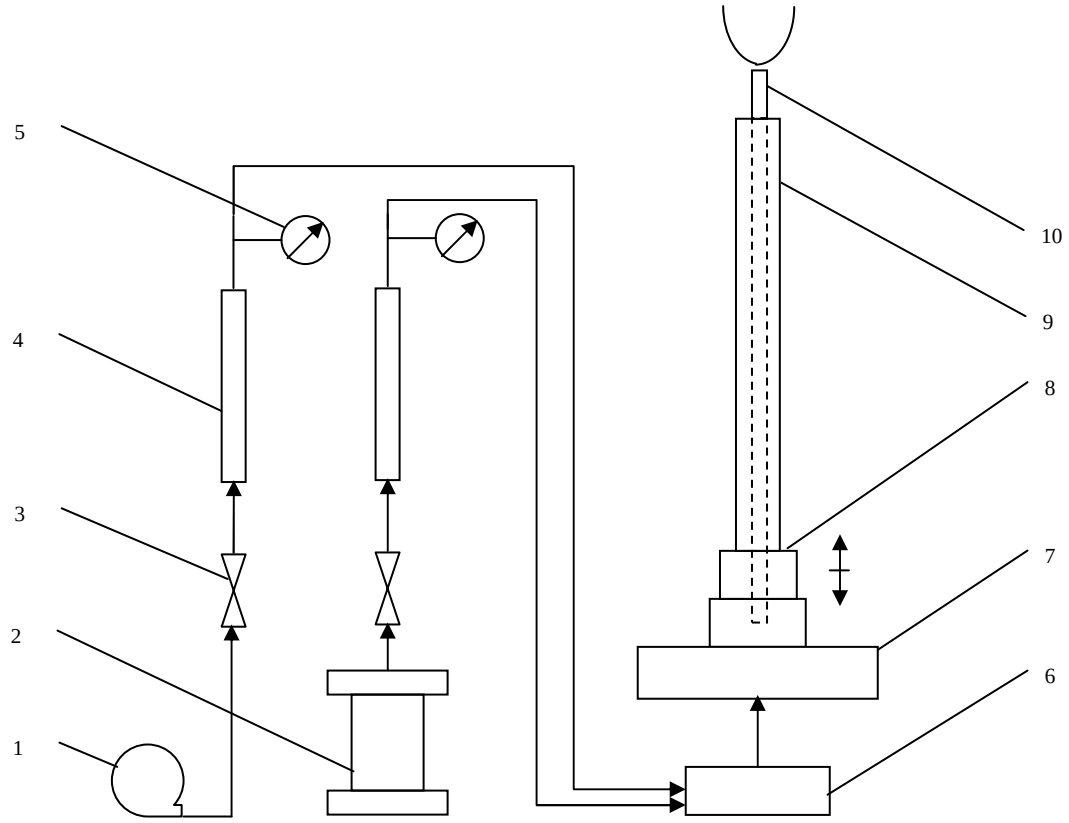

1. Compressed air line
2. Fuel tank
3. Valves
4. Flowmeter
5. Pressure gauge
6. Premixed chamber
7. Equalization chamber
8. Vertical positioner
9. Flame holder
10. Stabilizing rod

Figure 2.1. Schematic of the setup used for the study of the flammable characteristics.

premixed and equalization chambers are filled with stainless steel mesh, enabling more uniform flow and arresting the flashback.

The flame holder is made up from a tube and an exchangeable and adjustable stabilizing rod. The tube is 30 mm long with a bore diameter of 19.55 mm and a thickness of 1.5 mm thickness. A vertical positioner enables the attached tube to change its height relative to the rod. Solid rods are of 9.55, 8.00, 6.45 and 4.00 mm in diameter.

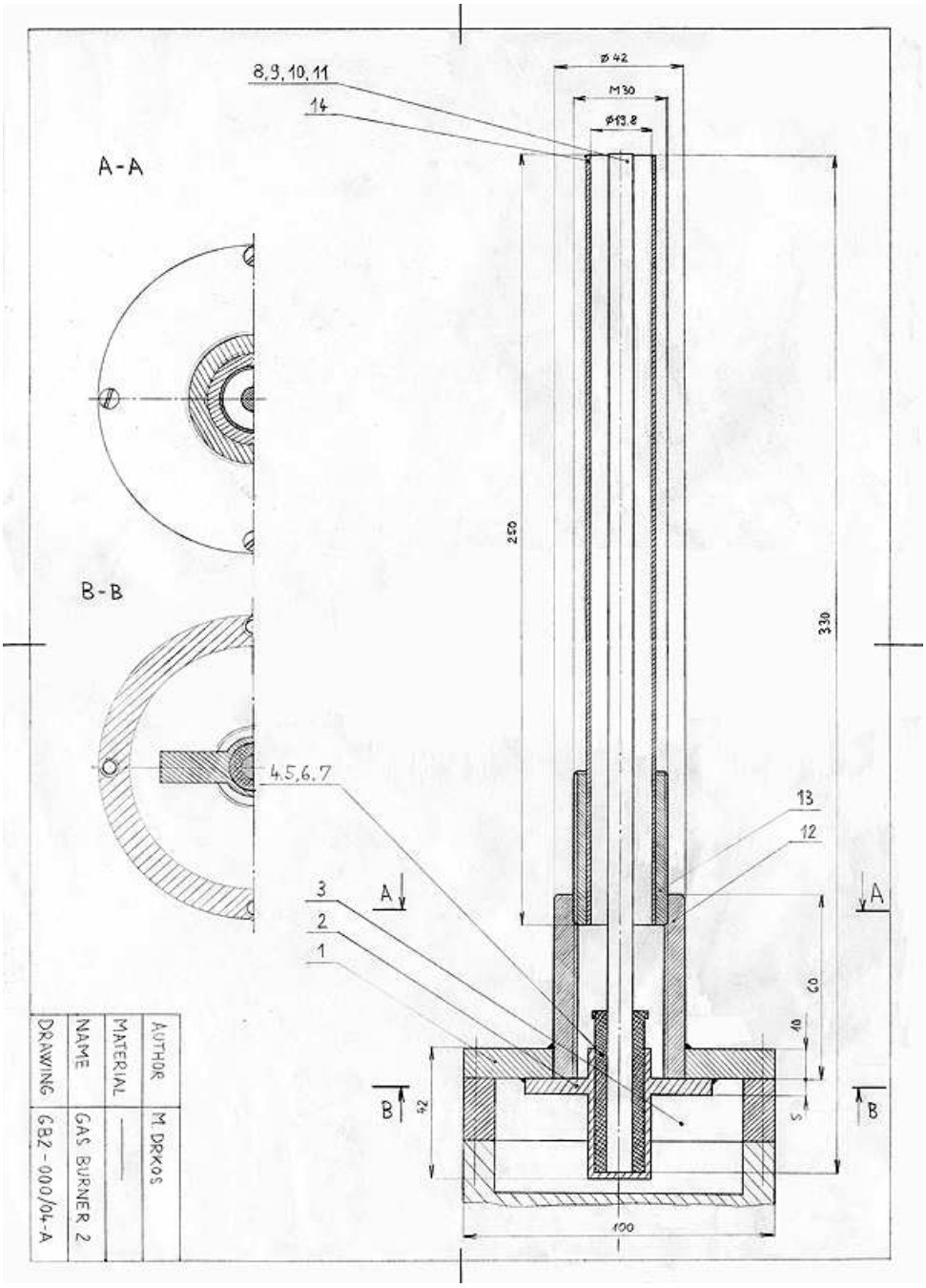

Figure 2.2. Assembly drawing of the burner.

A special designed core is axially-mounted and attached to the bottom of the tube for the insertion of a rod. The tolerance of concentricity, measured at the tip of the

rod, is within ± 0.5 mm. Concentricity of the rod has been measured and adjusted prior to every set of experiments in order to assure the accuracy of the data. Both tube and rods are made of selected brass with very smooth surface to achieve more uniform velocity profile. The assembly drawing of the burner is shown in Figure 2.2.

Temperature profiles have been obtained by measuring flame temperatures with a bare wire B-type thermocouple with Pt - 30% / Rh as the positive lead and Pt - 6% / Rh as the negative lead. It was calibrated by OMEGA company that provided voltage-to-temperature conversion chart.

A gas-fired micro-torch with maximum flame temperature of 1300^0C was employed as an ignition source.

2.1.2. Impinging flame setup

The laboratory burner setup for the impinging heat transfer study is schematically shown in Figure 2.3. A 3-D positioner enables the burner to change its horizontal (radial) position relative to stagnation point and its height towards the impinging plate.

The impingement surface is a flat square plate with a side of 500 mm and thickness of 8 mm. The tested area is circular, located within the square plate. It is made of copper, thus ensuring good thermal conductivity. A stainless steel frame supports the plate and maintains its horizontal position relative to the burner. Top of the plate is cooled by water, which is heated up to constant temperature of 38^0C to avoid the condensation of moisture in the combustion products on the impingement plate.

A Vatell HFM-6 D/H microsensor with rapid response time (6±2 µs), has been used as a heat flux transducer and to measure the surface temperature. The effective sensor face (of 3 mm in diameter) is embedded into the plate, centered and leveled symmetrically with the impinging surface. It consist of an inner thermopile heat flux sensor (HFS) that is responsible for heat flux measurement and the surrounding resistance temperature sensing element (RTS), made of thin platinum film. The output voltages are amplified using a battery-powered Vatel AMP-6 amplifier. A/D conversion is carried out by IOtech Personal Daq, an USB Data acquisition module. Time-averaged data has been recorded for each data point consecutively for period of 30 s at a frequency of 3 Hz.

The same bare wire B-type thermocouple with Pt-30% / Rh as the positive lead and Pt-6% / Rh as the negative lead has been used to measure flame temperatures of impinging flames.

Both heat flux sensor and B-type thermocouple were calibrated by respective manufactures. Heat flux sensor was calibrated by Vatell Corporation that provided a calibration certificate valid with specified validity that provided all the information necessary to convert the signals from the sensor to their heat flux values with accuracy +-3%. B-type thermocouple was calibrated by OMEGA company that provided voltage-to-temperature conversion chart.

The ambient temperature in the air-conditioned laboratory was maintained constant at 19.5 ± 0.5^{0}C during the experimental investigation.

Photographs were made with 35 mm Nikon F60 analog camera, using Nikkor AF lens 50 mm with a constant aperture of 5.6 and shutter speed at 1/250 and 1/15.

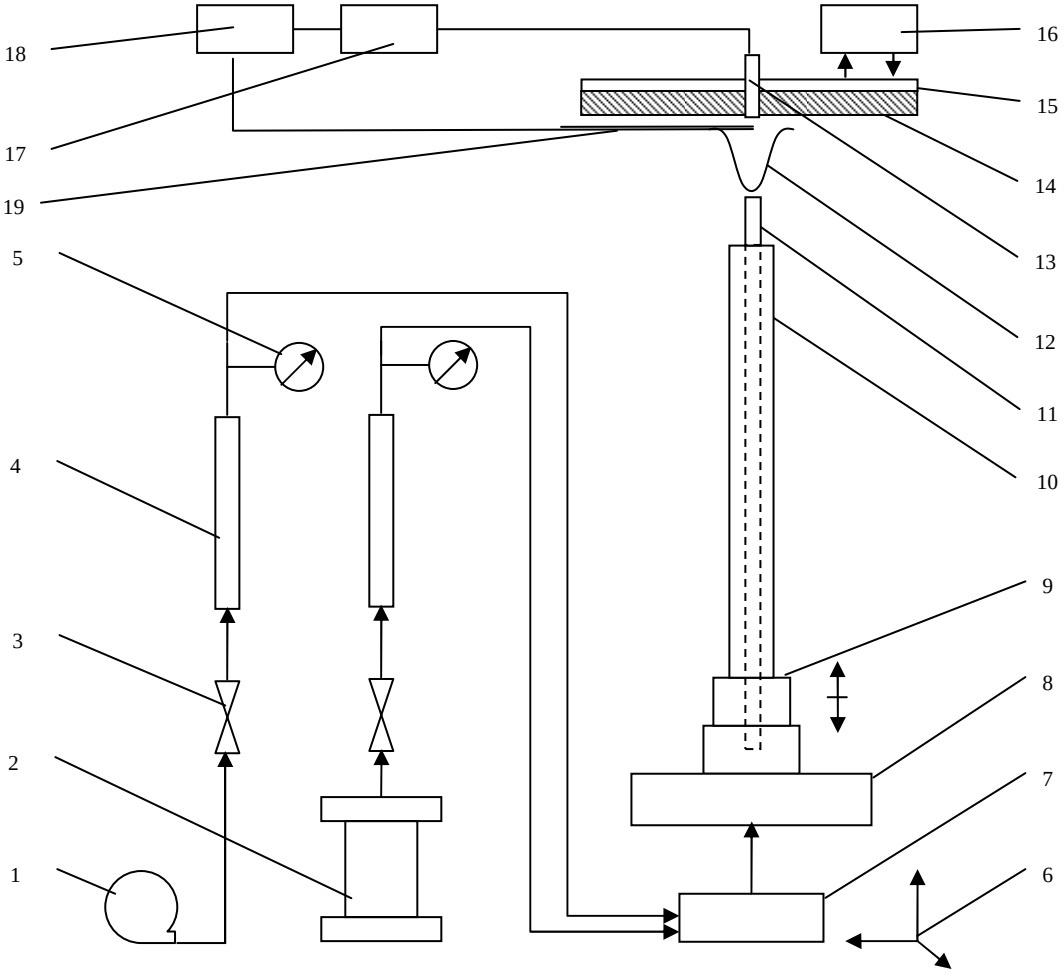

1. Compressed air line
2. Fuel tank
3. Valves
4. Flowmeter
5. Pressure gauge
6. 3D positioner
7. Premixed chamber
8. Equalization chamber
9. Vertical positioner
10. Tube
11. Stabilizing rod
12. Flame jet
13. Impinging plate
14. Heat flux sensor
15. Thermostat
16. Water-cooling system
17. Amplifier
18. A/D converter
19. B-type thermocouple

2.2. Experimental procedures

2.2.1. Flammable characteristics measurement

In order to cover the operating range of the experimental setup, the measurements were performed for the equivalence ratio ranging from 0.1 to 3.0, with a step of 0.1. Reynolds number was varied from 100 to 3600 at moderate low pressure. Flames remain predominantly laminar up to *Re* ~ 2000, for higher *Re* noticeable flickering characteristics of a turbulent flame appears.

For the present investigation there were three rod protrusions used, i.e. B_R = 0, 1 and 2, whereas the rod-to-tube ratio varied from 0.51 to 0.80. In the first investigation, diameters of tube and rod were maintained constant. However the rod diameter was varied at constant tube diameter in the second investigation.

Blow-off data were obtained at selected *Re* by progressively decreasing the fuel flow rate until the blow-off occurred. For the data points obtained nearby the flashback region, the flame holder had been cooled in between measurements for sufficient time by applying only the air flow at high pressure.

To observe the effect of ignition position on the flame characteristics, the flame ignition had been subsequently conducted from two vertical distances about 10 mm and 50 mm from the burner rim as shown in Figure 2.4. For each vertical distance, two radial directions (tangential and secant) of the ignition source (i.e. flame torch) relative to the flow had been investigated.

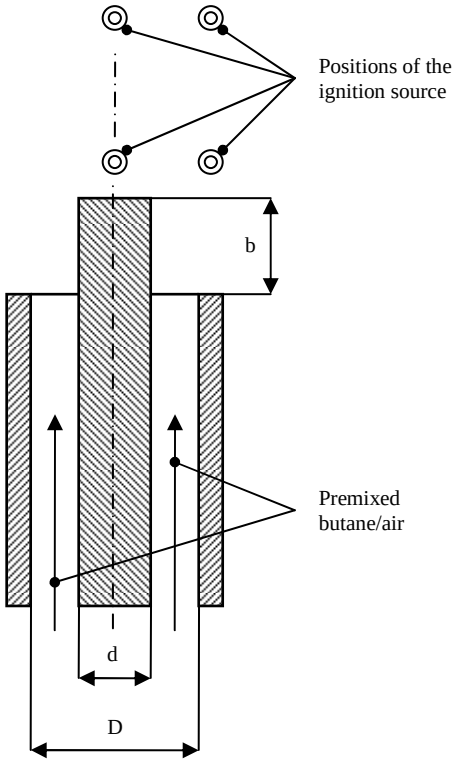

Figure 2.4. Geometrical dimensions of the flame

2.2.2. Flame temperature measurements

Temperature profiles of free-jet flames and flame temperatures of impinging flames have been obtained by shifting the burner in radial direction and axial direction with a resolution of 2 mm and only half-plane has been measured due to the flame symmetry. Measurements of temperature profiles were conducted at *Re* = 2000 with equivalence ratio of 0.9 and 1.4 for inverted and partially-inverted flames respectively. Flame temperatures of impinging flames have been obtained at axial distance of 1 mm from the impingement plate.

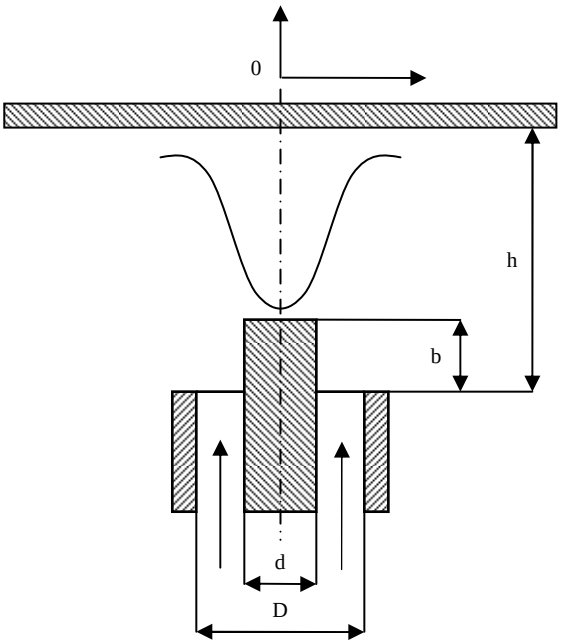

Figure. 2.5. Geometrical dimensions of the impinging flame.

2.2.3. Local heat flux and surface temperature measurements

Radial heat flux distributions have been obtained by shifting the burner in radial direction from the stagnation point (where the microsensor is situated) with resolution of 2 mm for r = 0 – 20 mm and 4 mm for r > 20 mm. The flame symmetry allows measurements at one specific radial direction only. Surface temperature measurement, utilizing identical microsensor, has been obtained simultaneously.

Values of equivalence ratio and Reynolds number for each type of the flame have been selected in accordance with Figure 3.1 and are with specific regions (Region I for inverted flames and Region III for partially-inverted flames). Constant

equivalence ratio of 0.9 and 1.4 has been set for inverted and partially-inverted flames respectively.

The effect of Reynolds number had been investigated for both types of the flame for identical values of *Re* = 1600, 1800, 2000, 2200, 2400 and 2600 at two specific values of *H* = 1.0 and 3.0. The influence of nozzle-to-plate ratio has also been carried out for both types at constant *Re* = 2000, with values of *H* ranging from 0.5 to 4.0 with a step of 0.5.

Measurements of effects of rod protrusion and rod-to-tube ratio have been obtained at constant *Re* = 2000 for each type of the flame. Rod protrusion varied from 0 to 2 and has been investigated for *H* = 1.0 and 3.0, while rod-to-tube ratio investigation has been carried out at *H* = 4.0.

2.3. Calculation procedures

2.3.1. Effective nozzle diameter calculation

With reference to Figure 2.5, effective diameter for the annulus cross-sectional area of the burner nozzle is defined as:

$$d_e = D - d \qquad \text{(mm)} \qquad (2.1)$$

Hence, nozzle-to-plate ratio *H* and non-dimensional radial distance from stagnation point R are expressed as:

$$H = \frac{h}{d_e} \qquad (2.2)$$

And

$$R = \frac{r}{d_e} \tag{2.3}$$

Consequently, Reynolds number is calculated from:

$$Re = \frac{u_{exit} \cdot d_e}{v} \tag{2.4}$$

2.3.2. Rod protrusion calculation

Two additional non-dimensional parameters have been introduced to facilitate the definition of geometrical configurations as shown in Figure 2.5. The rod protrusion B_R denotes the non-dimensional height of the rod tip above the tube rim, defined as a ratio of axial distance between rod tip and tube rim relative to the effective diameter:

$$B_R = \frac{b}{d_e} \tag{2.5}$$

2.3.3. Rod-to-tube ratio calculation

Likewise, a non-dimensional parameter B_T (rod-to-tube ratio) represents a variability of the flow area and is defined as a ratio of the effective diameter relative to the tube bore diameter:

$$B_T = \frac{d_e}{D} \tag{2.6}$$

2.3.4. Flame temperature correction

Bradley and Matthews (1968) suggested that conduction losses can be neglected for fine wires longer then 1 mm. Hence the measured values of flame temperature have been corrected for radiation heat losses only, according to the method suggested by Friedman (1953). Corrected flame temperature has been derived from heat balance for an unshielded spherical thermocouple in a hot gas stream:

$$T_f = T_t + \frac{\varepsilon \cdot \sigma \cdot d_{bead}}{Nu \cdot \lambda} \cdot (T_t^4 - T_a^4) \qquad [^0\mathrm{C}] \tag{2.7}$$

For *Re* ranged from 0.01 to 10 000, *Nu* is determined from:

$$Nu = 0.42 \cdot \mathrm{Pr}^{0.2} + 0.57 \cdot \mathrm{Pr}^{0.33} \cdot \mathrm{Re}^{0.5} \tag{2.8}$$

With bead diameter equal to 0.254 mm and assumed emissivity of 0.1, the maximum correction was less then 70 K.

2.3.5. Area-averaged heat flux calculation

With axisymmetric distribution of local heat flux, the area-averaged heat flux is calculated as function of non-dimensional radial distance *R*:

$$\bar{\dot{q}} = \frac{2 \cdot \int_0^R \dot{q} \cdot R \cdot dR}{R^2} \qquad [\mathrm{kW/m^2}] \tag{2.9}$$

The total heat transfer from the flame jet to the impinging plate could be determined by measuring the cooling water's flow rate and its temperature rise when passing through the water jacket.

However, in the case of the present experimental setup, it is more complicated as the heat flux sensor couldn't be immersed into water and there is a significant space between the transducer and the water tank that makes up large amount of tested area.

The water cooling has been installed due to following reasons:

- Not to overheat the impinging plate and more importantly not to overheat the heat flux sensor that operates only at certain temperatures)
- To avoid condensation

In the present experiments, the cooling water temperature has been maintained constant at 38^0C and flow rate has been kept constant due to already enough variable parameters at the study.

In order to achieve repeatability, measurements were only made when steady-state conditions had been achieved.

Recent studies have been investigating the effects of different cooling temperatures and flow rates on the total heat transfer rate. It includes the quenching effect. This effect has been also observed when the flame was ignited before steady-state conditions were met.

2.3.6. Nusselt number calculation

Local heat transfer coefficient is expressed from:

$$h = \frac{\dot{q}}{(T_f - T_s)} \qquad [\text{kW/m}^2\text{K}] \qquad (2.10)$$

where T_f is flame temperature, T_{sl} is impingement surface temperature. Consequently, in non-dimensional form, h can be calculated as local Nusselt number:

$$Nu = \frac{h \cdot d_e}{k(\tilde{T})} \tag{2.11}$$

Where k is thermal conductivity of hot gas as a function of temperature $\tilde{T}$. By substituting Equation 2.10 into Equation 2.11, Nu can be expressed as:

$$Nu = \frac{\dot{q} \cdot d_e}{(T_f - T_s)k(\tilde{T})} \tag{2.12}$$

Area-averaged Nusselt number can be expressed by substituting Equation 2.9 into Equation 2.12:

$$\overline{Nu} = \frac{2 \cdot \int_0^R \dot{q} \cdot R \cdot dR}{R^2 \cdot (T_f - T_s)} \cdot \frac{d_e}{k(\tilde{T})} \tag{2.13}$$

2.3.7. Thermal efficiency calculation

To facilitate overall thermal performance of the impinging flame, thermal efficiency can be calculated from:

$$\eta = \frac{\overline{\dot{q}} \cdot \pi \cdot r^2}{2 \cdot \dot{Q}_{fuel} \cdot \rho_{fuel} \cdot LHV} \quad [\%] \tag{2.14}$$

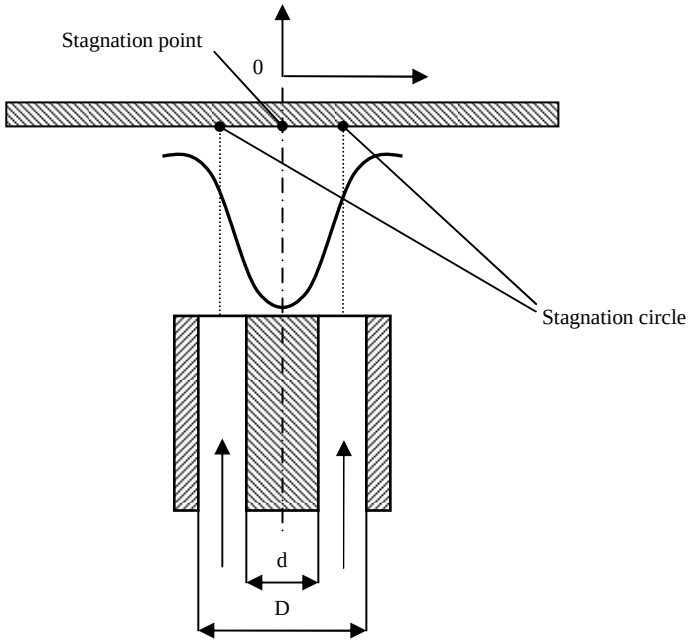

Figure. 2.6. Determination of stagnation circle.

where $\dot{Q}_{fuel}$ is flow rate of fuel (m^3 / s), ρ_{fuel} is fuel density (kg / m^3) and LHV stands for Low Heating Value (kJ / kg) of the fuel. The fuel was a liquefied petroleum gas (LPG), containing 70% of butane (C_4H_{10}) and 30% of propane (C_3H_8).

It is assumed that heat loss to the surrounding is constant and input energy is the chemical energy of the fuel.

2.3.8. Stagnation circle determination

In addition to stagnation point, a stagnation circle is introduced to facilitate the surface impingement of a jet, which exit area has a shape of an annulus.

Analogically, stagnation circle theoretically determines the points where the flow is fully arrested. Envelope of stagnations points forms a circle (Figure 2.6). Position of stagnation circle on the impingement plate can be calculated from:

$$r_{stagcircle} = \frac{D+d}{4} \qquad \text{[mm]} \tag{2.15}$$

2.4. Experimental uncertainty analysis and repeatability

2.4.1. Uncertainty due to calculation

The total uncertainty in calculated values was estimated using root-sum-square (RMS) method, suggested by Moffat (1998) and Figueroa et al. (2005). It was assumed that the uncertainties were known to 95% confidence. Assuming that the measured parameters X_i and their absolute uncertainties U_{xi} are independent of one another, the total uncertainty for any calculated quantity:

$$\frac{U_y}{Y} = \sqrt{\sum \left(\frac{X_i}{Y}\frac{\delta Y}{\delta X_i}\right)^2 \left(\frac{U_{x_i}}{X_i}\right)^2} \tag{2.16}$$

Where U_y is the absolute uncertainty in calculated quantity, Y is maximum value of the quantity.

The parameters with their corresponding uncertainty percentages are given in Table 2.1. The total uncertainty for B_R, B_T, H and R was 2.2% at 95% confidence level. For both equivalence ratio and *Re*, the total uncertainty was 6.2% at 95% confidence level.

Parameter	*Uncertainty percentage*
Effective diameter of the burner exit area, d_e	2%
Distance between rod tip and tube rim, b	1%
Distance between the nozzle and the plate, h	1%
Radial distance from stagnation point, r	1%
Dynamic viscosity of air, μ_{air}	4%
Dynamic viscosity of fuel, μ_{fuel}	4%
Density of air, ρ_{air}	1%
Density of fuel, ρ_{fuel}	1%

Table 2.1. Parameters and their uncertainty percentage.

2.4.2. Uncertainty due to instrumentation

Table 2.2 summarizes accuracy of instruments used during experimental investigation. The overall uncertainty of heat flux measurement due to instrumentation was 5.1%, while for the surface and flame temperature it was 4.5% and 0.3% respectively.

Instrument	*Accuracy*
Heat flux microsensor	3%
Amplifier gain - temperature channel	1.5% (for gain = 500)
Amplifier gain - heat flux channel	2.1% (for gain =1000)
B-thermocouple	0.25%
Air flowmeter (603)	2%
Fuel flowmeter (605)	2%
Pressure gauge	2%
Personal Daq	0.015% (of reading)

Table 2.2. Instrumentation accuracy.

2.4.3. Repeatability

Experimental sets have been repeated accordingly, using the identical operational conditions, in order to ensure the repeatability.

As for heat flux and surface temperature measurement, each set of experiments has been repeated three times, and the results were then averaged. Maximum standard deviations of the local heat flux were less than 6% of the mean value, while for surface temperature it was less than 2%.

Temperature profiles set has been taken three times, with maximum standard deviation of less then 2% of the mean value.

For the flammable characteristics, the process has also been repeated three times, with exception of data points nearby blow-off curve and inter-regions, where more than a single flame type can be induced. Here the flame stabilization has had been repeated ten times in order to provide 90% confidence level of the measurement.

3. FLAMMABILITY CHARACTERISTICS OF FREE-JET FLAMES

The present investigation was performed to determine quantitatively the operating range and the characteristic regions of flame stability of a rod-stabilized premixed free-jet flame. Various geometrical configurations had been tested and the influences in changing the rod protrusion and rod-to-tube ratio had been reported. The influence of the position of the ignition source in producing a flame in the inter-regions had also been studied.

3.1. Classification of regions with stable flame

Collected data points at various Reynolds numbers and equivalence ratios are plotted and presented in Figure 3.1. As mentioned above, the rod-stabilized flames present complex characteristics and are very sensitive to variations of Reynolds number and equivalence ratio. As a result, three different types of stable flame can be identified: inverted flame for lean mixtures, partially-inverted flame for stoichiometric and rich mixtures and regular (Bunsen) flame for very rich mixtures. These regions, however, overlap with each other, creating so called inter-regions, where more than a single flame type can be induced. As shown from the diagrams, regions I, III and V are those with the occurrence of only a single flame type, while areas II and IV

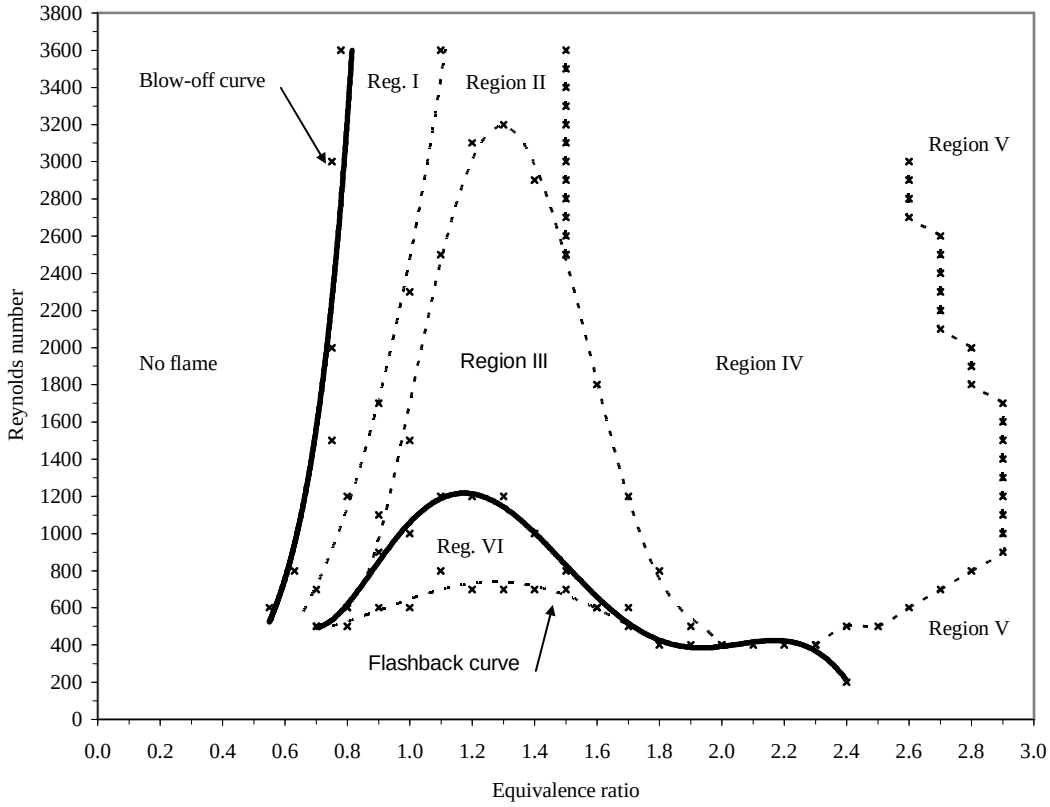

Figure 3.1. Diagram of the characteristic regions of flame stability for d = 9.55 mm, B_R = 0.

represent inter-regions. Concerning the location of stabilization, the reaction zone can be stabilized either on the rod tip (an inverted flame) or at the tube rim (a regular flame), or even both (partially-inverted flame). The shape of partially-inverted flames is affected by *Re* as described in the later section. Particular regions and inter-regions of stable and unstable flames are classified, summarized and further discussed in the following sections.

3.1.1. Effect of position of ignition source

It has been observed that for the inter-regions II and IV, which exist between those with only a single flame type, i.e. Regions I, III and V, different flame types may occur due to different positions of the ignition source: axial distance from the rod tip and radial distance from the axis (Figure 2.4). As shown in the Region II, if the ignition source is in a close axial distance to the rod tip and its radial distance is close to zero (the ignition flame intersects the z-axis), a very high chance for the flame to be stabilized at the rod tip to create only an inverted flame. However, when the ignition source is positioned at a certain radial distance away from the z-axis and the direction of the flame torch is secant or tangent, the reaction zone tends to stabilize itself also at the tube rim to create a partially-inverted flame. As shown in the Region IV, a similar behavior can be observed. An intersectional ignition creates both reaction zones and hence a partially-inverted flame, whereas the tangential ignition produces only one reaction zone stabilized at the tube rim giving a regular flame. Their interpretations are described below in separate paragraphs as there are several driving forces behind the common one: the flow velocity distribution. Moreover, experimental uncertainties of these observations may be decreased if a point ignition source, such as a hot wire, is used instead of a flame torch.

3.1.2. Region I – Inverted flame

The area, where only the inverted flame can exist, is limited by the steep blow-off curve. Its size has been observed to be the widest (between Φ = 0.55 – 1.1) for the most stable geometrical configuration (B_R = 0 and d = 9.55 mm). The ability to

operate at such lean mixtures is mainly due to the absence of the diluent effect of ambient atmosphere (Lewis & von Elbe, 1987). It is also affected by the cross-sectional shape of the jet and the convex shape of the flame: the rod tip is surrounded by the air / fuel mixture with a flow field of large velocities, which prevents the surrounding air to enter and dilute the air / fuel mixture. It extends the blow-off region down to the value at which the flame stabilized at the tube rim will already be blown off. Such a flame is shown in Figure 3.2a.

3.1.3. Region II – Inverted and partially-inverted flames

With an increased percentage of gaseous fuel in the mixture, the fuel-rich flame meets the conditions that the reaction zone can be stabilized at both the rod tip and the tube rim. For low Reynolds numbers and equivalence ratios, the flame is attached only partially to the rim but not for the entire rim perimeter. As mentioned earlier, the effect of the position of ignition source is significant on the flame type. Closer axial and radial distances of the source to the rod tip means that the flame is stabilized at the rod only. Besides, placing the source at the tangential direction and an axial distance further away from the tube rim creates a partially-inverted flame. This phenomenon seems to be more complex. It is primarily due to distribution of the flow velocities and consequently dilution of the air/fuel mixture by the surrounding air. As mentioned earlier, due to the annulus shape of the jet, the rate of dilution above the rod tip remains relatively small in comparison with that at the burner rim. At constant Reynolds number but variable equivalence ratios, the reaction zone blows off at the burner rim first. In fact, the borderline between

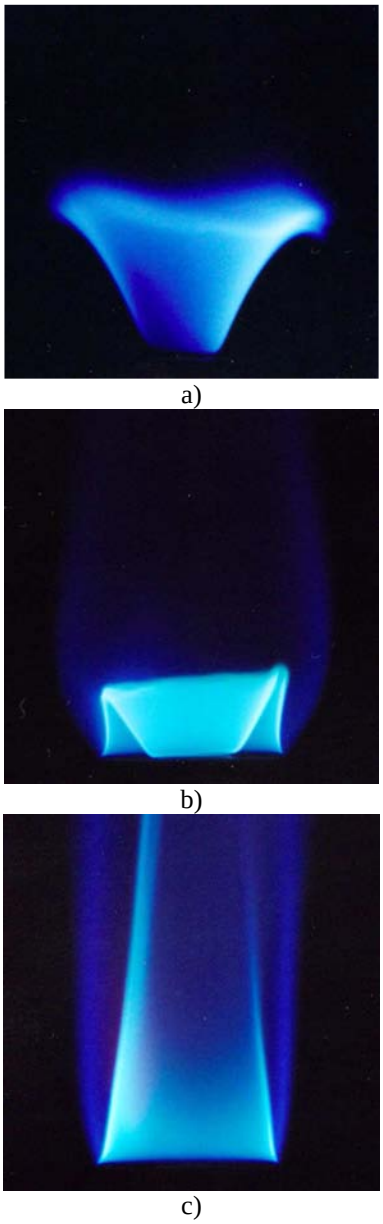

Figure 3.2. Photographs of three fundamental flames at Re = 2000, d = 9.55 mm, B_R = 0; a) inverted flame (Φ = 0.9); b) partially-inverted flame (Φ = 1.4); c) regular (Bunsen) flame (Φ = 1.9).

Regions I and II can be assumed as the “partial” blow-off curve as its data points are the critical values for blow-off to occur at the rim. Thus in case of the intersectional

ignition within a certain axial distance, high dilution of the air/fuel mixture nearby the rim does not allow upstream propagation of the burning zone towards the rim and therefore only the inner reaction zone is stabilized. It may also be taken into account that the separation of inner and outer reaction zones at higher Reynolds numbers as shown in Figure 3.3a, which is due to the turbulent nature of the air / fuel flow. Another factor to be considered is the differences in flame shape and flame stretch: the inner reaction zone is an inverted flame, which is positively curved and is of a convex shape, whereas the outer reaction zone (a regular flame) is negatively curved and is of a concave shape.

3.1.4. Region III – Partially-inverted flame

It represents the conditions, in which both the inner and outer reaction zones can be stabilized, creating a partially-inverted flame. The flame shape is highly affected by the Reynolds number: at higher *Re*, the flames start to flicker and eventually separate due to the enhanced turbulence. The region is limited by a peak value of *Re* = 2900 to 3400. Data points close to the intersection of Regions II, III and IV give the values of *Re* and Φ, at which all three main types of the flame can be stabilized. Figure 3.2b presents the partially-inverted flame with both reaction zones connected, while the inner and outer waves are partially-separated on the right hand side as shown in Figure 3.3a.

3.1.5. Region IV – Partially-inverted and regular flames

For fuel-rich mixtures of equivalence ratio between 1.5 and 2.5, it is possible to generate either the partially-inverted or regular (Bunsen) flame. Effect of the

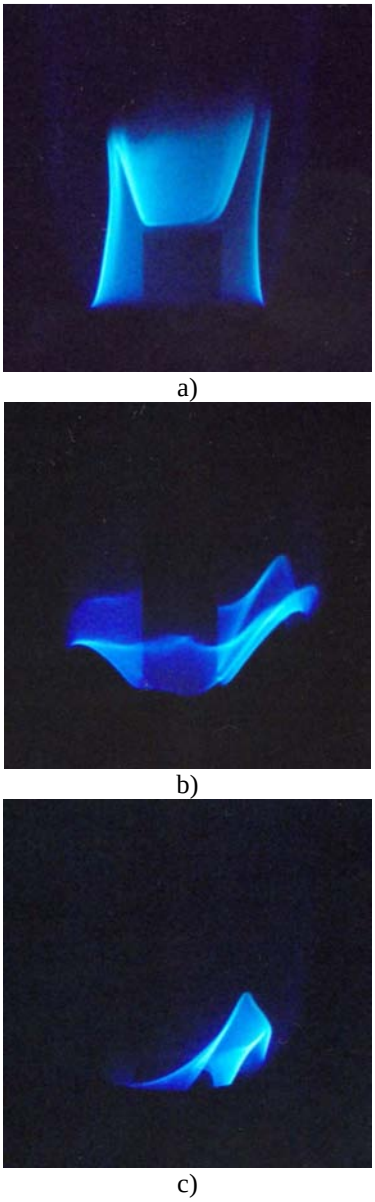

Figure 3.3. Photographs of flames at constant d = 9.55 mm; a) separation of combustion waves in partially-inverted flame (Re = 2000, Φ = 1.6, B_R = 1); b) upstream propagation of inverted flame (Re = 2000, Φ = 1.3, B_R = 2); c) upstream propagation of tilted flame with an asymmetric distortion (Re = 1100, Φ = 1.3, B_R = 0).

position of the ignition source is similar to those in the case of Region II: locating the source at the tangential direction and an axial distance further away from the rim helps stabilizing only the outer reaction zone to create a regular flame, while putting

the source at a closer axial distance and the intersectional direction enables generating the partially-inverted flame. Similar to the Region II, the high flow velocity field prevents the surrounding air to enter the inner part, thus, resulting in a deficiency of air in the air/fuel mixture. For the tangential ignition at further distance, both factors suppress the upstream propagation of burning zone towards the rod tip, so the conditions for stabilizing the inner reaction zone are not established. For the intersectional ignition at closer distance, the deficiency of air is easily observable as the inner zone is distinctly less luminous. The outer and inner reaction zones are separated and with an increased equivalence ratio, the inner wave becomes narrower and thinner due to the further reduction of air.

3.1.6. Region V – Regular (Bunsen) flame

For very high Φ from 2.2 to 2.8, only a regular (Bunsen) flame with yellowish tip can exist as shown in Figure 3.2c. For very fuel-rich mixtures there is not enough surrounding air to penetrate into the central region. Under such conditions, the inner reaction zone does not occur and the flame is stabilized at the burner rim only. Low flow velocities (Re < 1000) shift the border line of Region V towards lower values of Φ and a similar but slighter effect can be observed for higher Reynolds numbers for all geometrical configurations of B_R and B_T.

3.2. Classification of regions with unstable flame

Apart from the blow-off curve and flashback areas, the unstable region VI is characterized by time-delayed and relatively slow upstream propagation of the flame, resulting in flashback.

3.2.1. Region VI – Inverted flames, partially-inverted flames and flashback

The area above flashback, with an occurrence of the "tilted" flames, can be observed in round or slot jets (Lewis and von Elbe, 1987). However, in the case of rod-stabilized flames this region appears to be more profound. When the flow rate becomes sufficiently small, the inner reaction zone occurs much closer to the rod tip. With increased temperature of the rod, preheating of the unburned air/fuel mixture takes place inside the burner tube. Quenching effect of the rod and the tube wall is reduced and the flame starts to propagate upstream and consequently heats the rod and the tube wall, and eventually develops into flashback. Heating of the rod is very rapid, because of the enormous heat transfer directly from the surrounding flame. Thus, it is highly recommended to avoid this unstable area by applying higher flow rates. It is possible to partly eliminate this region by cooling the stabilizing rod and the tube wall sufficiently. Occurrence of this region is at an equivalence ratio in the range from 0.7 to 1.7 for all geometrical configurations, with the peak values occurred around Φ = 1.1 to 1.4. For higher values of Φ, the region reduces significantly and becomes negligible, and flashback develops almost immediately at the critical value of *Re*. It should be taken into account that for higher Reynolds numbers (*Re* > 2000), due to the high flow velocities, the upstream flame propagation is sufficiently delayed.

3.2.2. Flashback

The flashback curves have been plotted to include the data points at which the flame starts to penetrate into the tube immediately after ignition. For Φ > 1.7, the curve is

assumed to be identical with the boundary line of the Region VI. The upper limits generally occur at Φ = 1.2 to 1.5 for all geometrical configurations.

3.2.3. Blow-off curve

The blow-off curve is very steep and it occurs within a narrow range of equivalence ratio ranging from 0.55 to 0.83. In relation to the blow-off aspect, the inverted flames show significant advantage: they can operate with very fuel-lean mixtures. Such advantage has also been suggested in other studies (Edmondson and Heap, 1970; Coghe et al., 2002). It has been suggested by Lewis & von Elbe (1942), that a larger rod diameter retains the flame better due to the appreciable reduction in gas velocity.

Flame oscillation phenomenon can be observed near the blow-off region. One of the explanations is that it may be caused by a slight fluctuation of the pressure to which the blow-off is very sensitive.

3.2.4. Area of extinction

The butan/air mixture at Φ from 0.55 to 0.83 produces no flame. Data points at Re < 500 for fuel-lean and stoichiometric mixtures, Re < 400 for fuel-rich mixtures, and Re < 100 for very fuel-rich mixtures have not been recorded by using the present experimental setup.

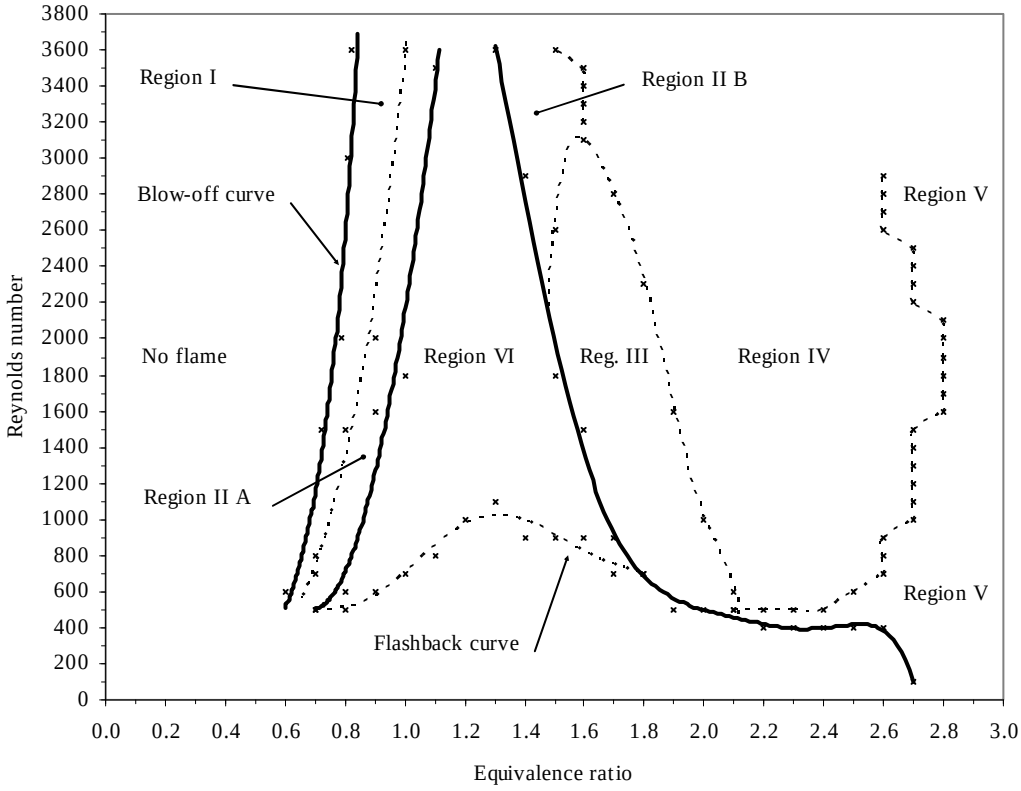

Figure 3.4. Diagram of the characteristic regions of flame stability for d = 9.55 mm, B_R = 1.

3.3. Effect of rod protrusion

Size and shape of the regions vary as function of the rod protrusion as shown in Figures 3.4 – 3.5. Influence on Regions I, IV and V was observed to be negligible. Considerable effects on other regions are summarized below:

- If B_R is increased, part of the Region II becomes unstable and these data points are included in Region VI. Thus in case of B_R = 1 (as shown in Figure 3.4), the region is split into two parts. When B_R = 2 (as shown in Figure 3.5), part A even vanishes entirely. The lowest peak value at Re = 1200 denotes the most stable

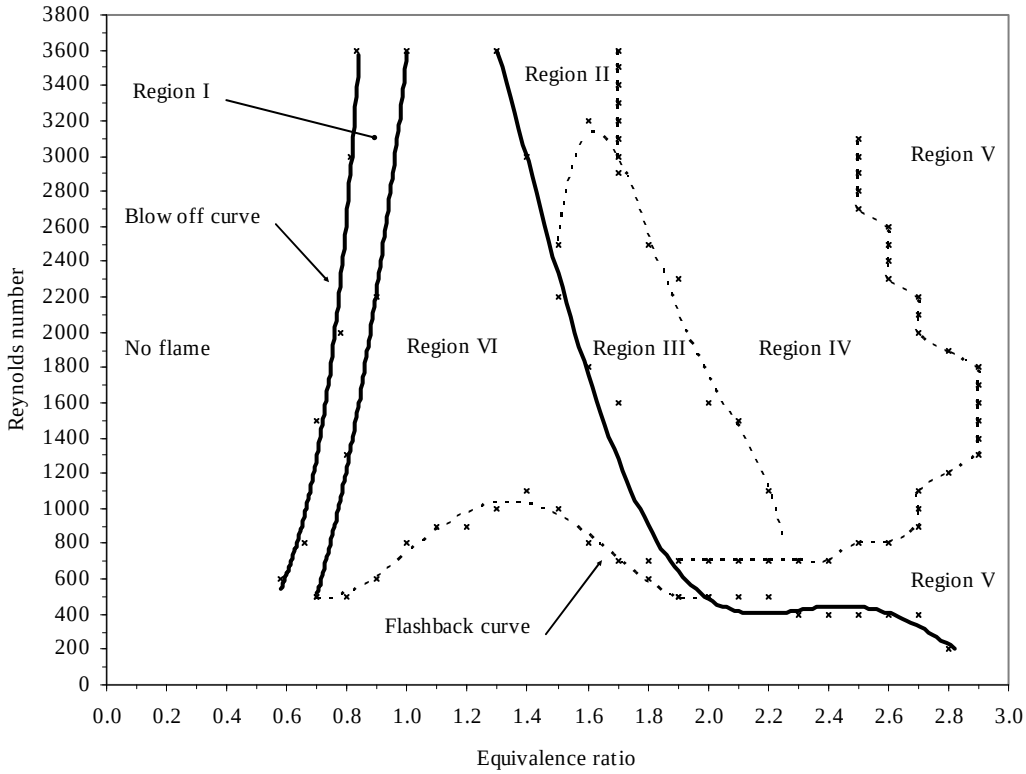

Figure 3.5. Diagram of the characteristic regions of flame stability for d = 9.55 mm, B_R = 2.

configuration (B_R = 0, d = 9.55 mm). The upper limit of equivalence ratio (i.e. Φ = 1.4), which is in fact the maximum value for the inverted flame to be stabilized is lowest at B_R = 0 and increases up to Φ =1.7 at B_R = 2.

- Lower limits of the Region III are considerably dependable on B_R. When B_R increases, there is a size reduction of the region and it is simultaneously shifted towards the higher values of Φ (up to 2.2).

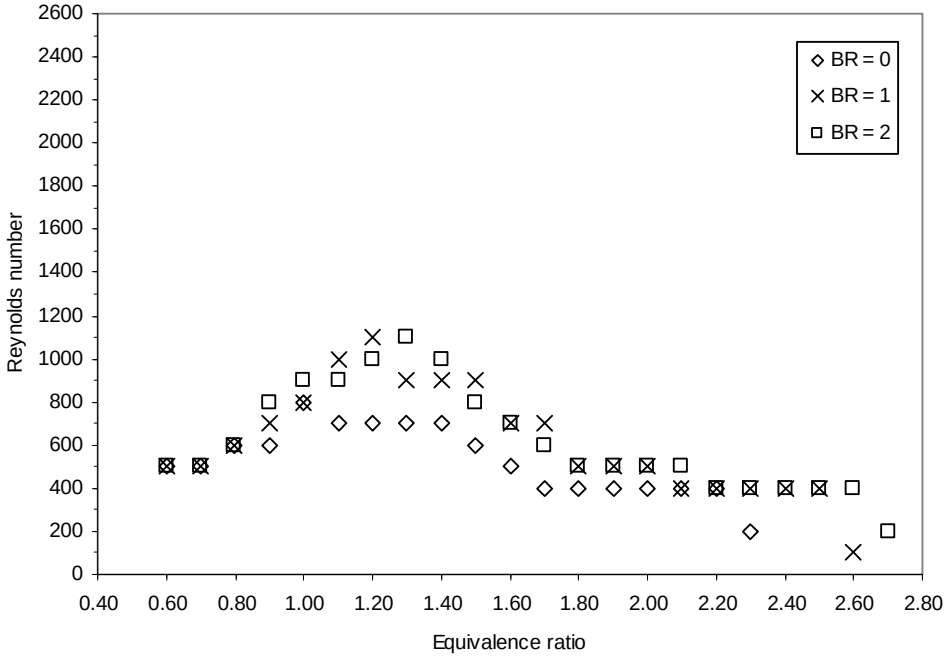

Figure 3.6. Critical data points for flashback at constant d = 9.55 mm.

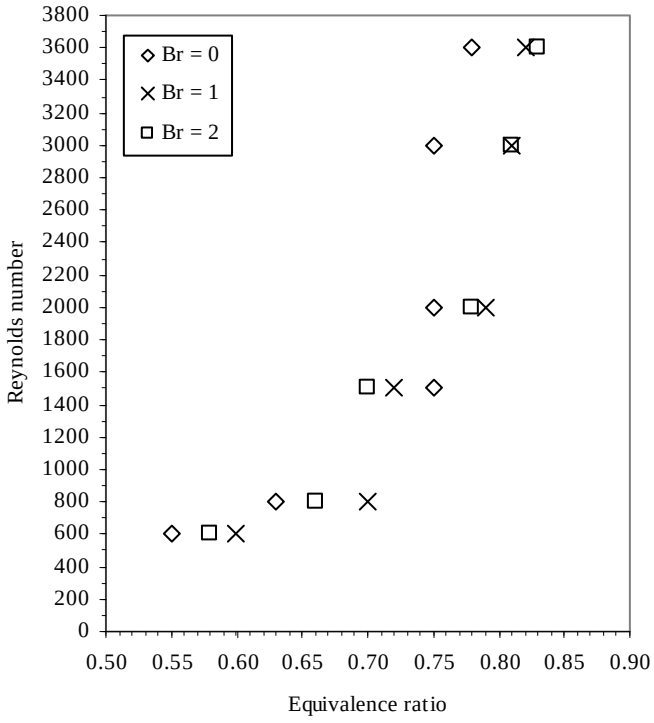

Figure 3.7. Critical data points for blow-off at constant d = 9.55 mm.

- The smallest size of the unstable Region VI is obtained at B_R = 0 with the upper limit of *Re* at about 1200 as it is seen from Figures 3.4 and 3.5. With increased value of B_R and for higher Reynolds numbers, it extends at the expense of the Region II as the upper limits of *Re* are occurred beyond the operating range of the present setup. The decrease of flow velocity with further distance away from the tube rim is the reason behind. The originally stabilized flame can be either partially-inverted or inverted, however, it turns into an inverted flame just before entering the tube rim during the heating-up process. Figures 3.3b and 3.3c show the photographs of flames which propagate upstream for different B_R: inverted flame at B_R = 2 and the tilted flame with an asymmetric distortion at B_R = 0, respectively.

- At B_R = 1 and 2, value of *Re* at which flashback occurs will be increased to higher values in comparison with that at B_R = 0 (Re_{fl} = 1100 at B_R = 1 and 2, and Re_{fl} = 700 at B_R = 0), as in Figure 3.6.

- Effects of B_R on blow-off are demonstrated in Figure 3.7. For B_R = 1 and 2, the blow-off curves are steeper in comparison with those for B_R = 0. For higher values of B_R, the flames will be affected more due to a dilution of the air/fuel mixture by the surrounding air and also the reduced gas velocity at an axial distance further away from the tube rim.

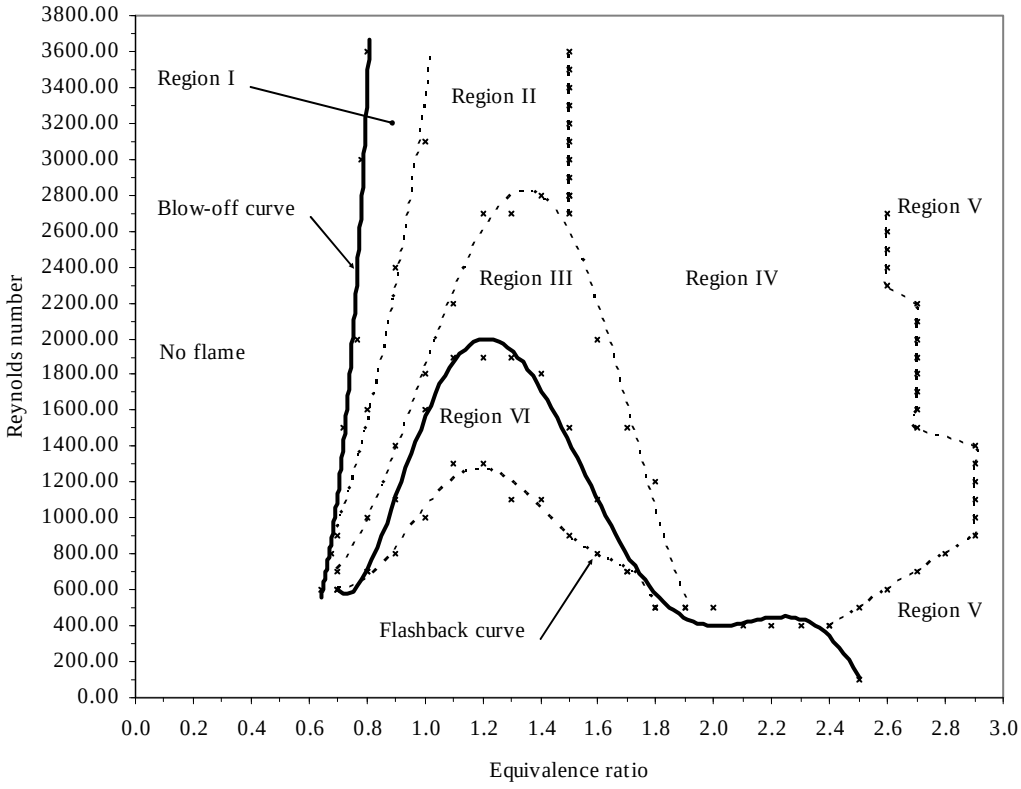

Figure 3.8. Diagram of the characteristic regions of flame stability for d = 8.00 mm, B_R = 0.

3.4. Effect of rod-to-tube ratio

Similarly, characteristic regions of flame stability with variation of rod-to-tube ratio are shown in Figures 3.8 – 3.10. Regions IV and V are assumed to be unchanged and as shown in Figure 3.11, for the conditions at which the blow-off occurs, the effect of B_T is almost negligible. Summary of considerable effects on other regions is presented below:

- An increase of B_T reduces the Region I slightly to the range within Φ = 0.6 to 0.9.

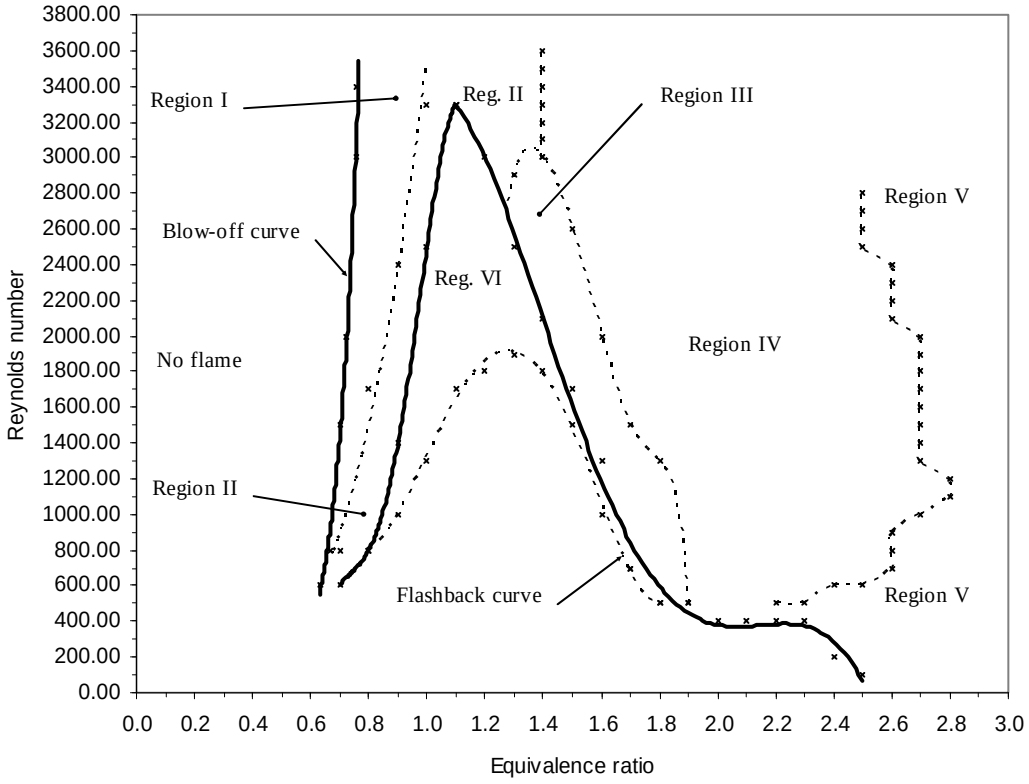

Figure 3.9. Diagram of the characteristic regions of flame stability for d = 6.45 mm, B_R = 0.

- The effect of B_T on the Region II is slightly similar to the influence of B_R. The difference is that the stable area is split only for the smallest rod diameter (4.0 mm), as shown in Figure 3.10. The borderline convergence indicates the peak values will be obtained somewhere beyond the operating range of the setup. The upper limit of equivalence ratio (i.e. Φ = 1.4) is lowest at smaller diameters, and increases up to Φ =1.7 at bigger diameters.

- Similarly with an effect of B_R, the lower limits of the Region III are dependable on B_T. With B_T increases, data points for lower flow rate exhibit unstable behavior and consequently become part of the Region VI, reducing significantly

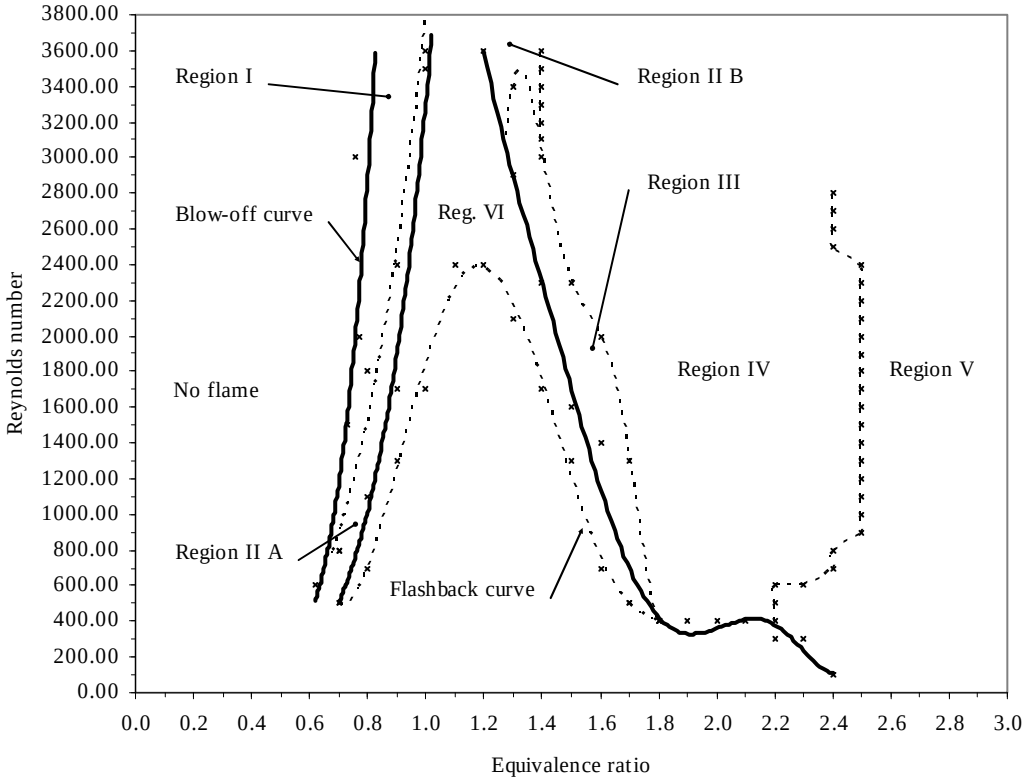

Figure 3.10. Diagram of the characteristic regions of flame stability for d = 4.00 mm, B_R = 0.

the area of the partially-inverted flames to a narrow strip as shown in Figures 3.9 and 3.10. However there is no shift of the region towards the higher values of Φ as in the case of the effect of B_R.

- With the Region VI, larger cross-sectional areas (smaller rod diameters at the constant tube diameter - higher B_T) shift the upper limits towards the higher values of *Re*, which will be beyond the present operation range. Also, the heat conduction for thinner rods is higher, which speeds up the upstream propagation of the flame.

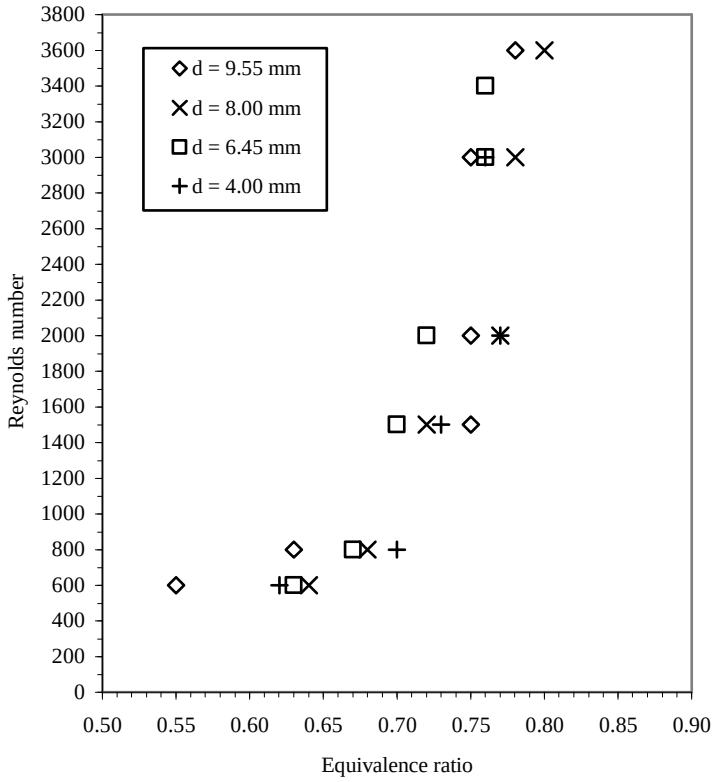

Figure 3.11. Critical data points for blow-off at constant $B_R = 0$.

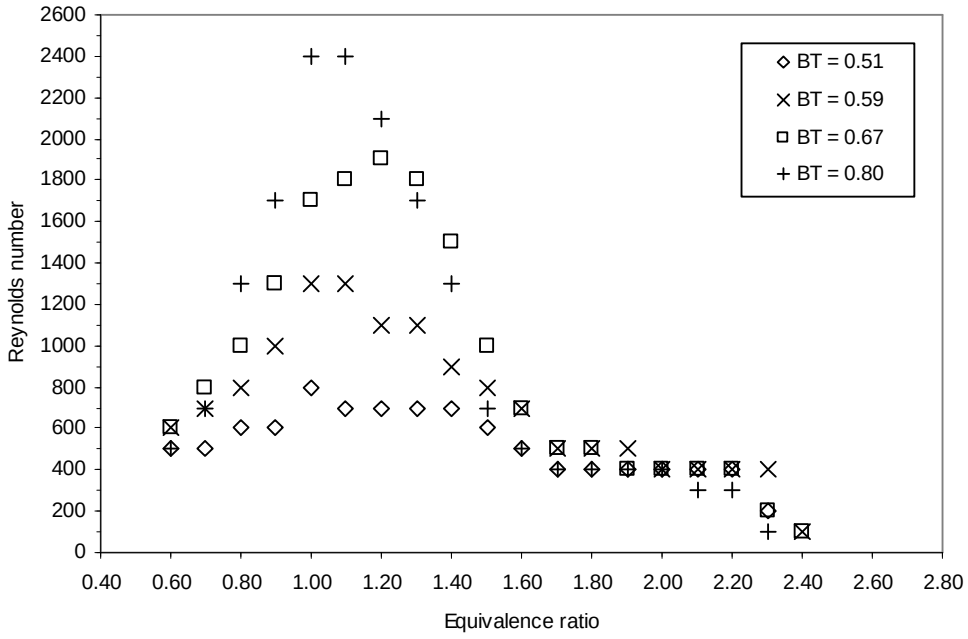

Figure 3.12. Critical data points for flashback at constant $B_R = 0$.

- At the same time, with an increase of B_T, the upper limits of flashback are shifted towards the higher values of *Re*. They generally occur at Φ = 1.2 to 1.5 for and vary from minimum *Re* = 700 (obtained at *d* = 9.55 mm) to maximum *Re* = 2400 (obtained at *d* = 4.00 mm) as in Figure 3.12.

3.5. Summary

1) Experimentally determined stability data indicates three fundamental types of premixed butane/air flame which can be stabilized by using an axially-mounted stabilizing rod: inverted, partially-inverted, and regular (Bunsen) flames. In dependence of equivalence ratio Φ, data points obtained from a stable flame are divided into five stable regions: inverted flames (Region I) exist predominantly in fuel-lean mixtures, while partially-inverted flames (Region III) and regular flames (Region V) appear in fuel-rich and very fuel-rich mixtures, respectively. Between the overlapping areas, inter-regions (Regions II and IV) are characterized by the availability of more than one stabilized flame.

2) As for the inter-regions, it is shown that the explicitness of whether the reaction zone can be stabilized at the burner rim (regular flame), at the rod tip (inverted flame) or at both positions (partially-inverted flame), is certainly affected by the axial and radial positions of the ignition source. The situation becomes more complex when there are other parameters involved. In the Region IV, cross-sectional ignition at closer distance creates both reaction zones, while tangential ignition at a further distance can only stabilize the flame at the burner rim and a deficiency of air in the air/fuel mixture is the main reason. Certainly, disturbance

from the high velocity distribution across the flame jet is another major cause. In the Region II, apart from radial distance and axial direction of the ignition source, the high rate of dilution with surrounding air, the steep flow velocity distribution across the flame jet, the different shapes of flame and the separation of reaction zones at high Reynolds numbers should also be considered.

3) There is an elongated unstable area (Region VI) above the flashback curve, at which lower flow velocity causes the inner reaction zone of the originally partially-inverted flame to heat up the rod tip, thus reducing the quenching effect. Consequently, it propagates upstream to induce a slow motion flashback. The size of this region is strongly affected by the height of the rod tip above the tube rim, expressed by the non-dimensional rod protrusion (B_R). Increase of B_R results in widening of the region at the expense of the stable regions, as the flow velocity decreases and the rod tip is more exposed to the surrounding air.

4) Similarly, a negative impact on the size of the stable regions has been observed for another non-dimensional parameter, rod-to-tube ratio (B_T), which represents the variation of rod diameter for a constant tube bore diameter. With an increase of B_T (use of a smaller rod diameter), a bigger cross-sectional area is obtained, which increases the size of the Region VI and the occurrence of a higher rate of heat conduction makes the flame propagating upstream faster. Flashback limits are also shifted up. Hence the default configuration of the largest diameter (d = 9.55 mm) and B_T = 0 appears to be the most stable condition among all tested configurations.

5) The influences of both B_R and B_T on blow-off limits appear to be less significant. Variation of B_T shows negligible effect while higher values of B_R tend to move the blow-off curve towards higher Φ because of the higher rate of dilution of the air/fuel mixture by the surrounding air. However, the accuracy may also be affected by a low resolution of the flowmeters, which should be avoided. In comparison with the round and slot flame jets, a rod-stabilized burner can operate with very fuel-lean mixtures (up to Φ = 0.55), which is a definite advantage in terms of emissions, since the generation of NO_x and CO emissions can be reduced.

4. STRUCTURE AND TEMPERATURE PROFILES OF FREE-JET FLAMES

Out of the three characteristic flames identified in Chapter 3, inverted flames (Region I &II) and partially-inverted flames (Region III) have been further studied as they present significant types that can be used in the practical solutions.

Prior to the study of impinging flames, it is essential to understand the structure and flame shape of each flame type, which is the goal of this chapter. The effects of *Re*, Φ, B_R and B_T on flame shape are also described.

Temperature distributions of both flame types were recorded as a function of radial distance and temperature profiles were plotted for selected heights. These were used to identify the structure of each flame type in relation to geometrical design of the flame jet. Based on that, the regions of free-jet flame for each particular flame type are determined.

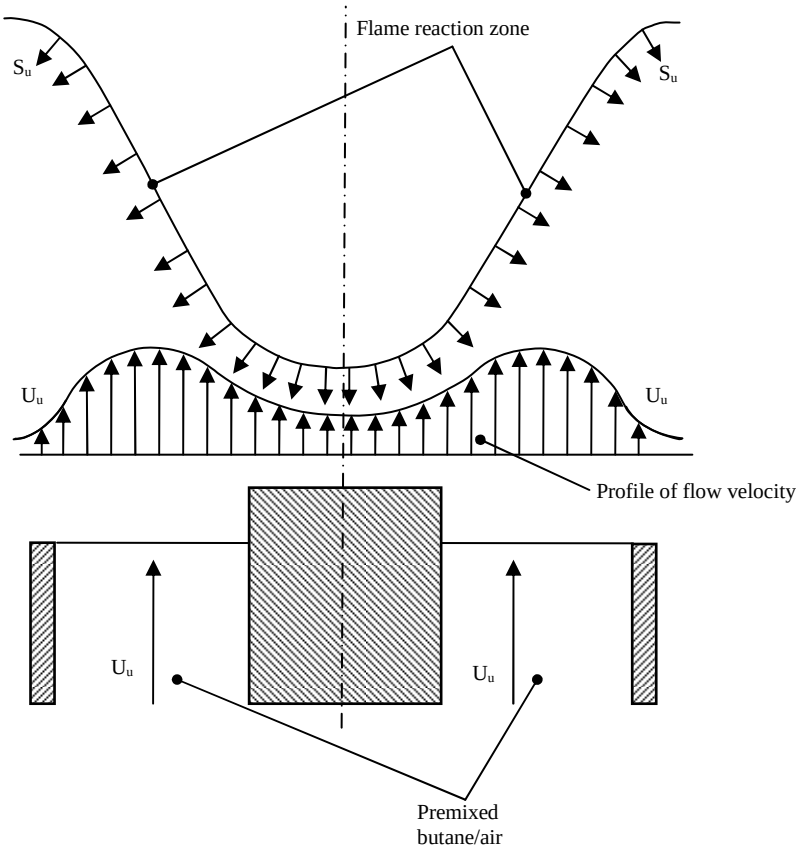

Figure 4.1. Scheme of flame stabilization of inverted premixed laminar flame.

4.1. Structure and temperature profiles of inverted flames

4.1.1. Structure of inverted flames

The gas-air mixtures are in a state of flow and in contact with solid surfaces. It means that there are various interactions between the flame reaction zone, the gas-air flow and heat sinks (e.g. tube rim and rod).

As discussed in Chapter 3, inverted flames are characterized by the presence of inner reaction zone only, which is established above the rod tip. The outer zone (above the

tube rim) will not form due to diluent effect of surrounding atmosphere as the burner operates in very lean mixtures (up to Φ = 0.55). On the other hand, the rod tip is surrounded by the air / fuel mixture with a flow field of large velocities, which prevents the surrounding air to enter and dilute the air / fuel mixture, thus enabling creation of inner reaction zone above the rod tip (Figure 4.1). Due to the convex shape of the flame, the tip of the flame cone rests above the rod tip and the flame base lies in the boundary layer diluted with surrounding atmosphere.

Burning velocity can be determined from Figure 4.2, which shows schematic of the inverted flame. Similarly to the calculation of burning velocity for Bunsen flames, the relationship between the burning velocity S_u and the flow velocity U is:

$$S_u = U.sin\ \alpha \tag{4.1}$$

where α is the angle between the reaction zone and the gas flow direction. It is assumed that the flow is parallel and the flow lines are equally refracted.

The actual flame cone is deformed from its theoretical shape. Figure 4.3 shows such flame. Assuming that the S_u remains constant over the entire reaction zone, the main deformations can be found at the tip of the flame cone and the flame cone base.

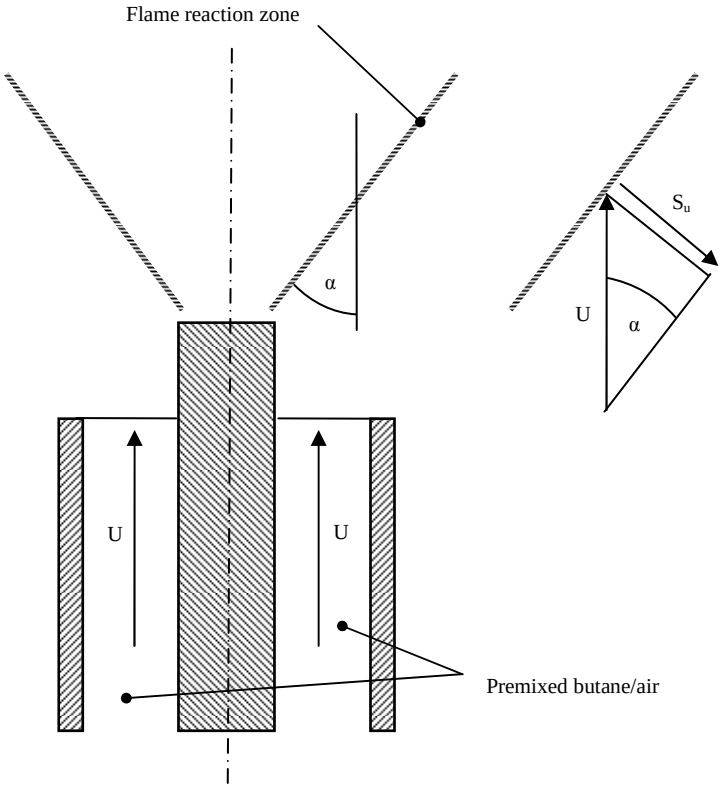

Figure 4.2. Schematic of ideal inverted flame and geometry

The base of the flame cone

Due to the thermal expansion of the air / fuel mixture passing the reaction zone, the streamlines diverge outwards to the surrounding atmosphere. As the distance from the burner increases, so increases the distance between such diverged streamlines and decreases the flow velocity. If the burning velocity remains constant, the reaction zone within the diluted boundary layer rounds and becomes parallel to the diverged streamlines of the unburned gas-air mixture.

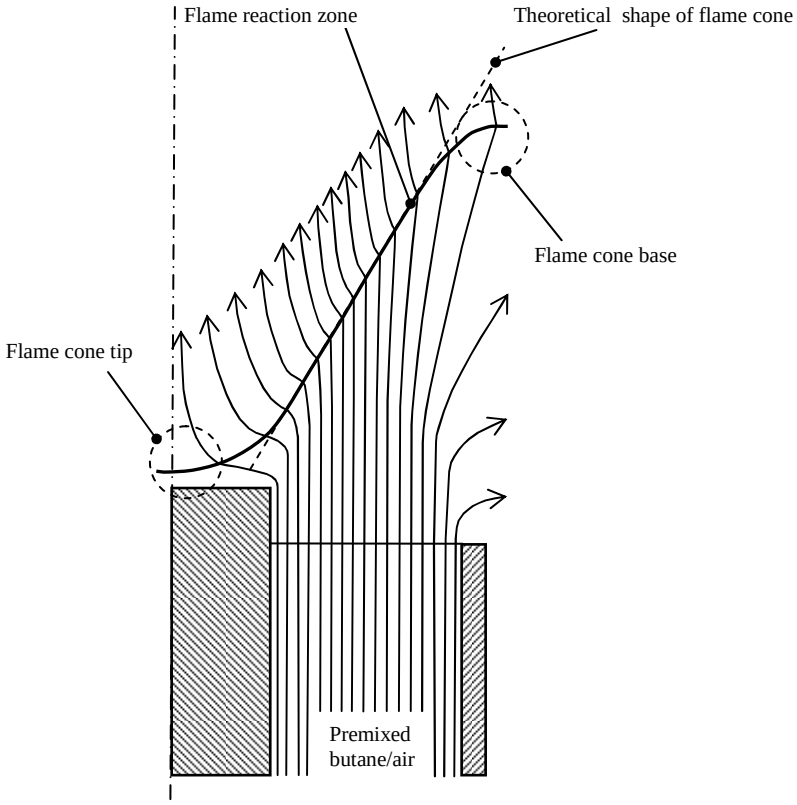

Figure 4.3. Scheme of flow streamlines in inverted flame.

It has been observed for lower *Re* that the base of the flame cone might appear inclined and horizontally uneven. The shape of rod-stabilized flames is highly affected by the geometrical centricity of the rod in the tube. For a very long rod, it is very difficult to keep it perfectly centric inside the tube. The results are uneven velocity profiles at the nozzle exit that subsequently affect the flame shape.

The tip of the flame cone

Analog to the case of burner rim of Bunsen flame, the rod acts as a heat sink. Thus the quenching effect of the rod reduces the burning velocity to zero at the rod tip.

The burning velocity is also decreasing somewhere nearby the rod as there is a significant loss of heat and active radicals to the rod, causing the tip of the flame cone to round. The reaction zone becomes parallel with the air / fuel flow and stabilizes at some distance above the rod tip, where the burning velocity S_u finds its equilibrium with flow velocity, decelerated by frictional drag along the rod.

As mentioned in Chapter 1, Lewis and von Elbe (1987) reported the presence of stagnant eddies or even a vortex street above the solid body (e.g. wire), introduced into the air / fuel stream. Once the air / fuel mixture is ignited, these vortexes reduce their size and the reaction zone is stabilized just above them. However in the present experiments, the Reynolds numbers are in the laminar and partly in the transient region. In such case it is assumed that the vortexes do not occur and the flow is perfectly laminar.

Figure 4.3 also shows schematic of flow streamlines. It can be assumed that the thermal expansion causes the streamlines in the unburned gas to diverge while in the burned gas the streamlines become substantially parallel.

4.1.2. Effect of Re, Φ, B_R and B_T on flame shape

The flame shape can be affected by changing the variable parameters, such as Reynolds number, equivalence ratio, rod protrusion and rod-to-tube ratio.

Increasing the Reynolds number *Re* means that the axial distance between the rod tip and the tip of the flame cone increases as the point, where burning velocity equals flow velocity, shifts upper. Consequently, the flame cone becomes more elongated

at its entire length. Also, once *Re* reaches the transient region, the appearance of the vortexes above the rod tip might be taken into account.

The effect of equivalence ratio Φ to the flame shape is assumed to be negligible, a fact which is not surprising since the regions are within very narrow range of Φ.

The influence of geometrical parameters on flame shape varies. While in case of rod protrusion B_R, the effect is negligible, variations of rod-to-tube ratio B_T has bigger impact. With increased B_T (e.g. larger cross-sectional area, smaller rod diameters), the tip of the cone becomes more narrow and tapered, as in fact the area, where the burning velocity found its equilibrium with flow velocity above the rod tip, diminishes.

4.1.3. Temperature profile of inverted flame

Temperature distribution of free-jet flame is one of the major indicators of heat flux distribution of impinged flame. Temperature contour diagram of collected data points at various radial and axial distances is presented in Figure 4.4. The flame shape is assumed to be symmetrical, thus only half plane of the flame is shown.

Figure 4.5 shows temperature profiles for selected heights, ranged between 1 – 50 mm at the axial direction. At z = 1 mm, measured just below the tip of the flame cone, the temperature maximum reaches maximum of 500 ^{0}C. This clearly confirms existence of a preheat zone ahead of the reaction zone. The preheat zone can also be observed all the way along the luminous reaction zone until it reaches the flame cone base.

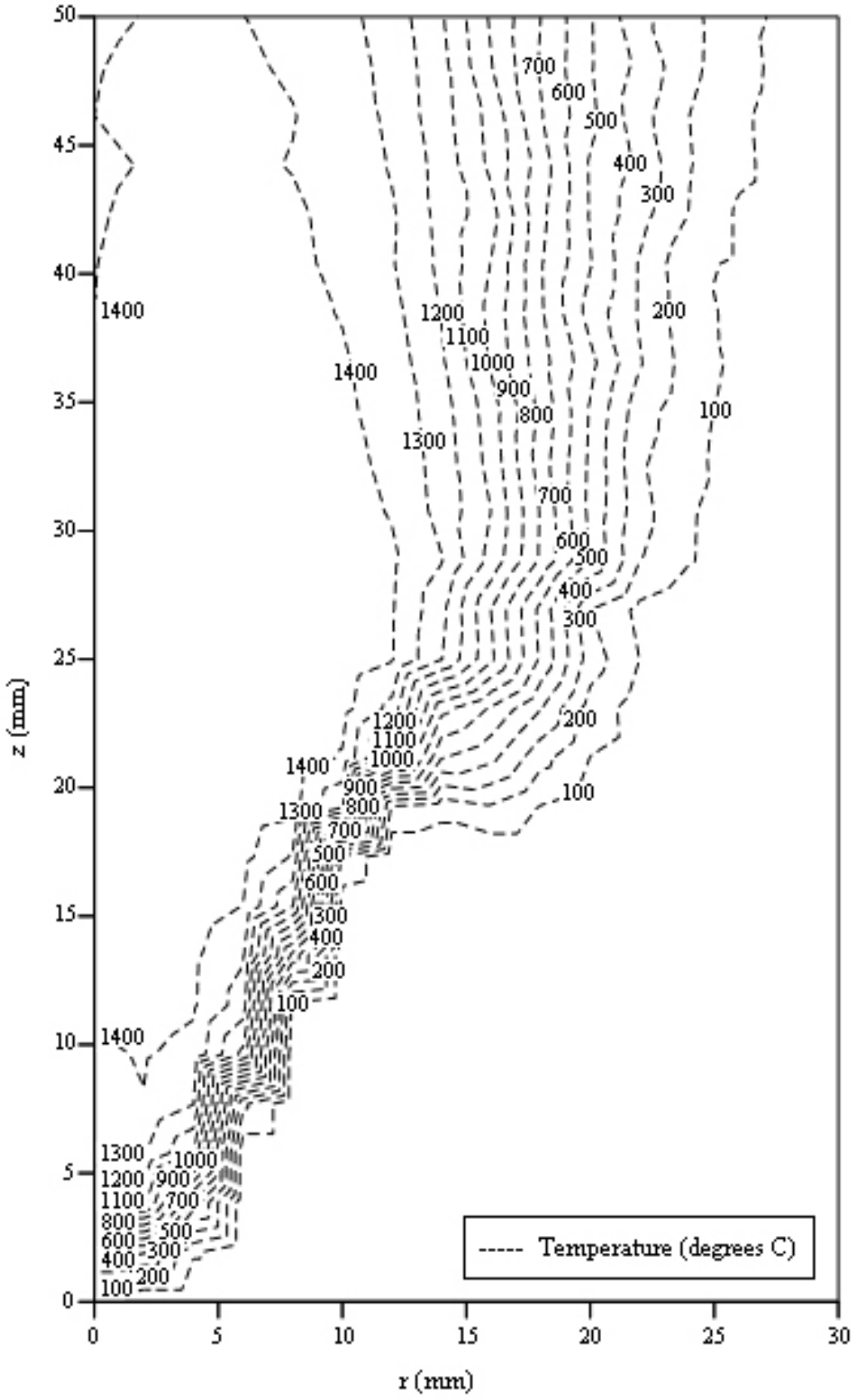

Figure 4.4. Radial temperature distribution of free-jet inverted flame at Re = 2000, Φ = 0.9, B_T = 0.51, B_R = 0.

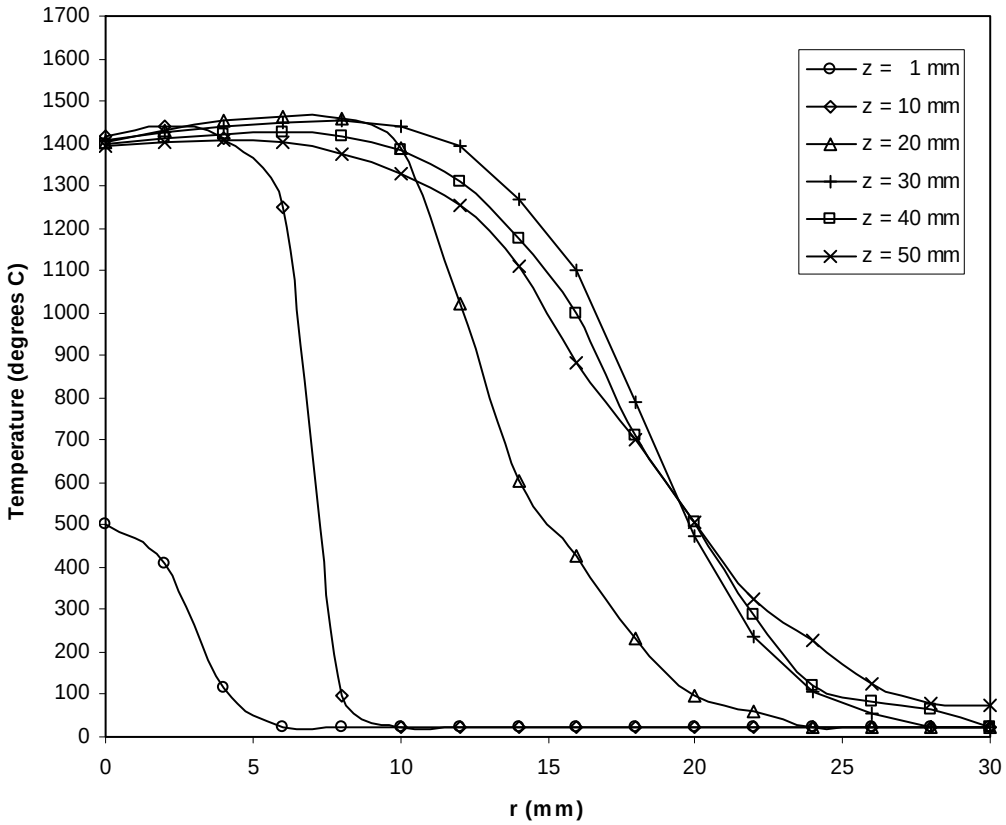

Figure 4.5. Radial temperature profiles of inverted flame at Re = 2000, Φ = 0.9, B_T = 0.51, B_R = 0, for selected heights.

The maximum flame temperature recorded was about 1400 ^{0}C, just above the luminous reaction zone. The area of burned gas with the maximum temperature creates a large central core, which has a cone shape similar to the shape of the reaction zone. Also, the maximum flame temperature in the central core prevails up to double of height of the reaction zone. This is demonstrated in Figure 4.5, where temperature profiles of heights above the flame cone base, i.e. z = 30, 40 and 50 mm, show very wide plateau of maximum temperature before it steadily decreases.

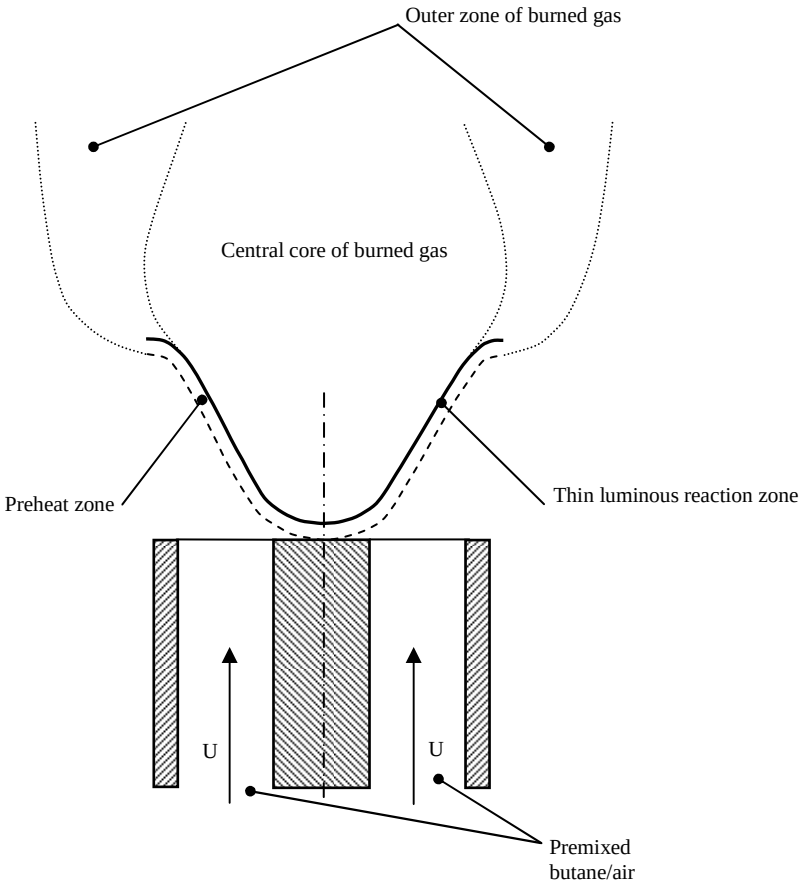

Figure 4.6. Free-jet flame regions of inverted flame.

The two main characteristics of the central core, i.e. its large radial and axial proportions, give us perfect condition for uniform heat flux and temperature distributions over target surface (i.e. flat plate). The effective height for the impingement could be just above the flame cone base, where the radial size of the central core is the largest. The outer zone of burned gas, where the temperature constantly drops, has similar radial size as the central core. Isotherms in this zone are substantially parallel with the axis.

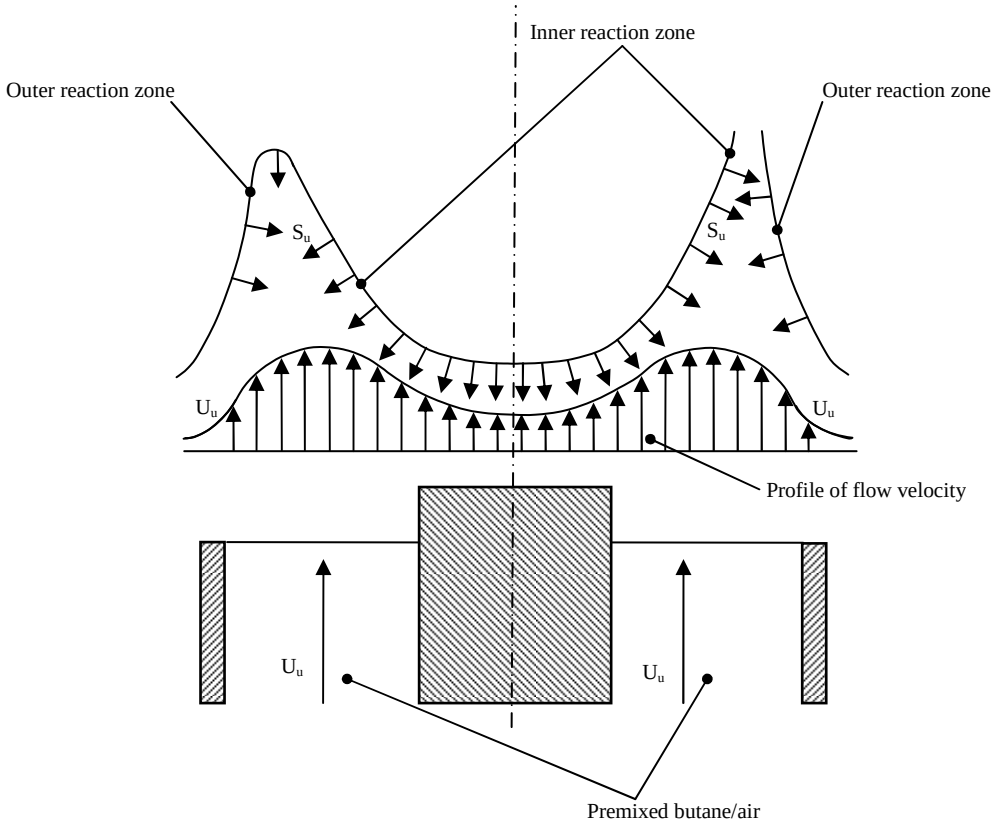

Figure 4.7. Scheme of flame stabilization of partially-inverted premixed laminar

Based on the temperature distribution (Figure 4.4), the structure of free-jet inverted flame with all identified regions (e.g. preheat zone, luminous reaction zone, central core of burned gas and outer zone of burned gas) is schematically represented in Figure 4.6.

4.2. Structure and temperature profiles of partially-inverted flames

4.2.1. Structure of partially-inverted flames

Partially-inverted flames represent more complex and sophisticated structure when compared to the inverted flames. As it has been found out in the Chapter 3, partially-inverted flames are characterized by presence of both inner and outer reaction zone. Partially-inverted flames operate mostly at stoichiometric and fuel-rich mixtures (up to Φ = 2.00) and it is the increased percentage of gaseous fuel in the mixture that creates the conditions, where the reaction zone is stabilized at both the rod tip and the tube rim (Figure 4.7).

These two reaction zones are different in terms of the flame shape. Inner reaction zone has a convex shape, while the outer reaction zone is of concave shape of the flame. The tip of the inner reaction zone rests above the rod (the same as in the case of inverted flames). The base of the outer reaction zone rests above the tube rim. The base of the inner reaction zone might or might not be connected with the tip of the outer reaction zone. This is discussed further in the chapter.

In the case of burning velocity determination, it is clear from the schematic in Figure 4.8 that simplified model applies only to inner reaction zone, where it is assumed that the flow velocity is substantially parallel with the axis and the flow lines are equally refracted. The correlation between the burning velocity S_u and the flow velocity U_i is:

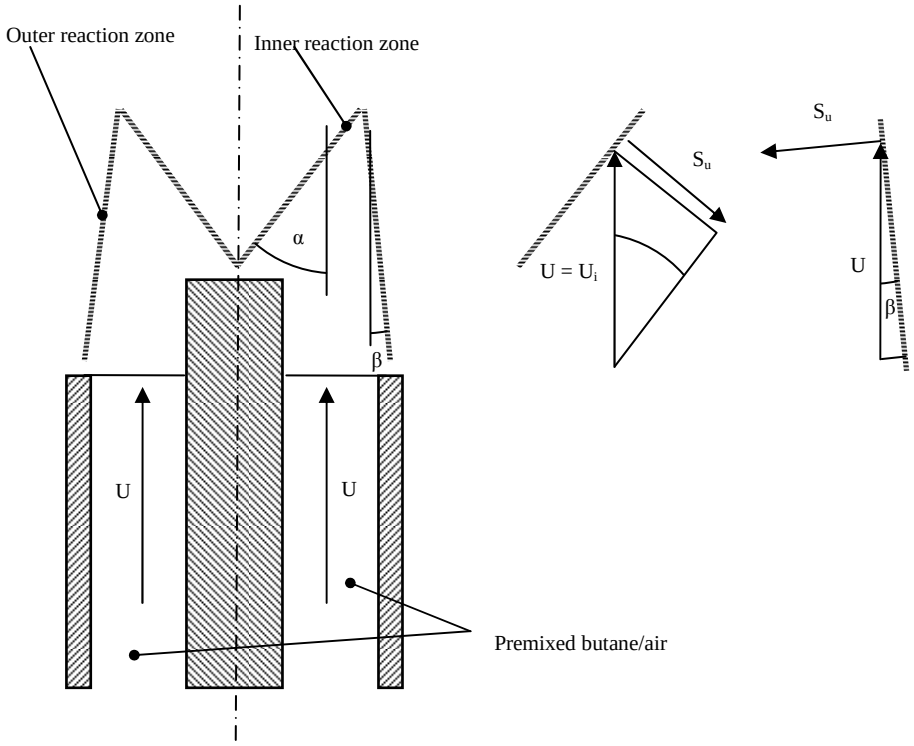

Figure 4.8. Schematic of ideal partially-inverted flame and geometry

$$S_u = U_i.sin\ \alpha \qquad (4.2)$$

where α is the angle between the reaction zone and the air / fuel flow direction and U_i is a flow velocity in the inner reaction zone. It is assumed that U_i is approximately equal to flow velocity U at the muzzle of the burner.

As of the outer reaction zone, such simplified model can not be applied. The angle between the burning velocity S_u and the flow velocity U is much smaller. There is a strong divergence of the flow and the proximity of inner reaction zone may indicate preheating. Also, the flow lines here are not equally refracted. Measurement of

burning velocity in this case is subject to sophisticated methods that are beyond the scope of this work.

Figure 4.9 shows the actual shape of the partially-inverted flame. Based on the terminology of reaction zones and flame shape (concave / convex), the actual flame shape can be consequently divided into inner flame cone and outer flame cone. The main deformations from the theoretical shape are represented by the tip of the inner flame cone, the base of the outer flame cone and the flame top (e.g. the tip of the inner flame cone or the base of the inner flame cone).

The tip of the inner flame cone

The mechanism is the same as in the case of inverted flame. The rod acts like a heat sink and its quenching effect reduces the burning velocity nearby the rod tip where the flow velocity is also decelerated by frictional drag. The reaction zone stabilizes at some distance above the rod tip, where the burning velocity finds its equilibrium with flow velocity. The tip of the inner flame cone is flat due to significant loss of heat and active radicals to the rod.

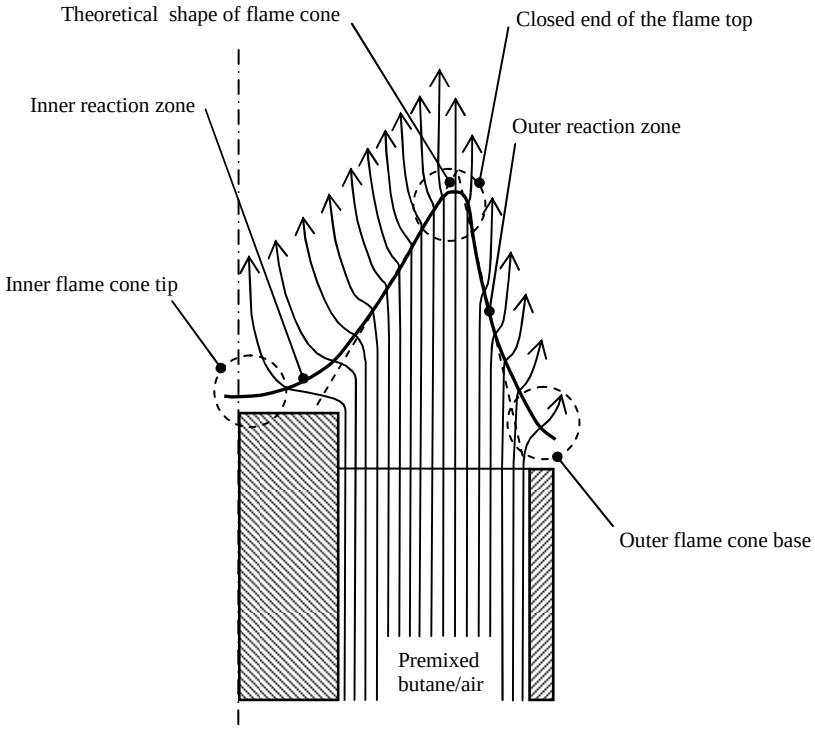
Theoretical shape of flame cone
Closed end of the flame top
Inner reaction zone
Outer reaction zone
Inner flame cone tip
Outer flame cone base
Premixed
butane/air

a)

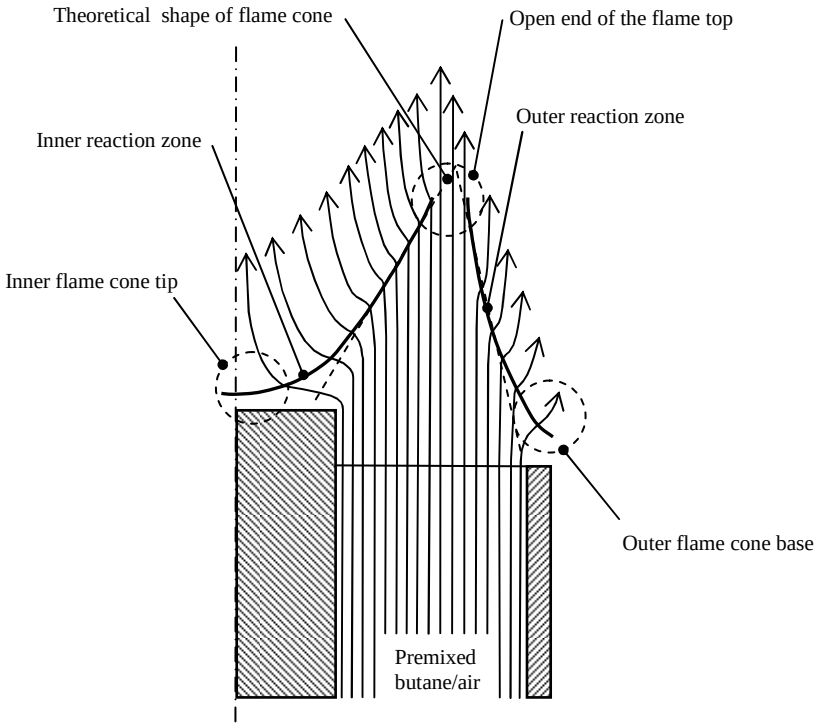
Theoretical shape of flame cone
Open end of the flame top
Outer reaction zone
Inner reaction zone
Inner flame cone tip
Outer flame cone base
Premixed
butane/air

b)

The base of the outer flame cone

The situation at the base of the outer flame cone is similar to the Bunsen flame. The tube rim is a heat sink, nearby which the flow of unburned air / fuel into the outer reaction zone decreases and eventually becomes zero. Thus the burning velocity decreases to zero near the tube rim. The reaction zone stabilizes at quenching distance from the tube rim, where burning velocity and the flow velocity are equal.

The flame top (the tip of the outer flame cone / the base of the inner flame cone)

The conditions at the flame top, where the inner reaction zone meets with the outer reaction zone, are more complex. It is a place with strong heat flow convergence and at the same time with diffusion flow of reactants from burned to unburned air / fuel mixture being divergent. Such situation creates two eventualities of flame top end:

- Closed end – due to strong heat flow convergence, the isotherms tend to bend downstream and the inner and outer reaction zones are connected.
- Open end – due to the significant loss of the reactants, the burning velocity is decreased and eventually drops to zero and the not inflamed air / fuel mixture passes through.

It has been observed that both cases of flame top may occur independently or may occur together for the same input parameters. Figure 4.10 shows the top view of the burner with three possible cases of flame top appearance.

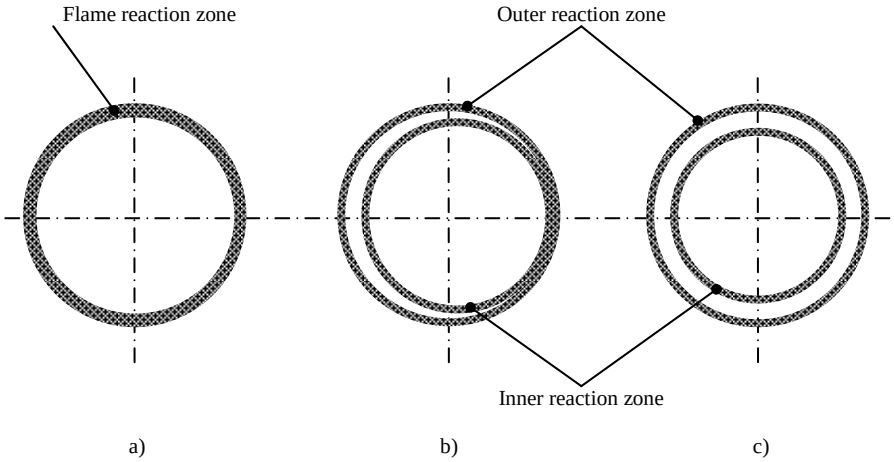

Figure 4.10. Three observed cases of the partially-inverted flame top appearance. View from the top of the burner. a) inner and outer reaction zones are fully attached, b) inner zone is partially detached from outer zone, c) both reaction zones are detached.

There are also other factors that determine whether the flame top is closed-ended or open-ended. It is the geometrical centricity of the rod in the tube that might play the major role. Since the tube and the rod are substantially long to ensure the fully developed flow, it is very difficult to keep the rod perfectly centric inside the tube. Thus the flow profile might not be circumferencially the same. This may result in the situation where the outer and inner reaction zones are partially-attached (Figure 4.10b).

Another factor is the presence of turbulence in transient flow. It has been observed that for higher *Re*, the flame top is predominantly open-ended (Figure 4.10c).

4.2.2. Effect of Re, Φ, B_R and B_T on flame shape

Likewise the inverted flames, partially-inverted flames are also affected by variable parameters, such as Reynolds number, equivalence ratio, rod protrusion and rod-to-tube ratio.

Similarly to the inverted flames, with increased Reynolds number *Re*, the axial distance between the rod tip and the tip of the inner flame cone increases as the equilibrium point of burning velocity and flow velocity is shifted upper. Inner flame cone becomes more elongated. Analogously, the axial distance between the tube rim and the base of the outer flame cone increases and consequently, the outer flame cone also elongates.

For low *Re*, the inner and outer flame cones appear to be mostly attached. Once *Re* starts to reach the transient region, the presence of turbulent flow patterns might break open the flame top, thus partially or fully detaching inner and outer flame cones.

The increase of equivalence ratio Φ causes the inner reaction zone to become narrower and thinner due to the further reduction of air inside the stream. Also the outer and inner reaction zones are likely to be separated.

The influence of rod protrusion B_R is mainly on the outer flame cone. Higher values of B_R cause the outer flame cone to elongate, such that its tip matches with the base of the inner flame cone, which is positioned above. There is a negligible impact on

the inner flame cone. Moreover, increased B_R also increases the chance that the outer and inner zones would be partially or fully detached from each other.

On the other hand, the effect of rod-to-tube ratio B_T has predominantly impact on the inner reaction zone. Decreasing B_T (e.g. smaller cross-sectional area, bigger rod diameters) causes the tip of the inner flame cone to be wider and more flattened. The proximity of inner flame cone causes slight outwards shifting of the outer flame cone.

4.2.3. Temperature profile of partially-inverted flame

Temperature contour diagram of collected data points of partially-inverted flame at various radial and axial distances is presented in Figure 4.11. The flame shape is assumed to be symmetrical, thus only half plane of the flame is shown. Figure 4.12 shows temperature profiles for selected heights, ranged between 1 – 50 mm at the axial direction.

It is evident from Figure 4.11, that the preheat zone is clearly large and does not follow the flame cones pattern. At z = 1 mm, the temperature maximum varies from 900 ^{0}C above the rod tip to 1500 ^{0}C above the tube rim. It shows that the preheat zone is rather flattened. It also means that the tip of the inner flame cone is positioned slightly higher above the rod tip than the base of the outer flame cone is above the tube rim.

The maximum flame temperature recorded was about 1600 ^{0}C in the area around the flame top, where inner reaction zone meets the outer reaction zone (in the case the

zones are attached) or comes very close to the outer reaction zone (in the case the zones are detached). Very large central core has slightly lower temperature of 1500 ^{0}C. This area extends beyond the luminous reaction zones to the unburned gas. That might suggest that there is an enormous heat flow to the unburned gas, especially in the area with strong convergence of reaction zones.

The limits of applied measurement method, e.g. the use of thermocouple, should also be taken into account. In such conditions, where the radial distance between inner and outer reaction zone is very small, the data points at this area might be affected by the presence of thermocouple wires.

The central core of burned gas of partially-inverted flames with approximately maximum flame temperature is much larger and wider than the central core of inverted flames, due to the presence of outer reaction zone. This is demonstrated in Figure 4.12, where the very wide plateau of maximum temperature, that reaches up to 1.6 times of tube perimeter, can be observed even at lower heights, e.g. z = 10 or 20 mm. Also the maximum flame temperature prevails mostly more than the double height of the flame.

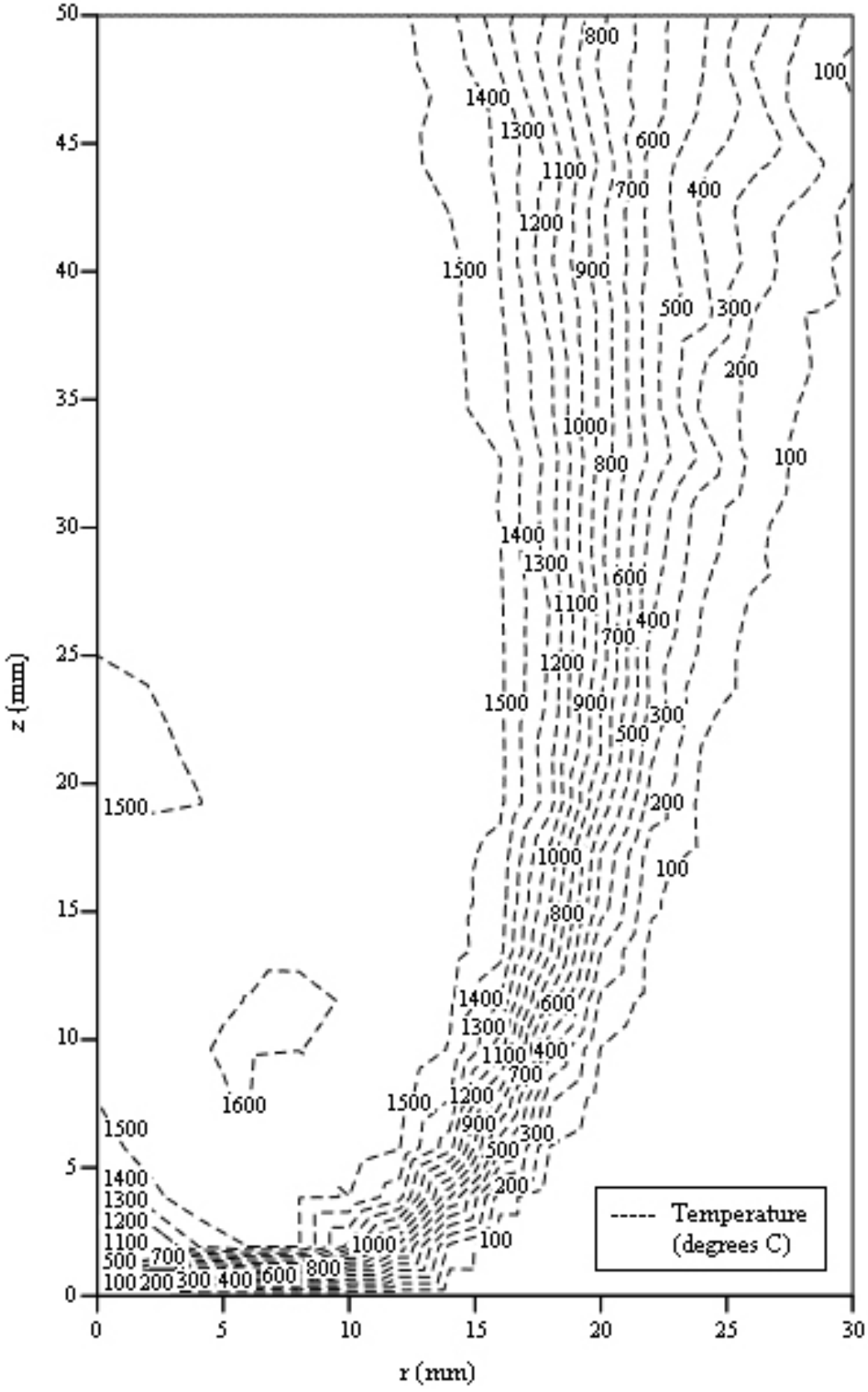

Figure 4.11. Radial temperature distribution of partially-inverted flame at Re = 2000, Φ = 1.4, B_T = 0.51, B_R = 0.

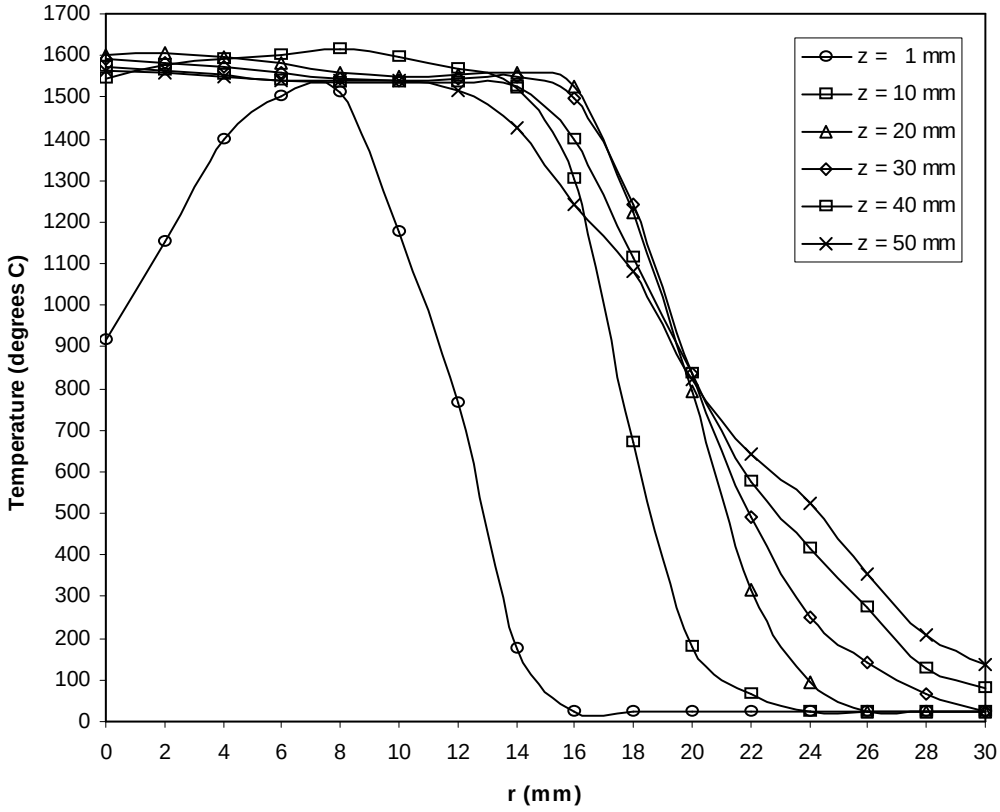

Figure 4.12. Radial temperature profiles of partially-inverted flame at Re = 2000, Φ = 1.4, B_T = 0.51, B_R = 0, for selected heights.

As previously stated in Chapter 4.1.3., a wide central core of burned gas gives very good precondition for uniform heat flux and temperature distributions over the target surface. It makes partially-inverted flame type to be the perfect candidate for such requirements. The effective height for the impingement starts around the flame top, within the area of maximum temperature, and goes up to twice of the flame height, where the radial size of the central core is the largest.

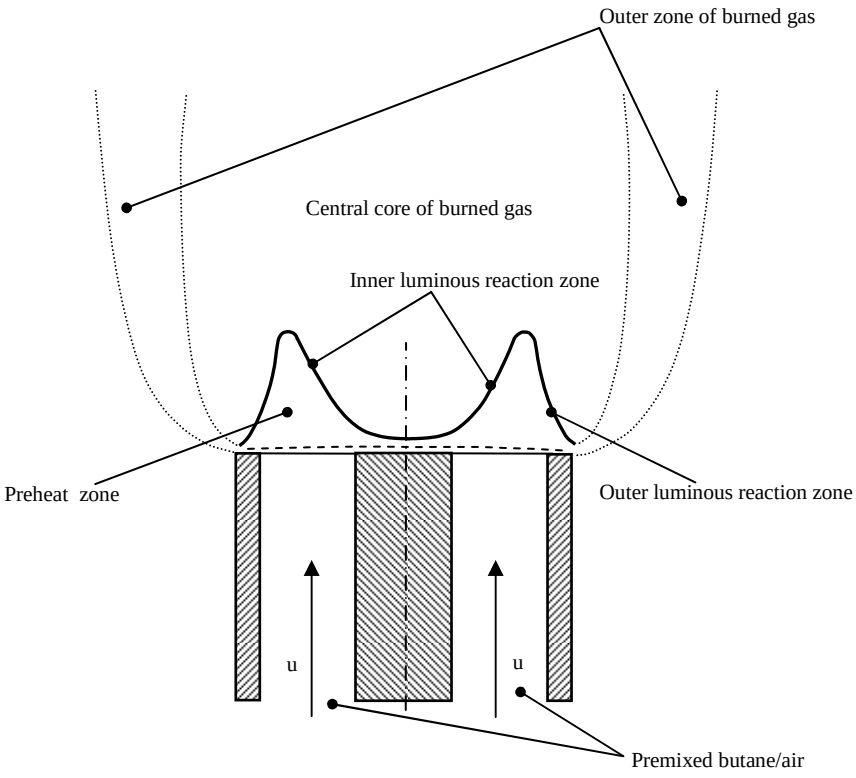

Figure 4.13. Free-jet flame regions of partially-inverted flame.

The size of outer zone of burned gas is narrower than in the case of inverted flames. It stretches up to approximately 0.7 – 0.8 of a radial size of central core. Isotherms of constantly dropping temperature are substantially parallel with the axis.

Figure 4.13 shows schematically the structure of free-jet partially-inverted flames with all identified regions (e.g. preheat zone, outer and inner reaction zones, central core of burned gas and outer zone of burned gas).

4.3. Summary

1) Inverted flame is characterized by the presence of one (the inner) reaction zone stabilized above the rod tip as the conditions of lean mixtures does not allow creation of outer reaction zone above the tube rim. The flame has a convex shape with the flame cone tip situated above the rod tip and the flame cone base resting in diluted boundary layer.

2) The effect of variable parameters on inverted flame shape varies. As of Reynolds number *Re*, with increased value, the flame cone tip is shifted upwards from the rod tip and the flame cone becomes more elongated at its entire length. The effect of equivalence ratio Φ has been found to be negligible and variation of rod protrusion B_R shows only minor effect. Rod–to-tube ration B_T affects the flame cone in the way that either narrows its tip (for larger B_T) or widens (for smaller B_T).

3) Temperature distribution and radial profiles of inverted flame reveal wide and large central core of burner gas with maximum temperature that is situated above the luminous reaction zone. The presence of such zone is a favorable indication of uniform heat flux distribution of impinged flame. Outer zone of burned gas with gradually decreasing temperature has approximately the same radial size as the central core. Preheat zone is follows the pattern of flame cone of the luminous reaction zone.

4) Partially-inverted flame is a more complex type. Both inner and outer reaction zones are present due to increased percentage of gaseous fuel in the mixture.

Inner reaction zone has a convex shape and the outer reaction zone is of concave shape. The tip of the inner reaction zone rests above the rod and the base of the outer reaction zone rests above the tube rim. The base of the inner reaction zone might be fully attached, partially-detached or fully detached from the tip of the outer reaction zone. Equivalence ratio Φ, Reynolds number *Re* and rod protrusion B_R. are the factors, that affect the flame cone tip appearance includes centricity of the rod in the tube.

5) Similarly to the inverted flames, with an increase of Reynolds number *Re*, the inner flame cone tip is shifted upwards from the rod tip and the flame cone is more elongated at its entire length. Also, for higher values of *Re*, the presence of turbulent flow patterns might partially or fully detach the inner and outer flame cones. Increase of equivalence ratio Φ causes the inner reaction zone to be narrower and thinner due to the further reduction of air inside the stream. Also the outer and inner reaction zones are likely to be separated. Higher values of rod protrusion B_R elongate the outer flame cone to match with the inner flame cone, which is positioned above. Increased B_R causes the outer and inner zones more likely to be detached. Variation of rod–to-tube ration B_T affects the inner flame cone in the way that higher values of B_T narrow its tip.

6) Very large central core of burner gas with approximately maximum temperature is a main characteristic that has been observed from temperature distribution diagrams of partially-inverted flame. The central core is wider in comparison with its counterpart in inverted flames, due to the presence of outer reaction

zone. As in the case of inverted flames, the central core of burned gas with maximum temperature is a preferred flame type to achieve uniform heat flux distribution of impinged flame. Outer zone of burned gas with gradually decreasing temperature has narrower radial size in comparison with central core. Preheat zone is rather flattened and does not follow the cone pattern of luminous reaction zone. It indicates high heat flow to the unburned air / flow mixture due to proximity of two reaction zones.

5. HEAT TRANSFER CHARACTERISTICS OF IMPINGING INVERTED FLAMES

As mentioned in Chapter 1, main drawback of impinging isothermal and flame jets is that the distribution of heat flux and temperature on the surface is not uniform. This applies to both round and slot jets configurations that have been extensively studied over several decades. The non-uniformity disadvantage has been confirmed by several reviews by Viskanta (1993, 1996) and Baukal and Gebhart (1994). A study by Mohr et al. (1997) addressed this issue by changing the aerodynamics of the impinging flame; their specially designed Radial Jet Reattachment Combustion (RJRC) nozzle produced a diffusion flame with high convective heat transfer to the impinging surface. Concerning the premixed flames, no such study has been reported.

The prime objective of the present study is to explore and investigate possibilities of uniform heat transfer distribution of impinging premixed flame along the flat surface. Completely novel approach to solve this problem for premixed flame is to introduce a solid body into the air / fuel stream that radically changes flame shape and its structure. Such concept has been applied in design of burner with axially-mounted rod that produces rod-stabilized flames. Preliminary investigation revealed

that such flames might be ideal candidates. It can be suggested from observation of temperature profiles of free-jet inverted and partially-inverted flames that the convex shape and positive curvature of the (inner) reaction zone of inverted and partially-inverted flames are the main factors behind presumably non-existent central cold core.

Not known experimental study has been reported about the local and average heat transfer distributions of rod-stabilized premixed flame, impinging on the flat surface. Thus the following joint study of inverted and partially-inverted impinging premixed flames is the very first of its kind and its results should be used as pilot study for these flames types. Various parameters have been tested in order to figure out the optimal values with regard to the uniform distribution. Chapter 5 covers inverted flames, while the results of investigation of partially-inverted flames are presented in Chapter 6.

The effects of various parameters are presented in local and area-averaged variables. The local variables include radial, stagnation point, stagnation circle and maximum values of local heat flux $\dot{q}$ and local Nusselt number *Nu*. Area-averaged variables, i.e. heat flux $\overline{q}$, Nusselt number $N\overline{u}$, are determined for stagnation, impingement and wall-jet region, and for the entire impingement region. Thermal efficiency η represents the entire impinging region. Related equations are defined in Chapter 2.

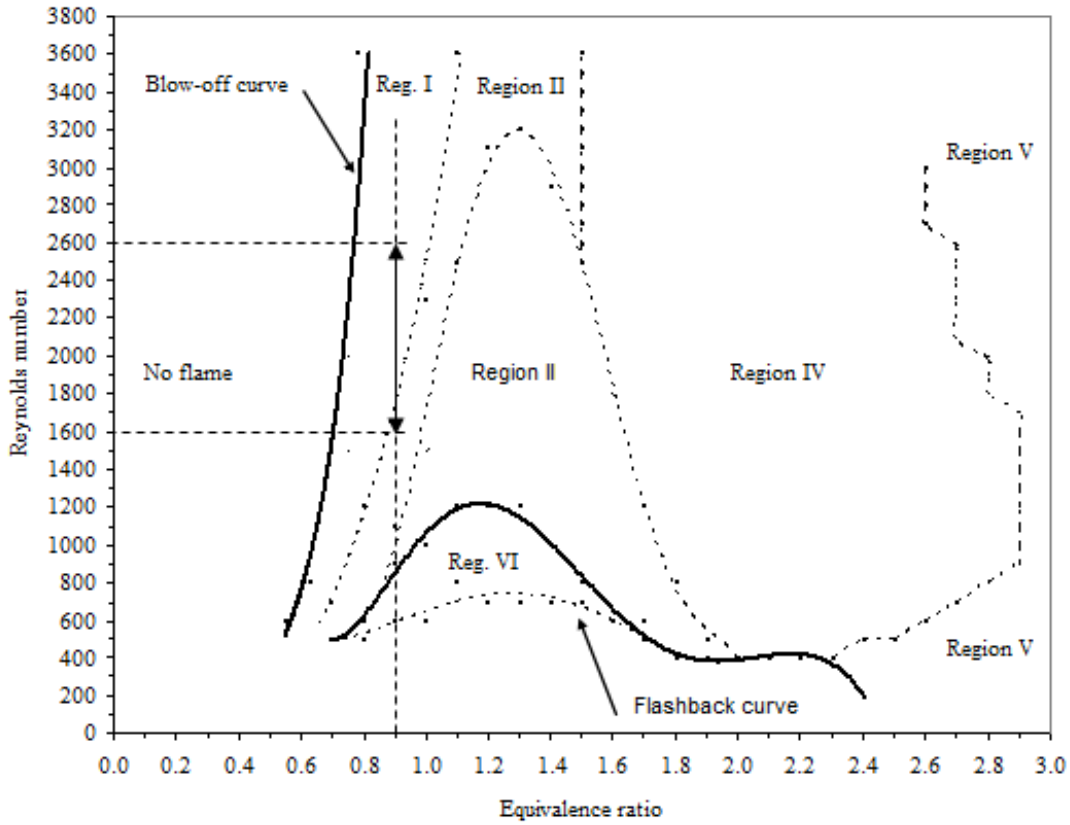

Figure 5.1. Range selection of Reynolds number and equivalence ratio for impinging inverted flames.

5.1. Parameters range selection

Investigation of flammability characteristics of the rod-stabilized flames for various geometrical configurations (Chapter 3) revealed that the occurrence of inverted flames is in the range of Φ = 0.55 to 1.1, for the most stable configuration (B_R = 0, B_T = 0.51), and covers both Region I and II. However, with an increase of rod protrusion B_R and rod-to-tube ratio B_T, Region I narrows down and Region II even diminishes at the expense of unstable Region VI. Considering all geometrical

configurations, the range of Φ shortens to 0.6 to 1.0. Available range of Reynolds number *Re* for inverted flames is limited by the presence of unstable Region VI at the bottom and by the blow-off curve at top. The investigation predominantly focuses on laminar premixed flames, thus the range of *Re* for inverted flames has been set to 1600 – 2600, well within the laminar a transient region. Consequently, the representative value of equivalence ratio Φ has been set to constant Φ = 0.9, as presented in Figure 5.1.

No significant difference in stability diagrams for free-jet flames and impinging flames has been observed for inverted flames, in contrast to partially-inverted flames (Chapter 6.1).

Geometrical parameters of the burner, i.e. rod protrusion B_R and rod-to-tube B_T, have been kept same as in the experimental study of free-jet flames. Rod protrusion B_R varies from 0 to 2, while rod-to-tube values are in the range of 0.51 – 0.80. Both parameters are calculated using equations in Chapter 2.

Preliminary study demonstrated that the effective range of nozzle-to-plate ratio *H* is between 0 to 4. With further distances from the impinging plate, the local heat flux values decreases steadily. This is primarily due to the length of the inverted flames that is considerable shorter in comparison with regular Bunsen flame. Similarly, non-dimensional radial distance from stagnation point *R* has been selected in the range from 0 to 4.

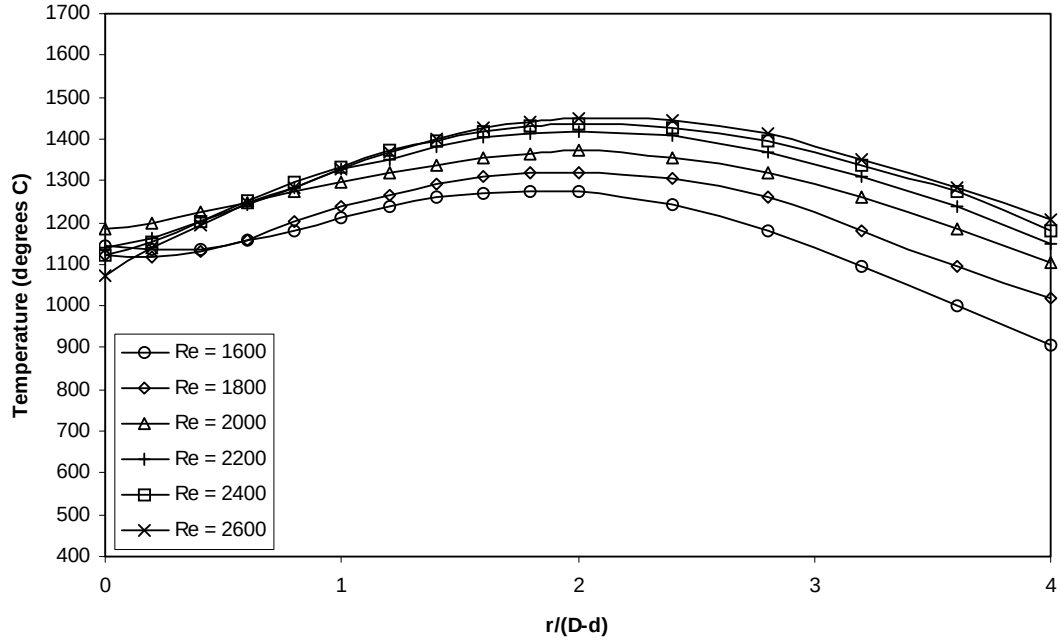

Figure 5.2. Radial flame temperature distribution for various *Re* at $H = 3$, $\Phi = 0.9$, $B_T = 0.51$, $B_R = 0$.

5.2. Flame structure and temperature

To fully understand the impinging process of the inverted flames, temperature distributions were recorded as a function of radial distance and temperature profiles were plotted for two nozzle-to-plate ratios that represent two different vertical cases: 1) impingement plate is situated above the flame reaction zone height; 2) impingement plate is situated within the flame reaction zone height. These were used to identify the structure of impinging inverted flames in relation to nozzle-to-plate ratio H. Based on that, the horizontal regions of impinging flame are also determined.

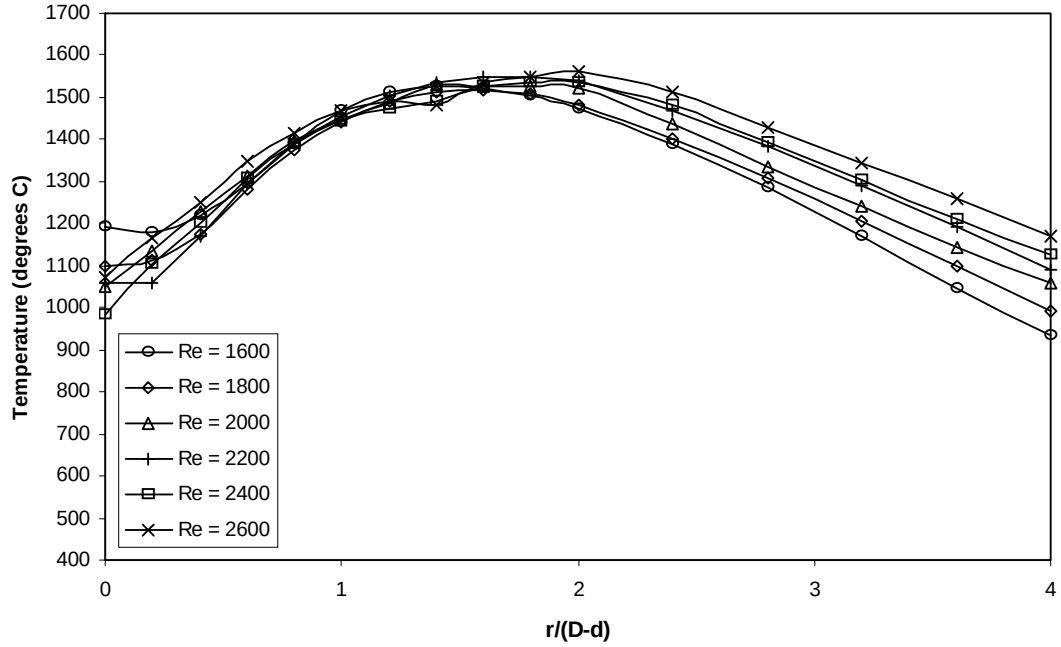

Figure 5.3. Radial flame temperature distribution for various *Re* at $H = 1$, $\Phi = 0.9$, $B_T = 0.51$, $B_R = 0$.

5.2.1. Flame temperature

Flame temperature distribution for $H = 3$, where impingement plate is situated just above the flame reaction zone height, is presented in Figure 5.2. It can be observed that flame temperature is relatively low around the stagnation point and up to stagnation circle ($R = 0.725$). It inclines with further radial distance and peaks around $R = 2 – 2.5$, follow by steady decline. Peak values were obtained at radial position just above the base of the flame cone, where the reaction zone's position is the closest to the impingement plate. Variation of *Re* has impact on temperature increase / decrease; however the radial distribution patterns remain the same. With

further radial distance there is an increased divergence in temperature profiles for different Re.

Figure 5.3 shows temperature profiles for closer nozzle-to-plate distance: H = 1. In this case, the impingement plate is well within the height of flame reaction zone. Due to closer proximity to the impingement plate, recorded peaks of flame temperatures are generally higher, while flame temperature values at and around the stagnation point / circle remain the same as in the previous case. The peaks are slightly shifted inwards and occur around R = 1.5 – 2. Consequently, the decline with further radial distance displays divergence in temperature profiles for different *Re*.

The maximum recorded temperatures were higher than those of free-jet flames, i.e. 1560 ^{0}C for impingement flames against 1517 ^{0}C for free-jet flames. It corresponds well with a study by Milson and Chigier (1973), who concluded that impingement flames are associated with higher temperatures due to improved combustion, enhanced by better mixing due to increased turbulence, caused by the proximity of impingement plate. However it has to be taken into account that for impingement purposes (i.e. calculation of heat transfer coefficient), flame temperatures have been obtained just below the impingement surface. Thus the actual maximum temperatures in the reaction zone might be higher.

5.2.2. Flame structure

In accordance with previous studies, e.g. Milson and Chigier (1973) and Kwok at al. (2003), and based on the preliminary heat flux measurements and data from flame temperature distributions, the impinging plate can be divided into specific regions that represent and reflect different mechanisms of impinging flame jet. For rod-stabilized flames, these regions are defined as follows:

- Stagnation region ($0 \leq R \leq 1$). An area of central core of burned gas impinging onto the plate, high temperatures.

- Impingement region ($1 \leq R \leq 2$). An area with intense combustion and maximum temperatures, where flame reaction zone interacts with the plate.

- Wall-jet region ($2 \leq R \leq 4$), an area with lower temperatures, where combustion products start to diffuse outwards into the surrounding atmosphere.

Figure 5.4 represents case with an impingement plate situated above the flame reaction zone (Case 1). The turbulence caused by the presence of impingement plate has small impact and does not affect shape of the reaction zone. Central core of burner gas with high temperature covers both stagnation and impinging region, thus diminishing the difference between them.

Photographs of inverted impingement flames for such case are shown in Figures 5.6a and 5.6b. The reaction zone of the flame remains intact and it can be assumed to be identical as in free-jet flame. The flame cone base might appear horizontally

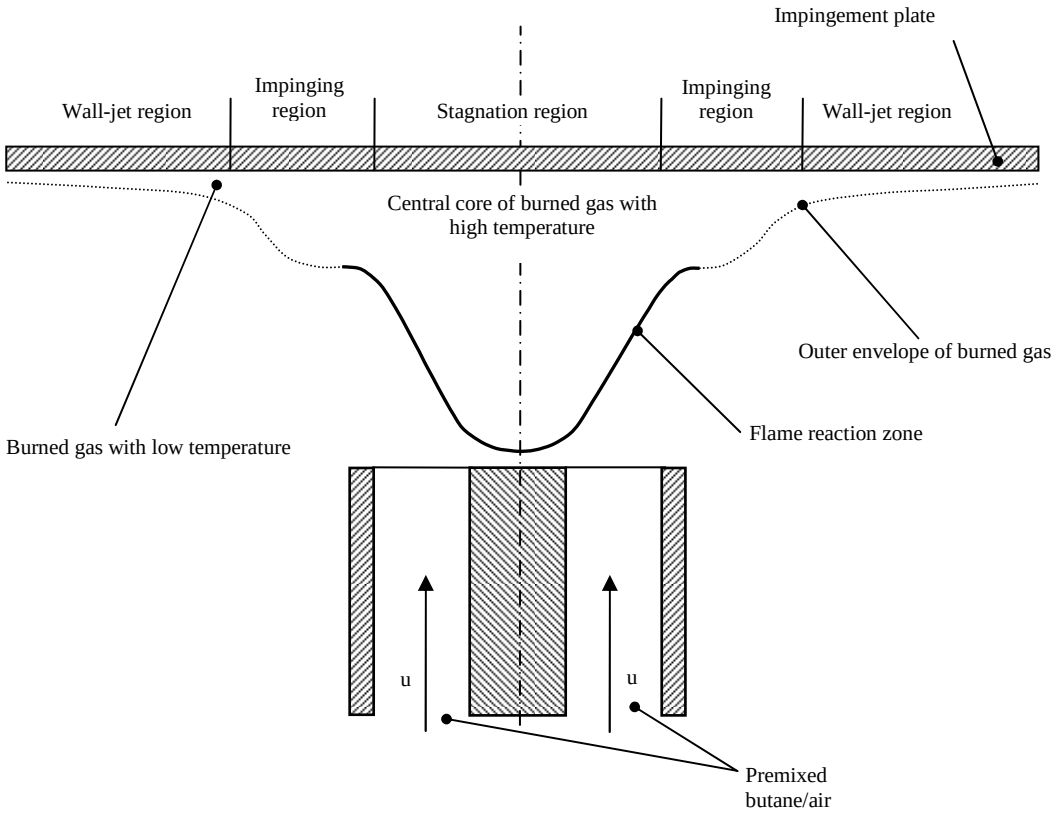

Figure 5.4. Structure of impinging inverted flame: impingement plate is situated above the flame reaction zone

uneven and inclined, a phenomenon that has been observed for lower *Re*. As described in Chapter 4, the factor behind is related to geometrical centricity of the rod in the tube as it is very difficult to keep very long rod perfectly centric inside the tube.

The second case (Case 2) is featured in Figure 5.5. The impingement plate is situated within the height of reaction zone. This causes the reaction zone to stretch out as it impinges with a wider angle. Increased turbulence causes increased mixing, hence the temperature. Consequently, reaction zone becomes more settled and its tip is drawn nearer to the rod tip. The base of the reaction zone is drawn towards the

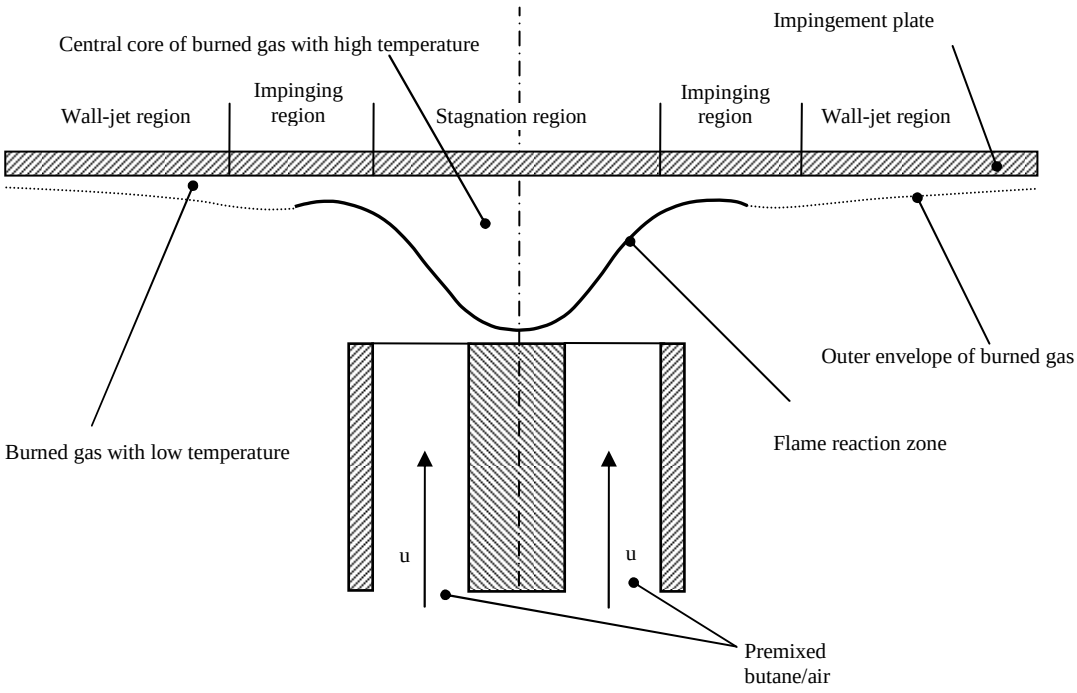

Figure 5.5. Structure of impinging inverted flame: impingement plate is situated within the flame reaction zone height

impingement plate and its base shows extensive flickering, denoting presence of an extensive turbulence in the region.

Photographs in Figure 5.6c and 5.6d show inverted flames of Case 2. The base of the flame cone might appear thicker; however it is a result of long exposure as flickering occurs.

In comparison with Case 1, all three regions, i.e. stagnation, impingement and wall-jet, are clearly identified by steep differences in their respective temperature profiles.

a)

b)

c)

d)

Figure 5.6. Photographs of impinging inverted flames at Re = 2000, Φ = 0.9, B_T = 0.51, B_R = 0; a) and b) at H = 3; c) and d) at H = 1.

5.3. Effect of Nozzle-to-plate ratio

Experiments at different nozzle-to-plate ratio H, as defined in Equation 2.2, have been performed as first, due to its significance in determination of testing range of other parameters, notably rod protrusion B_R, and also to determine the optimal nozzle-to-plate ratio H_{opt} in terms of uniformity of heat transfer to the plate. The values of H have been set in the range from 0.5 to 4.0, with a step of 0.5. In comparison with experiments carried with round or slot burners producing regular Bunsen type of the flame, the values of H are comparably small. Length of the flame is the major factor here, as explained above.

5.3.1. Local heat flux and Nusselt number distribution

Distributions of local heat flux and local Nusselt number have been obtained for stagnation point and stagnation circle, as well as a function of non-dimensional radial distance R. Maximum values have also been determined.

5.3.1.1. Radial distribution

Figure 5.7 shows radial distribution of heat flux for various nozzle-to-plate ratios. It is evident that nozzle-to-plate ratio significantly affects the heat transfer rates.

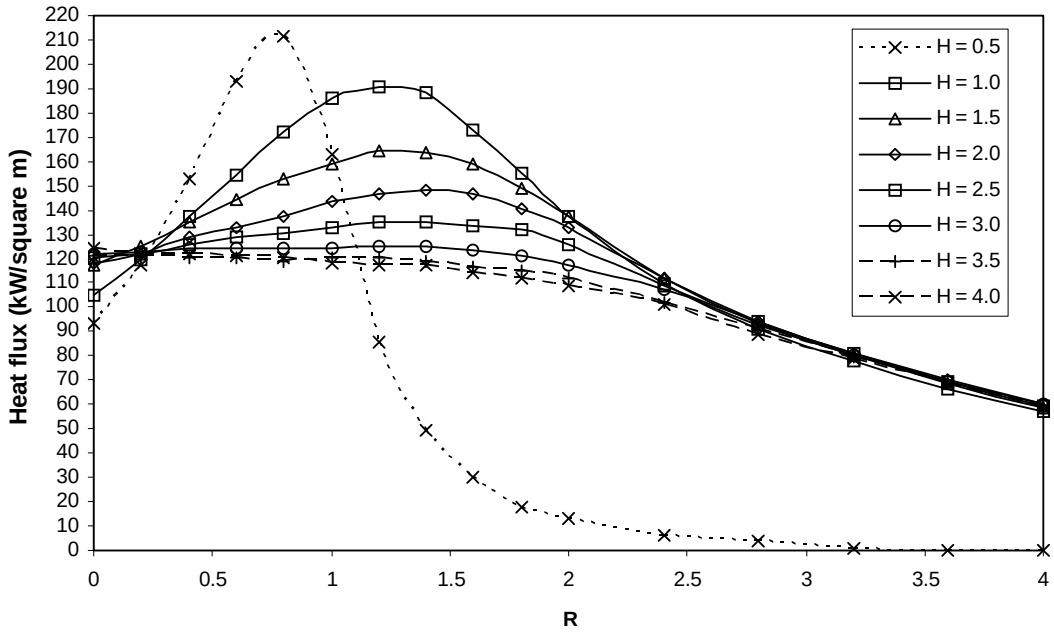

Figure 5.7. Effect of H on radial heat flux distribution at $\Phi = 0.9$, $Re = 2000$, $B_R = 0$, $B_T = 0.51$.

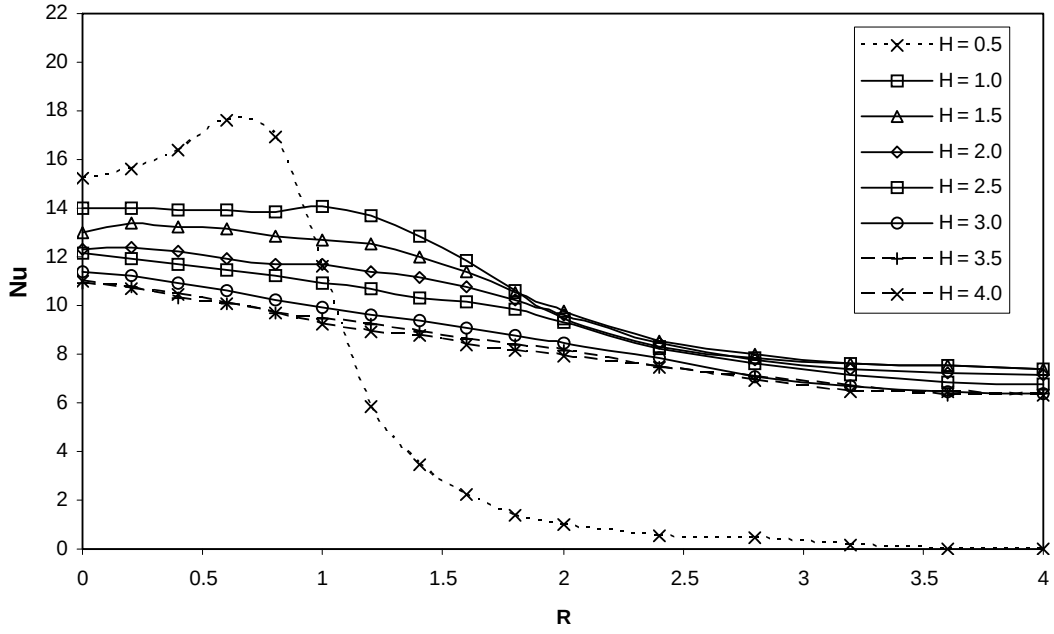

Figure 5.8. Effect of H on radial Nu distribution at $\Phi = 0.9$, $Re = 2000$, $B_R = 0$, $B_T = 0.51$.

It has been observed that at H = 0.5, which is the closest selected distance to the impingement plate, the flame exhibits very unstable behavior. Due to the extreme turbulence in the stagnation region, the flame might not cover the entire perimeter of the nozzle, and it has very high potential to blow-off. In some cases, the flame reduces its shape to very intense reaction zone with high temperature, without a presence of outer envelope of burner gas. Such case is demonstrated in Figure 5.9. The heat transfer rate is the highest at the impingement region, at the point, where reaction zone interacts with the impingement plate. At the stagnation region, it exhibits the biggest drop in heat flux. Absence of outer envelope of burned gas implies sharp drop in heat flux beyond its peak at R = 1. Since there is a significant change in flame shape and the flame is unstable at this nozzle-to-plate ratio, values at H = 0.5 were excluded from further experiments and computational processes.

Such phenomenon can be explained by the quenching effect of the cold impingement plate. Extreme proximity of impingement at the H = 0.5 inhibits chemical reactions at the stagnation and wall-jet region. Impingement region remains unaffected due to very high temperatures inside the reaction zone.

With H ranging from 1.0 to 2.5, heat transfer rate shows analogous patterns. Slight drop in stagnation region is compensated by steep increase that peaks in the range of R = 1.2 – 1.4, that is in the impingement region. Heat transfer rate steadily decreases in wall-jet region (R > 2) and the decrease is constant and not affected by H.

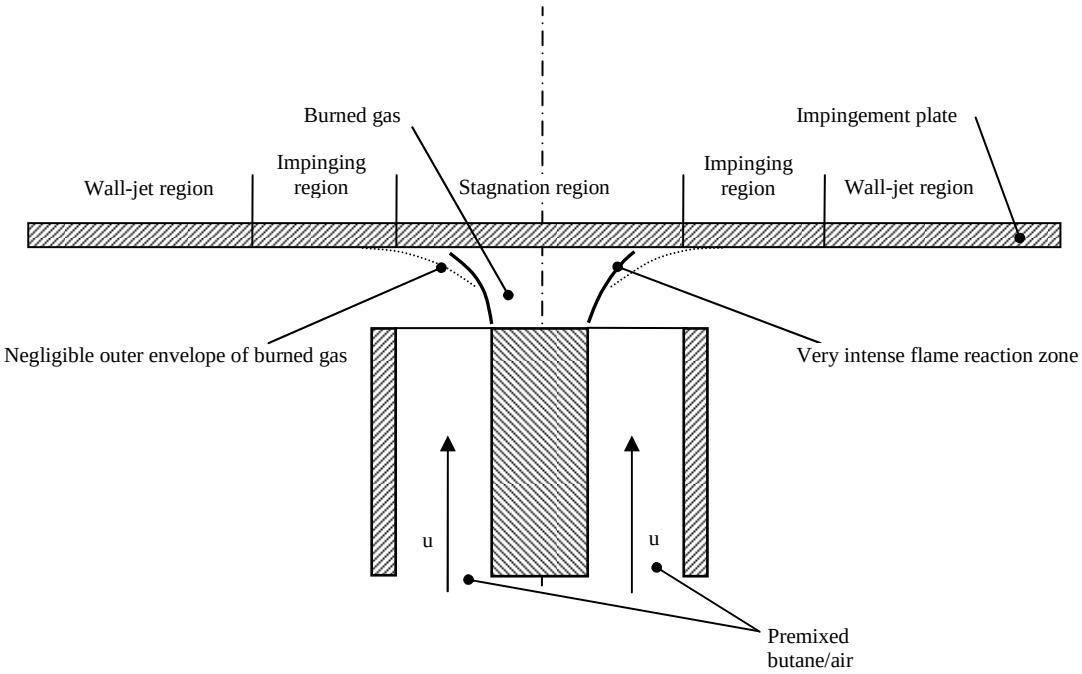

Figure 5.9. Structure of impinging inverted flame: appearance of very intense flame reaction zone at very small nozzle-to-plate ratio

Nusselt number distribution follows similar patterns as heat flux distribution, with an exception in stagnation region, where the values remain very constant in the range with those of impingement region. This fact is associated with high flame temperatures of burned gas in the central core that have positive impact on uniform Nusselt number distribution.

With further distance from the impingement plate ($H \geq 3$), radial distributions of heat flux and Nu happen to be very uniform with steady peak values extending up to $R = 2$. In terms of uniformity, it can be determined from Figure 5.7 that $H_{opt} = 3$. As H increases, the difference between peak values at different H is more negligible. This is associated with the fact that the flame is not stretched out as in the case of close distance to the impingement plate. Thus the central core of burned gas with high temperatures extends beyond the stagnation region and covers very wide area.

5.3.1.2. Stagnation point, stagnation circle and maximum heat flux and *Nu*

Corresponding heat transfer rate and Nusselt number values are represented by Figures 5.10 and 5.11. It compares heat transfer at stagnation point and stagnation circle with peak values of heat flux and *Nu* as a function of nozzle-to-plate ratio *H*. The difference between the commonly used stagnation point and newly introduced stagnation circle is explained in Chapter 2.3.8, Figure 2.6 respectively.

Stagnation point heat transfer is the lowest at the closest distance to the impingement plate, slightly increases with further distance and becomes steady at $H > 2.5$.

Theoretically, maximum heat transfer should occur at the stagnation circle. However it is evident, that the maximums are shifted further, especially at very low nozzle-to-plate ratios. Again, this is due to the impingement flame shape of Case 2 that stretches out the reaction zone. The biggest difference between stagnation circle heat flux and maximum heat flux is circa 15% at $H = 1$.

All three curves converge and from $H = 3$, there is negligible difference, i.e. the maximum heat transfer rate occurs at both stagnation point and stagnation circle. This means that starting from $H = 3$, heat transfer characteristics are very uniform along wide impingement region.

Figure 5.11 shows stagnation point *Nu* to be equal to Nu_{max} for the entire range of nozzle-to-plate ratio. That means stagnation point is the peak spot for *Nu*. The reasons are explained in Chapter 5.3.1.1.

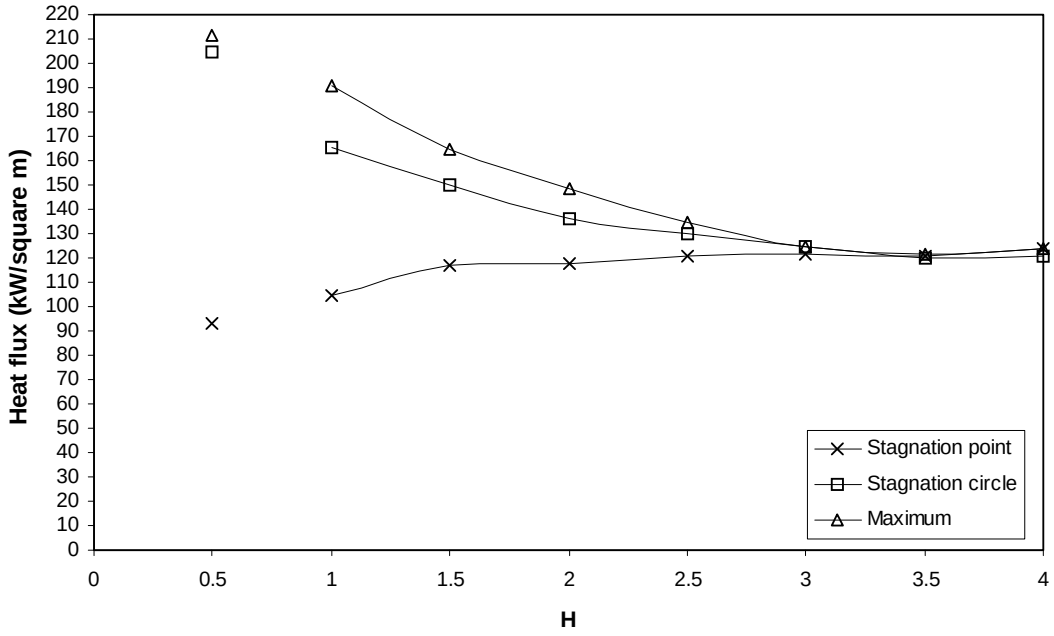

Figure 5.10. Effect of H on stagnation point, stagnation circle and maximum heat flux at Φ = 0.9, Re = 2000, B_R = 0, B_T = 0.51.

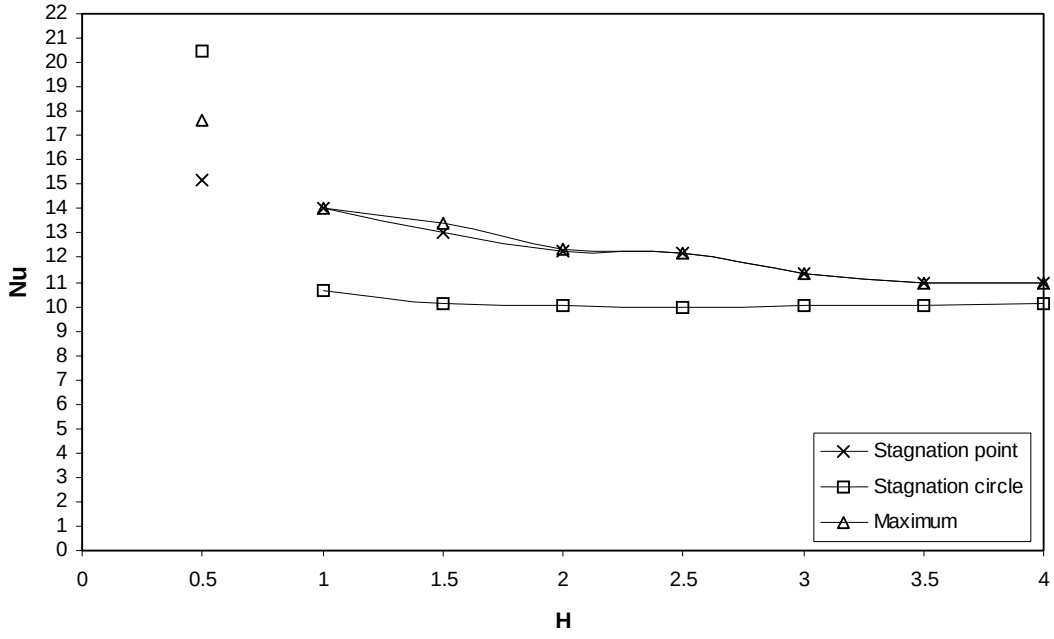

Figure 5.11. Effect of H on stagnation point, stagnation circle and maximum Nu at Φ = 0.9, Re = 2000, B_R = 0, B_T = 0.51.

Obtained values of heat flux and *Nu* at $H = 0.5$ are shown for the reference only and they are not further analyzed.

5.3.2. Area-averaged heat flux and Nusselt number distribution

Area-averaged distributions of heat flux and *Nu* has been obtained by integrating local values over the impingement surface as defined by equations 2.9 and 2.13. The integrating area has been divided into three parts that correspond with regions defined in Chapter 5.2.2., i.e. stagnation, impingement and wall-jet region. Total heat flux and Nu for the entire regions has been obtained as well.

Figures 5.12 and 5.13 compare area-averaged distributions at each region as a function of nozzle-to-plate distance *H*. Again, values of heat flux and *Nu* at $H = 0.5$ are shown for reference only.

As expected, the lowest averaged values were recorded at wall-jet region, where heat transfer rate remains constant and it can be assumed that it is not affected by the distance from the impingement plate.

Both average heat flux and *Nu* for stagnation and impingement regions decrease with increased nozzle-to-plate ratio up to $H = 2.5$, from where they remains approximately constant.

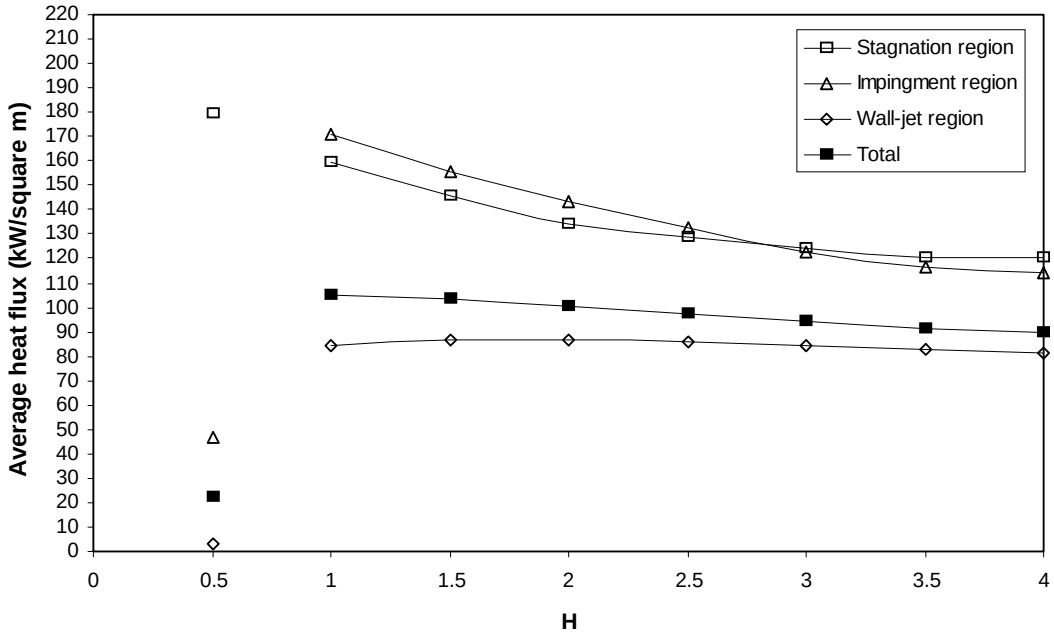

Figure 5.12. Variation of average heat flux with H at different impingement regions at Φ = 0.9, Re = 2000, B_R = 0, B_T = 0.51.

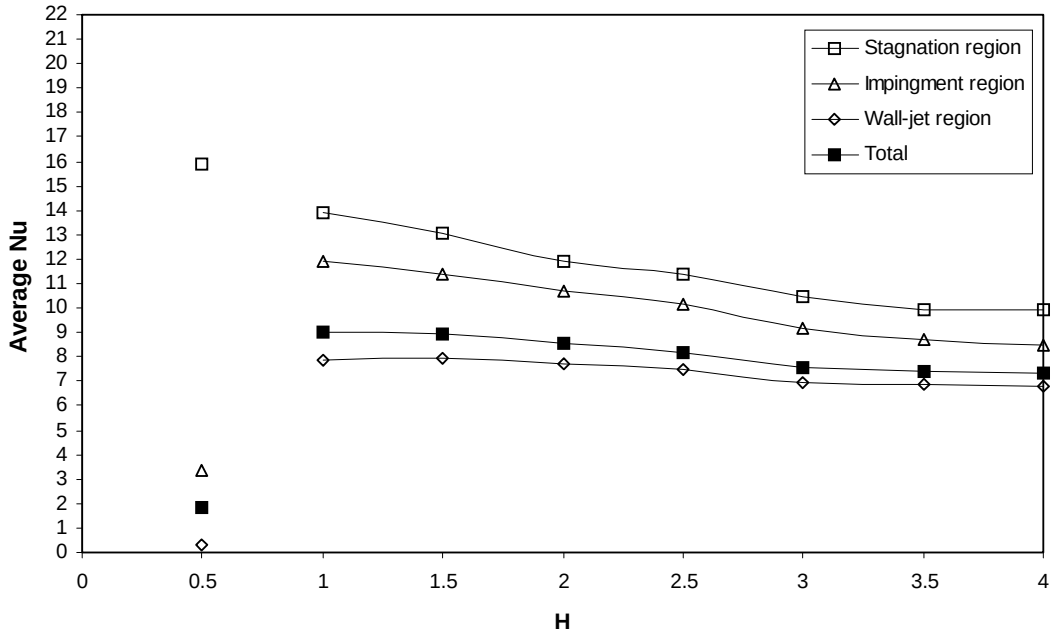

Figure 5.13. Variation of average Nu with H at different impingement regions at Φ = 0.9, Re = 2000, B_R = 0, B_T = 0.51.

Maximum values for heat flux have been recorded for impingement region. The presence of intense reaction zone with maximum flame temperatures is the factor here. Overall, the total average heat flux and average *Nu* decrease constantly with increased nozzle-to-plate ratio at rate of approximately 5% per unit. Such constant decrease is not surprising as the decrease of heat transfer rate at the stagnation region is compensated by its peak values at the impingement region.

In the contrast, maximum values for *Nu* are situated in the stagnation region. It has been previously explained that constant distribution of flame temperature over stagnation and impingement region is the factor that affects the uniform distribution of *Nu*, despite there is a decrease of heat flux in the stagnation region.

5.3.3. Thermal efficiency

Overall thermal performance for the burner setup is specified by thermal efficiency η. Its definition and assumptions are presented in Chapter 2.3.7.

Figure 5.14 shows thermal efficiency η as the function of nozzle-to-plate H. The difference between maximum and minimum values is within 15% for H ranging from 1 to 4. Again, the drop is constant and modest and corresponds with total area-averaged values of heat flux and *Nu*. Maximum efficiency was 47.6% at $H = 1$. For the reference only, the thermal efficiency at $H = 0.5$ was low, only about 10%.

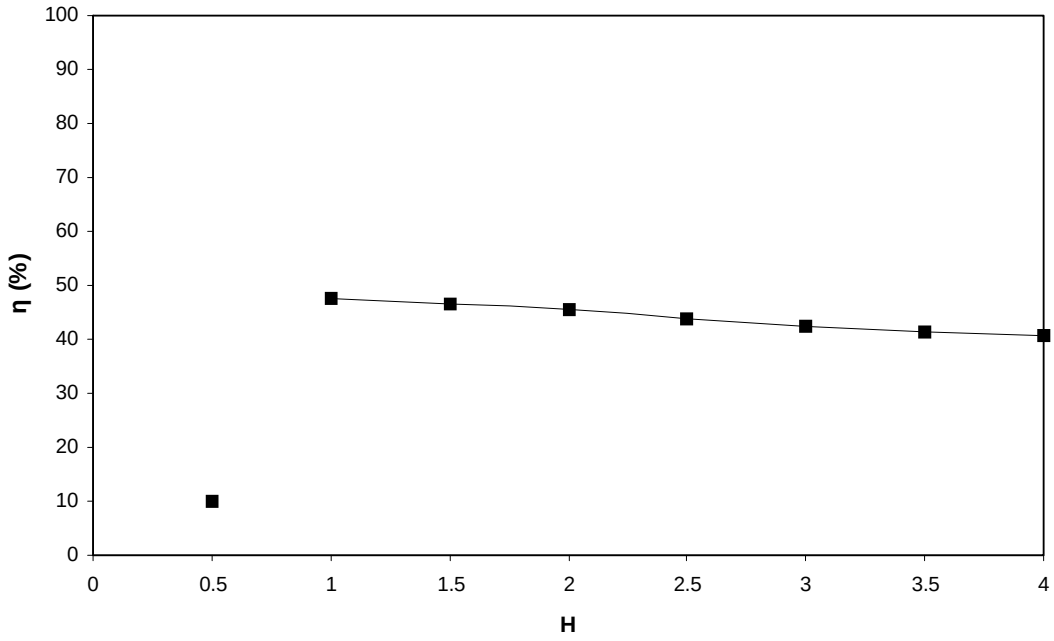

Figure 5.14. Thermal efficiency for various H at Φ = 0.9, Re = 2000, B_R = 0, B_T = 0.51.

5.4. Effect of Reynolds number

Second set of experiments has been carried out in order to investigate the effect of Reynolds number *Re*. Many previous studies of premixed impinging flames (e.g. Dong, 2002) suggested that the effect of *Re* on heat transfer characteristics is significant. The values are ranging from 1600 to 2600, with a step of 200. Range selection is defined in Chapter 5.1. Data were recorded at two different nozzle-to-plate ratios: H = 1 and 3, denoting Case 2 and Case 1 respectively.

5.4.1. Local heat flux and Nusselt number distribution

Local heat flux and Nusselt number distributions were obtained as a function of non-dimensional radial distance R for various Reynolds numbers. Stagnation point,

stagnation circle and maximum heat transfer rates and Nusselt numbers as a function of *Re* are also determined.

5.4.1.1. Radial distribution

Figures 5.15 and 5.16 show radial heat flux and Nu distributions for various Reynolds number at $H = 1$ (Case 2). It is clear that variations of *Re* have significant impact, especially if the nozzle is in close proximity to the impingement plate.

Similarly to the experiments with variations of *H*, radial distributions exhibit lower values around the stagnation point with steep increase up to $R = 1.0 – 1.2$, followed by steady decrease. Technically, there is no drop in the stagnation region. It is the peak that becomes more profound with increased *Re*. This can be explained as there is increased turbulence in the region that adds to better mixing, thus causing flame temperatures in the reaction zone to increase. Consequently, heat transfer rate increases in the impingement region.

This confirms that the inverted flame is valuable asset for application purposes, since there is no presence of central core zone of cold unburned gas, marked by a steep drop of heat transfer rate. The non-uniform gain of heat flux due to increased *Re* is in the positive range, Figure 5.15.

Nusselt number identically increases with increased *Re* along the entire region, predominately in the impingement region. In the stagnation region, however, the patterns of are more diverged than those of heat flux. Constantly high temperatures in the central core keep the values in the range with impingement region, however

certain fluctuations can be observed. Increased turbulence in the region associated with increased *Re* is probably the factor behind.

At $Re \geq 2200$, a flow noise has been reported due to the increased turbulence that causes the local pressure and flow velocity to fluctuate. The base of the reaction zone exhibits severe flickering.

Case 1 ($H = 3$) is demonstrated in Figures 5.17 and 5.18. Here, at the further distance from the impingement plate, the impact of increased *Re* is less significant. While in Case 2, the maximum difference for between stagnation point heat flux and its peak value for the same *Re* was almost 100%, in Case 1, it accounts only 15%. Maximum values for $Re \geq 2200$ are shifted outwards and peak around $R = 1.5$.

The maximums for $Re < 2200$ create a plateau in the stagnation region, followed by steady drops that start around $R = 1.3$.

Nusselt number steadily decreases with increased radial distance as there are no peak values of the heat flux at the impingement region and flame temperatures remain constant in the stagnation region and steadily decreases in the impingement and wall-jet regions.

In terms of heat transfer uniformity, the optimal value of Re_{opt} for inverted flames can be observed from Figures 5.17. For $H_{opt} = 3$, the most uniform heat flux distribution is at $Re_{opt} = 2000$.

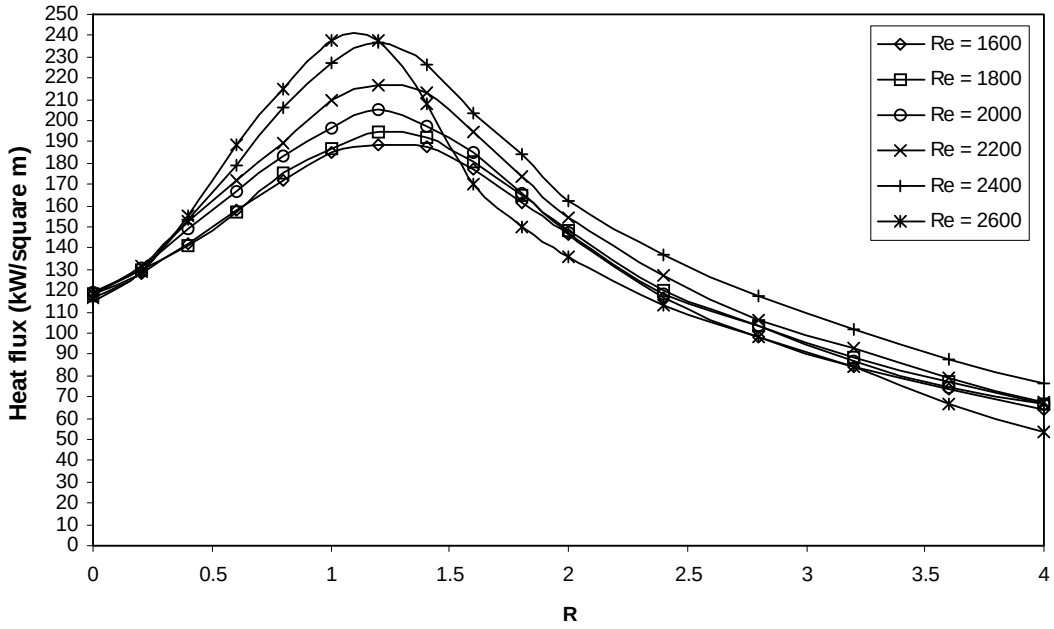

Figure 5.15. Effect of *Re* on radial heat flux distribution at $\Phi = 0.9$, $H = 1$, $B_R = 0$, $B_T = 0.51$.

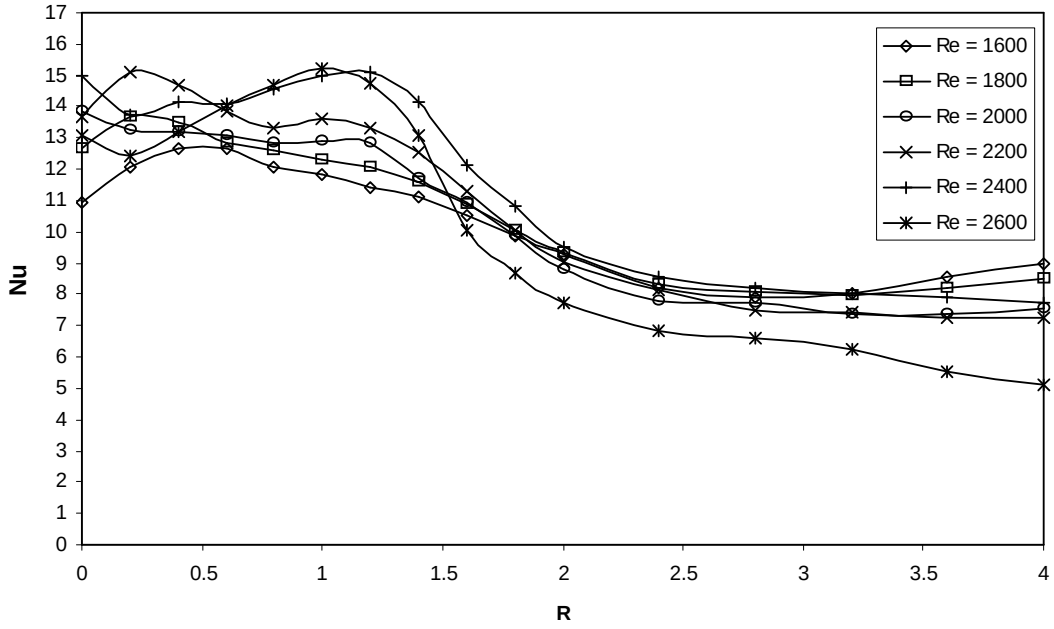

Figure 5.16. Effect of *Re* on radial Nusselt number distribution at $\Phi = 0.9$, $H = 1$, $B_R = 0$, $B_T = 0.51$.

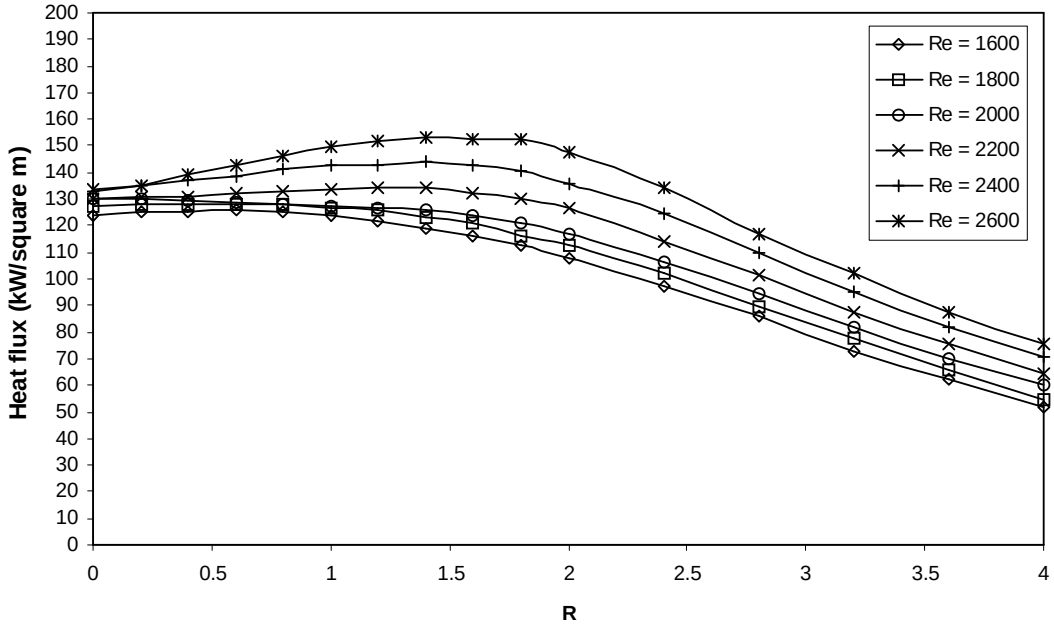

Figure 5.17. Effect of *Re* on radial heat flux distribution at $\Phi = 0.9$, $H = 3$, $B_R = 0$, $B_T = 0.51$.

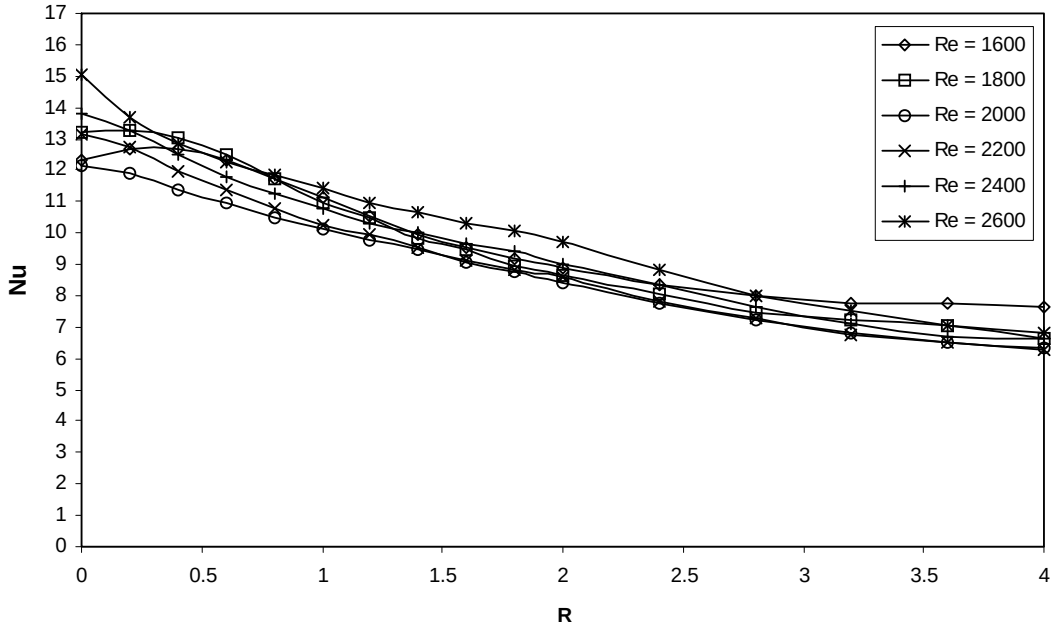

Figure 5.18. Effect of *Re* on radial Nusselt number distribution at $\Phi = 0.9$, $H = 3$, $B_R = 0$, $B_T = 0.51$.

5.4.1.2. Stagnation point, stagnation circle and maximum heat flux and *Nu*

Relevant data are presented in Figures 5.19 – 5.20 that cover Case 2 (H = 1) and in Figures 5.21 – 5.22 that represent Case 1 (H = 3).

The stagnation point heat transfer in both cases is very steady and there is no sharp drop reported. In Case 2, it remains almost constant with negligible variation (3%). Thus it can be assumed that effect of Reynolds number at for small nozzle-to-plate ratio is negligible. In Case 1, there is slight and steady increase with increased *Re*.

An increase in flame temperatures and heat transfer rates in the impingement region is due to increased turbulence associated with increased Re. Increased turbulence enhances mixing of combustion reactants, consequently the flame temperature in the reaction zone increases.

Stagnation point *Nu* is very close to maximum values in the range of *Re* = 1600 – 2400 for Case 2. In Case 1, the maximum values of *Nu* are those of stagnation point for the entire range of *Re*.

Heat transfer characteristics at stagnation circle are defined by increase of heat transfer rate with increased *Re*. Values of *Nu* remain constant. In Case 2, the increase is more profound, the overall increase is 29%. In Case 2, it can be assumed constant up to *Re* = 2000, then it starts to increase steadily and reaches its peak at *Re* = 2600.

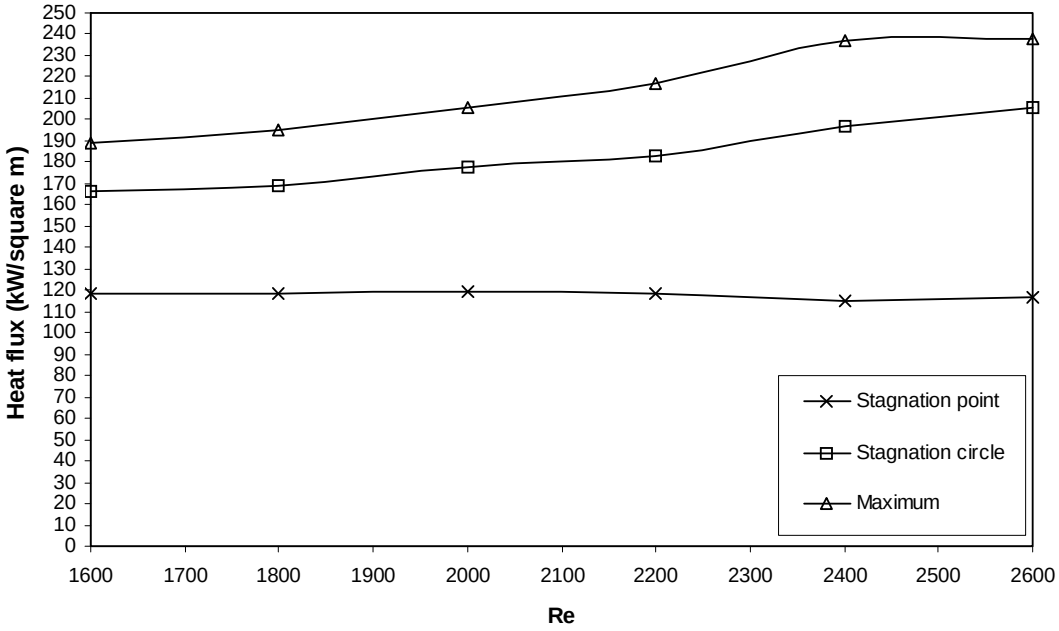

Figure 5.19. Effect of *Re* on stagnation point, stagnation circle and maximum heat flux at $\Phi = 0.9$, $H = 1$, $B_R = 0$, $B_T = 0.51$.

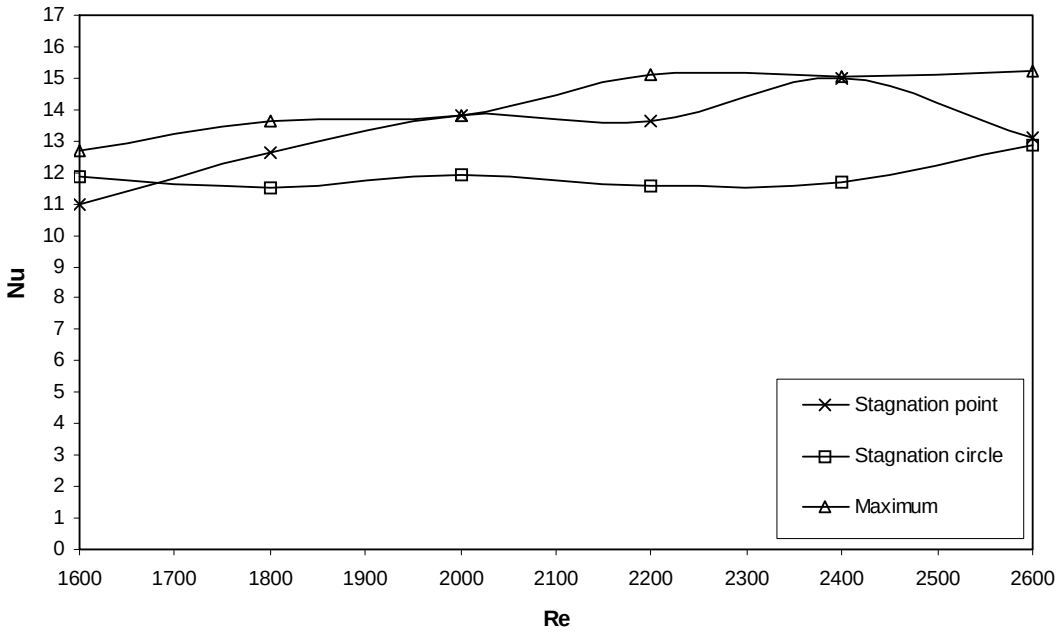

Figure 5.20. Effect of *Re* on stagnation point, stagnation circle and maximum Nusselt number at $\Phi = 0.9$, $H = 1$, $B_R = 0$, $B_T = 0.51$.

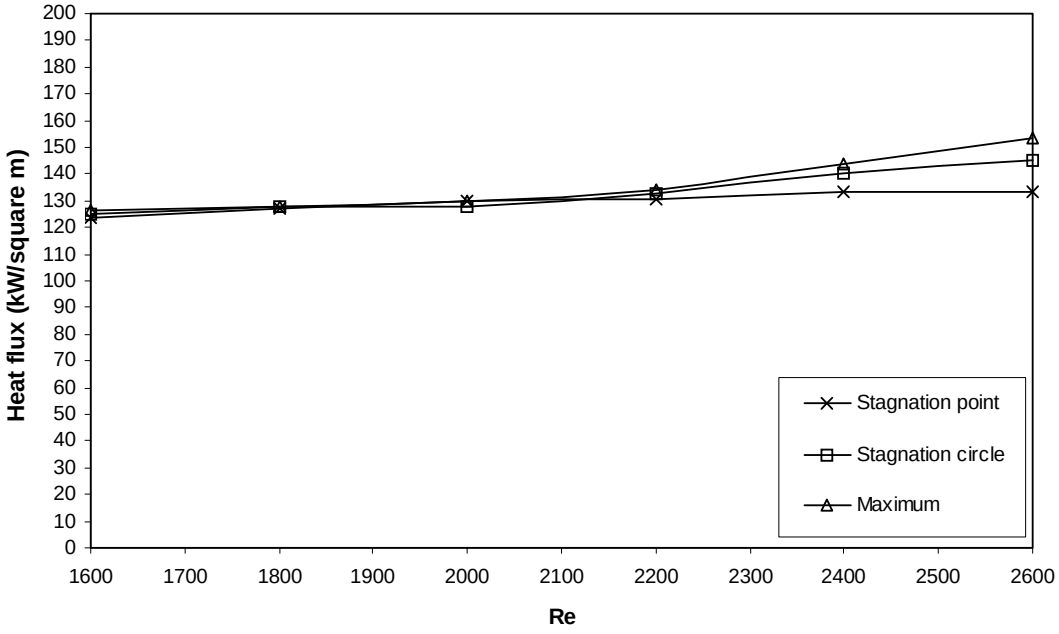

Figure 5.21. Effect of *Re* on stagnation point, stagnation circle and maximum heat flux at $\Phi = 0.9$, $H = 3$, $B_R = 0$, $B_T = 0.51$.

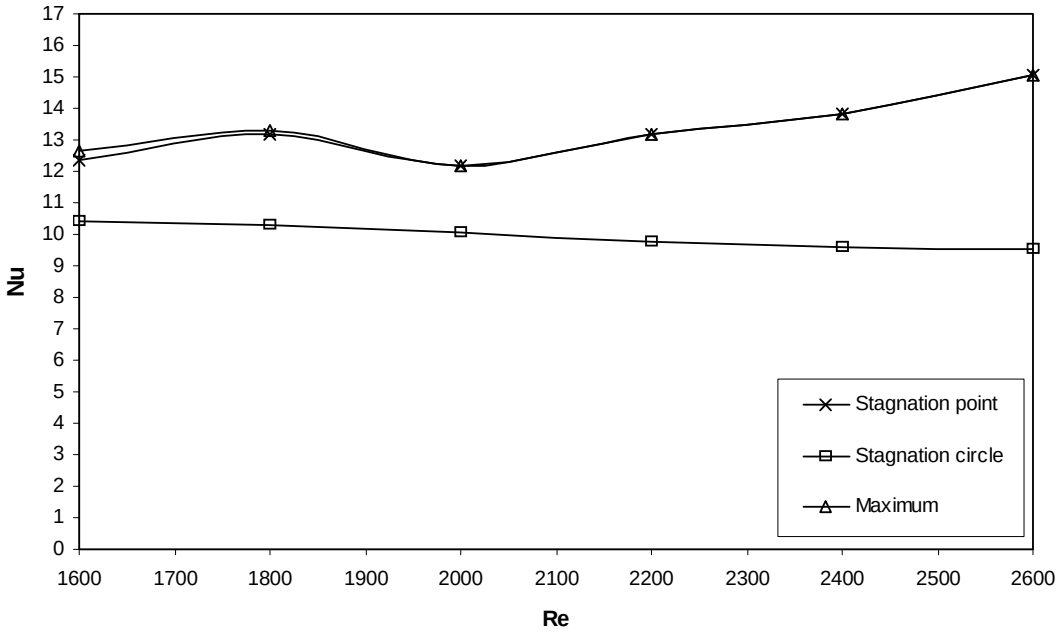

Figure 5.22. Effect of *Re* on stagnation point, stagnation circle and maximum Nusselt number at $\Phi = 0.9$, $H = 3$, $B_R = 0$, $B_T = 0.51$.

Values of *Nu* remain constant for stagnation circle for both cases, slight increase can be observed at *Re* = 2600 in Case 2 (*H* = 1), where it is equal with *Nu* value at stagnation point.

Higher values of *Re* consequently increase the maximum values of heat flux and *Nu*. Such increase is more significant at *H* = 1, the difference between *Re* = 1600 and *Re* = 2600 is approximately 26%. At *H* = 3, the difference between same *Re* values is 21%. Maximum values at the range of *Re* = 1600 – 2200 are equal to those of stagnation point and stagnation circle. Again, this confirms very uniform heat transfer of impinging inverted flames.

5.4.2. Area-averaged heat flux and Nusselt number distribution

Area-averaged distributions of heat flux and *Nu* are presented in Figures 5.23 – 26. The regions, i.e. stagnation, impingement and wall-jet region, have exact sizes as those in Chapter 5.3. Total values of heat flux and *Nu* for the entire region have been obtained as well.

Heat transfer characteristics at stagnation region show similar behavior as those for stagnation point. With an increased *Re*, the heat transfer rate steadily increases for both Case 1 and Case 2. The difference between heat flux values at *Re* = 1600 and *Re* = 2600 is 21% for Case 2 and 15% for Case 1. Nusselt number slightly increases by approximately 16% in Case 2, and remains relatively constant in Case 1.

Impingement region heat transfer also increases with an increased *Re*. However, as seen in Figure 5.23, the increase is halted at *Re* = 2200, where it peaks. At *Re* =

2400, it shares the same value with averaged heat flux of stagnation region. Further, it decreases even below values of stagnation region at *Re* = 2600. This can explained by the fact observed from figure 5.15. Starting from *Re* = 2200, the peaks are gradually shifted inwards, but still within the impingement region. But there is steeper decrease afterwards that decreases the overall heat transfer rate in the impingement region.

Average Nusselt number for the impingement region reflects the inward shift of heat flux peaks associated with higher *Re*. It increases up to *Re* = 2400 and drops down at *Re* = 2600.

In contrast to Case 2, the heat flux values of stagnation region are slightly below of those of impingement region in Case 1 (*H* = 3). Turning point is *Re* = 2200, from where the maximum recorded heat transfer rates are in the impingement region.

Total averaged heat flux modestly increases with increased Re for the entire range of *Re* in Case 1. Average *Nu* remains relatively constant. In Case 2, the turn at *Re* = 2200 for heat flux and *Re* = 2400 for *Nu* reflexes the decrease in impingement region, as demonstrated in Figures 5.23 and 5.24.

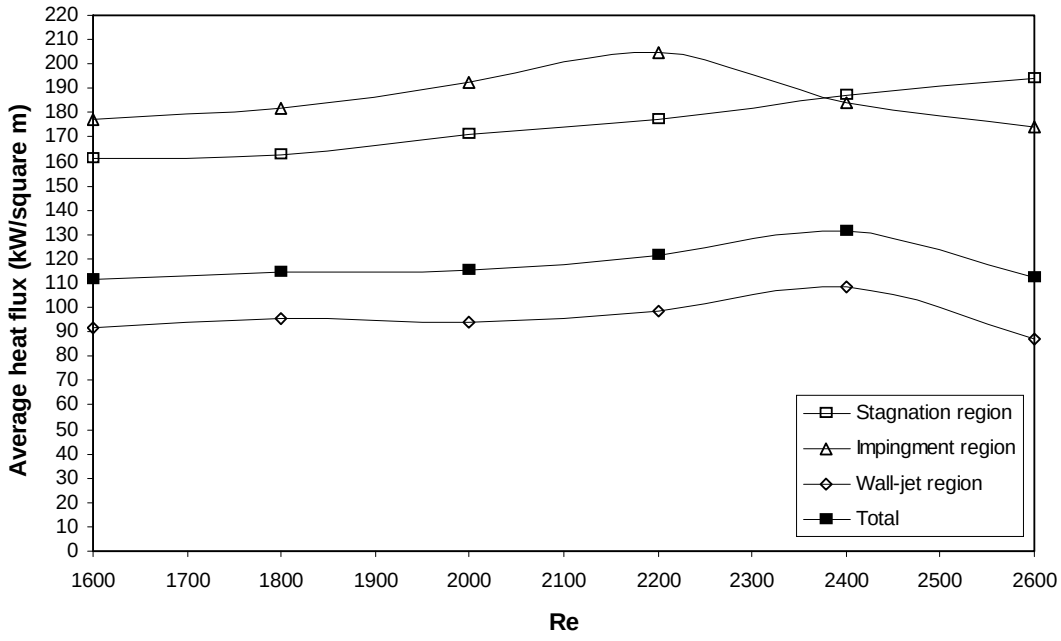

Figure 5.23. Variation of average heat flux with *Re* at different impingement regions at $\Phi = 0.9$, $H = 1$, $B_R = 0$, $B_T = 0.51$.

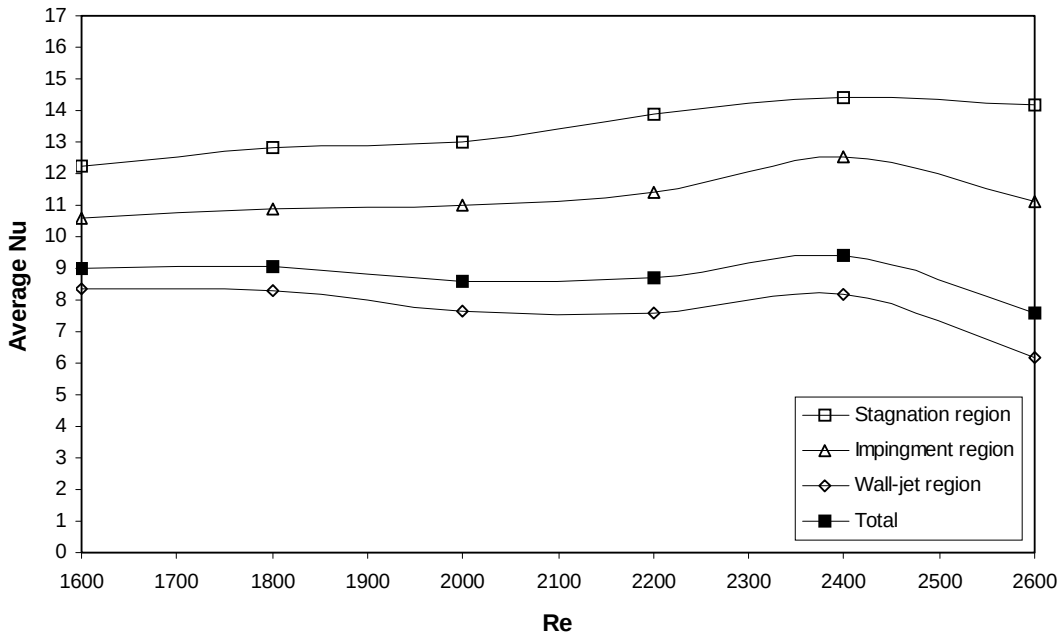

Figure 5.24. Variation of average *Nu* with *Re* at different impingement regions at $\Phi = 0.9$, $H = 1$, $B_R = 0$, $B_T = 0.51$.

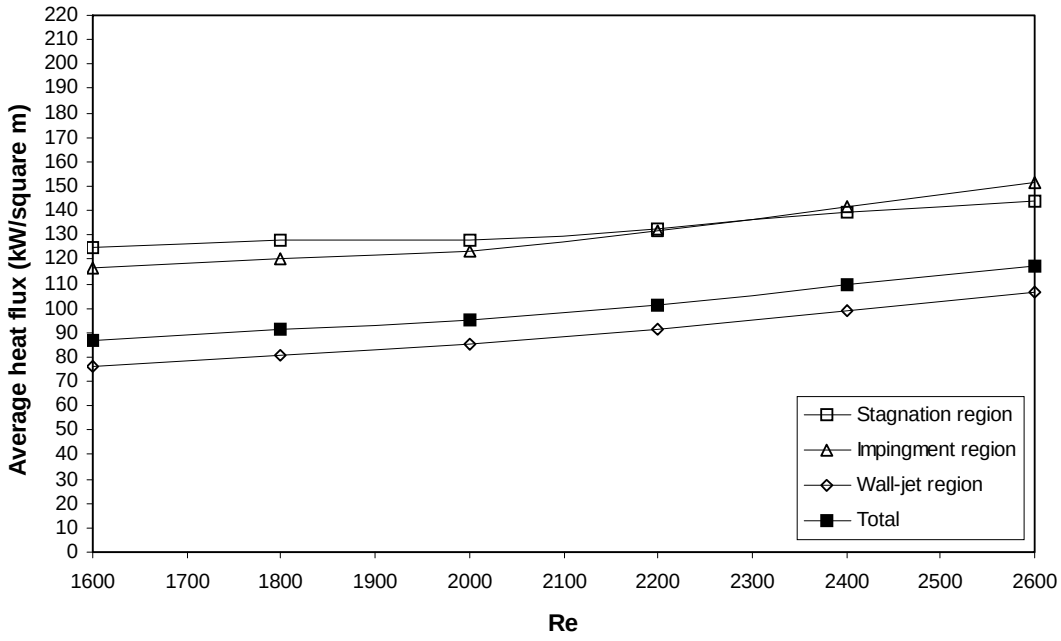

Figure 5.25. Variation of average heat flux with *Re* at different impingement regions at $\Phi = 0.9$, $H = 3$, $B_R = 0$, $B_T = 0.51$.

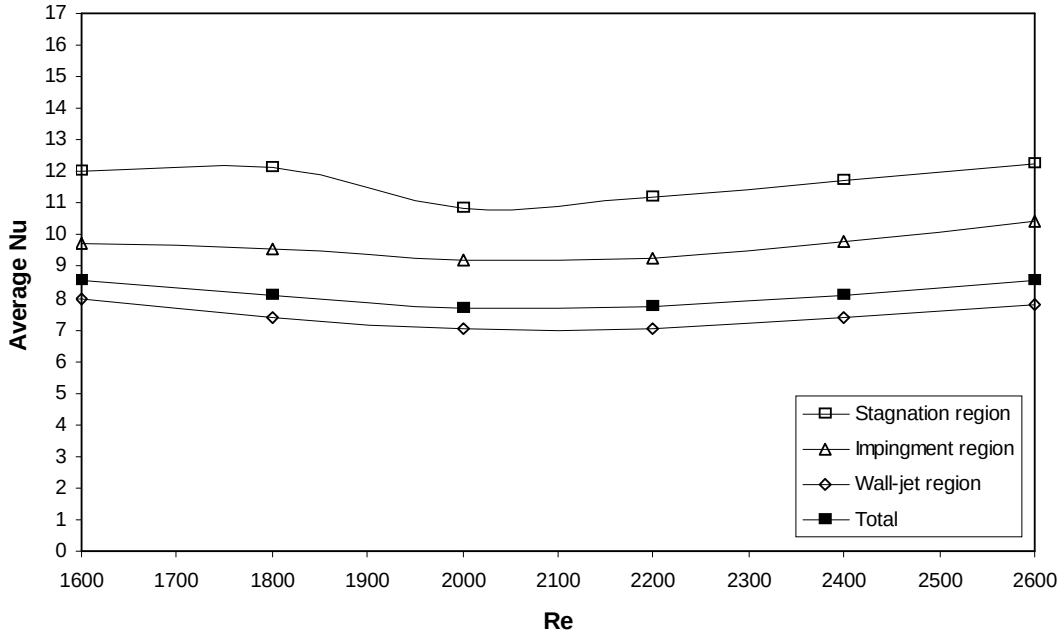

Figure 5.26. Variation of average *Nu* with *Re* at different impingement regions at $\Phi = 0.9$, $H = 3$, $B_R = 0$, $B_T = 0.51$.

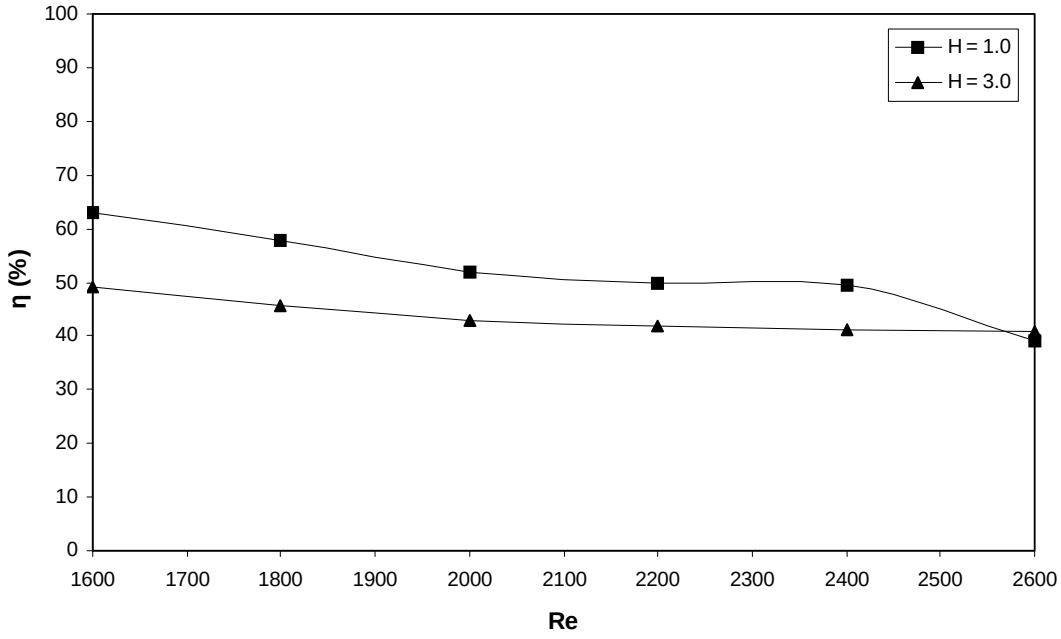

Figure 5.27. Thermal efficiency for various *Re* at Φ = 0.9, *H* = 1 and 3, B_R = 0, B_T = 0.51.

5.4.3. Thermal efficiency

Figure 5.27 shows thermal efficiency η as the function of Reynolds number for *H* = 1 (Case 2) and *H* = 3 (Case 1). For obvious reasons, at closer distance to the impingement plate, the thermal efficiency is generally higher and decreases with further distance. Maximum efficiency is 62.9% at *H* = 1 and *Re* = 1600, while at *H* = 3, it is only 49.1%. In both cases, the efficiency drops with increased *Re*. At *Re* = 2600 the values are almost the same in both cases. The difference between maximum and minimum values is within 61% for *H* = 1 and 21% for *H* = 3.

5.5. Effect of Rod protrusion

Third set of experiments covers the effect of rod protrusion B_R, which is one of newly defined non-dimensional geometrical parameters, introduced for the burner with axially-mounted rod. Related definition is in Chapter 2.3.2. The values of B_R are ranging from 0 to 2, with a step of 0.5. Data were recorded at the largest nozzle-to-plate ratio (H = 4) in order to facilitate the protruding rod.

5.5.1. Local heat flux and Nusselt number distribution

Similarly to the previous sets of experiments, local heat flux and Nusselt number distributions have been obtained as a function of non-dimensional radial distance R for various values of rod protrusion. Stagnation point, stagnation circle and maximum heat transfer rates as a function of B_R are also included.

5.5.1.1. Radial distribution

Radial heat flux and Nu distributions are shown in Figures 5.28 and 5.29. It can be observed that the patterns are somewhat similar to those with variation of nozzle-to-plate ratio. The incline from stagnation point and the peak at R = 1.5 with consequent decline are characteristic for B_R at 1.5 and 2.0. For smaller rod protrusion values, the heat transfer rate remains constant over a large area, with a decline, starting from R = 1.5. Nusselt number steadily decreases with further radial distance.

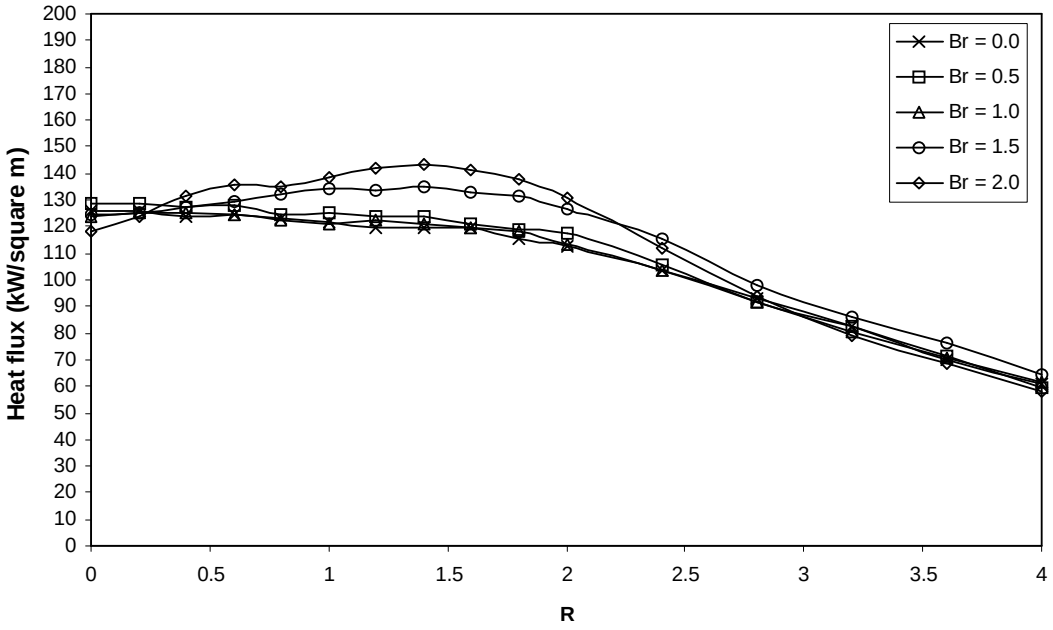

Figure 5.28. Effect of B_R on radial heat flux distribution at Φ = 0.9, Re = 2000, H = 4, B_T = 0.51.

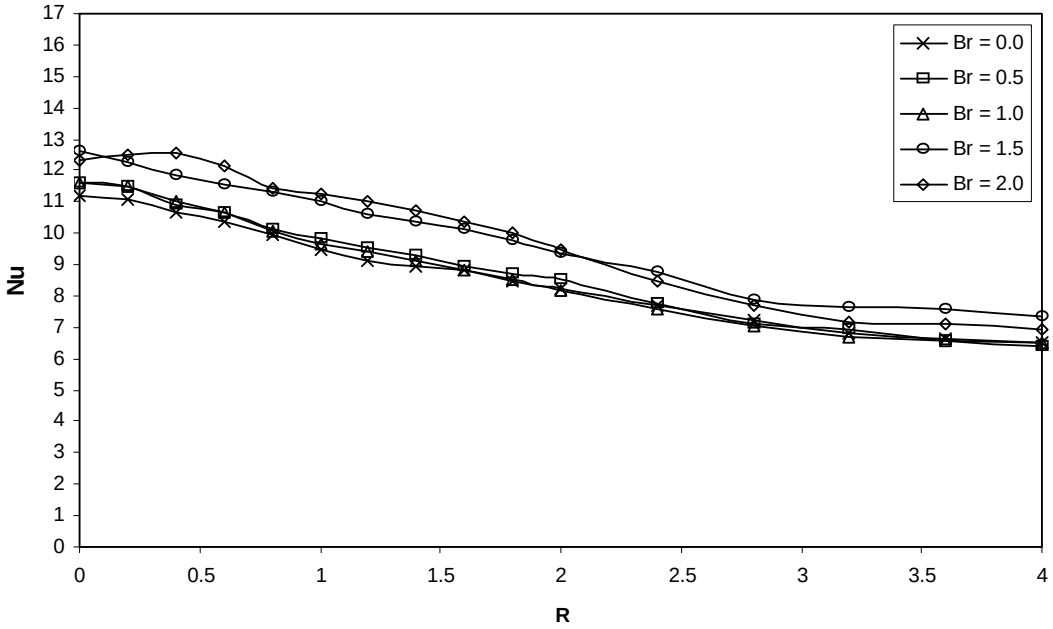

Figure 5.29. Effect of B_R on radial Nusselt number distribution at Φ = 0.9, Re = 2000, H = 4, B_T = 0.51.

By comparing radial heat flux data obtained at different nozzle-to-plate ratios (Figure 5.7) with those obtained at different rod protrusions (Figure 5.28), it can be assumed that there is negligible difference (within 5%) among the set of data obtained at e.g. $H = 4$ and $B_R = 1$ and $H = 3$ with $B_R = 0$. That means there is almost no difference between the heat transfer rate of an inverted flame at certain nozzle-to-plate distance with no rod protrusion and an inverted flame at wider nozzle-to-plate distance but with a rod that protrudes to the level of the nozzle-to-plate distance of the former inverted flame. It means that:

$$\dot{q}(H - B_R, B_R) = \dot{q}(H, B_R = 0) \tag{5.1}$$

This can be explained by the fact that the nozzle-to-plate distance h is defined as the axial distance from the tube rim to the impingement plate and not from the rod tip. So the variation of the length of rod protrusion b affects heat transfer rates as if the distance would be from the rod tip to the impingement plate. Such distance, nozzle-to-rod distance, can be defined as:

$$h' = h - b \tag{5.2}$$

Related geometry is presented in Figure 5.30. Consequently, nozzle-to-rod ratio can be defined as:

$$H' = H - B_R \tag{5.3}$$

Thus the heat flux distribution for inverted flames can be rewritten in the form:

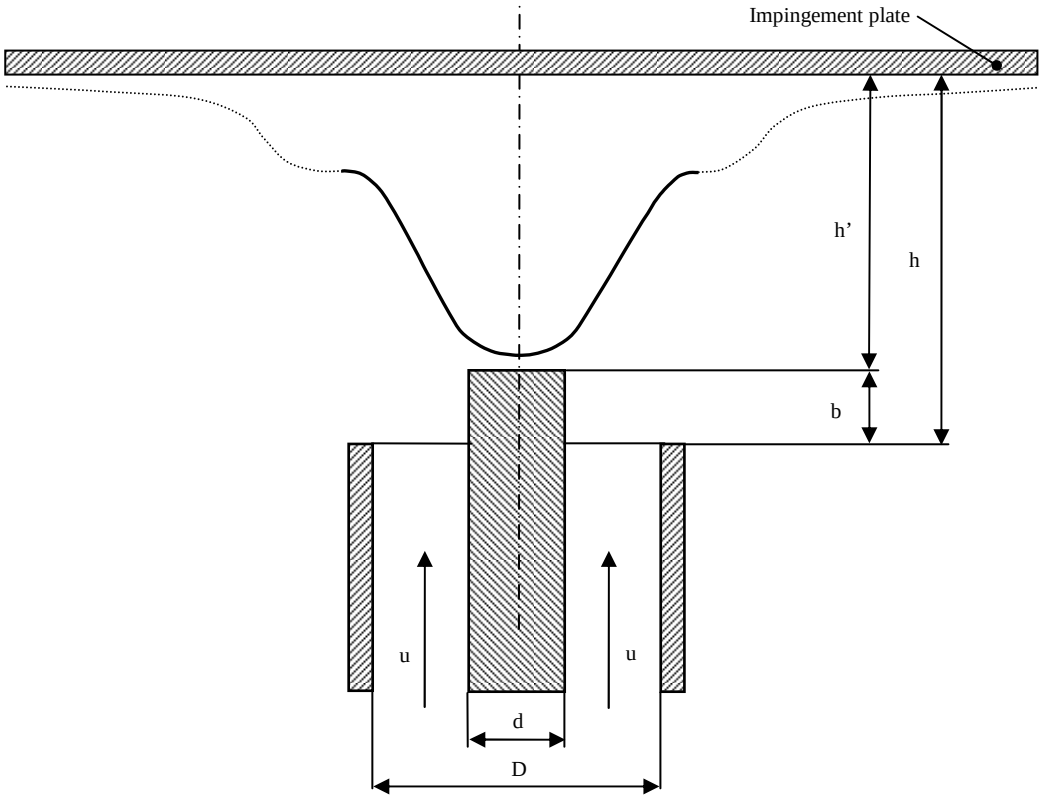

$$\dot{q}(H', B_R) = \dot{q}(H, B_R = 0) \tag{5.4}$$

It denotes, which level of H with no protrusion is required to achieve the same heat transfer distribution for a given rod protrusion B_R.

Since Nusselt number Nu is a function of heat flux, Equation 5.4 can be written also in the following form:

$$Nu(H', B_R) = Nu(H, B_R = 0) \tag{5.5}$$

5.5.1.2. Stagnation point, stagnation circle and maximum heat flux and *Nu*

Heat flux and Nusselt number distributions at stagnation point and stagnation circle as a function of B_R are represented by Figures 5.31 and 5.32 respectively. Maximum heat flux and *Nu* values are also plotted.

Both stagnation point heat flux and *Nu* appear to be constant up to B_R = 1, denoting there is no effect of rod protrusion on heat transfer characteristics. At B_R = 1 – 2, both heat transfer characteristics slightly increases.

Stagnation circle heat flux has the same values as at the stagnation point for the entire range of B_R, while stagnation circle *Nu* remains constant and well below its maximum at stagnation point.

Maximum heat flux occurs at stagnation point, except for B_R = 2. Nu_{max} is paired with stagnation point *Nu* for the entire range of B_R. As for heat flux, it is shifted further from stagnation point, starting from B_R = 1. Overall increase in maximum heat flux is approximately 13.5%, Nu_{max} is increased by 12.5%.

5.5.2. Area-averaged heat flux and Nusselt number distribution

Area-averaged distributions of heat flux and *Nu* for corresponding regions, i.e. stagnation, impingement and wall-jet region and total heat flux and *Nu* for the entire region are presented in this chapter. Figures 5.33 and 5.34 show area-averaged distributions for each region as a function of B_R.

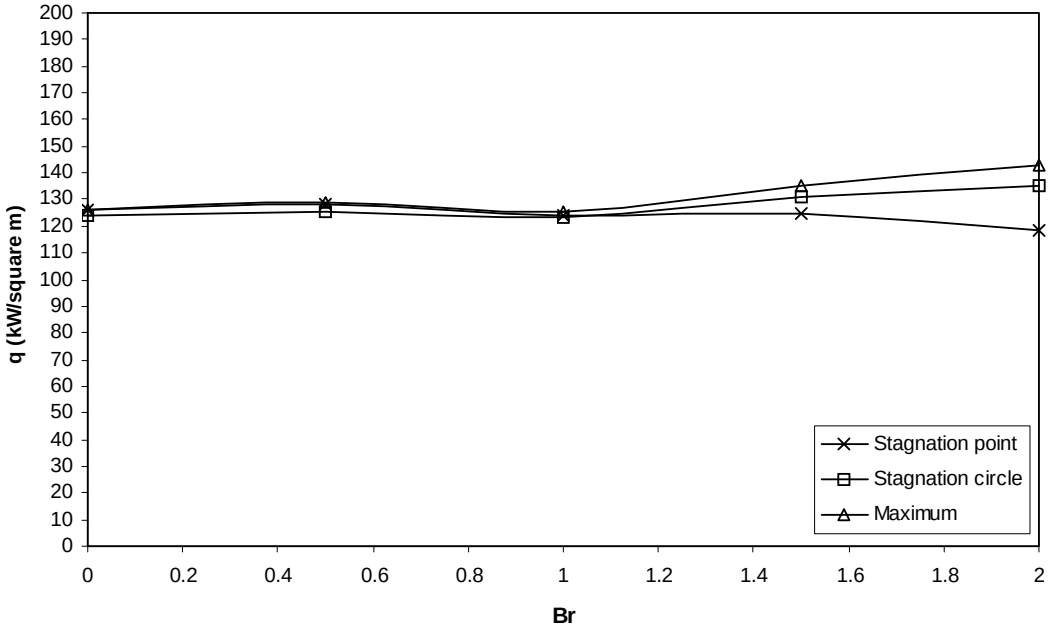

Figure 5.31. Effect of B_R on stagnation point, stagnation circle and maximum heat flux at Φ = 0.9, Re = 2000, H = 4, B_T = 0.51.

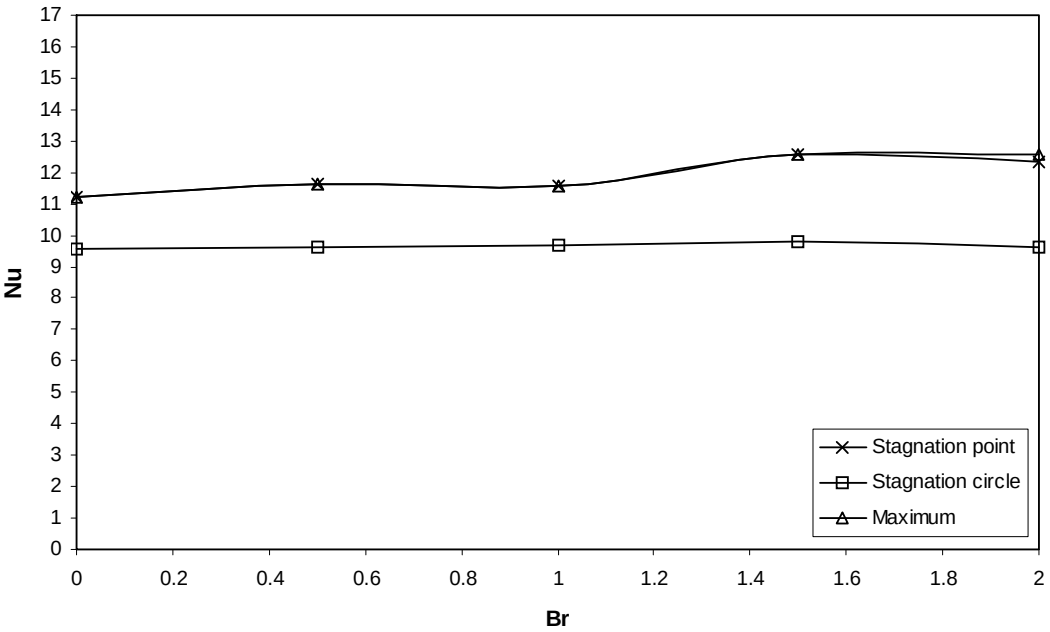

Figure 5.32. Effect of B_R on stagnation point, stagnation circle and maximum Nusselt number at Φ = 0.9, Re = 2000, H = 4, B_T = 0.51.

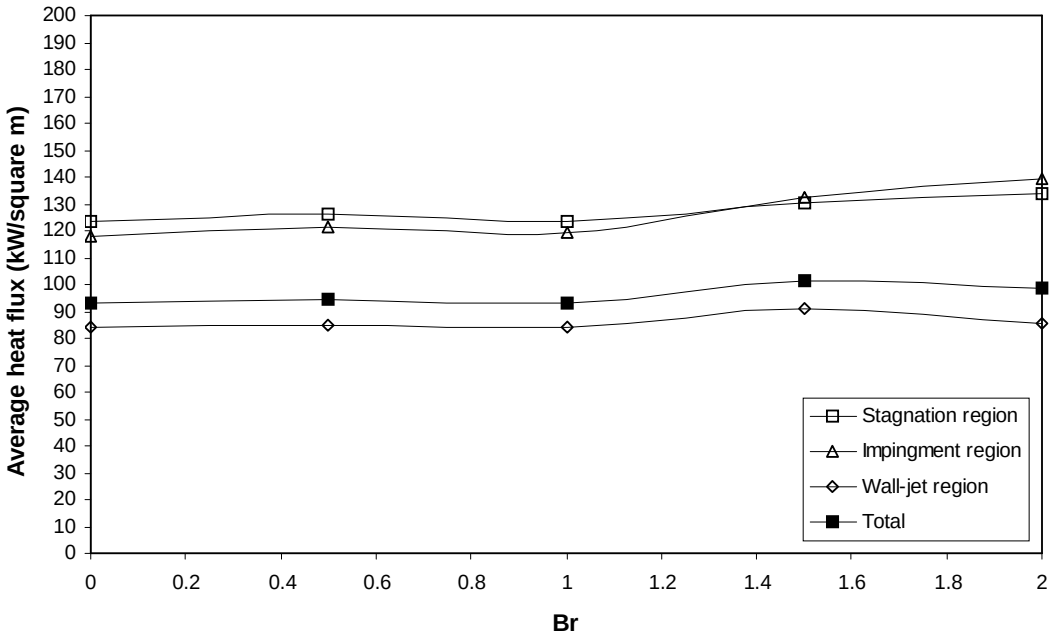

Figure 5.33. Variation of average heat flux with B_R at different impingement regions at Φ = 0.9, Re = 2000, H = 4, B_T = 0.51.

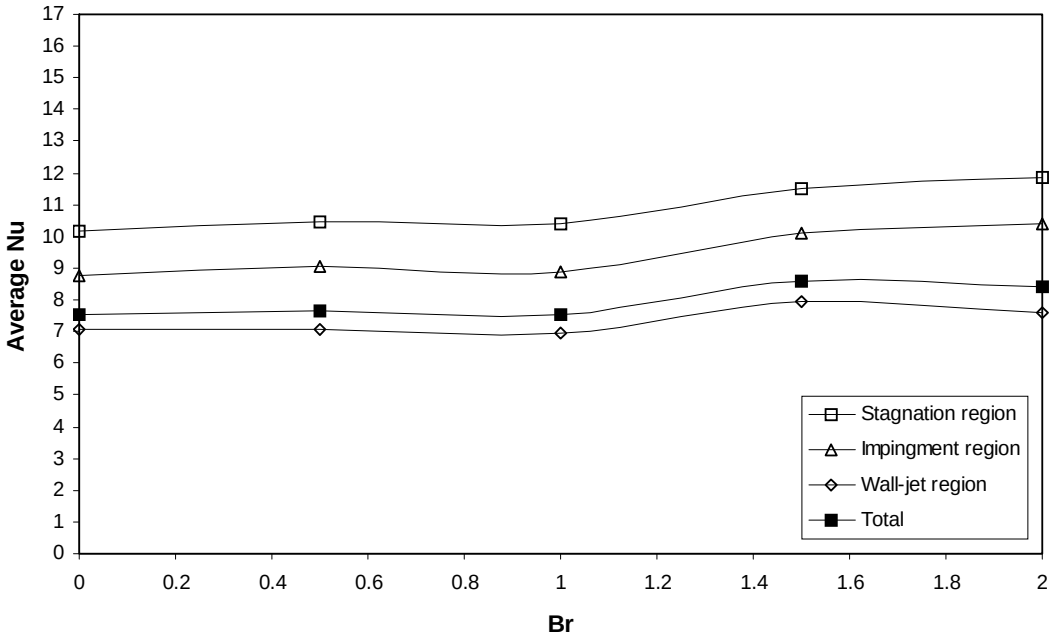

Figure 5.34. Variation of average Nu with B_R at different impingement regions at Φ = 0.9, Re = 2000, H = 4, B_T = 0.51.

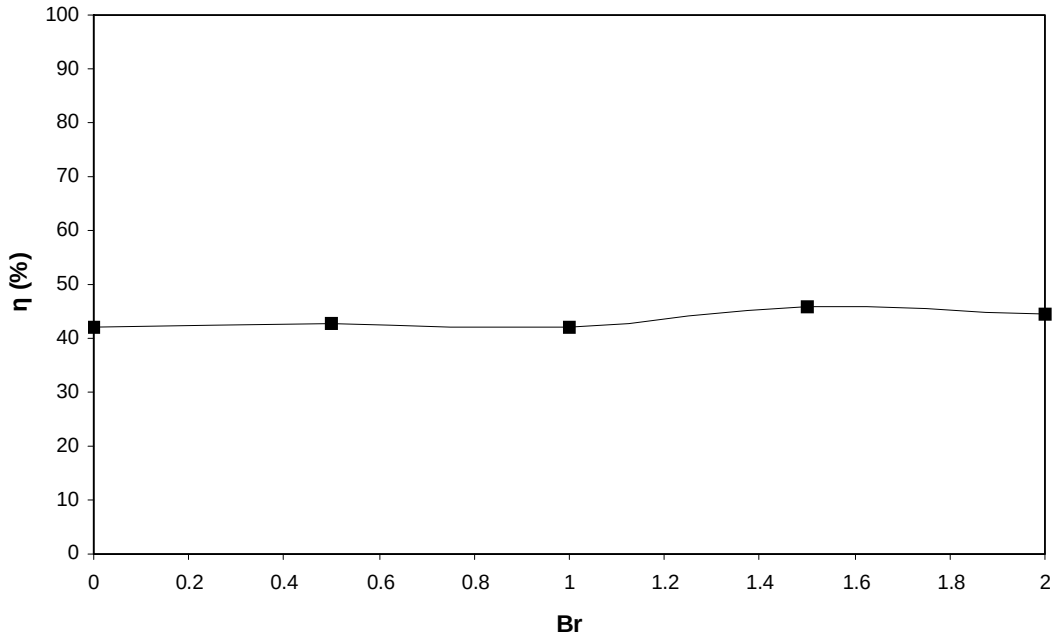

Figure 5.35. Thermal efficiency for various B_R at Φ = 0.9, Re = 2000, H = 4, B_T = 0.51.

Heat transfer rates at both stagnation and impingement regions are the highest and slightly increases from B_R = 1. Stagnation region is the area with the maximum values up to B_R = 1.3, from there, the maximum values shift to the impingement region. Nusselt number at stagnation region is the highest and is impaired from values at impingement region.

Overall, as the flame cone is drawn closer to the impingement plate with an increased B_R, heat transfer increases. Specifically, total heat flux increase accounts for 9 %, while total Nu increase is by 11%.

Likewise the effect of nozzle-to-plate ratio H, the effect of rod protrusion B_R on wall-jet region is minimal and heat transfer rate remains constant over the entire range of B_R.

5.5.3. Thermal efficiency

Thermal efficiency η plotted against B_R is presented in Figure 5.35. It appears to be considerably constant over the entire range. Maximum and minimum values are within 6%. This again confirms the fact that the effect of rod protrusion on impinging heat transfer characteristics is negligible.

5.6. Effect of Rod-to-tube ratio

The fourth set deals with the effect of rod-to-tube ratio B_T, which is the second newly defined non-dimensional geometrical parameter, introduced for the burner with axially-mounted rod. It facilitates the effect of variation of rod diameters, i.e. variation in nozzle exit area, on impingement heat transfer characteristics. Related definition is in Chapter 2.3.2. There were four rods of different diameters used in the experiments: 9.55 mm, 8.00 mm, 6.45 mm and 4.00 mm, with corresponding values of B_T: 0.51, 0.59, 0.67 and 0.80. The tube inner diameter was kept constant at 19.55 mm. Data were recorded at two different nozzle-to-plate ratios: H = 1 and 3, denoting Case 2 and 1 respectively.

5.6.1. Local heat flux and Nusselt number distribution

For specified rod-to-tube ratios, local heat flux and Nusselt number distributions are presented in this chapter. In order to compare different rod-tube-ratios (i.e. different rod diameters), the distributions are plotted against radial distance *r* (mm) instead of non-dimensional distance *R*, since the effective diameter varies with different rod diameters. Stagnation point, stagnation circle and maximum heat transfer rates as a function of B_T are also determined.

5.6.1.1. Radial distribution

Radial heat flux and *Nu* distributions are presented in Figures 5.36 and 5.37 for the Case 2 (H = 1) and in Figures 5.39 and 5.40 for Case 1 (H = 3).

The distributions in Case 2 follow typical patterns of inverted flames, described in previous chapters. That means there is constant increase from the stagnation point to the peak that occurs around r = 12 – 14 mm, followed by steady decrease with further distance.

The largest rod diameter (B_T = 0.51) has the highest peak in heat flux and a plateau with the highest *Nu*. With decreased diameter (i.e. increased B_T), peaks are slightly shifted outwards. Contrary to the expectations, peaks are least steep for the smallest diameter (B_T = 0.80), while distribution of Nu is observed to be relatively constant. This can be explained by the difference in spread angle γ. Figure 5.38 defines the spread angle as the angle between reaction zone of impinging inverted flames and vertical axis of the burner.

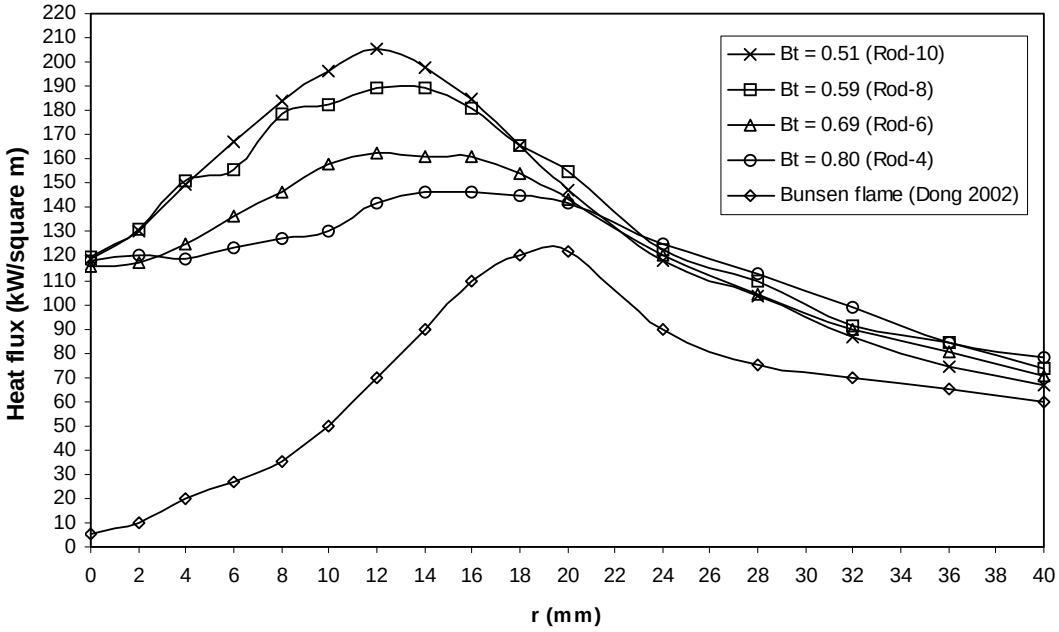

Figure 5.36. Effect of B_T on radial heat flux distribution at Φ = 0.9, Re = 2000, H = 1, B_R = 0. Comparison with Bunsen flames from round nozzle (Φ = 1.0, Re = 1500, H = 1).

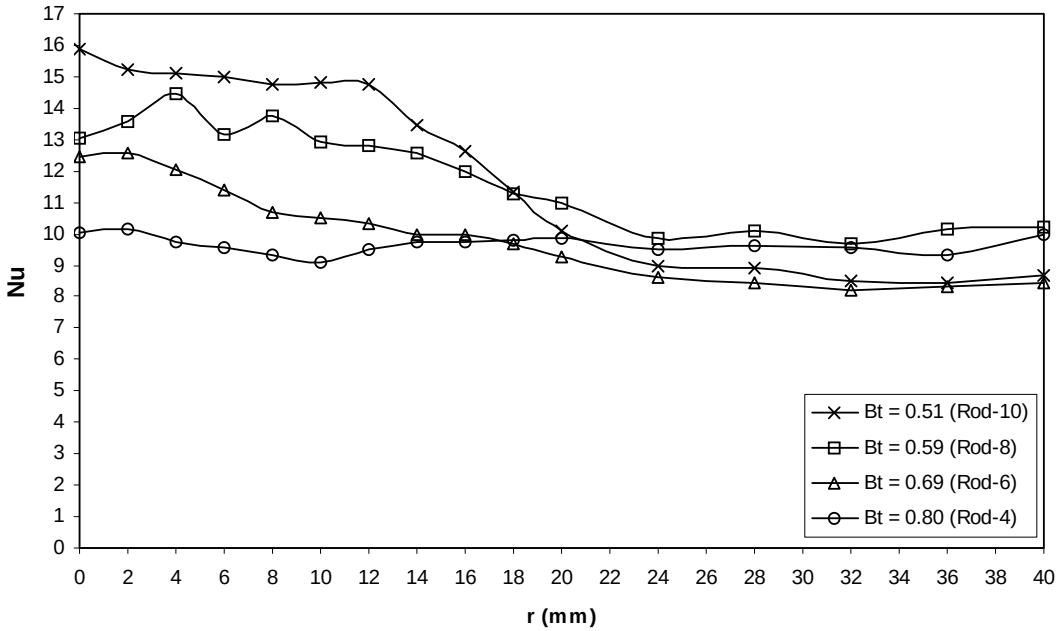

Figure 5.37. Effect of B_T on radial Nusselt number distribution at Φ = 0.9, Re = 2000, H = 1, B_R = 0.

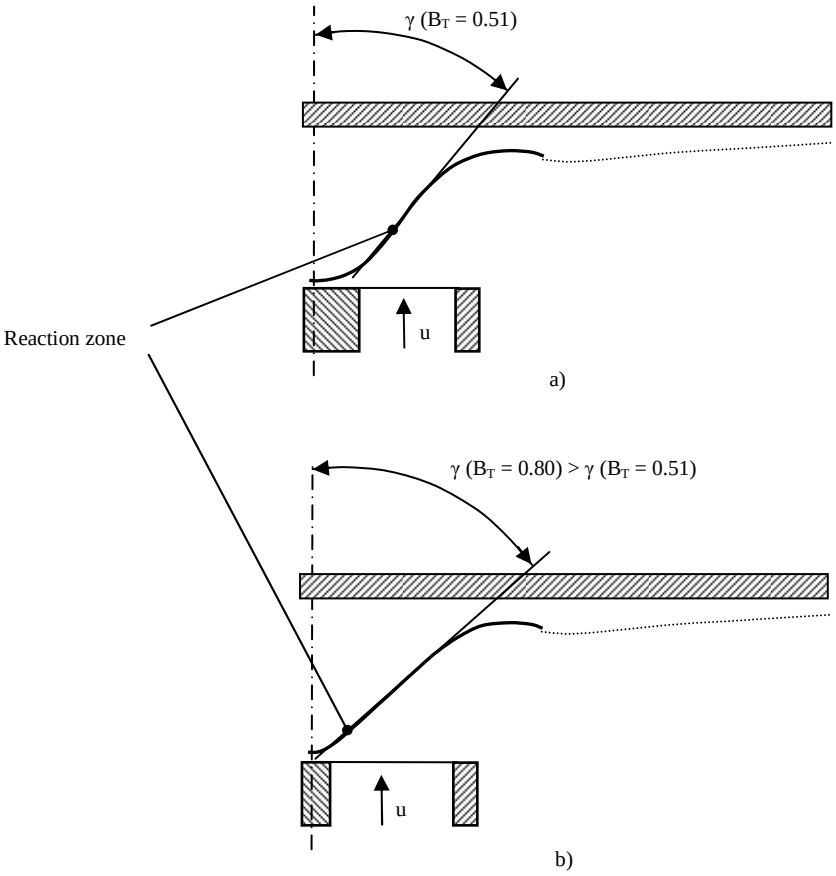

The spread angle is a function of B_T and increases with increasing B_T / decreasing rod diameter. In case of higher B_T, as in Figure 5.38b, the cross-sectional area of the nozzle is bigger due to smaller rod diameter (while inner tube diameter is kept constant). Obviously, this affects the flame shape. The tip of the flame cone is much smaller due to smaller rod diameter, thus the flame cone spread out at wider angle.

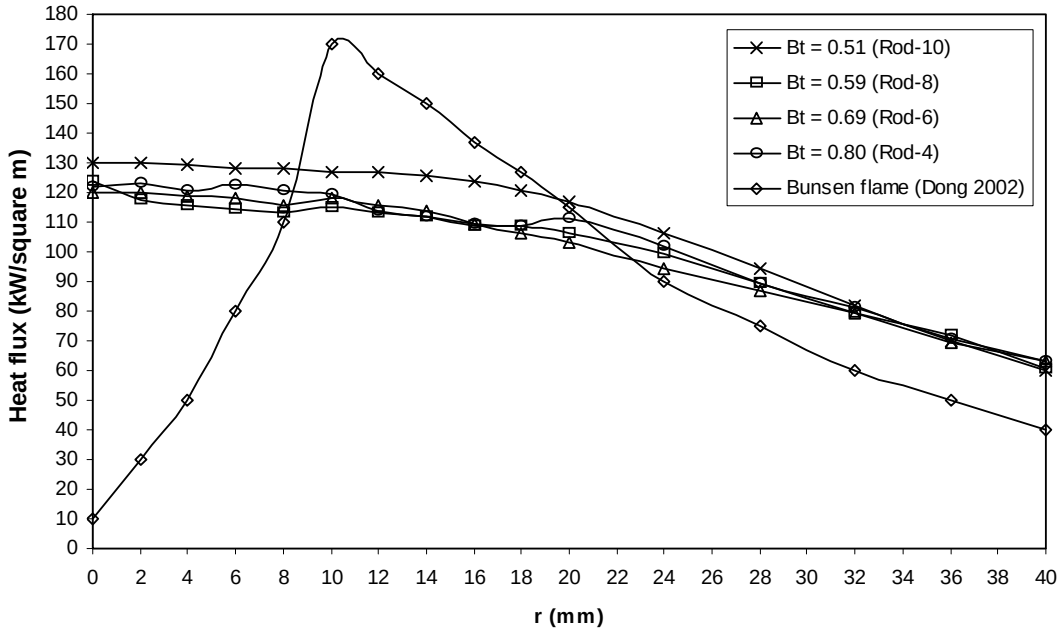

Figure 5.39. Effect of B_T on radial heat flux distribution at Φ = 0.9, Re = 2000, H = 3, B_R = 0. Comparison with Bunsen flames from round nozzle (Φ = 0.9, Re = 1500, H = 5).

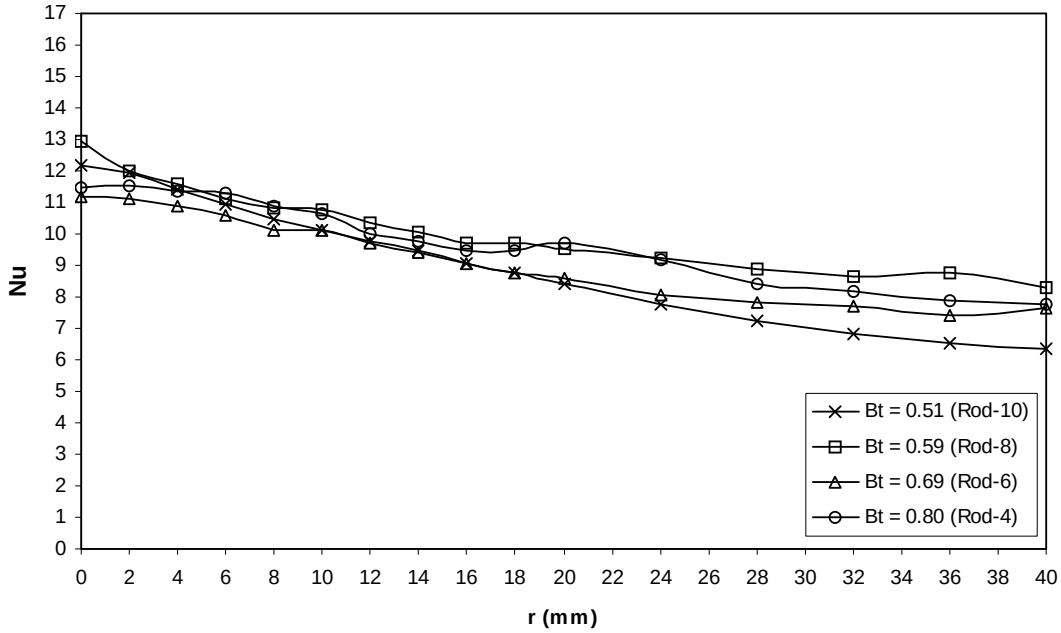

Figure 5.40. Effect of B_T on radial Nusselt number distribution at Φ = 0.9, Re = 2000, H = 3, B_R = 0.

It also means that it is more flat, in the impingement region, thus creating a plateau with maximum values rather than a steep peak. In case of *Nu* distribution it means that the values remain relatively constant over the entire investigated region due to more uniform distribution of flame temperatures.

With further distance from the impingement plate, the spread angle factor is less significant as it can be observed for $H = 3$ (Case 1), Figures 5.39 and 5.40. While it still keeps heat flux distributions constant over a large radial distance, *Nu* steadily decreases.

Data for boundary value of $B_T = 1$ (e.g. no rod) could not be obtained as it was not possible to stabilize the flame. Such flame would be classified as Bunsen flame as reaction zones could stabilize only at the tube rim. Comparison with such flame is in Figures 5.36 and 5.39. It is clear that the absence of the rod creates a sharp drop of the heat flux in the central core, a phenomenon that the variation with no rod highly non-uniform . Further comparison is in Chapter 5.7.

5.6.1.2. Stagnation point, stagnation circle and maximum heat flux and *Nu*

Relevant data are presented in Figures 5.41 – 5.42 that cover Case 2 ($H = 1$) and in Figures 5.43 – 5.44 that represent Case 1 ($H = 3$).

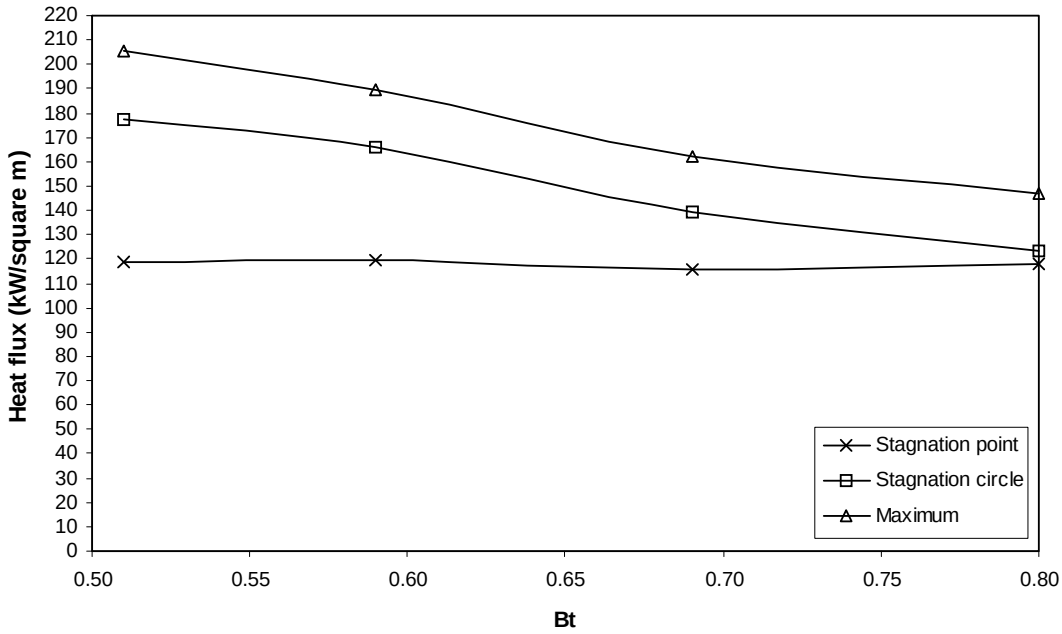

Figure 5.41. Effect of B_T on stagnation point, stagnation circle and maximum heat flux at Φ = 0.9, Re = 2000, H = 1, B_R = 0.

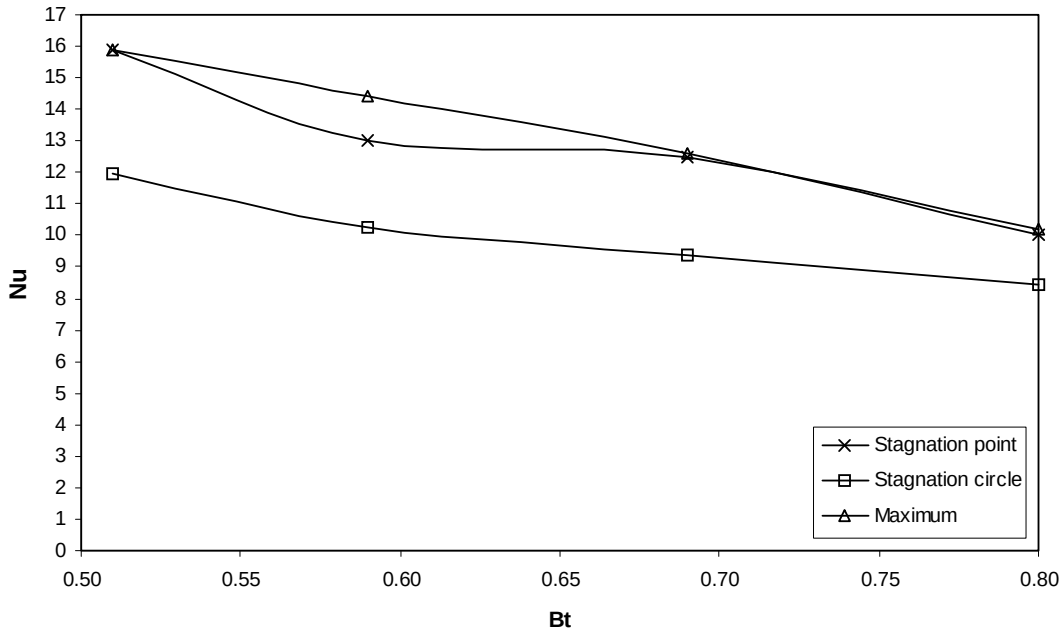

Figure 5.42. Effect of B_T on stagnation point, stagnation circle and maximum Nusselt number at Φ = 0.9, Re = 2000, H = 1, B_R = 0.

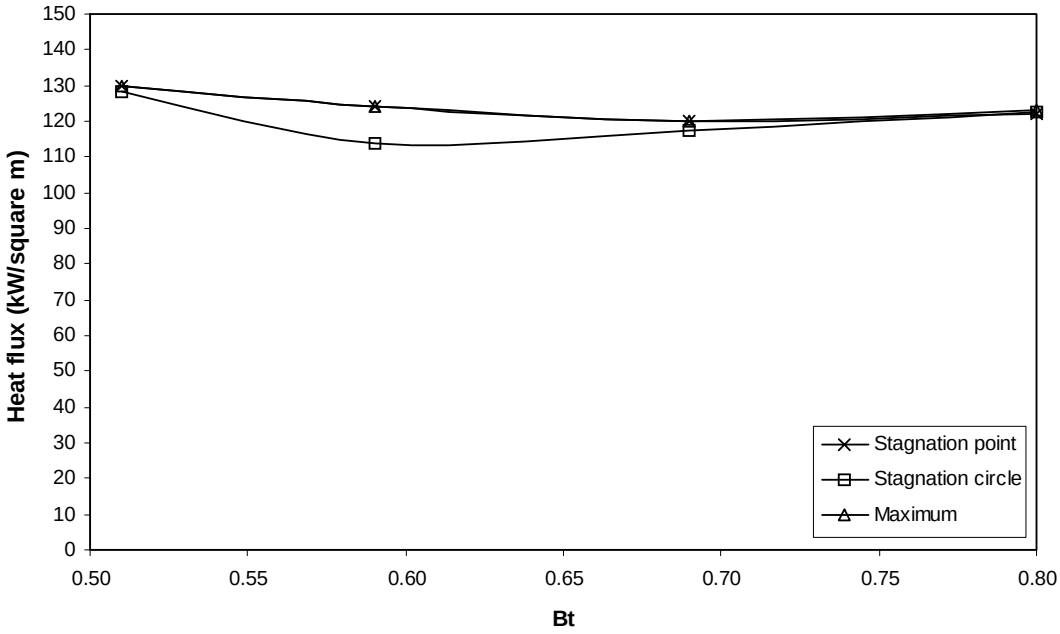

Figure 5.43. Effect of B_T on stagnation point, stagnation circle and maximum heat flux at Φ = 0.9, Re = 2000, H = 3, B_R = 0.

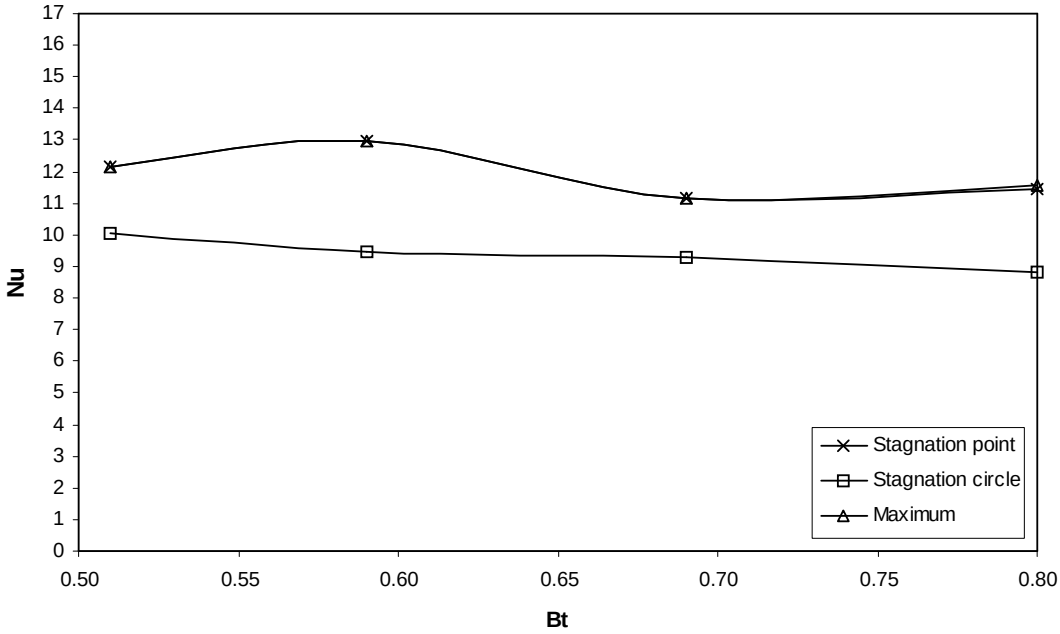

Figure 5.44. Effect of B_T on stagnation point, stagnation circle and maximum Nusselt number at Φ = 0.9, Re = 2000, H = 3, B_R = 0.

For closer nozzle-to-plate distance (Case 2), stagnation point heat flux remains constant for all variations of B_T, while stagnation point *Nu* decreases from its maximum at B_T = 0.50 and is identical with Nu_{max}. At further nozzle-to-plate distance (Case 1), both heat flux and *Nu* at stagnation point are identical with respective maximum values and are marginally higher for the two largest rod diameters (i.e. B_T = 0.51 and 0.59).

Heat flux at stagnation circle is higher in Case 2 than in the stagnation point and decreases with increases B_T. However the maximum heat flux is much higher, implying that peaks occur in further distance from stagnation circle. *Nu* at stagnation point exhibits similar pattern.

As for Case 1, heat flux at stagnation point is identical with stagnation point and maximum heat transfer rate, with an exception at B_T = 0.59. It confirms the presence of a plateau with maximum heat flux. In contrast, stagnation circle *Nu* is way below Nu_{max} obtained at the stagnation point.

5.6.2. Area-averaged heat flux and Nusselt number distribution

Area-averaged distributions of heat flux and Nu for stagnation region, impingement region and wall-jet region are compared with respective total values for the entire region and presented in Figures 5.45 – 5.48.

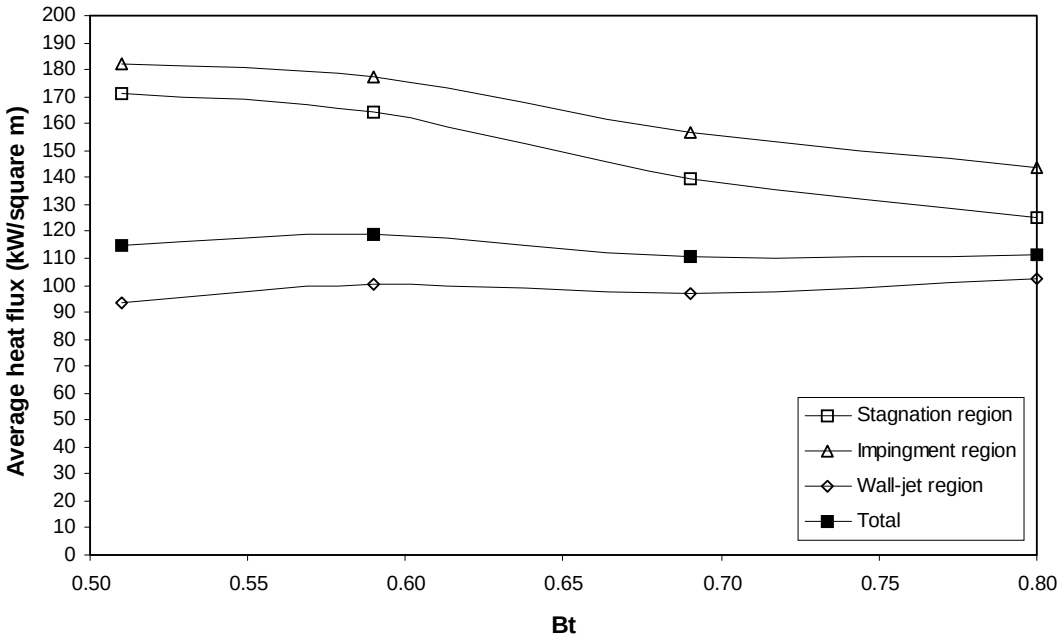

Figure 5.45. Variation of average heat flux with B_T at different impingement regions at Φ = 0.9, Re = 2000, H = 1, B_R = 0.

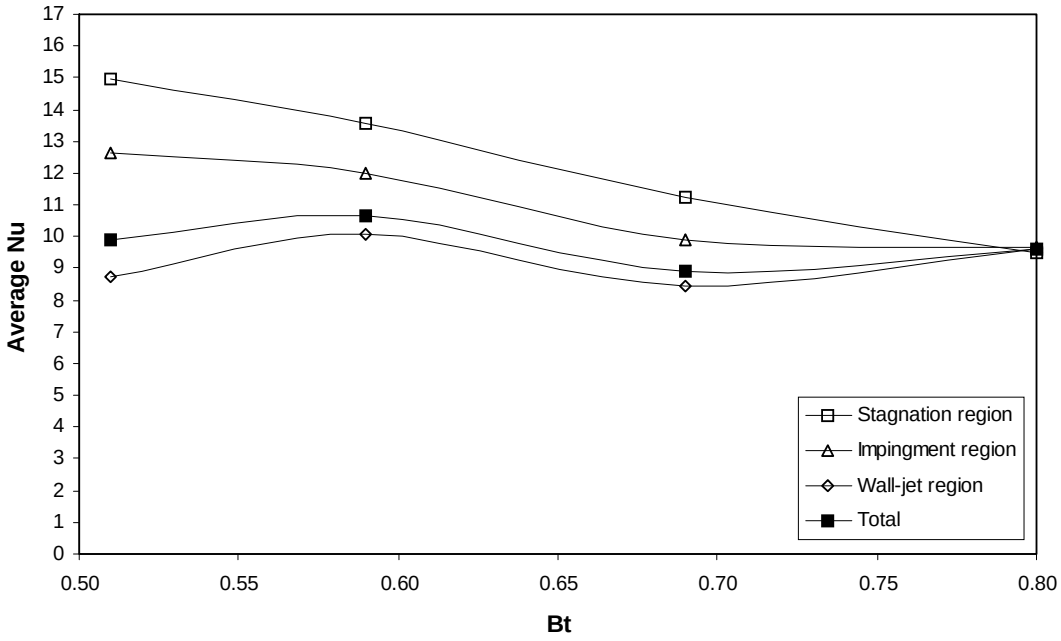

Figure 5.46. Variation of average Nu with B_T at different impingement regions at Φ = 0.9, Re = 2000, H = 1, B_R = 0.

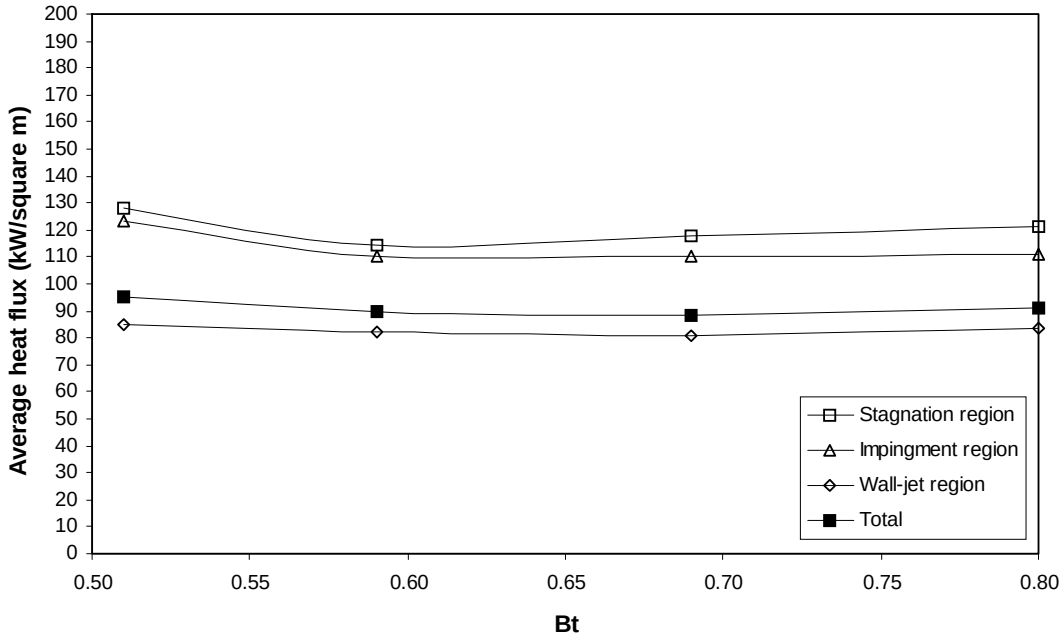

Figure 5.47. Variation of average heat flux with B_R at different impingement regions at Φ = 0.9, Re = 2000, H = 3, B_T = 0.51.

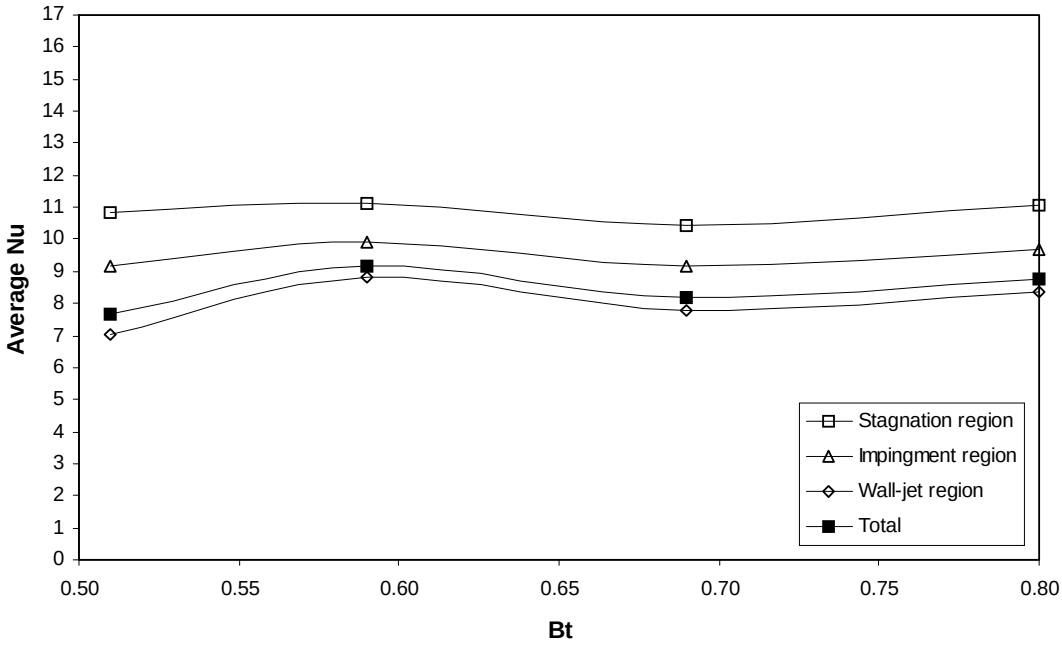

Figure 5.48. Variation of average Nu with B_R at different impingement regions at Φ = 0.9, Re = 2000, H = 3, B_T = 0.51.

At H = 1 (Case 2), Figures 5.45 and 5.46, the highest averaged heat flux is at the impinging region, where peaks occur. Values at stagnation region are lower, approximately 6% less in average. Both values are declining with increased B_T and slightly converge towards higher B_T. Such convergence is more significant in *Nu* distribution. With consequent decline in flame temperature, *Nu* becomes constant at all regions at B_T = 0.80. It means that in terms of uniformity, the rod with the smallest diameter (d = 4.00 mm) displays the optimal (constant) values of *Nu* distribution.

Thus it can be concluded that for small nozzle-to-plate distances, e.g. H = 1, and for given *Re*, smaller the rod diameter is, more optimal heat transfer characteristics occur.

There is no such big difference with variation of B_T with further distances from the impingement plate (H = 3, Case 1). Average heat flux at stagnation and impingement region is slightly bigger for the largest rod diameter (B_T = 0.51) and remains relatively constant with a constant gap between stagnation region heat flux and impingement region heat flux. *Nu* distribution slightly varies, however in general, the highest average *Nu* is in stagnation region followed by impingement region with an average 14% decrease.

It is evident that there is a correlation between nozzle-to-plate ratio and rod-to-tube ratio. With increased nozzle-to-plate ratio, the rod-to-tube ratio should be decreasing. In other words, it can be assumed that for given *Re*, the optimal distribution of heat flux and *Nu* over an impingement plate in terms of its uniformity

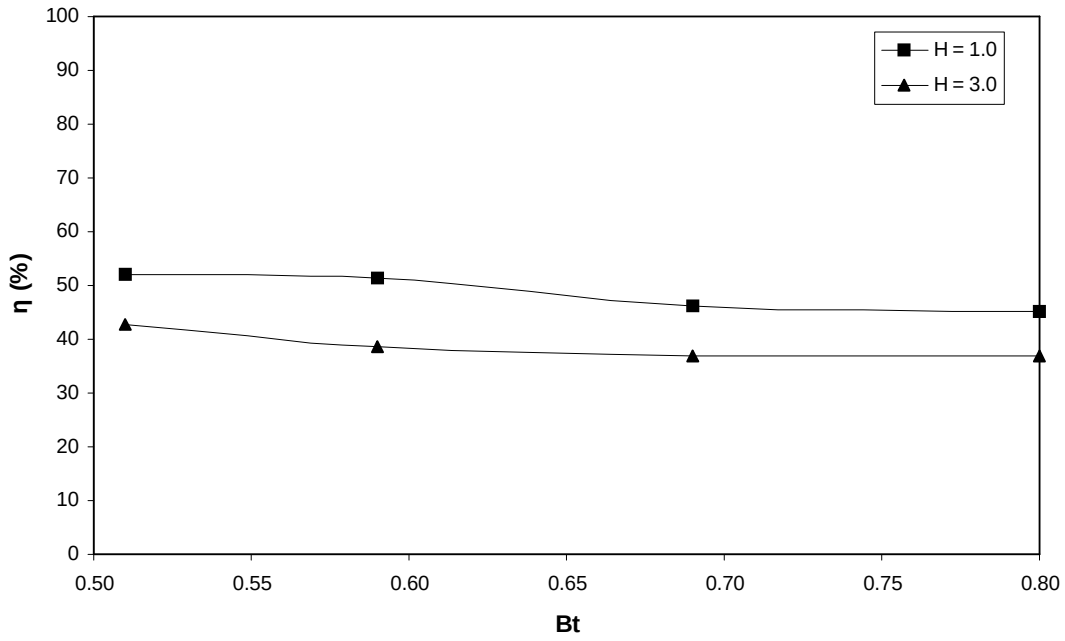

Figure 5.49. Thermal efficiency for various B_T at Φ = 0.9, Re = 2000, H = 1 and 3, B_R = 0.

is a function of nozzle-to-plate distance and rod diameter. To achieve uniform heat transfer characteristics, the designer should choose smaller rod diameters for close nozzle-to-plate distances and larger rod diameters for further distances from impingement plate.

5.6.3. Thermal efficiency

Figure 5.49 shows thermal efficiency η as the function of rod-to-tube ratio for H = 1 (Case 2) and H = 3 (Case 1). In correspondence with previous thermal efficiency dependences, the thermal efficiency is higher for closer nozzle-to-plate distance H. Thermal efficiency slightly decreases with increased B_T, accounting 13.7% for Case 1 (H = 3) and 15.5% for Case 2 (H = 1).

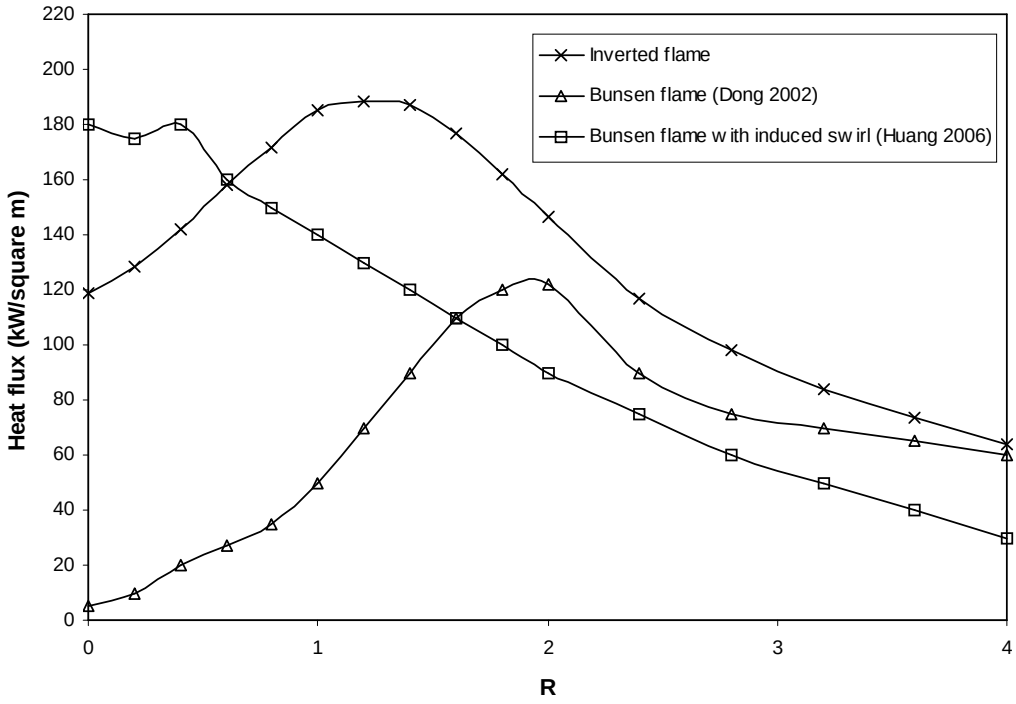

Figure 5.50. Comparison of radial heat flux distribution of inverted flames (Φ = 0.9, *Re* = 1600, *H* = 1, B_R = 0, B_T = 0.51) with Bunsen flames from round nozzle (Φ = 1.0, *Re* = 1500, *H* = 1) and Bunsen flames with induced swirl (Φ = 1.0, *Re* = 1500, *H* = 1, *S* = 2.53).

5.7. Comparison with other premixed impinging flames

The results, related to impinging inverted flames and presented so far in this chapter, are compared with previous studies that dealt with premixed impinging flames using similar configuration and similar input parameters, i.e. equivalence ratio and *Re*, fuel, etc.

Dong (2002), studied regular (Bunsen) flames generated by single round jet using butane / air. Huang (2006) studied swirl induced Bunsen flames generated also by single round jet. Both studies used flat plate as an impingement surface.

Since the geometrical parameters of the nozzle, especially nozzle diameter, are not the same, comparison is made with intention to observe the impact of each flame type on uniform heat transfer characteristics along the impingement plate.

At first, the comparison is made for small nozzle-to-plate ratio, i.e. H = 1. Figure 5.50 shows radial heat flux distributions of inverted flames at Φ = 0.9, Re = 1600, H = 1, B_R = 0, B_T = 0.51, regular Bunsen flames from round nozzle at Φ = 1.0, Re = 1500, H = 1 and Bunsen flames with induced swirl at Φ = 1.0, Re = 1500, H = 1, S = 2.53).

It is evident that inverted flames have the highest average heat flux distribution over the entire region as there is no significant drop in heat flux. In comparison to the regular Bunsen flame, the peak is shifted outwards, thus further delaying decline in wall-jet region. Swirl induced flame exhibits similar peak, however in comparison with inverted flame, there is a sharp drop at stagnation region.

Second comparison presents data at further nozzle-to-plate ratio, i.e. H = 3 and 5. Figure 5.51 shows radial heat flux distributions of inverted flames at Φ = 0.9, Re = 1600, H = 3, B_R = 0, B_T = 0.51, regular Bunsen flames from round nozzle at Φ = 0.9, Re = 1500, H = 1 and Bunsen flames with induced swirl at Φ = 1.0, Re = 1200, H = 3, S = 2.53).

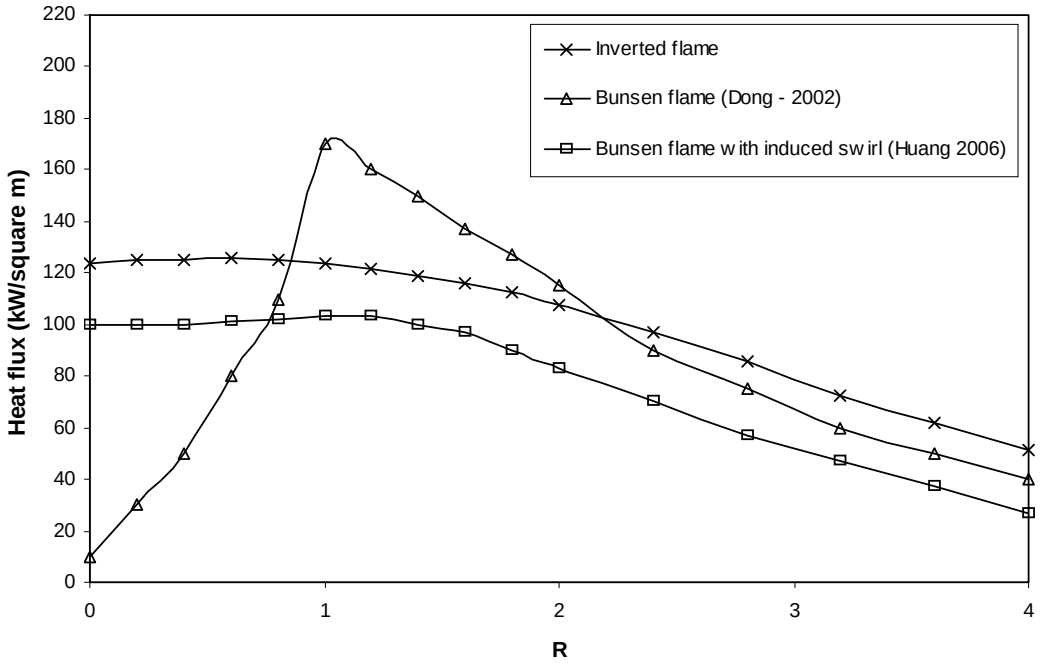

Figure 5.51. Comparison of radial heat flux distribution of inverted flames (Φ = 0.9, Re = 1600, H = 3, B_R = 0, B_T = 0.51) with Bunsen flames from round nozzle (Φ = 0.9, Re = 1500, H = 5) and Bunsen flames with induced swirl (Φ = 1.0, Re = 1200, H = 3, S = 2.53).

In this case, both inverted flames and Bunsen flames with induced swirl perform similarly. Radial heat flux values remain relatively constant up to approximately R = 1.5, followed by moderate decline. Regular Bunsen flame, despite further nozzle-to plate distance (H = 5) than the other flames, is still associated with sharp drop in the central core, where there is unburned gas with low temperature. Followed by the sharp peak, the heat flux pattern for the rest of the investigated region is similar to that of inverted flame.

5.8. Summary

1) Complete investigation of heat transfer characteristics of rod-stabilized impinging premixed inverted flames, generated by nozzle with axially-mounted rod has been performed. For reference purposes, all results are presented in three output parameters: heat transfer rate (kW/m2), non-dimensional heat transfer coefficient (Nusselt number *Nu*) and thermal efficiency η. Heat transfer rate and *Nu* are presented as a local values (those includes radial distribution, stagnation point and maximum values) as well as area-averaged values for the entire region and specific sub-regions (i.e. stagnation, impingement and wall-jet region). Thermal efficiency is calculated for the entire investigated region.

2) Flame structure reflects proximity of the nozzle to the impinging plate. For close nozzle-to-plate distance the flame is characterized by stretched out reaction zone, causing peak values of heat flux to be shifted outwards. With further distance, this effect diminishes and heat transfer distribution is more constant with no sharp peaks. Flame temperatures remain very high in the central core due to the presence of burned gas and positively affect the uniformity of heat flux and *Nu* distributions.

3) The effect of nozzle-to-plate ratio *H* is significant. Increasing *H* is associated with slight drop of heat flux in stagnation region followed by sharp peak with subsequent decline. Nusselt number remains constant in the stagnation and impingement region. On the other side, further increase of *H* creates

more constant heat flux distribution over large area with Nusselt number steadily decreasing. For very small *H*, the flame becomes unstable due to the quenching effect of impingement plate. It terms of optimal uniform heat transfer characteristics, nozzle-to-plate ratio is strongly related to the selected rod diameter (rod-to-tube ratio).

4) Variations of Reynolds number have major impact of heat flux and Nusselt number distributions. Increasing *Re* increases turbulence in the stagnation region, especially for smaller *H*, and better mixing enhances combustion, consequently the temperature arises, so the heat transfer rate. Increased turbulence however causes slight fluctuation in Nusselt number distributions.

5) It has been found that variation of rod protrusion B_R affects the heat transfer rate as if the distance would be from the rod tip to the impingement plate. The impact of rod protrusion variations on heat transfer characteristics is not significant and together with the fact that with increased rod protrusion there is an arising issue of flame stability, the use of rod protrusion is not recommended for laminar / transient flames.

6) With increased rod-to-tube ratio B_T and for small *H*, heat flux and *Nu* distributions show constant patterns, a fact that is related to the newly defined spread angle γ of the reaction zone. Spread angle is a function of B_T and increases with increasing B_T. Smaller rod diameters have wider spread angle, thus more uniform distribution in the stagnation and impingement

region. To achieve optimal uniform distribution, B_T must be correlated with H, e.g. for small H, smaller rod diameter (higher B_T) should be chosen.

7) Thermal efficiency of the inverted flames varies with input parameters. In general, it is in the range of 36 – 63 % and is generally higher for small nozzle-to-plate ratios and smaller *Re*. Rod protrusion has negligible effect, while increased rod-to-tube ratio decreases thermal efficiency.

8) Compelling comparison with regular Bunsen flames and Bunsen flames with induced swirl denotes that inverted flames present uniform heat flux distributions with no associated drops in stagnation region, in contrast with regular Bunsen flames.

6. HEAT TRANSFER CHARACTERISTICS OF IMPINGING PARTIALLY-INVERTED FLAMES

Second part of joint study that deals with impingement heat transfer characteristics of flames generated by the burner with axially-mounted rod that produces rod-stabilized flames is presented in this chapter.

As there is not known experimental study that has been reported (e.g. by major reviews by Viskanta (1993, 1996) and Baukal and Gebhart (1994)) about local and average heat transfer distributions of the rod-stabilized premixed flame impinging on the flat surface, this study is the first of its kind to cover inverted and partially-inverted impinging premixed flames. Inverted flames have been covered in Chapter 5; this chapter presents the results of investigation of partially-inverted flames.

It aims the same objectives, i.e. to explore and investigate the possibility of uniform heat transfer distribution of impinging premixed flame along the flat surface.

Various parameters have been tested in order to figure out the optimal values with regard to the uniform distribution and the results are presented as both local and area-averaged variables.

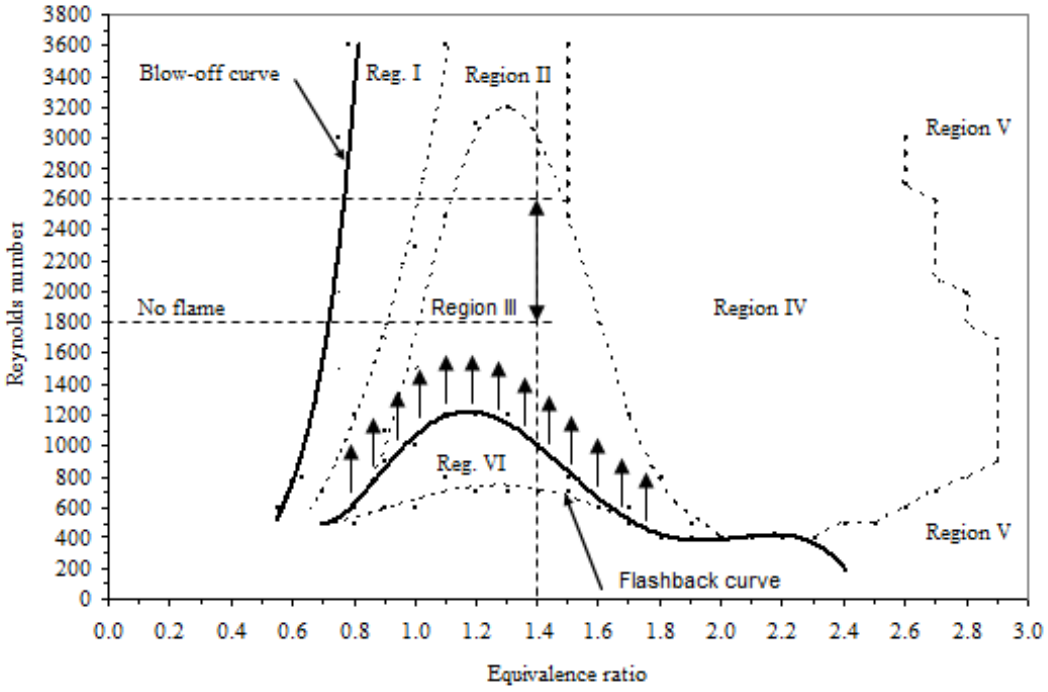

Figure 6.1. Range selection of Reynolds number and equivalence ratio for impinging partially-inverted flames.

The local variables include radial, stagnation point, stagnation circle and maximum values of local heat flux $\dot{q}$ and local Nusselt number *Nu*. Area-averaged variables, i.e. heat flux $\overline{q}$, Nusselt number $N\overline{u}$, are determined for stagnation, impingement and wall-jet region, and for the entire impingement region. Thermal efficiency η is determined for the entire impinging region. Related equations are defined in Chapter 2.

6.1. Parameters range selection

Based on the investigation of flammability characteristics of the rod-stabilized flames for various geometrical configurations in Chapter 3, the occurrence of

partially-inverted flames is in the range of Φ = 0.7 up to 2.1, for the most stable configuration (B_R = 0, B_T = 0.51), and covers Region II, III and IV. Out of these regions, Region III is the only region with sole appearance of partially-inverted flames. The other two mentioned regions are cross-areas with occurrence of more than one type of the flame, as described in details in Chapter 3. Equivalence ratio Φ for the Region III is approximately in the range of Φ = 1.0 - 1.6.

The effective range of Reynolds number was to be set the same as in the case of impinging inverted flames. However, a preliminary study revealed that there is a significant difference in stability diagrams for free-jet flames and impinging flames, particularly in the area of flashback area and unstable Region VI, which situated above the flashback curve. As described in Figure 6.1, size of Region VI increases at the expense of Region III. It can be explained by the fact that the proximity of impingement plate increases turbulence in the space between the nozzle and the plate. This enhances mixing that promotes better combustion, which in turn increases temperatures in the area above the nozzle. As the flame temperatures increase, both inner and outer reaction zones of partially-inverted flames are drawn closer to the rod tip and tube rim respectively and heat up the rod and tube rim. With increased temperature of the rod and the tube, preheating of unburned air/fuel mixture takes place inside the burner tube. Quenching effect of the rod and the tube wall is reduced and the flame starts to propagate upstream and consequently heats the rod and the tube wall, and eventually develops into flashback. Heating of the rod is very rapid, because of the enormous heat transfer directly from the surrounding flame. In order to avoid such effect, flow rates were adjusted higher and the range of

Re for partially-inverted flames was set between 1800 and 2600. Consequently, for the desired *Re* range, the equivalence ratio Φ is set to 1.4 that is well within Region III.

Moreover, the above mentioned increase of unstable Region VI has a negative impact on the geometrical configurations that involve rod protrusion B_R and rod-to-tube ratio B_T. With variations of these parameters at free-jet flames, Region III is heavily affected, scaled down and shifted towards higher Φ, where flame shape changes considerably. For $\Phi \geq 1.6$, the outer reaction zone is more profound, while inner reaction zone diminishes as there is not enough surrounding air to penetrate into the central region.

For variations of rod B_R and B_T at impinging flames, the Region III is almost non-existent and flames show the same unstable behavior as described in the above paragraph. It means that for partially-inverted flames, the effects of geometrical parameters of the burner, i.e. variations of rod protrusion B_R and rod-to-tube B_T can not be investigated and were excluded from the study.

The effective range of nozzle-to-plate ratio *H* has been kept in the same range as in the case of impinging inverted flames, i.e. from 0 to 4. Such close nozzle-to-plate distances were set due to relatively short length of partially-inverted flames, much shorter in comparison with regular Bunsen flame. Non-dimensional radial distance from stagnation point *R* has been selected in the range from 0 to 4.

6.2. Flame structure and temperature

Similarly to the study of impinging inverted flames, temperature distribution were recorded as a function of radial distance and temperature profiles were plotted for two nozzle-to-plate ratios that represent two different vertical cases: 1) impingement plate is situated above the height flame reaction zones (i.e. above the flame top); 2) impingement plate is situated within height of reaction zones of the flame. These were used to identify the structure of impinging partially-inverted flames in relation to nozzle-to-plate ratio *H*. Horizontal regions of impinging flame were kept the same.

6.2.1. Flame temperature

Figure 6.2 presents flame temperature distribution for $H = 3$, i.e. impingement plate is situated just above the height of flame reaction zones (above the flame top). It can be stated that flame temperatures remain relatively constant, starting from stagnation point to approximately $R = 2$, then there is a slight decline. Peak values correspond with these constant values. Variation of *Re* increases / decreases the flame temperature while the radial distribution patterns remain the same. It is evident that the presence of outer reaction zone positively contributes to the uniform distribution of flame temperatures and delays their decline to further distance. Temperatures are within the range of 1100 – 1400 ^{0}C.

Figure 6.3 shows temperature profiles for closer nozzle-to-plate distance, i.e. $H = 1$. In this case, the impingement plate is situated within the height of reaction zones of the flame. Flame temperatures around stagnation point and in the further distance

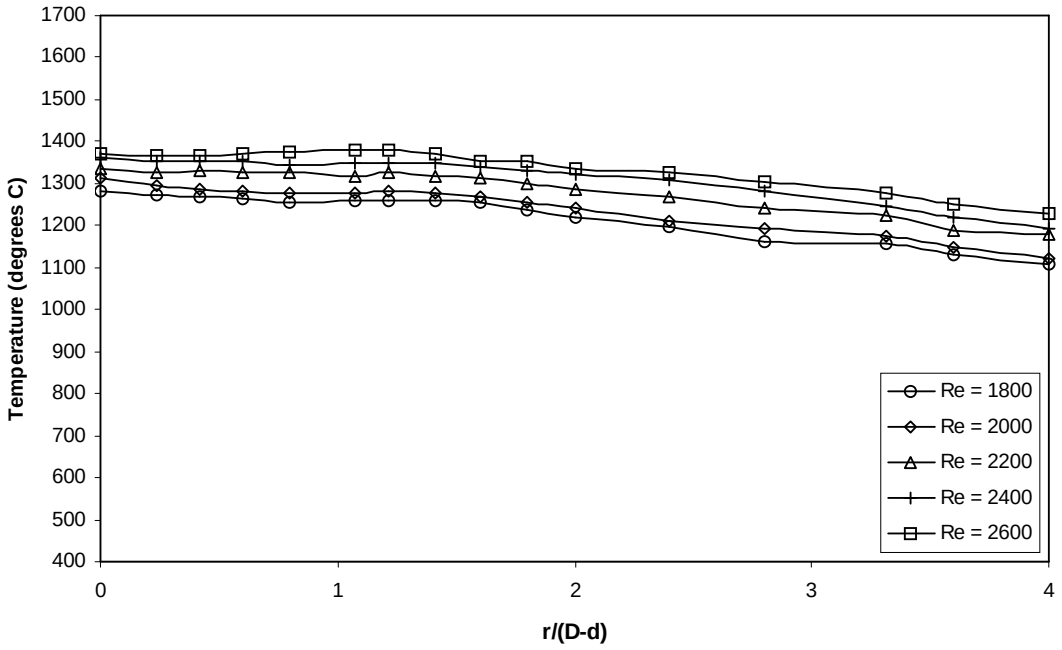

Figure 6.2. Radial flame temperature distribution for various *Re* at $H = 3$, $\Phi = 1.4$, $B_T = 0.51$, $B_R = 0$.

(i.e. $R > 2$) are within the above mentioned range, i.e. above 1100 ^{0}C. There is a gradual increase of flame temperature around $R = 1$ due to closer proximity of the flame tip to the impingement plate. Peaks are rather flat, a credit of the presence of both reaction zones in partially-inverted flames.

The maximum recorded temperatures were lower than those of free-jet flames, i.e. 1546^{0}C for impingement flames against 1617^{0}C for free-jet flames. However the maximum temperature of free-jet flames corresponds to the reaction zone, while in case of or impingement purposes (i.e. calculation of heat transfer coefficient), flame temperatures have been obtained just below the impingement surface. Actual maximum temperatures in the reaction zone of impinging partially-inverted flames thus might be higher.

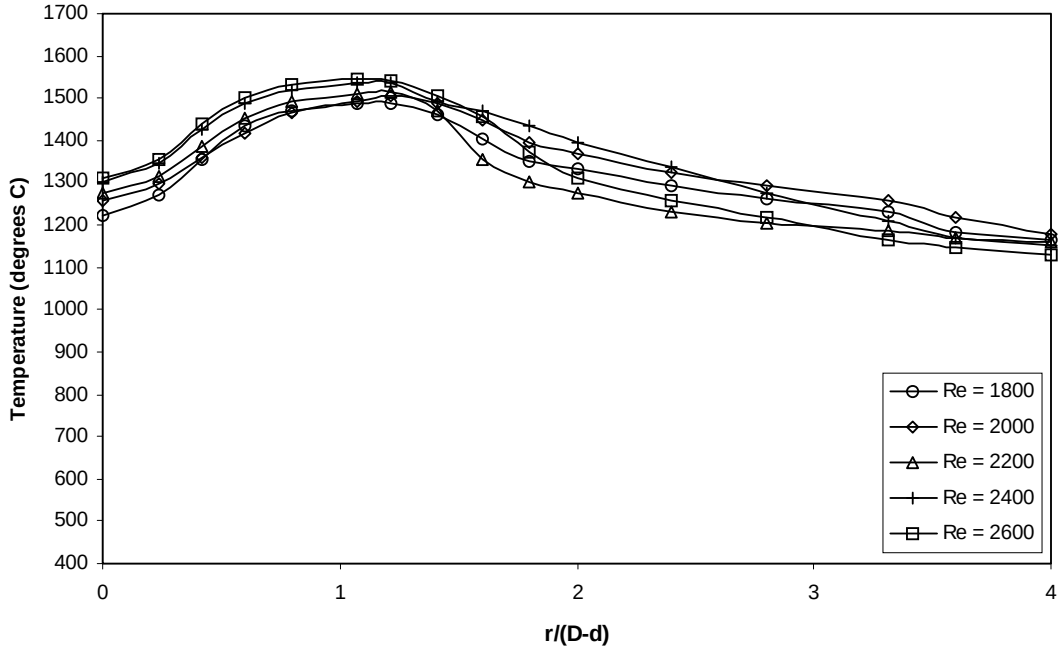

Figure 6.3. Radial flame temperature distribution for various *Re* at $H = 1$, $\Phi = 1.4$, $B_T = 0.51$, $B_R = 0$.

6.2.2. Flame structure

Impingement plate has been divided into same areas as in the case of impinging inverted flames. These regions represent and reflect different mechanisms of impinging flame jet:

- Stagnation region ($0 \leq R \leq 1$). An area of central core of burned gas impinging onto the plate, high temperatures.

- Impingement region ($1 \leq R \leq 2$). An area with intense combustion and maximum temperatures, where flame reaction zone interacts with the plate.

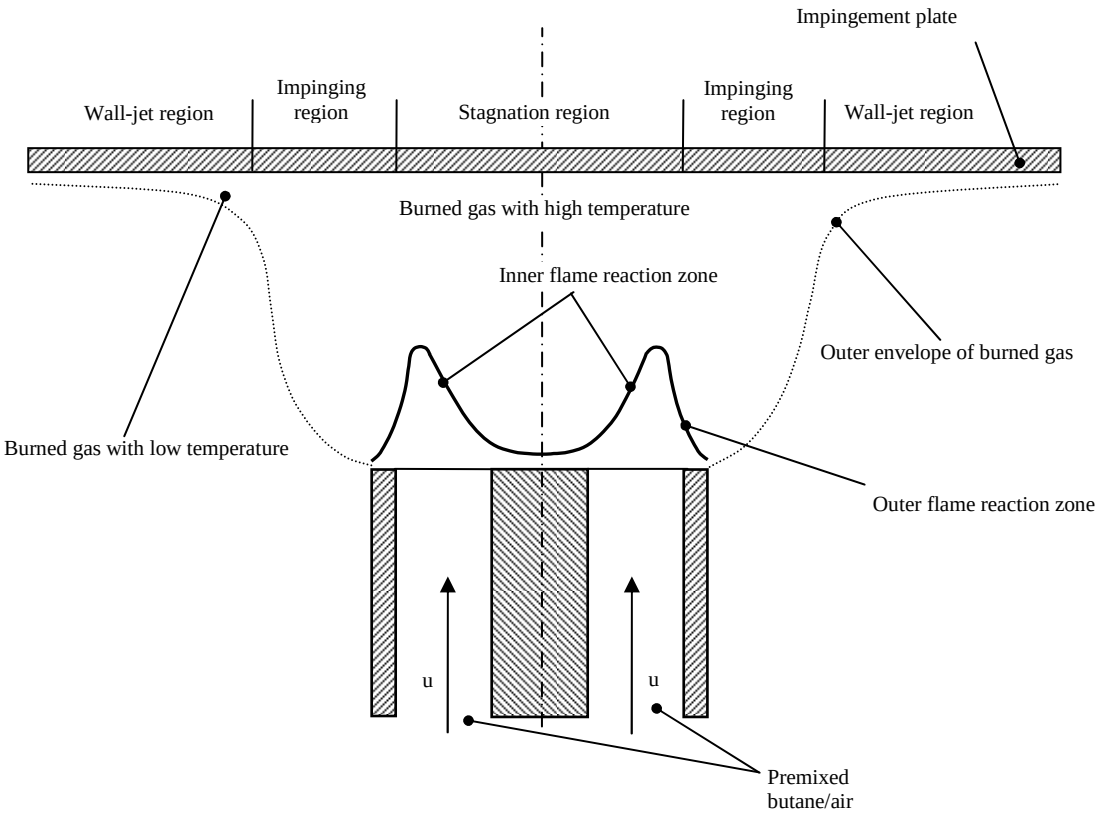

Figure 6.4. Structure of impinging partially-inverted flame: impingement plate is situated above the flame reaction zone height

- Wall-jet region ($2 \leq R \leq 4$), an area with lower temperature, where combustion products start to diffuse outwards into the surrounding atmosphere.

Figure 6.4 represents case with an impingement plate situated above the flame reaction zone (Case 1). Shape of both reaction zones is not affected by turbulence, caused by the proximity of the impingement plate. Central core of burner gas with high temperature is very wide due to the presence of outer reaction zone and covers both stagnation and impinging region and partially wall-jet region.

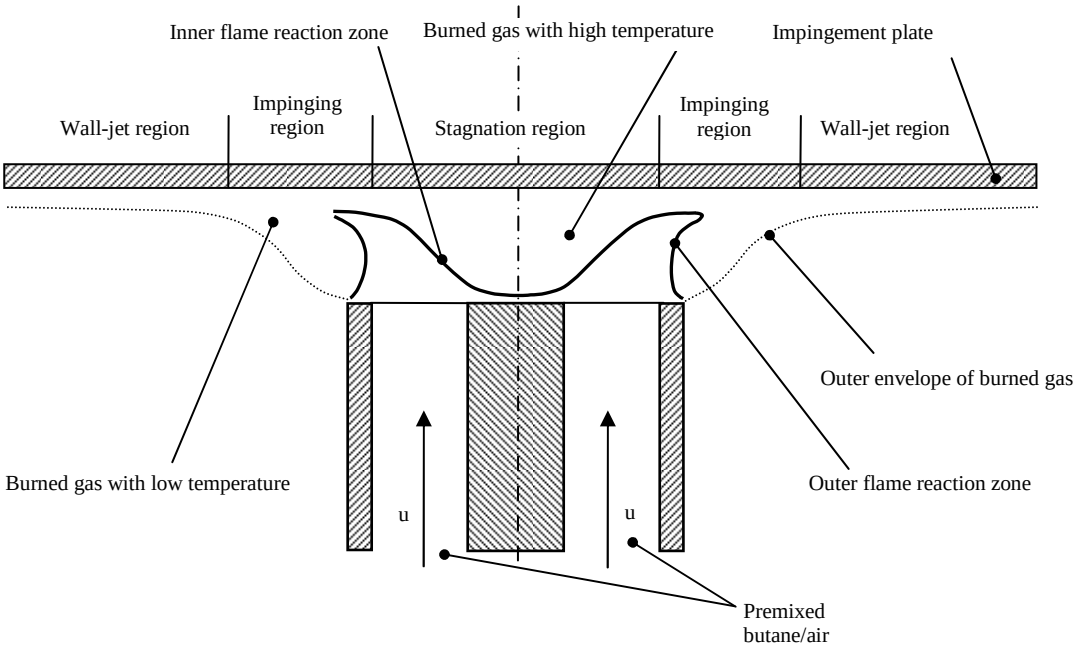

Figure 6.5. Structure of impinging partially-inverted flame, where impingement plate is situated within the flame reaction zone height

Figures 6.7a and 6.7b show photographs of partially-inverted impingement flames for such case. Reaction zones are visibly intact and their shape is assumed to be identical with free-jet flame. Also clearly visible is the wide outer envelope of burned gas.

Figure 6.5 features the second case (Case 2) with impingement plate situated within the height of reaction zones. Both reaction zones stretch out as well as the outer envelope of burned gas. The process, caused by increased turbulence (as described in Chapter 6.1), draws both reaction zones towards the nozzle and the flame appears to be more settled. Partially-inverted flames, impinging at H = 1 are shown in photographs in Figures 6.7c and 6.7d. Height of the reaction zones appears to be

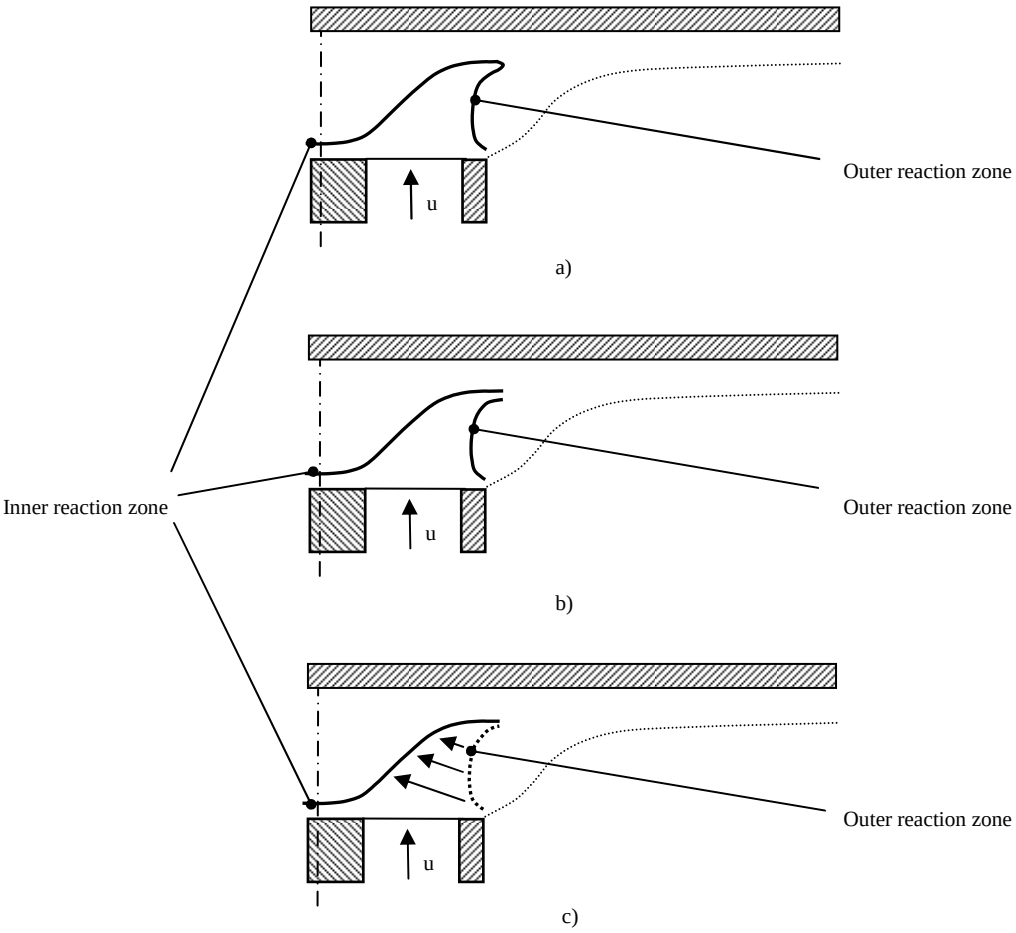

Figure 6.6. Three observed flame shape cases of partially-inverted impinging flame; a) inner and outer reaction zones are attached, b) inner and outer reaction zones are detached, c) Outer reaction zone merged with inner reaction zone.

smaller in comparison with Case 1 (H = 3), due to the fact that both zones are stretched out.

Three different flame shapes of partially-inverted flames have been observed and are presented in Figure 6.6. The mechanism of occurrence of first two cases (Figure 6.6a ad 6.6b) is identical to those cases in free-jet flames as described in Chapter 4.2.1.

a)

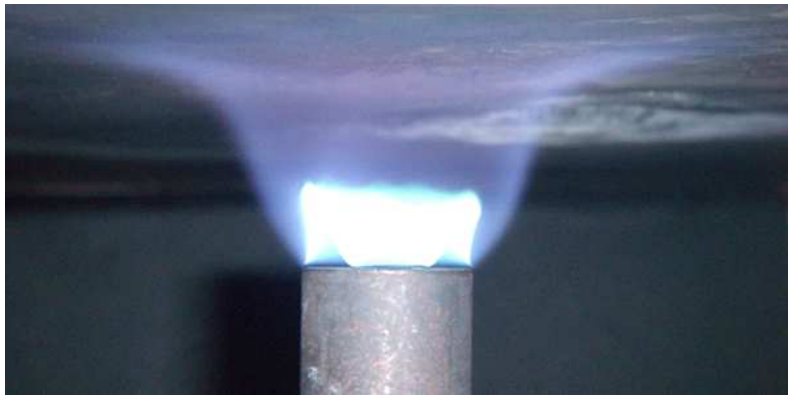

b)

c)

d)

Figure 6.7. Photographs of impinging partially-inverted flames at Re = 2000, Φ = 1.4, B_T = 0.51, B_R = 0; a) and b) at H = 3; c) and d) at H = 1.

In the first case, both inner and outer reaction zones are attached. This case has been observed predominantly for lower Re, where the flow is within laminar conditions. The second case represents the occurrence of open end, in which the outer and inner reaction zones are detached. This has been observed mainly at higher nozzle-to-plate ratios and Re, where there is presence of flickering of the flame due to increased turbulence. Third case (Figure 6.6c) is associated with very small nozzle-to-plate ratios. Originally, the flame is ignited with both reaction zones, however after some time, outer reaction zone shifts inwards and merges with inner reaction zone. Such phenomenon can described as there is an increase in temperature in the preheat zone just at the nozzle exit. As seen from the Figure 4.11, temperatures at this area are already very high. With further temperature increase, caused by increased turbulence, both reaction zones are drawn near to the point where they merge. Another factor to consider can be a stretch of the outer reaction zone.

6.3. Effect of Nozzle-to-plate ratio

First set of experiments covers variations of nozzle-to-plate ratio H for given Re, Optimal nozzle-to-plate ratio H_{opt} has been determined in terms of uniformity of heat transfer to the plate. Values of H have been set in the range from 0.5 to 4.0, with a step of 0.5. That is identical range as in case of the study of impinging inverted flames.

6.3.1. Local heat flux and Nusselt number distribution

Distributions of local heat flux and local Nusselt number have been obtained for stagnation point and stagnation circle, as well as a function of non-dimensional radial distance R. Maximum values have also been determined.

6.3.1.1. Radial distribution

Figure 6.8 shows radial distribution of heat flux for various nozzle-to-plate ratios. Distributions show similar patterns, characterized by increase of heat flux from the stagnation point up to its peak in the range of R = 1.0 – 1.5, followed by decline that becomes constant at larger radial distances.

Heat flux distribution at the closest distance (H = 0.5) is characterized by the steepest peak that marks the highest heat flux recorded for both partially-inverted and inverted impinging flames. However, due to stability issues, such close distances should be rather avoided. The peak at H = 1 is much lower, approximately 30% less. It seems that the quenching effect of impingement plate (as described in Chapter 5.3.1.1) has lesser impact on partially-inverted flames than it has on inverted flames. It might be due to higher equivalence ratio and also due to the presence of the outer reaction zone coupled with extensive outer envelope of burned gas that prevents steep decrease of heat flux with further radial distance.

With further increase of H, peaks appear to be more flattened, yet not constant. Heat transfer rate steadily decreases in wall-jet region (R > 2). The decrease is constant and not affected by H at R = 4.

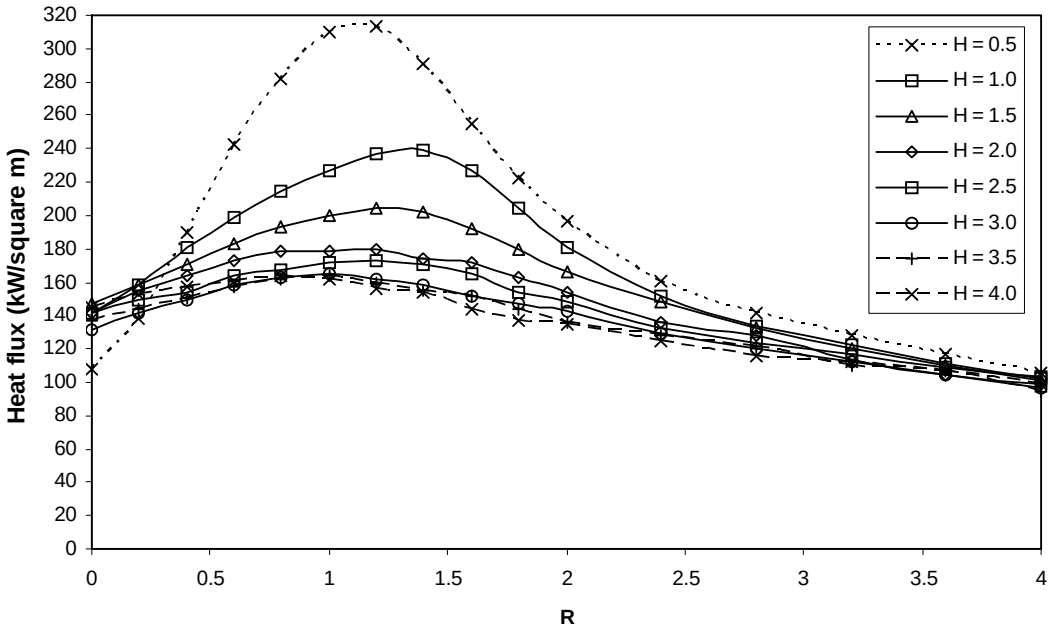

Figure 6.8. Effect of H on radial heat flux distribution at Φ = 1.4, Re = 2000, B_R = 0, B_T = 0.51.

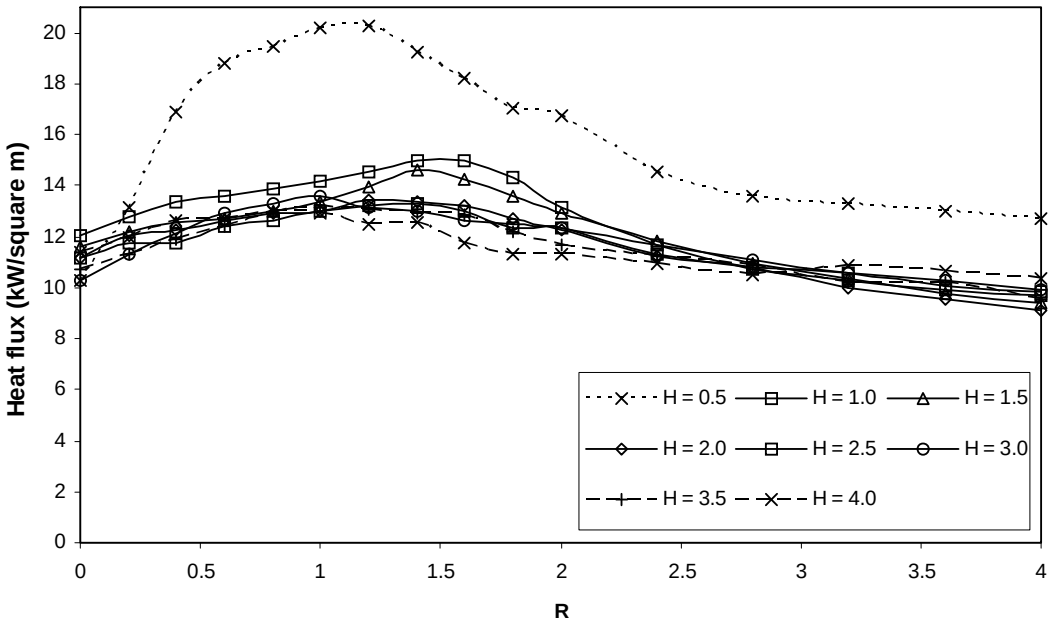

Figure 6.9. Effect of H on radial Nu distribution at Φ = 1.4, Re = 2000, B_R = 0, B_T = 0.51.

Nusselt number distribution (Figure 6.9) also shares similar patterns, characterized by slight increase from stagnation point to the peak that occurs around R = 1.5, followed by partial decline with further radial distance. With an exception for H = 0.5, Nu remains within a narrow range, denoting that variation of H has less significant effect on Nu than on heat flux. This fact is associated with high constant flame temperature of burned gas that keeps being constant for a very wide area. Nu at H = 0.5 exhibits very steep incline at stagnation region with the peak that is considerably higher than the rest.

6.3.1.2. Stagnation point, stagnation circle and maximum heat flux and *Nu*

Corresponding heat transfer rate and Nusselt number values are represented by Figures 6.10 and 6.11. Heat transfer at stagnation point and stagnation circle is compared with maximum values of heat flux and Nu as a function of nozzle-to-plate ratio H.

The stagnation point heat flux remains relatively constant within H = 1 – 4 and is way below the heat flux at stagnation circle. Heat flux at stagnation circle decreases with increased H.

Maximum heat flux occurs approximately at the stagnation circle for higher H, starting from H = 2. For closer nozzle-to-plate distance, the maximum heat flux is shifted away from stagnation circle. Again, this is due to the impingement flame shape at Case 2 that stretches out both reaction zones. The highest difference between stagnation circle heat flux and maximum heat flux is circa 15.5% at H = 1.

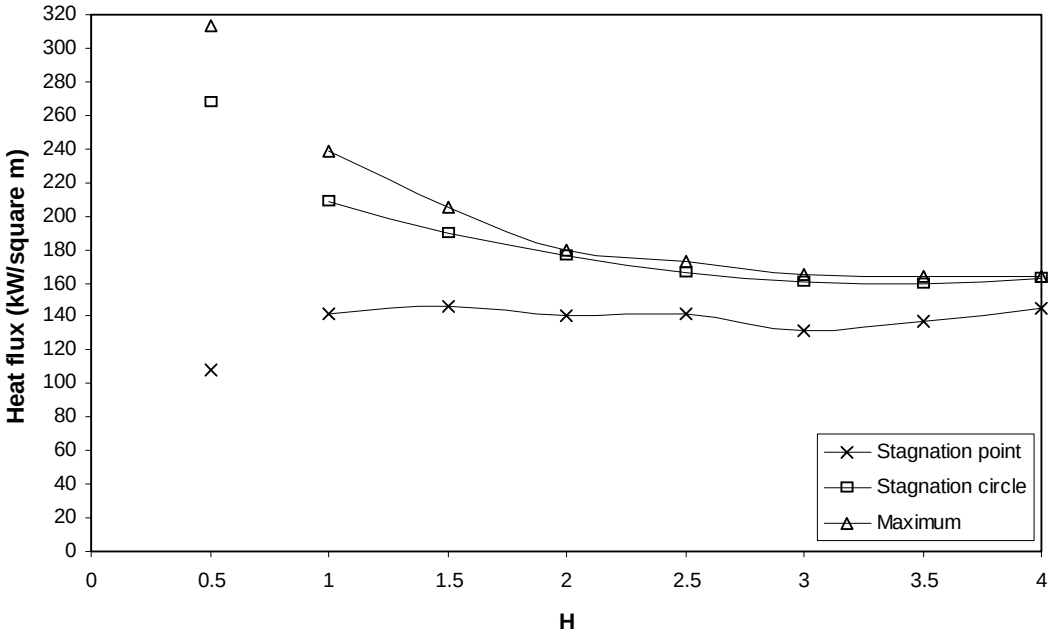

Figure 6.10. Effect of H on stagnation point, stagnation circle and maximum heat flux at $\Phi = 1.4$, $Re = 2000$, $B_R = 0$, $B_T = 0.51$.

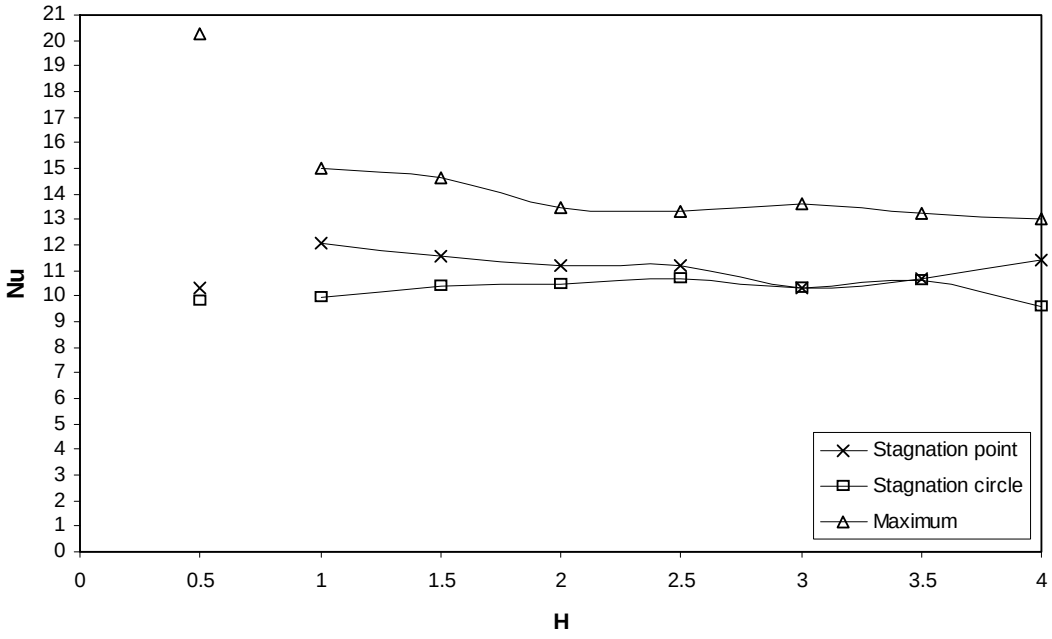

Figure 6.11. Effect of H on stagnation point, stagnation circle and maximum Nu at $\Phi = 1.4$, $Re = 2000$, $B_R = 0$, $B_T = 0.51$.

Nu at stagnation point and stagnation circle is in the same range at $H \geq 3$. For closer nozzle-to-plate distances, stagnation point *Nu* prevails. Nu_{max} is not associated with either stagnation point or stagnation circle. That confirms that Nu peaks in much further distance.

Obtained values of heat flux and *Nu* at H = 0.5 are shown for the reference only, and are not considered in further analysis.

6.3.2. Area-averaged heat flux and Nusselt number distribution

Identically with Chapter 5, area-averaged distributions of heat flux and *Nu* has been obtained by integrating local values over the impingement surface. Integrating area has been divided into three parts that correspond with regions defined in Chapter 6.2.2., i.e. stagnation, impingement and wall-jet region. Total heat flux and *Nu* for the entire regions has also been obtained. Figures 6.12 and 6.13 compares the area-averaged distributions at each region as function of nozzle-to-plate distance *H*. Values of heat flux and *Nu* at $H = 0.5$ are shown for reference only.

Average heat flux for stagnation and impingement regions decreases with increased *H*. Values at stagnation point are almost identical to those at stagnation circle, with an exception at $H = 1$. Average *Nu* at impingement region is marginally higher than at stagnation region, however this difference is negligible at $H = 3$ and 3.5.

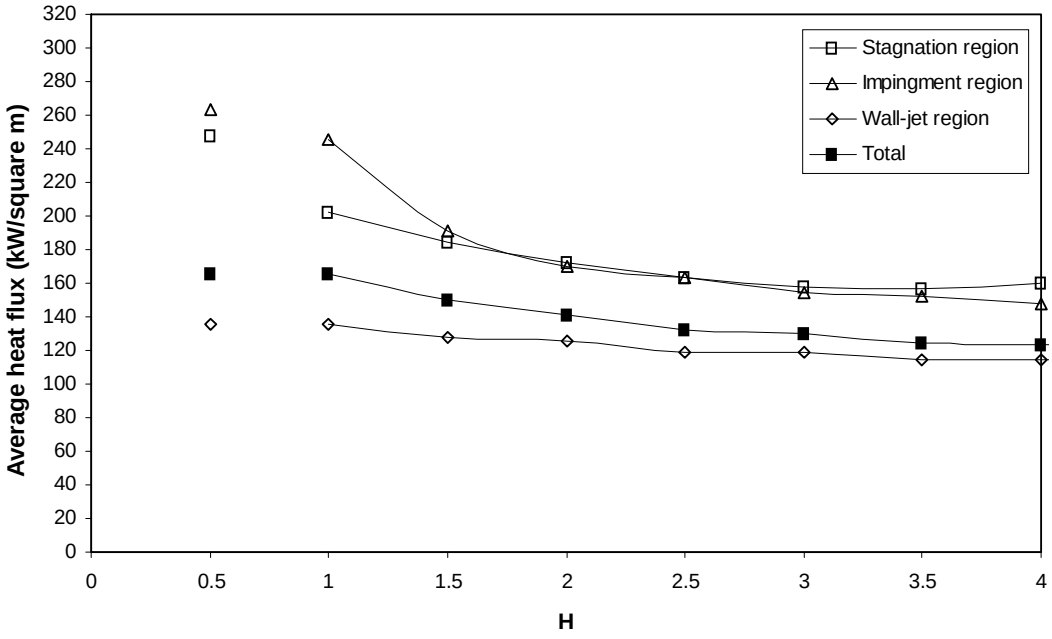

Figure 6.12. Variation of average heat flux with H at different impingement regions at Φ = 1.4, Re = 2000, B_R = 0, B_T = 0.51.

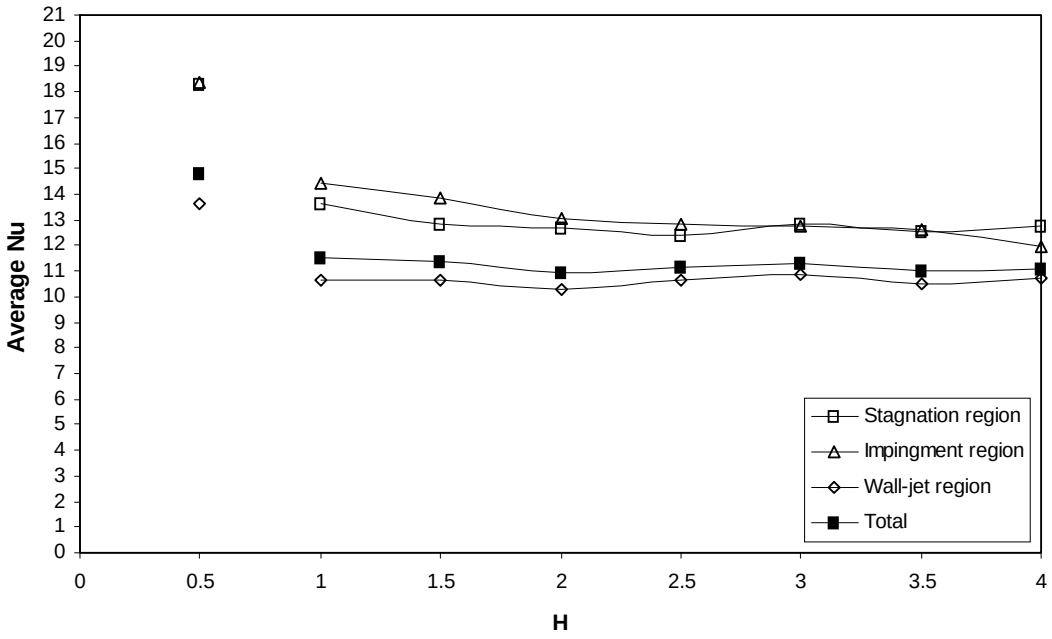

Figure 6.13. Variation of average Nu with H at different impingement regions at Φ = 1.4, Re = 2000, B_R = 0, B_T = 0.51.

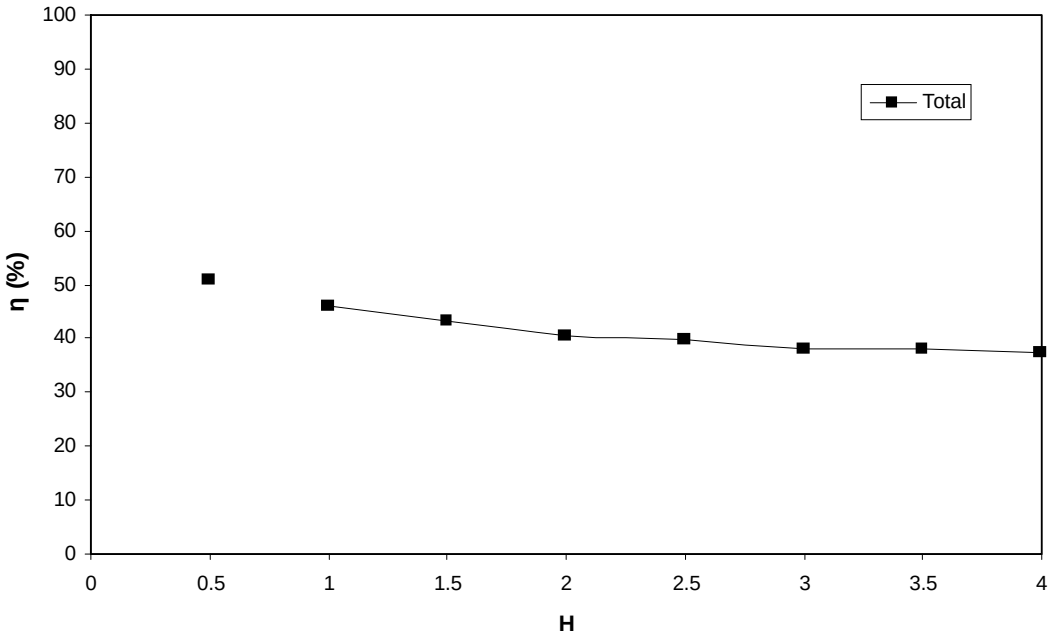

Figure 6.14. Thermal efficiency for various H at Φ = 1.4, Re = 2000, B_R = 0, B_T = 0.51.

Overall, total average heat flux decreases constantly with increased H. Total average Nu could be assumed to be constant despite small fluctuation at H = 2. It has been previously explained that constant distribution of flame temperature over stagnation and impingement region is the factor that affect the uniform distribution of Nu, despite the fact there is a decrease of heat flux.

The lowest averaged values for both heat flux and Nu were recorded at wall-jet region, where heat transfer remains constant and it can be assumed that it is not affected by the distance from the impingement plate.

6.3.3. Thermal efficiency

Figure 6.14 shows thermal efficiency η as the function of nozzle-to-plate H. As expected, it decreases with increased nozzle-to-plate distance. The difference between maximum and minimum values is within 22.7% for H ranging from 1 to 4. Maximum efficiency was 47.6% at H = 1. At H = 0.5 (that is not included in further analysis) the efficiency was 50.8%.

6.4. Effect of Reynolds number

Second set of experiments has been carried out in order to investigate the effect of Reynolds number *Re*. Range selection is covered in details in Chapter 5.1. Values are ranging from 1800 to 2600, with a step of 200. Data were recorded at two different nozzle-to-plate ratios: H = 1 and 3, denoting Case 2 and 1 respectively.

6.4.1. Local heat flux and Nusselt number distribution

Local heat flux and Nusselt number distributions have been obtained as a function of non-dimensional radial distance R for various Reynolds numbers at two different nozzle-to-plate distances. Stagnation point, stagnation circle and maximum heat transfer rates and Nusselt numbers as a function of *Re* are also determined.

6.4.1.1. Radial distribution

Figures 6.15 and 6.16 present radial heat flux and *Nu* distributions for various Reynolds number at H = 1 (Case 2). Similarly to the previous experiments with variations of H, radial distributions exhibit lower values around the stagnation point

with steep increase up to R = 1.1 – 1.3 and steady decrease afterwards. Peaks become more profound with increased *Re*, however the effect is more significant in inverted flames. It seems that increased turbulence that causes temperatures to arise has less impact due to higher equivalence ratio and presence of outer reaction zone; temperatures in the region are already at very high levels. Comparing the values at stagnation point with those in further distance, it can be assumed that non-uniform gain of heat flux due to increased *Re* is in the positive range.

Nusselt number distribution at Figure 6.16 increases similarly with increased R from the stagnation point. There are peaks at different *Re* that appear to be flat and are scattered between R = 1.0 up t 2.0. Despite some fluctuations it can be assumed that *Nu* slightly increases with increased *Re*. However, the patterns are more diverged at stagnation and wall-jet region than those of heat flux. Increased turbulence in the regions associated with increased *Re* is probably the factor behind fluctuations in flame temperatures that consequently affect *Nu*.

Similarly to the experiments with impinging inverted flames, at $Re \geq 2200$, a flow noise is present due to the increased turbulence that causes the local pressure and flow velocity to fluctuate.

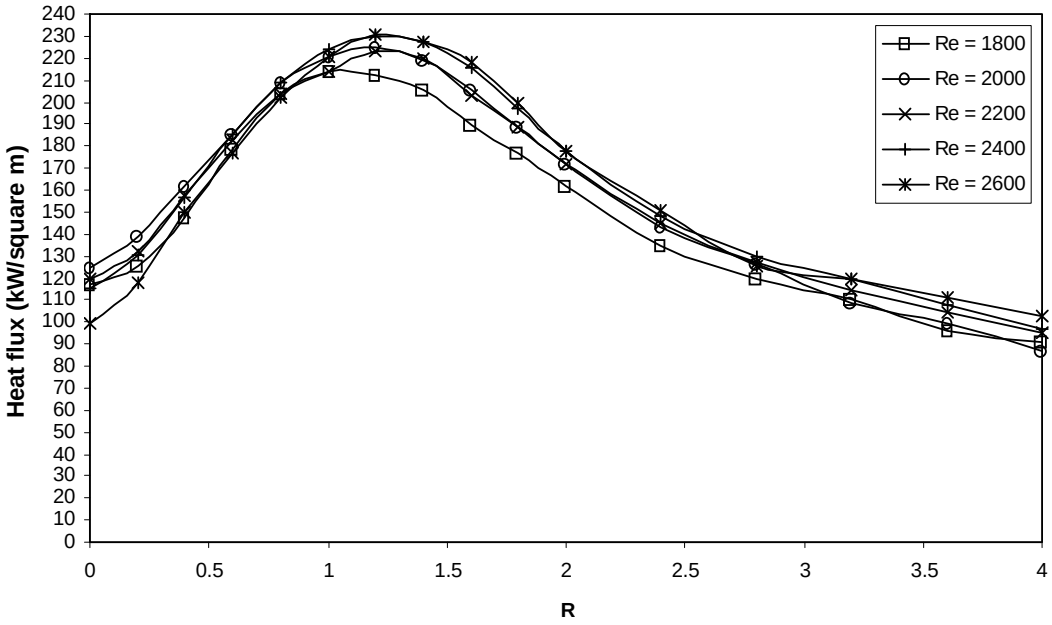

Figure 6.15. Effect of *Re* on radial heat flux distribution at Φ = 1.4, H = 1, B_R = 0, B_T = 0.51.

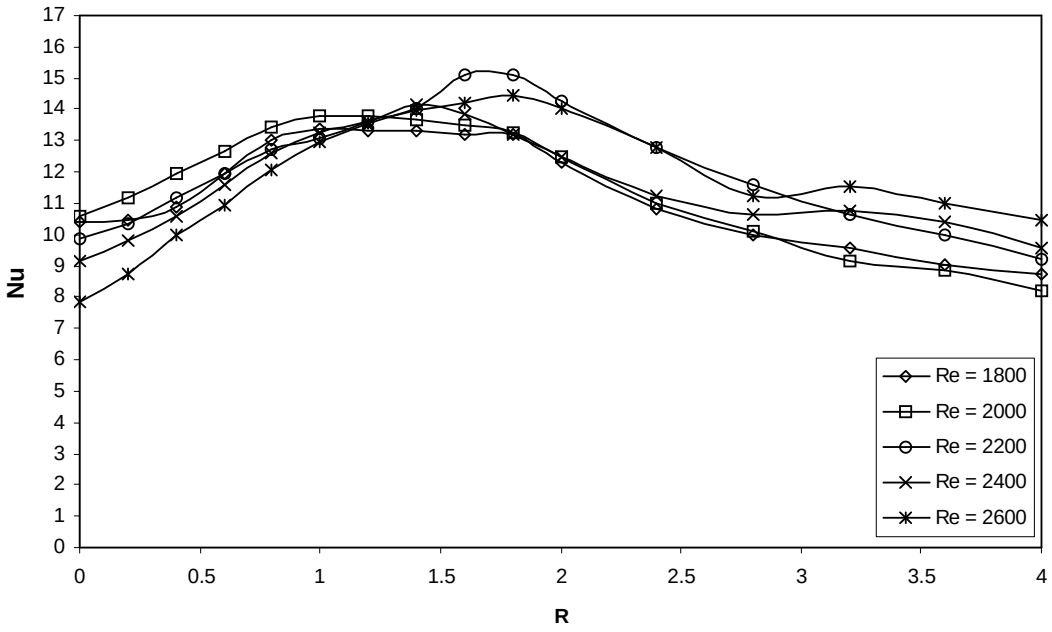

Figure 6.16. Effect of *Re* on radial Nusselt number distribution at Φ = 1.4, H = 1, B_R = 0, B_T = 0.51.

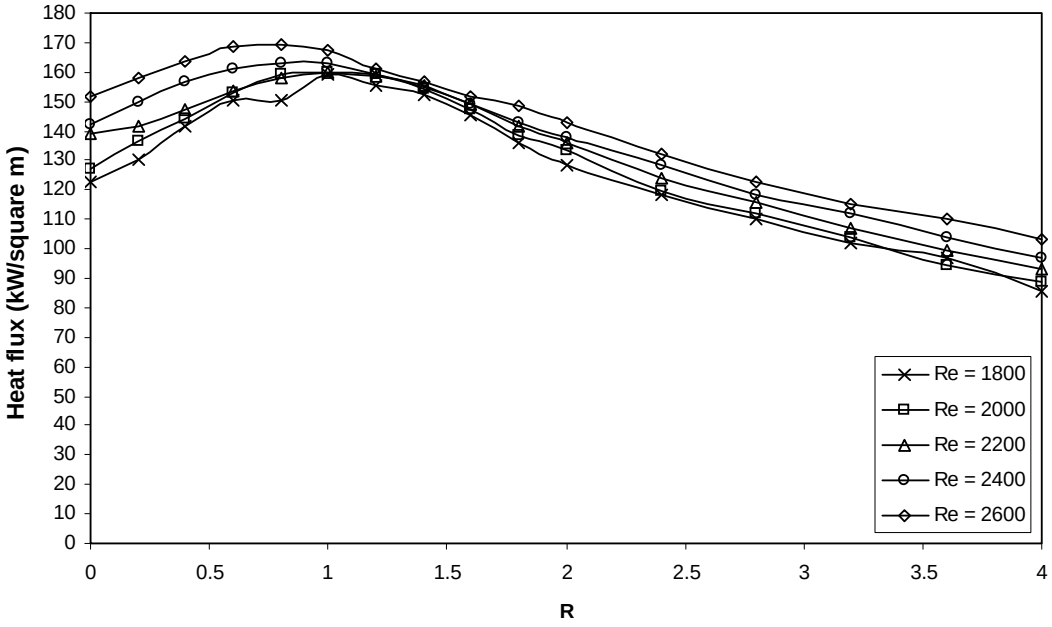

Figure 6.17. Effect of *Re* on radial heat flux distribution at Φ = 1.4, H = 3, B_R = 0, B_T = 0.51.

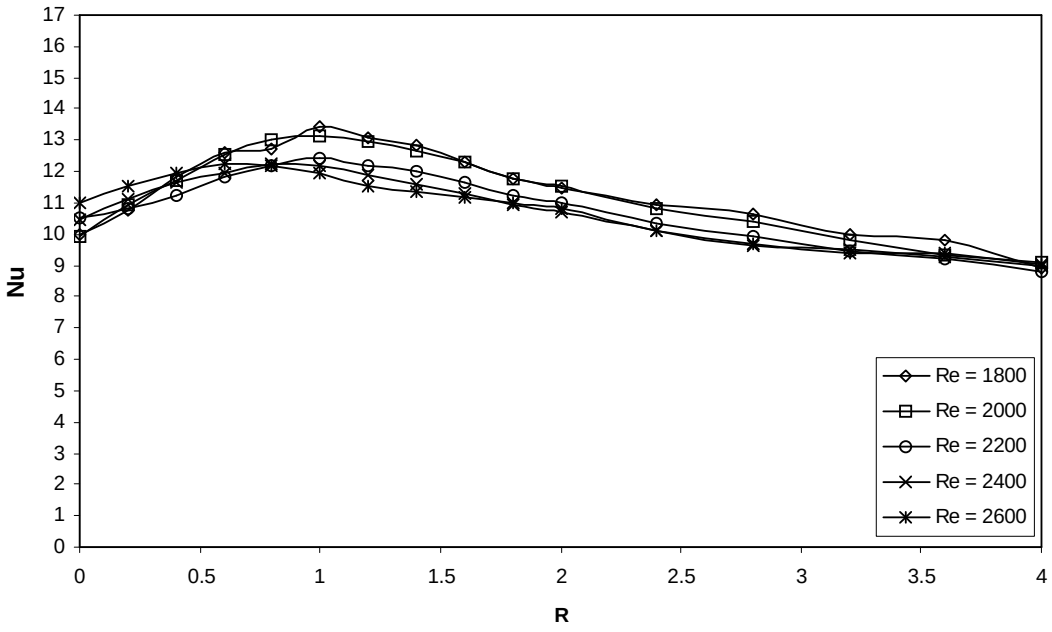

Figure 6.18. Effect of *Re* on radial Nusselt number distribution at Φ = 1.4, H = 3, B_R = 0, B_T = 0.51.

Case 1 (H = 3) is demonstrated in Figures 6.17 and 6.18. With further distance from the impingement plate, the impact of increased *Re* on both characteristics is less significant. Heat flux distributions appear to be more flat as they are shifted towards higher values at stagnation point. Maximum values are gradually shifted inwards and peaks occur in the range of R = 0.7 – 1.1. Nusselt number distributions follow the patterns of flame temperatures, i.e. increase from stagnation point and peak around R = 1. With further distance, *Nu* remains within relatively close range and drops only by 10% from its stagnation point value.

For partially-inverted flames, the optimal value of Re_{opt} can be observed from Figure 6.17. For H = 3, the most uniform heat flux distribution is at Re_{opt} = 2400 that is higher than in the case of inverted flames (Re_{opt} = 2000).

6.4.1.2. Stagnation point, stagnation circle and maximum heat flux and *Nu*

Relevant data are presented in Figures 6.19 – 6.20 that cover Case 2 (H = 1) and in Figures 6.21 – 6.22 that represent Case 1 (H = 3).

Stagnation point heat flux appears to be constant over the entire range of *Re* and its range is way below the maximum values. In Case 2, there is slight and steady increase with increased *Re*. In Case 1, on the other hand, it is slightly declining. In Case 2, stagnation point values are in a close range with stagnation circle values and increase with higher *Re*. In Case 1, *Nu* is marginally declining over the entire range of *Re*.

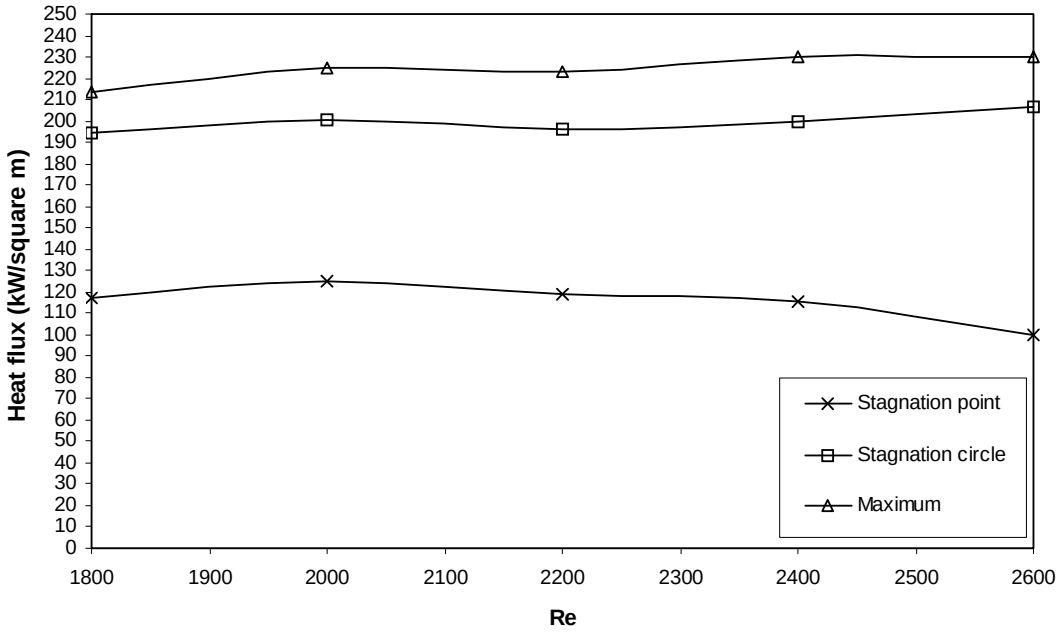

Figure 6.19. Effect of *Re* on stagnation point, stagnation circle and maximum heat flux at $\Phi = 1.4$, $H = 1$, $B_R = 0$, $B_T = 0.51$.

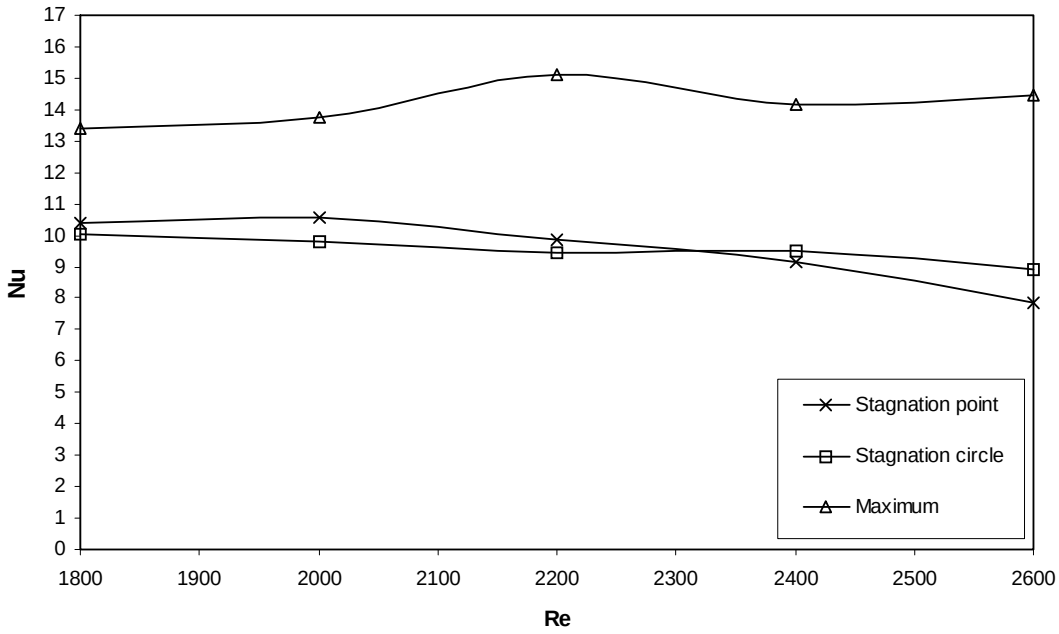

Figure 6.20. Effect of *Re* on stagnation point, stagnation circle and maximum Nusselt number at $\Phi = 1.4$, $H = 1$, $B_R = 0$, $B_T = 0.51$.

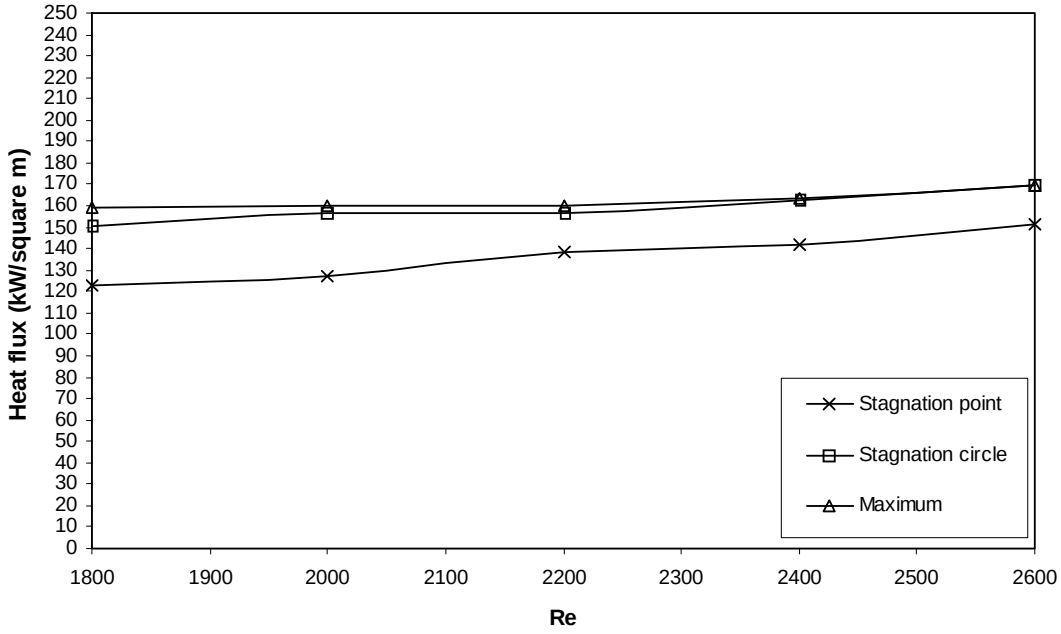

Figure 6.21. Effect of *Re* on stagnation point, stagnation circle and maximum heat flux at $\Phi = 1.4$, $H = 3$, $B_R = 0$, $B_T = 0.51$.

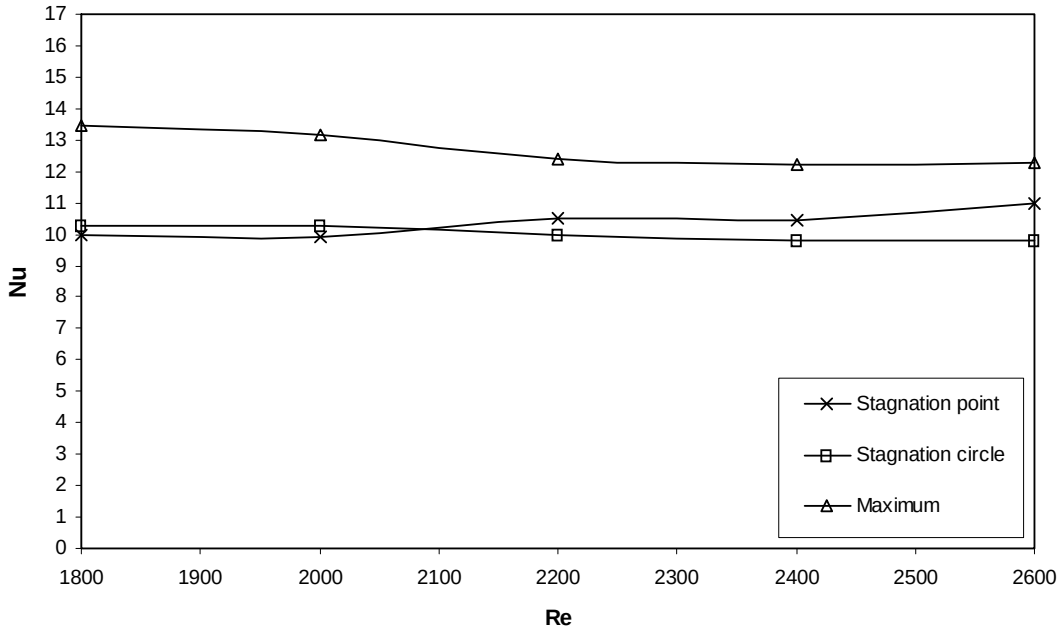

Figure 6.22. Effect of *Re* on stagnation point, stagnation circle and maximum Nusselt number at $\Phi = 1.4$, $H = 3$, $B_R = 0$, $B_T = 0.51$.

At stagnation circle, heat transfer characteristics are defined by an increase of heat transfer rate with an increased *Re* in Case 1 (12.3%), while in Case 2, the rate can be assumed to be constant as the increase accounts only for 6%. As for *Nu*, it remains constant for both cases. In Case 2 (H = 1), there are negligible variations (within 5%). Stagnation circle *Nu* is in the range with *Nu* at stagnation point, certain divergence is visible only at *Re* = 2600, where *Nu* at stagnation point is higher in Case 1 and lower in Case 2.

Maximum values of heat flux in Case 1 are assumed to be identical with values at stagnation circle for the entire range of *Re*. In Case 2, maximum values are above, denoting that peaks are shifted from stagnation point at closer nozzle-to-plate distances. In both cases, there is a certain increase of maximum heat flux with increased *Re*, 8% in Case 2 and 7% in Case 1. Nu_{max} is not related to stagnation point or stagnation circle, slightly decreases in Case 1 (H = 3) and slightly increases in Case 2 (H = 1).

6.4.2. Area-averaged heat flux and Nusselt number distribution

Area-averaged distributions of heat flux and Nu are presented in Figures 6.23 – 26 for specified regions, i.e. stagnation, impingement and wall-jet region, and as total values for the entire region.

At H = 1 (Case 1), Figures 6.23 and 6.24, the highest averaged heat flux and average *Nu* are at impinging region and both increases with increased *Re*. This not surprising as steep peaks are situated within this region. Values at stagnation region are lower.

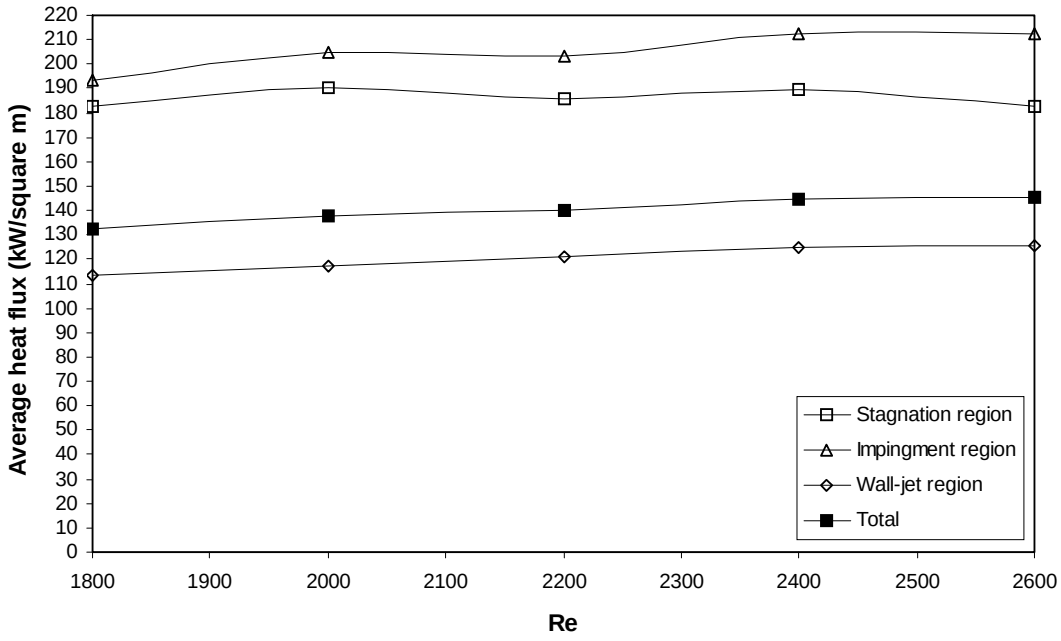

Figure 6.23. Variation of average heat flux with *Re* at different impingement regions at $\Phi = 1.4$, $H = 1$, $B_R = 0$, $B_T = 0.51$.

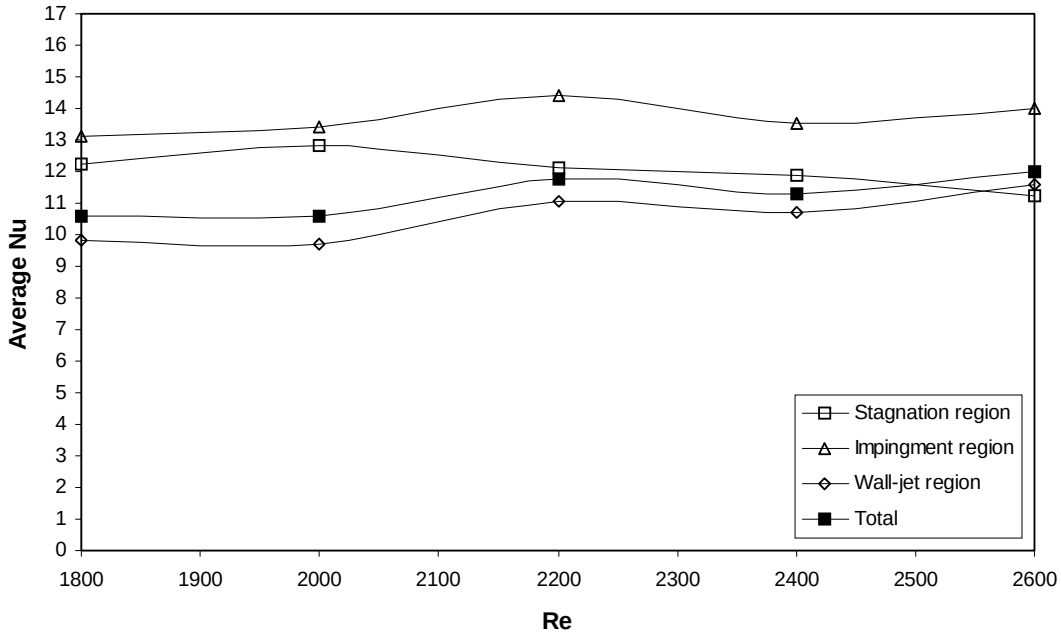

Figure 6.24. Variation of average *Nu* with *Re* at different impingement regions at $\Phi = 1.4$, $H = 1$, $B_R = 0$, $B_T = 0.51$.

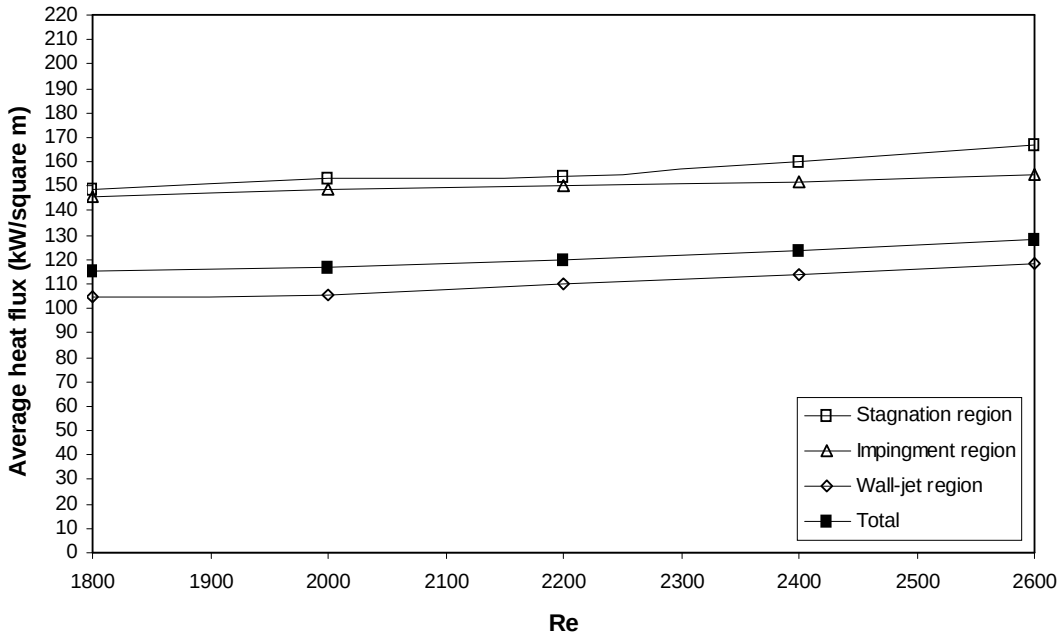

Figure 6.25. Variation of average heat flux with *Re* at different impingement regions at $\Phi = 1.4$, $H = 3$, $B_R = 0$, $B_T = 0.51$.

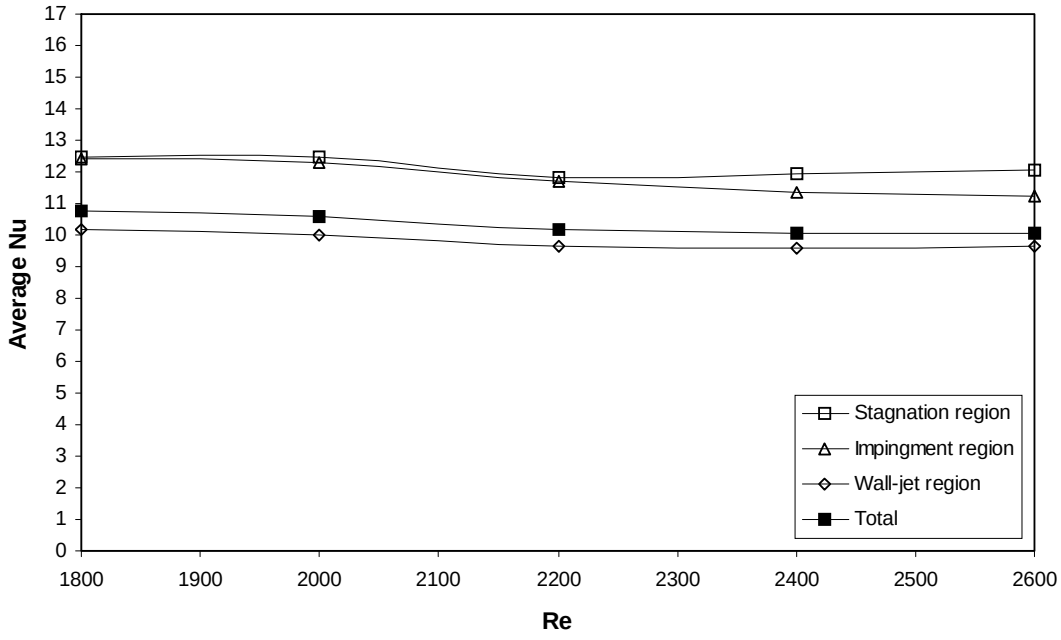

Figure 6.26. Variation of average *Nu* with *Re* at different impingement regions at $\Phi = 1.4$, $H = 3$, $B_R = 0$, $B_T = 0.51$.

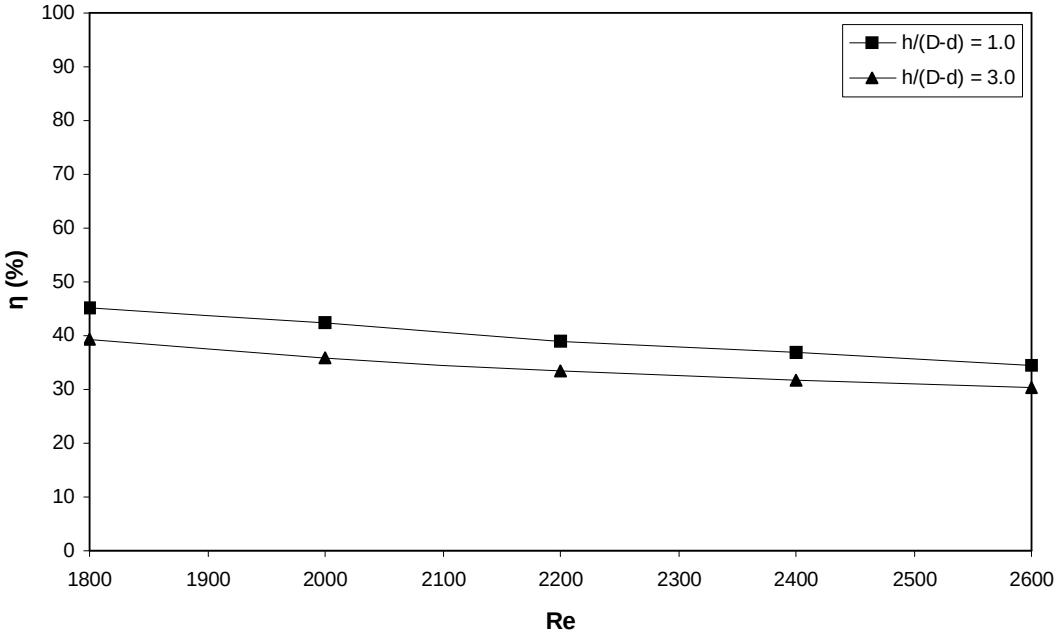

Figure 6.27. Thermal efficiency for various *Re* at Φ = 1.4, *H* = 1 and 3, B_R = 0, B_T = 0.51.

Nu at stagnation region declines with further increases of *Re* and at *Re* = 2600. It has the same value as *Nu* at wall-jet region. Both total average heat flux and *Nu* slightly increase with increased *Re*. As mentioned before, the effect of *Re* is not significant as flame temperatures of partially-inverted flames in the stagnation and impingement region are very high.

With further distances from the impingement plate (*H* = 3, Case 1), Figures 6.25 and 6.26, the difference between heat flux and *Nu* at stagnation and impingement region becomes much smaller. That means there are uniform heat flux and *Nu* distributions over these regions. There is one exception at *Re* = 2600, where the gap in both

characteristics is wider. Overall, total averaged heat flux slightly increases with *Re*, while average *Nu* slightly decreases.

6.4.3. Thermal efficiency

Thermal efficiency η as the function of Reynolds number for H = 1 (Case 2) and H = 3 (Case 1) is in Figure 6.27. Values are generally higher for closer distance to the impingement plate. Thermal efficiency decreases with increased *Re* for both H = 1 and 3. For H = 1, maximum efficiency is 45.2% at *Re* = 1800, for H = 3, it is 39.2%, also at *Re* = 1800. The difference between maximum and the minimum values is within 32% for H = 1 and 30% for H = 3.

6.5. Comparison with impinging inverted flames

Partially-inverted flames and inverted flames are both generated by the same burner with axially-mounted rod. Both flames are classified as rod-stabilized premixed flames. In terms of parameters, the only difference is in equivalence ratio Φ, impinging inverted flames in this study have Φ = 0.9, while impinging partially-inverted flames have Φ = 1.4. Both flame types are compared in terms of heat transfer uniformity and thermal efficiency.

Figures 6.28 and 6.29 display comparison of radial heat flux distributions and Nusselt number for both flames at close nozzle-to-plate distance, i.e. H = 1, at constant *Re* = 2000. It can be observed that both flames exhibit very similar patterns with almost identical peaks at around R = 1.25. Due to higher equivalence ratio, presence of outer reaction zone and wider outer envelope of burned gas, partially-

inverted flames have higher heat flux than inverted flame. The presence of outer reaction zone in partially-inverted flames is more visible at Nu distribution as it still peaks around R = 1.6, while Nu of inverted flames drops. However the gap is much smaller in stagnation region, since both flames feature central core of burned gas with high temperatures. Nusselt number is even higher for inverted flames at stagnation point.

With an increased nozzle-to-plate distance (Figures 6.29), the significance of two reaction zones in partially-inverted flames becomes more profound as there is presence of the peak around R = 1.1, while at the same distance, inverted flames show uniform distribution. H_{opt} for inverted flames is equal to 3, for partially-inverted flames the distance is higher (H = 4 or 5), for the same given Re. Nu distribution shows increase in partially-inverted flames, while at the same distance, Nu of inverted flames is steadily decreasing.

Thus it can be concluded that for optimal uniform heat flux and Nu distributions, the nozzle-to-plate ratio for given Re should be higher for partially-inverted flames than for inverted flames.

Comparison of total average heat fluxes and Nu for both impinging flames is presented in Figures 6.32 - 6.35. In both cases (i.e. H = 1 and H = 3), total averaged heat flux of partially-inverted flames is higher then of inverted flames. The same is valid for total averaged Nu. Such 10-20% increase is associated with the presence of outer reaction zone.

This might be due to the close proximity of both reaction zones. The outer zone is mostly suppressed by the inner reaction zone and the heat dissipation is more to the sides rather than upwards. The preheat zone is also large that signalizes heat losses to the tube and the rod. Despite higher equivalence ratio, some heat might be lost in this way, resulting in lower efficiency.

Based on this, and together with the stability issues of partially-inverted flames, inverted flames is more suitable for practical applications.

Figures 6.36 and 6.37 show thermal efficiency for both impinging flames for various nozzle-to-plate ratios as a function of *Re*. It is evident that inverted flames have higher thermal efficiency than partially-inverted flames.

6.6. Comparison with other premixed impinging flames

Results of impinging partially-inverted flames are compared with previous studies that deal with premixed impinging flames using similar configuration and similar input parameters, i.e. equivalence ratio and *Re*, fuel, etc. Those studies include Dong (2002) that studied regular (Bunsen) flames generated by single round jet using butane / air, and Huang (2006) that studied swirl induced Bunsen flames generated also by single round jet. Both studies used flat plate as an impingement surface.

Comparison is made with intention to observe the impact of each flame type on uniform heat transfer characteristics along the impingement plate.

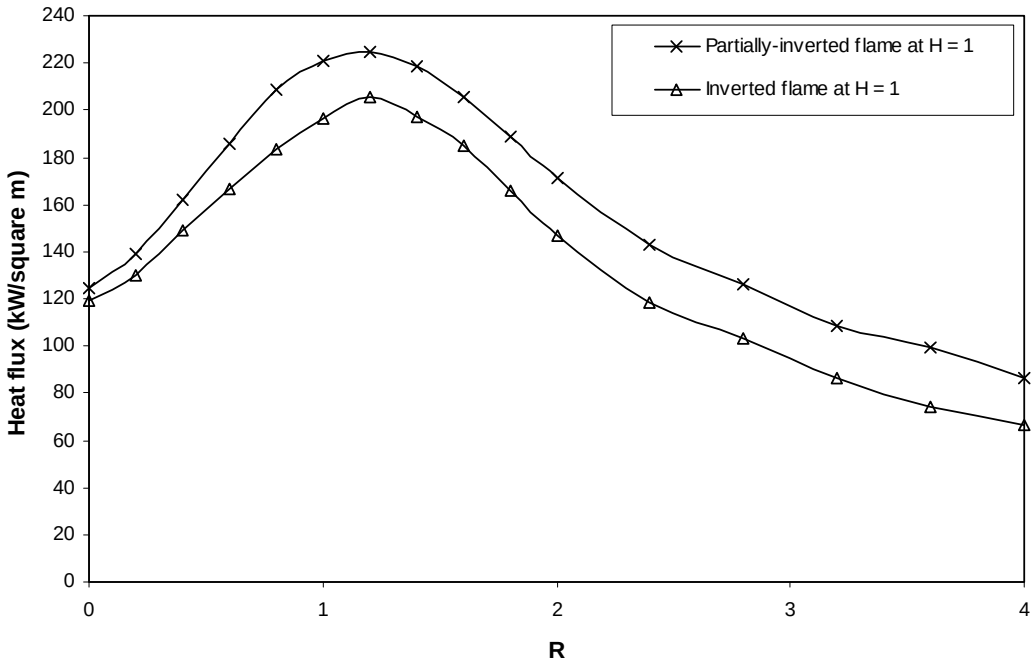

Figure 6.28. Comparison of radial heat flux distribution of partially-inverted flames (Φ = 1.4) with inverted flames (Φ = 0.9) at Re = 2000, H = 1, B_R = 0, B_T = 0.51.

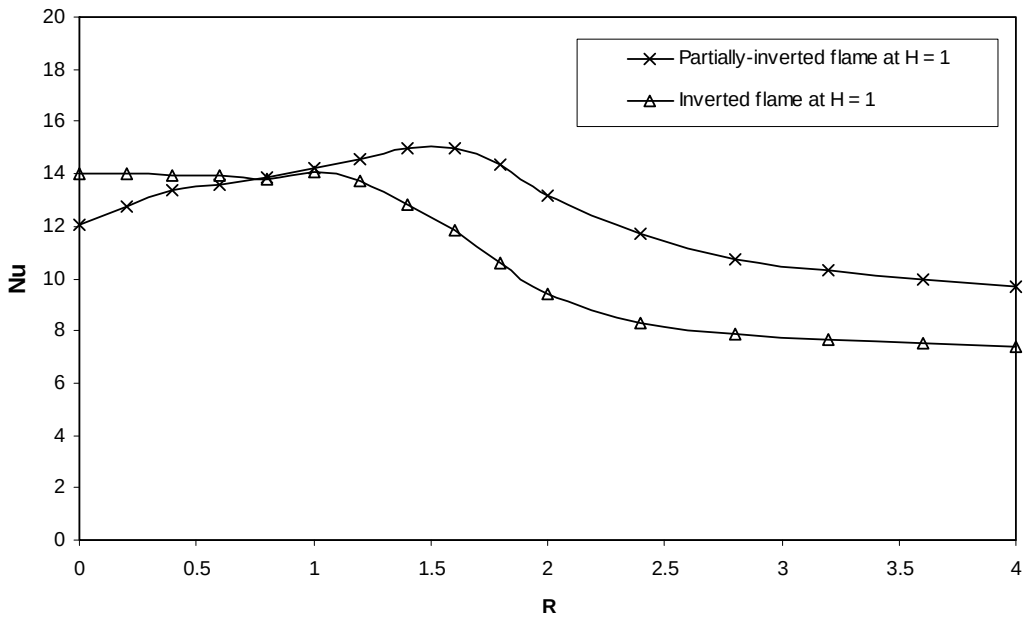

Figure 6.29. Comparison of radial Nu distribution of partially-inverted flames (Φ = 1.4) with inverted flames (Φ = 0.9) at Re = 2000, H = 1, B_R = 0, B_T = 0.51.

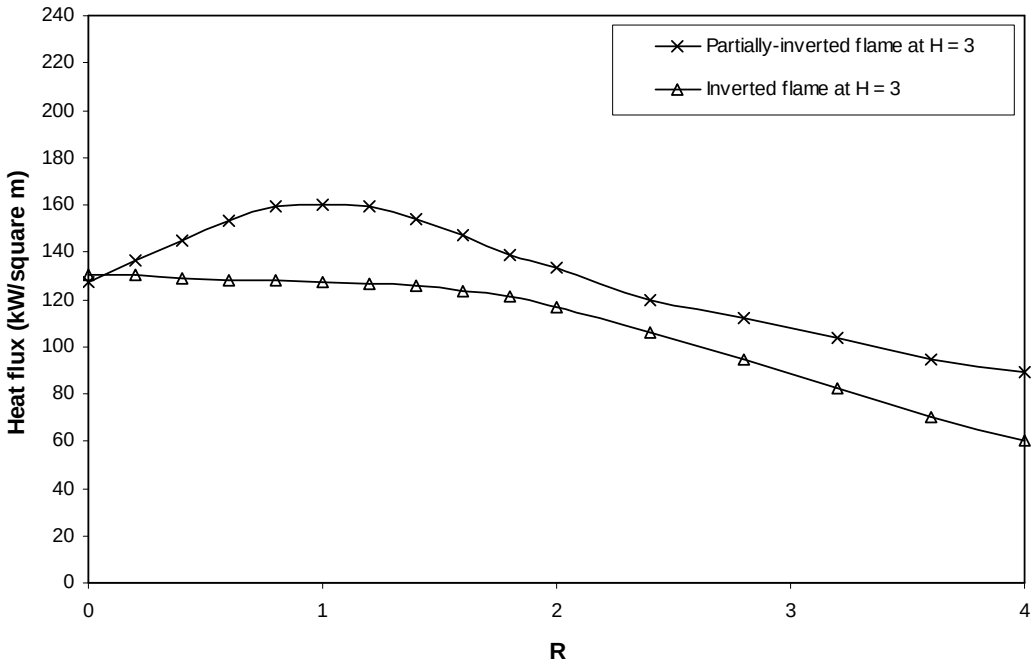

Figure 6.30. Comparison of radial heat flux distribution of partially-inverted flames (Φ = 1.4) with inverted flames (Φ = 0.9) at Re = 2000, H = 3, B_R = 0, B_T = 0.51.

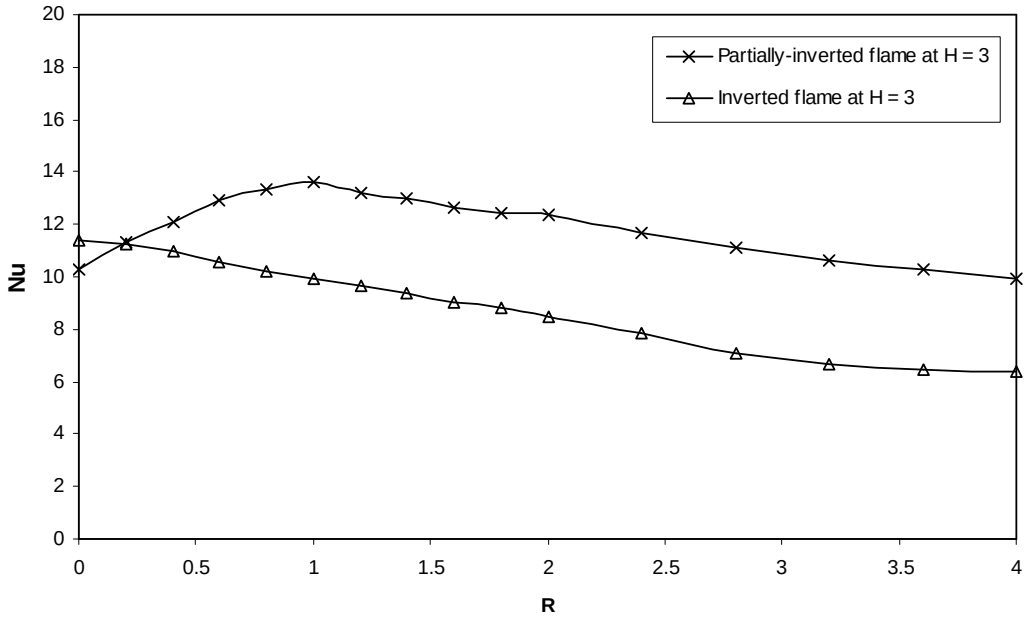

Figure 6.31. Comparison of radial Nu distribution of partially-inverted flames (Φ = 1.4) with inverted flames (Φ = 0.9) at Re = 2000, H = 3, B_R = 0, B_T = 0.51.

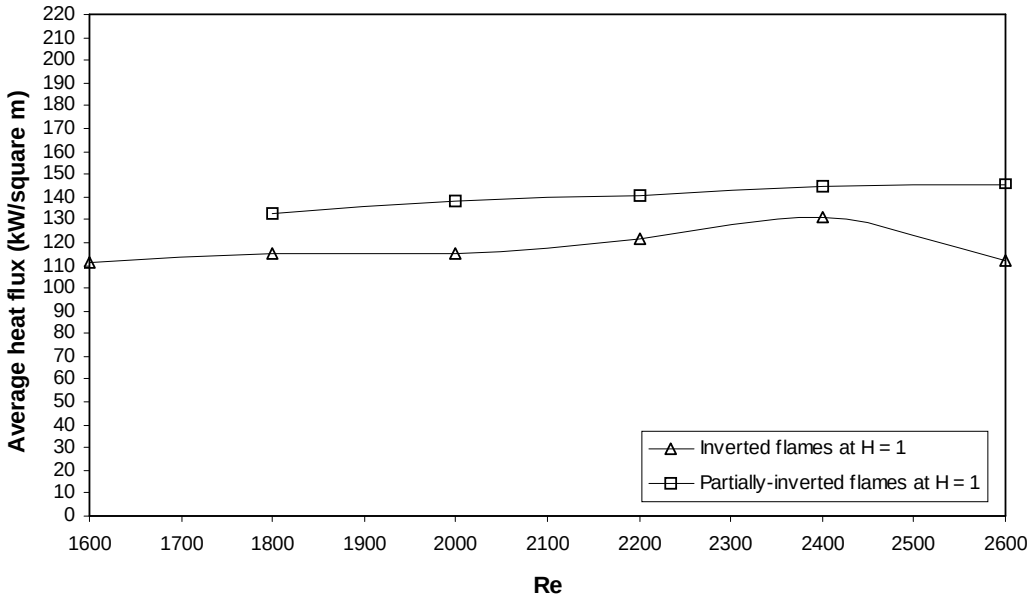

Figure 6.32. Comparison of total averaged heat flux of partially-inverted flames (Φ = 1.4) with inverted flames (Φ = 0.9) at Re = 2000, H = 1, B_R = 0, B_T = 0.51.

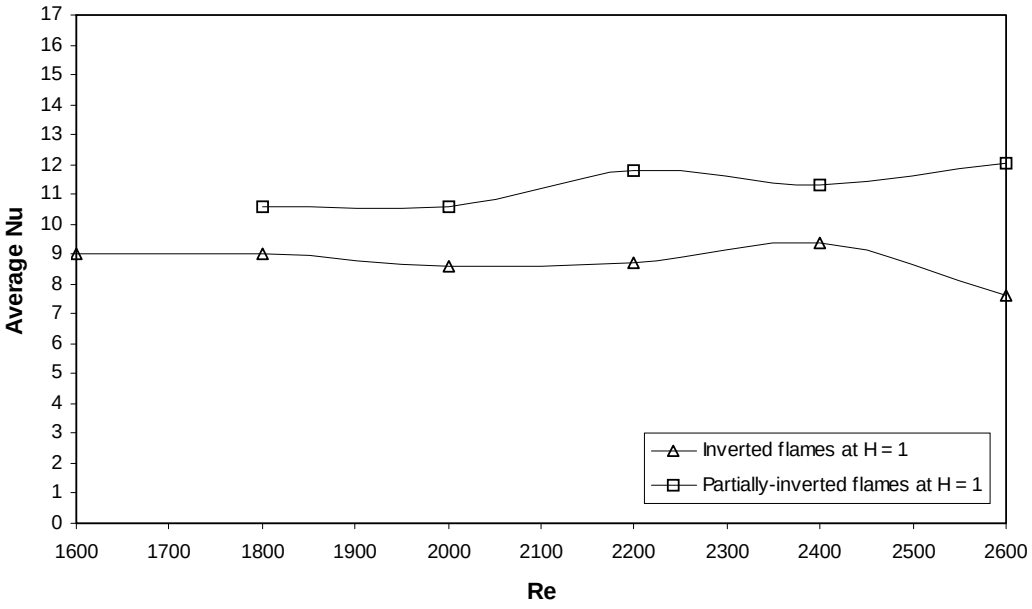

Figure 6.33 Comparison of total averaged Nu of partially-inverted flames (Φ = 1.4) with inverted flames (Φ = 0.9) at Re = 2000, H = 3, B_R = 0, B_T = 0.51.

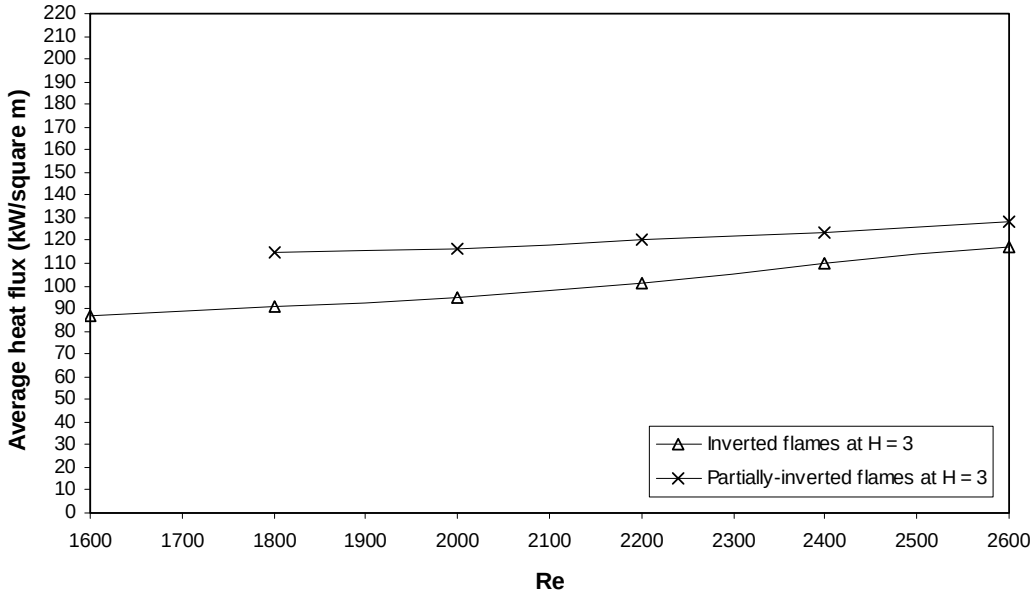

Figure 6.34. Comparison of total averaged heat flux of partially-inverted flames (Φ = 1.4) with inverted flames (Φ = 0.9) at Re = 2000, H = 1, B_R = 0, B_T = 0.51.

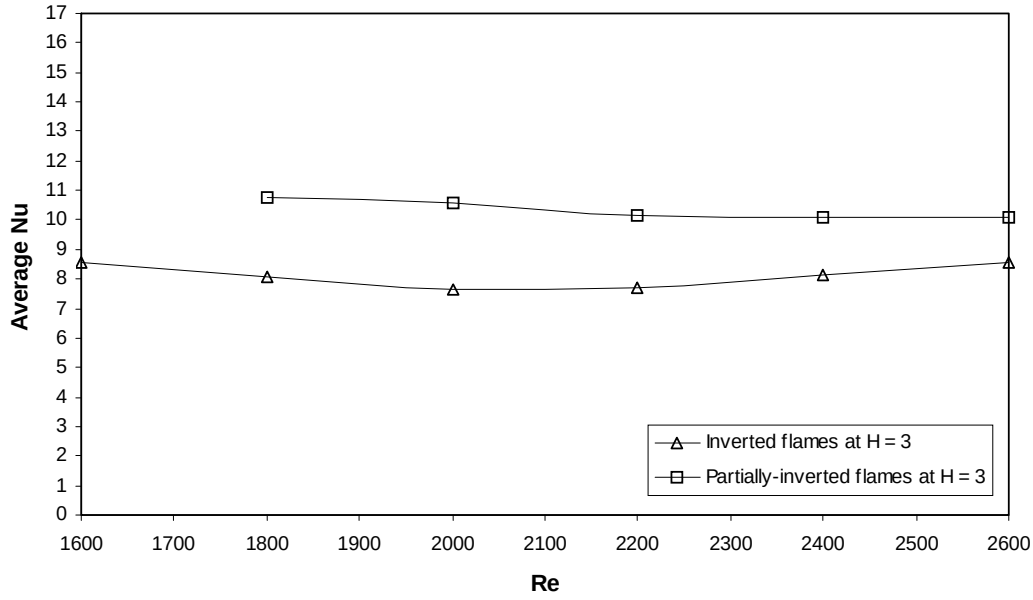

Figure 6.35. Comparison of total averaged Nu of partially-inverted flames (Φ = 1.4) with inverted flames (Φ = 0.9) at Re = 2000, H = 3, B_R = 0, B_T = 0.51.

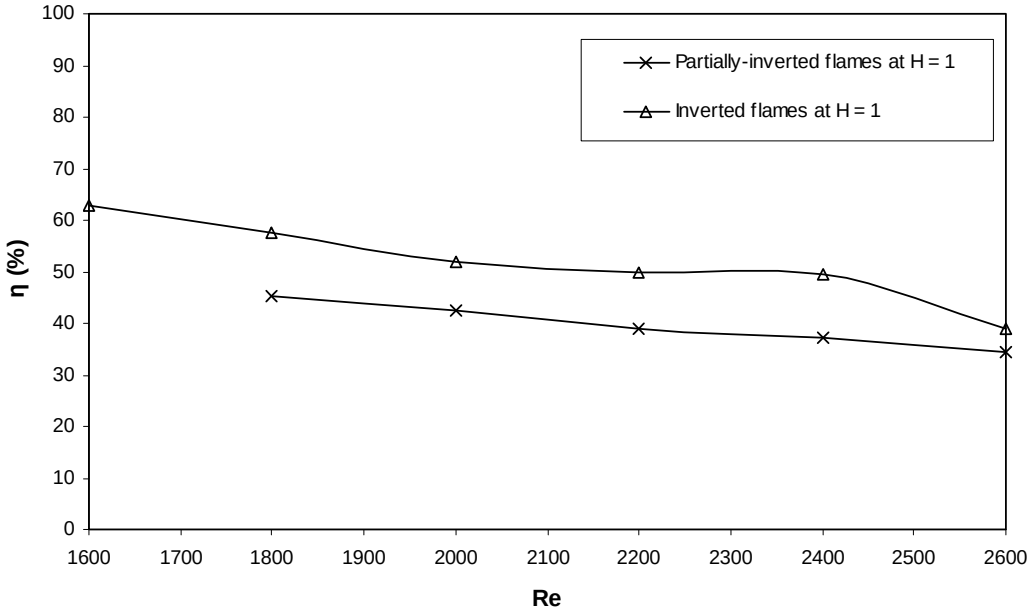

Figure 6.36. Comparison of thermal efficiency of partially-inverted flames (Φ = 1.4) with inverted flames (Φ = 0.9) at Re = 2000, H = 1, B_R = 0, B_T = 0.51.

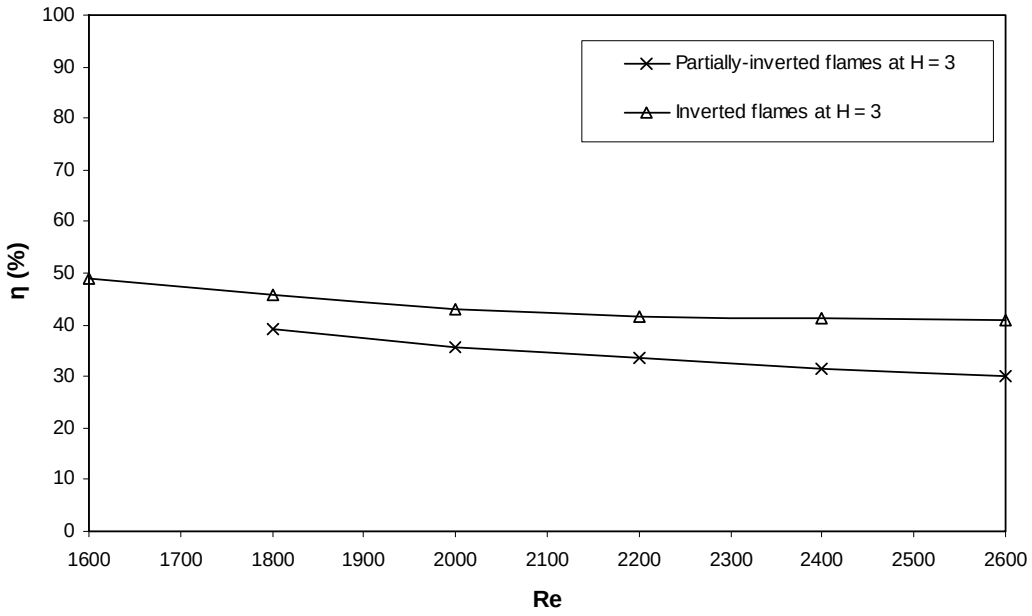

Figure 6.37. Comparison of thermal efficiency of partially-inverted flames (Φ = 1.4) with inverted flames (Φ = 0.9) at Re = 2000, H = 3, B_R = 0, B_T = 0.51.

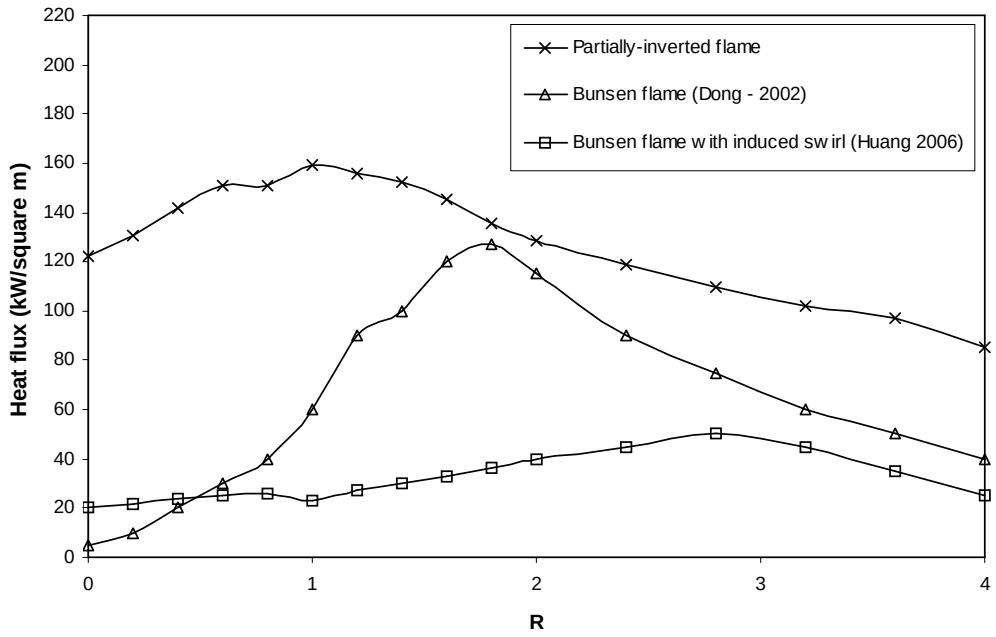

Figure 6.38. Comparison of radial heat flux distribution of partially-inverted flames (Φ = 1.4, Re = 1800, H = 3, B_R = 0, B_T = 0.51) with Bunsen flames from round nozzle (Φ = 1.1, Re = 1500, H = 5) and Bunsen flames with induced swirl (Φ = 1.4, Re = 1200, H = 2, S = 2.53).

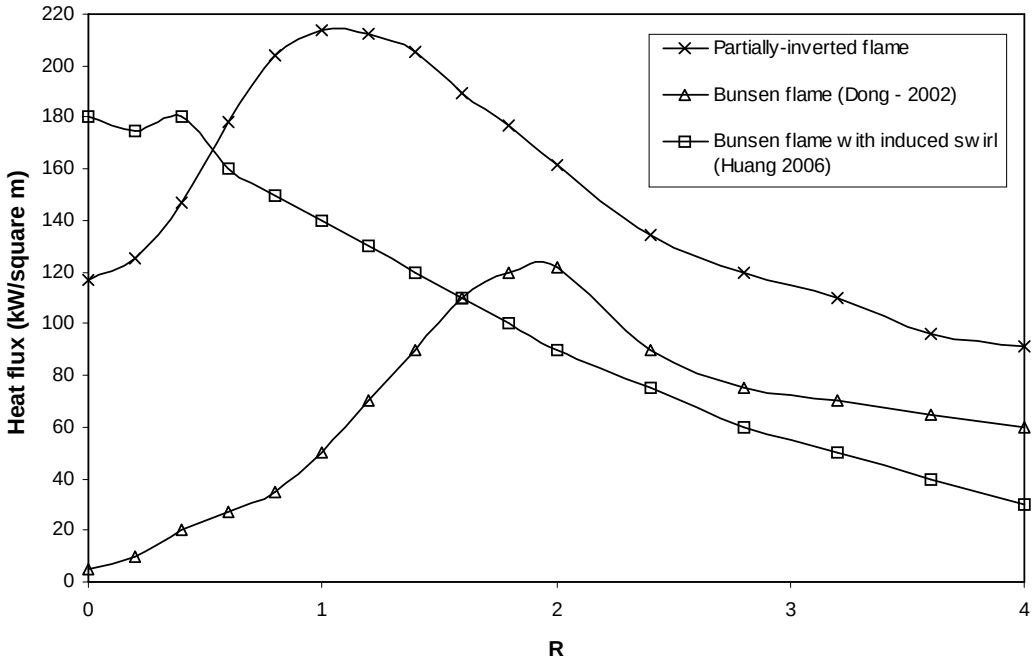

Figure 6.39. Comparison of radial heat flux distribution of partially-inverted flames (Φ = 1.4, Re = 1800, H = 1, B_R = 0, B_T = 0.51) with Bunsen flames from round nozzle (Φ = 1.0, Re = 1500, H = 1) and Bunsen flames with induced swirl (Φ = 1.0, Re = 1500, H = 2, S = 2.53).

Figure 6.38 shows radial heat flux distributions of partially-inverted flames at Φ = 1.4, Re = 1800, H = 3, B_R = 0, B_T = 0.51, regular Bunsen flames from round nozzle at Φ = 1.1, Re = 1500, H = 5 and Bunsen flames with induced swirl at Φ = 1.4, Re = 1200, H = 2, S = 2.53).

Evidently, partially-inverted flames have the highest average heat flux distribution over the entire region and there is no significant drop. On the other side, regular Bunsen flame, despite impinged at further nozzle-to-plate distance (H = 5), still displays sharp drop in stagnation region followed by a steep peak. Swirl induced flame appears have significantly lower heat flux values for the entire region. It can be assumed that partially-inverted flame aids heat transfer characteristics in terms of uniformity as its values remain relatively constant over large impingement surface.

Figure 6.39 compares radial heat flux distributions at small nozzle-to-plate distances. The swirl-induced flame has the highest stagnation point heat transfer, however it constantly declines with increased R. While both partially-inverted and Bunsen flames exhibit peaks (subjects of heat transfer from reaction zones), partially-inverted flames are not associated with a drop around stagnation zone.

6.7. Summary

1) Second part of investigation of heat transfer characteristics of rod-stabilized impinging premixed flames covers partially-inverted flames. For reference purposes, all results are presented in three output parameters: heat transfer rate (kW/m2), non-dimensional heat transfer coefficient (Nusselt number Nu)

and thermal efficiency η. Heat transfer rate and *Nu* are presented as local values (those includes radial distribution, stagnation point and maximum values) as well as area-averaged values for the entire region and specific sub-regions (stagnation, impingement and wall-jet region). Thermal efficiency is calculated for the entire investigated region.

2) Flame structure is dependable on proximity of the nozzle to the impinging plate. In close nozzle-to-plate distance, both reaction zones are stretched out, while in the further distance they appear not to be affected by the presence of impingement plate. Outer reaction zone can be attached to the inner reaction zone or detached. At very small nozzle-to-plate distance, the outer reaction zone might merge with inner reaction zone due to increased temperature in the preheat zone. Flame temperature remains constantly high in wide area due to the presence of burned gas and positively affects the uniformity of heat flux and Nu distribution.

3) Increase in nozzle-to-plate ratio *H* increases maximum values of heat flux and Nu. With further distances from the impingement plate, these peaks flatten thus create more constant heat flux and *Nu* distribution over large area. For very small *H*, the heat flux and *Nu* distributions show significant increase, however due to stability issue, such small nozzle-to-plate distances should be avoided for partially-inverted flames.

4) Reynolds number has less significant impact of heat flux and Nusselt number distributions than it has on inverted flames. Increasing of *Re* shifts values of

higher, due to increased turbulence that causes temperatures, however the gain is marginal due to temperatures in the region that are already at very high levels.

5) Thermal efficiency of partially-inverted flames is in the range of 30 – 51%. It increases with smaller nozzle-to-plate ratios and decreases with higher values of *Re*. Thermal efficiency is generally lower in partially-inverted flames than in inverted flames.

6) Comparison of partially-inverted flames with inverted flames reveals that the presence of outer reaction zone is more significant in further nozzle-to-plate distances as it further elongates plateaus with high heat flux and *Nu*. For optimal uniform heat flux and *Nu* distribution, the nozzle-to-plate ratio is higher for partially-inverted flames than for inverted flames. Thermal efficiency is generally higher in inverted flames.

7) In comparison with regular Bunsen flame and Bunsen flame with induced swirl, partially-inverted flame presents very uniform heat flux distribution, in contrast with regular Bunsen flames, whose drawback is marked by a significant drop in heat flux at stagnation region.

7. EMPIRICAL HEAT TRANSFER CORRELATIONS OF IMPINGING ROD-STABILIZED FLAMES

For purposes of design, it is useful to define prediction models from experimental data of heat transfer characteristics presented and discussed in Chapter 5 and 6, assuming that no such models exist for impinging premixed rod-stabilized flames. However, numerical models including those using commercial software such as Fluent are inconsistent with experimentally obtained data as detailed heat transfer mechanisms of flame impingement are not well understood and implemented. Moreover, comprehensive solution of a flow that is deflected from its axial direction to radial by the presence of impingement plate is yet to be fully understood. Also, nozzle with axially-mounted rod has even more complex flow characteristics than a single round jet. Turbulence and the presence of vortex eddies above the rod tip will have to be taken into account.

However, it is feasible to use empirical correlations to determine heat transfer rates that will provide simple yet effective prediction. Based on extensive experimental results from Chapter 5 and 6, multiple regression method was used to deduce empirical correlations for convective heat transfer for impinging inverted and partially-inverted flames.

7.1. Heat transfer prediction of impinging flames

There are four different heat transfer mechanisms identified in the flame impingement: convection, radiation, condensation and thermochemical heat release (TCHR). Due to the nature of experimental conditions at which the data were obtained, i.e. impinging flame onto a large plane surface, radiation is assumed to be negligible. Chemical dissociation was not taken into account, as well as process of condensation. Forced convection is assumed to be the predominant mechanism in this study. According to Viskanta (1996), the forced convection produces up to 98% of the total heat transfer and Beer and Chigier (1968) reported that convection contributed 80% to the total heat transferred.

Convective heat transfer is commonly expressed in terms of non-dimensional heat transfer coefficient, i.e. Nusselt Number *Nu*. For impingement flames, it is a function of Prandtl Number *Pr*, Reynolds Number *Re*, nozzle-to-plate ratio *H* and equivalence ratio ϕ:

$$Nu = Nu(Pr, Re, H, \phi) \tag{7.1}$$

$$Nu = a \cdot \mathrm{Pr}^{b} \cdot \mathrm{Re}^{c} \cdot H^{d} \cdot \phi^{e} \tag{7.2}$$

where *a*, *b*, *c*, *d* and *e* are constants. In terms of heat transfer rate characteristics, heat flux can be calculated from Equation 2.12 as:

$$\dot{q} = Nu \cdot \frac{k(\tilde{T})}{d_e} \cdot (T_f - T_s) \qquad [\mathrm{kW/m^2}] \tag{7.3}$$

where k is thermal conductivity of burned gas as a function of weighed average temperature $\tilde{T}$, d_e is effective diameter of the nozzle, T_f is flame temperature and T_s is surface temperature of the impingement plate.

7.2. Inverted flames heat transfer correlations

Firstly, heat transfer predictions are determined for inverted flames for both local and area-averaged values of *Nu*. The equivalence ratio is constant at ϕ = 0.9. Furthermore, it is assumed that Prandtl Number *Pr* is also constant at *Pr* = 0.4. Rod-stabilized flames are characterized by two non-dimensional parameters, rod protrusion B_R and rod-to-tube ratio B_T. Thus the commonly used formula (Equation 7.2) can be altered to:

$$Nu = a \cdot \mathrm{Re}^{b} \cdot H^{c} \cdot B_R^{d} \cdot B_T^{e} \tag{7.4}$$

where *a*, *b*, *c*, *d* and *e* are constants. Ranges of input parameters are kept same for all prediction models, i.e. *H* = 1.0 – 4.0, *Re* = 1600 – 2600, B_R = 0 – 2 and B_T = 0.51 – 0.80.

7.2.1. Local Nusselt Number correlations

Following empirical correlations have been obtained for maximum Nu and its local values at stagnation point and stagnation circle for inverted flames. Location of stagnation point is at *R* = 0, stagnation circle is located at *R* = 0.725. Figures B.1 – B.12 show correlations, fractioned for each independent input parameter, i.e. *Re*, *H*, B_R and B_T.

For maximum Nu_{max}:

$$Nu_{\max} = 0.722 \cdot \mathrm{Re}^{0.390} \cdot H^{-0.194} \cdot B_R^{0.038} \cdot B_T^{-0.975} \tag{7.5}$$

For stagnation point $Nu_{stagpoint}$:

$$Nu_{stagpo\,\mathrm{int}} = 0.489 \cdot \mathrm{Re}^{0.431} \cdot H^{-0.184} \cdot B_R^{0.035} \cdot B_T^{-0.941} \tag{7.6}$$

Stagnation circle $Nu_{stagcircle}$:

$$Nu_{stagcircle} = 5.203 \cdot \mathrm{Re}^{0.108} \cdot H^{-0.031} \cdot B_R^{0.004} \cdot B_T^{-0.754} \tag{7.7}$$

R-squared values for these models varied between 0.747 – 0.971, denoting moderate reliability.

It is evident that *Re* has positive effect on *Nu* for both stagnation locations as well as on maximum values with the similar magnitude. Power indexes of *H* are negative, indicating negative effect on *Nu*. This is comprehensible, since *Nu* generally declines with increased *H*. However the effect is less significant as the power indexes of *H* are low.

Effect of rod-to-tube ratio B_T is also negative, i.e. Nu_{max} and *Nu* at stagnation locations generally decline with smaller diameters. Significance of B_T is similar to that of *Re*.

With power indexes of rod protrusion being in thousandths, the effect of rod protrusion B_R can be assumed to be negligible, which is well with the conclusion of experimental work. Thus Equations 7.5 - 7.7 can be rewritten as:

$$Nu_{\max} = 0.722 \cdot \mathrm{Re}^{0.390} \cdot H^{-0.194} \cdot B_T^{-0.975} \tag{7.8}$$

$$Nu_{stagpo\,\mathrm{int}} = 0.489 \cdot \mathrm{Re}^{0.431} \cdot H^{-0.184} \cdot B_T^{-0.941} \tag{7.9}$$

$$Nu_{stagcircle} = 5.203 \cdot \mathrm{Re}^{0.108} \cdot H^{-0.031} \cdot B_T^{-0.754} \tag{7.10}$$

7.2.2. Area-averaged Nusselt Number correlations

Predictions of area-averaged Nu are calculated for the entire impingement region and separately for its parts defined in Chapter 5.2.2 as a function of non-dimensional radial distance R:

- Stagnation region: $0 \leq R \leq 1$
- Impingement region: $1 \leq R \leq 2$
- Wall-jet region: $2 \leq R \leq 4$

Correlations for independent input parameters, i.e. Re, H, B_R and B_T are presented in Figures B.13 – B.28. Resulting equations for each region are following:

Total area-averaged Nu_{total}:

$$Nu_{total} = 41.269 \cdot \mathrm{Re}^{-0.204} \cdot H^{-0.169} \cdot B_R^{0.036} \cdot B_T^{-0.178} \tag{7.11}$$

Stagnation region area-averaged $Nu_{stagregion}$:

$$Nu_{stagregion} = 0.996 \cdot \mathrm{Re}^{0.340} \cdot H^{-0.265} \cdot B_R^{0.045} \cdot B_T^{-1.032} \tag{7.12}$$

Impingement region area-averaged $Nu_{impgregion}$:

$$Nu_{impgregion} = 2.133 \cdot \mathrm{Re}^{0.218} \cdot H^{-0.260} \cdot B_R^{0.051} \cdot B_T^{-0.659} \quad (7.13)$$

Wall-jet region area-averaged $Nu_{wallregion}$:

$$Nu_{wallregion} = 223 \cdot \mathrm{Re}^{-0.442} \cdot H^{-0.125} \cdot B_R^{0.030} \cdot B_T^{0.060} \quad (7.14)$$

R-squared values for these models varied between 0.220 – 0.980, denoting moderate reliability.

Power indexes of *Re* are positive in stagnation and impingement regions, i.e. *Nu* increases with increased *Re*. However its effect in wall-jet region is opposite. Since wall-jet region has the largest area, the impact of *Re* on Nu_{total} is negative as well. Impact of *H* remains negative for the entire region, however low values of its power indexes denote that Nu is influenced marginally.

The effect of rod-to-tube ratio B_T is in the opposite of the effect of *Re*. It has negative power indexes in stagnation and impingement regions and positive in wall-jet region. It means that smaller diameters perform better in these regions. Analogously, the impact of B_T on Nu_{total} is also negative.

Similarly to local *Nu* correlations, power indexes of rod protrusion B_R are considerably small, thus the effect of rod protrusion B_R can be assumed to be negligible and the parameter can be excluded from correlations. Thus Equations 7.11 - 7.14 are rewritten into new formulas:

$$Nu_{total} = 41.269 \cdot \mathrm{Re}^{-0.204} \cdot H^{-0.169} \cdot B_T^{-0.178} \quad (7.15)$$

$$Nu_{stagregion} = 0.996 \cdot \mathrm{Re}^{0.340} \cdot H^{-0.265} \cdot B_T^{-1.032} \tag{7.16}$$

$$Nu_{impgregion} = 2.133 \cdot \mathrm{Re}^{0.218} \cdot H^{-0.260} \cdot B_T^{-0.659} \tag{7.17}$$

$$Nu_{wallregion} = 223 \cdot \mathrm{Re}^{-0.442} \cdot H^{-0.125} \cdot B_T^{0.060} \tag{7.18}$$

7.3. Partially-inverted flames heat transfer correlations

Second part covers heat transfer predictions for partially-inverted flames for local and area-averaged values of *Nu*. Equivalence ratio is constant at ϕ = 1.4 and *Pr* is also constant at *Pr* = 0.4. For partially-inverted flames, geometrical parameters of the nozzle, i.e. rod protrusion B_R and rod-to-tube ratio B_T, are maintained constant at B_R = 0 and B_T = 0.51 due to stability issues, as explained in Chapter 6.1. Thus Equation 7.2 is reduced to:

$$Nu = a \cdot \mathrm{Re}^{b} \cdot H^{c} \tag{7.19}$$

where *a*, *b* and *c* are constants. Ranges of input parameters are kept same for all prediction models, i.e. *H* = 1.0 – 4.0 and *Re* = 1800 – 2600.

7.3.1. Local Nusselt Number correlations

Correlations have been obtained for maximum Nu and its local values at stagnation point and stagnation circle for partially-inverted flames. Locations of stagnation point and stagnation circle are the same as in case of inverted flames, i.e. *R* = 0 and *R* = 0.725 respectively. Correlations for each input parameter (i.e. *Re* and *H*) are presented in Figures 7.29 – 7.34.

For maximum Nu_{max}:

$$Nu_{\max} = 2.815 \cdot \mathrm{Re}^{0.210} \cdot H^{-0.101} \tag{7.20}$$

For stagnation point $Nu_{stagpoint}$:

$$Nu_{stagpo\,int} = 3203 \cdot \mathrm{Re}^{-0.757} \cdot H^{-0.074} \tag{7.21}$$

Stagnation circle $Nu_{stagcircle}$:

$$Nu_{stagcircle} = 93 \cdot \mathrm{Re}^{-0.296} \cdot H^{-0.004} \tag{7.22}$$

R-squared values for these models varied between 0.44 – 0.87, denoting moderate reliability.

It can be observed that *Re* has positive effect on *Nu* at its maximum values, otherwise the effect is negative. The effect of *H* is negative for the entire region as power indexes of *H* are negative. As already explained, *Nu* generally declines with increased *H*. In comparison with models of inverted flames, the power indexes of *H* are even lower. It indicates that *Nu* distribution remains quite constant over the investigated range of *H*, i.e. 1.0 – 4.0.

7.3.2. Area-averaged Nusselt Number correlations

Predictions of area-averaged *Nu* are calculated for the entire impingement region and separately for its parts, i.e. stagnation, impingement and wall-jet regions. Their size is the same as in case of models of inverted flames. Correlations for both input

parameters, i.e. *Re* and *H* are presented in Figures B.35 – B.42. Resulting equations for each region are following:

Total area-averaged Nu_{total}:

$$\overline{Nu}_{total} = 0.777 \cdot \mathrm{Re}^{0.347} \cdot H^{-0.025} \tag{7.23}$$

Stagnation region area-averaged $Nu_{stagregion}$:

$$\overline{Nu}_{stagregion} = 85 \cdot \mathrm{Re}^{-0.254} \cdot H^{-0.045} \tag{7.24}$$

Impingement region area-averaged $Nu_{impgregion}$:

$$Nu_{impgregion} = 4.239 \cdot \mathrm{Re}^{0.152} \cdot H^{-0.124} \tag{7.25}$$

Wall-jet region area-averaged $Nu_{wallregion}$:

$$Nu_{wallregion} = 0.291 \cdot \mathrm{Re}^{0.467} \cdot H^{0.007} \tag{7.26}$$

R-squared values for these models varied between 0.37 – 0.95, denoting moderate reliability.

Power indexes for *H* are negative except wall-jet region, which means that an increase negatively influences average Nu distribution. Impact of *Re* is negative and more profound at stagnation region, while *H* is influencing impingement region. All power indexes are also generally low, which means that there is lesser impact of both *Re* and *H* on average Nu. This also indicates very steady and uniform *Nu* distribution over the entire impingement region.

7.4. Summary

1) Empirical heat transfer correlations for impinging inverted and partially-inverted flames have been determined by multiple regression method, using experimental data from Chapter 5 and 6. Correlations are presented in the form of non-dimensional parameters: $Nu = Nu(Pr, Re, H, \phi)$. Total 14 correlations have been deduced, representing local and area-averaged distributions. All presented models have decent reliability with 95% confidence and can be used for future design purposes.

2) Correlations for impinging inverted flames used Re, H, B_R and B_T as independent input parameters. The effect of rod protrusion B_R has been found to be negligible thus the parameter was excluded from correlations. The effect of H has generally negative effect on Nu distributions. Both Re and B_T are more significant than H. All parameters have less significant impact on area-averaged Nu.

3) Correlations for impinging partially-inverted flames used Re, H as independent input parameters. In comparison with inverted flames, effect of H is less profound. Effect of Re is more significant than H. The positive effect of Re on Nu is at stagnation point, impingement and wall-jet regions.

8. CONCLUSIONS AND RECOMMENDATIONS

The prime objective of the present study, i.e. to investigate feasible approach to improve heat transfer characteristics of impinging premixed flames, has been accomplished.

Based on the literature overview and the study of background materials, it was decided to alter the aerodynamics of regular (Bunsen) flame jet by introducing a solid body into a flow in order to achieve the objective. An axially-mounted rod has been selected that produces rod-stabilized flames. Several burners were designed before optimal geometrical parameters were found.

However, preliminary experiments with free-jets revealed that such flames exhibit unstable behaviors, thus the stability characteristics had to be investigated prior to the study of impinging flames. It was found that rod-stabilized flames can be stabilized as three different types: inverted, partially-inverted and as regular (Bunsen) flame.

Once the study of stability characteristic was completed, the investigation of structure, incl. temperature profiles was performed that gave a deeper understanding of both inverted and partially-inverted flames.

Studies of impinging inverted and partially-inverted flames had been performed. Both studies independently confirmed prediction that rod-stabilized flames produce uniform heat transfer distribution over the impingement surface.

Furthermore, for design purposes, empirical correlations to predict convective heat transfer had been determined.

It has to be said that the study of rod-stabilized flames is the very first one, especially in the area of impinging flames. Inverted and partially-inverted flames are very complex. Several new non-dimensional parameters had to be introduced to facilitate their complexity. There is scarce information on this topic in the literature and literally no report on impinging rod-stabilized flames existed before this study.

Following chapter breaks down the conclusion into details related to each part of the study.

8.1. Conclusions

8.1.1. Free-jet flames

Stability and flammability characteristics

Experimentally determined stability data indicates three fundamental types of premixed butane/air flame which can be stabilized by using an axially-mounted stabilizing rod: inverted, partially-inverted, and regular (Bunsen) flames. In dependence of equivalence ratio Φ, data points obtained from a stable flame are divided into five stable regions: inverted flames (Region I) exist predominantly in

fuel-lean mixtures, while partially-inverted flames (Region III) and regular flames (Region V) appear in fuel-rich and very fuel-rich mixtures, respectively. Between the overlapping areas, inter-regions (Regions II and IV) are characterized by the availability of more than one stabilized flame.

As for the inter-regions, it is shown that the explicitness of whether the reaction zone can be stabilized at the burner rim (regular flame), at the rod tip (inverted flame) or at both positions (partially-inverted flame), is certainly affected by the axial and radial positions of the ignition source. The situation becomes more complex when there are other parameters involved. In the Region IV, cross-sectional ignition at closer distance creates both reaction zones, while tangential ignition at a further distance can only stabilize the flame at the burner rim and a deficiency of air in the air/fuel mixture is the main reason. Certainly, disturbance from the high velocity distribution across the flame jet is another major cause. In the Region II, apart from radial distance and axial direction of the ignition source, the high rate of dilution with surrounding air, the steep flow velocity distribution across the flame jet, the different shapes of flame and the separation of reaction zones at high Reynolds numbers should also be considered.

There is an elongated unstable area (Region VI) above the flashback curve, at which lower flow velocity causes the inner reaction zone of the originally partially-inverted flame to heat up the rod tip, thus reducing the quenching effect. Consequently, it propagates upstream to induce a slow motion flashback. The size of this region is strongly affected by the height of the rod tip above the tube rim, expressed by the

non-dimensional rod protrusion (B_R). Increase of B_R results in widening of the region at the expense of the stable regions, as the flow velocity decreases and the rod tip is more exposed to the surrounding air.

Similarly, a negative impact on the size of the stable regions has been observed for another non-dimensional parameter, rod-to-tube ratio (B_T), which represents the variation of rod diameter for a constant tube bore diameter. With an increase of B_T (use of a smaller rod diameter), a bigger cross-sectional area is obtained, which increases the size of the Region VI and the occurrence of a higher rate of heat conduction makes the flame propagating upstream faster. Flashback limits are also shifted up. Hence the default configuration of the largest diameter (d = 9.55 mm) and B_T = 0 appears to be the most stable condition among all tested configurations.

The influences of both B_R and B_T on blow-off limits appear to be less significant. Variation of B_T shows negligible effect while higher values of B_R tend to move the blow-off curve towards higher Φ because of the higher rate of dilution of the air/fuel mixture by the surrounding air. However, the accuracy may also be affected by a low resolution of the flowmeters, which should be avoided. In comparison with the round and slot flame jets, a rod-stabilized burner can operate with very fuel-lean mixtures (up to Φ = 0.55), which is a definite advantage in terms of emissions, since the generation of NO_x and CO emissions can be reduced.

Inverted flame is characterized by the presence of one (the inner) reaction zone stabilized above the rod tip as the conditions of lean mixtures does not allow creation of outer reaction zone above the tube rim. The flame has a convex shape

with the flame cone tip situated above the rod tip and the flame cone base resting in diluted boundary layer.

The effect of variable parameters on inverted flame shape varies. As of Reynolds number *Re*, with increased value, the flame cone tip is shifted upwards from the rod tip and the flame cone becomes more elongated at its entire length. The effect of equivalence ratio Φ has been found to be negligible and variation of rod protrusion B_R shows only minor effect. Rod–to-tube ration B_T affects the flame cone in the way that either narrows its tip (for larger B_T) or widens (for smaller B_T).

Flame structure and temperature profiles

Temperature distribution and radial profiles of inverted flame reveal wide and large central core of burner gas with maximum temperature that is situated above the luminous reaction zone. The presence of such zone is a favorable indication of uniform heat flux distribution of impinged flame. Outer zone of burned gas with gradually decreasing temperature has approximately the same radial size as the central core. Preheat zone follows the pattern of flame cone of the luminous reaction zone.

Partially-inverted flame is more complex type. Both inner and outer reaction zones are present due to increased percentage of gaseous fuel in the mixture. Inner reaction zone has a convex shape and the outer reaction zone is of concave shape. The tip of the inner reaction zone rests above the rod and the base of the outer reaction zone rests above the tube rim. The base of the inner reaction zone might be fully attached,

partially-detached or fully detached from the tip of the outer reaction zone. Equivalence ratio Φ, Reynolds number *Re* and rod protrusion B_R. are the factors, that affect the flame cone tip appearance includes centricity of the rod in the tube.

Similarly to the inverted flames, with an increase of Reynolds number *Re*, the inner flame cone tip is shifted upwards from the rod tip and the flame cone is more elongated at its entire length. Also, for higher values of *Re*, the presence of turbulent flow patterns might partially or fully detach the inner and outer flame cones. Increase of equivalence ratio Φ causes the inner reaction zone to be narrower and thinner due to the further reduction of air inside the stream. Also the outer and inner reaction zones are likely to be separated. Higher values of rod protrusion B_R elongate the outer flame cone to match with the inner flame cone, which is positioned above. Increased B_R causes the outer and inner zones more likely to be detached. Variation of rod–to-tube ration B_T affects the inner flame cone in the way that higher values of B_T narrow its tip.

Very large central core of burner gas with approximately maximum temperature is the main characteristic that has been observed from temperature distribution diagrams of partially-inverted flame. The central core is wider in comparison with its counterpart in inverted flames, due to the presence of outer reaction zone. As in the case of inverted flames, the central core of burned gas with maximum temperature is the preferred flame type to achieve uniform heat flux distribution of impinged flame. Outer zone of burned gas with gradually decreasing temperature has narrower radial size in comparison with central core. Preheat zone is rather

flattened and does not follow the cone pattern of luminous reaction zone. It indicates high heat flow to the unburned air / flow mixture due to proximity of two reaction zones.

8.1.2. Impinging flames

Impinging inverted flames

Flame structure reflects proximity of the nozzle to the impinging plate. For close nozzle-to-plate distance, the flame is characterized by the stretched out reaction zone, causing peak values of heat flux to be shifted outwards. With further distance, this effect diminishes and heat transfer distribution is more constant with no sharp peaks. Flame temperature remains very high in the central core due to the presence of burned gas and positively affects the uniformity of heat flux and Nu distributions.

The effect of nozzle-to-plate ratio *H* is significant. Increasing *H* is associated with slight drop of heat flux in stagnation region followed by sharp peak with subsequent decline. Nusselt number remains constant in the stagnation and impingement region. On the other side, further increase of *H* creates more constant heat flux distribution over large area with Nusselt number steadily decreasing. For very small *H*, flame becomes unstable due to the quenching effect of impingement plate. It terms of optimal uniform heat transfer characteristics, nozzle-to-plate ratio is strongly related to the selected rod diameter (rod-to-tube ratio).

Variations of Reynolds number have also significant impact of heat flux and Nusselt number distributions. Increasing *Re* increases turbulence in the stagnation region,

especially for smaller *H*, and better mixing enhances combustion, consequently the temperature arises, thus heat transfer rate. Increased turbulence however causes slight fluctuation in Nusselt number distribution.

It has been found that variation of rod protrusion B_R affects the heat transfer rate as if the distance would be from the rod tip to the impingement plate. The impact of rod protrusion variations on heat transfer characteristics is not significant and together with the fact that with increased rod protrusion there is an arising issue of flame stability, the use of rod protrusion is not recommended for laminar / transient flames.

With increased rod-to-tube ratio B_T and for small *H*, heat flux and *Nu* distributions show constant patterns, a fact that is related to the newly defined spread angle γ of the reaction zone. Spread angle is a function of B_T and increases with increasing B_T. Smaller rod diameters have wider spread angle, thus more uniform distribution in the stagnation and impingement region. To achieve optimal uniform distribution, B_T must be correlated with *H*, e.g. for small *H*, smaller rod diameter (higher B_T) should be chosen.

Thermal efficiency of inverted flames varies with input parameters. In general, it is in the range of 36 – 63 % and is generally higher at small nozzle-to-plate ratios and smaller *Re*. Rod protrusion has negligible effect, while increased rod-to-tube ratio decreases thermal efficiency.

Comparison with regular Bunsen flames and Bunsen flames with induced swirl denotes that inverted flames present uniform heat flux distributions with no associated drops in stagnation region, in contrast with regular Bunsen flames.

Impinging partially-inverted flames

Flame structure is dependable on proximity of the nozzle to the impinging plate. For close nozzle-to-plate distances both reaction zones are stretched out, while in further distances they appear not to be affected by the presence of impingement plate. Outer reaction zone can be attached to the inner reaction zone or detached. At very small nozzle-to-plate distances, the outer reaction zone might merge with inner reaction zone due to increased temperature in the preheat zone. Flame temperatures remain constantly high in wide area due to the presence of burned gas and positively affect the uniformity of heat flux and Nu distributions.

An increase in nozzle-to-plate ratio *H* increases maximum values of heat flux and *Nu*. With further distances from the impingement plate, these peaks flatten thus creating more constant heat flux and *Nu* distributions over large area. For very small *H*, the heat flux and *Nu* distributions show significant increase. However due to stability issue, partially-inverted flame for small nozzle to plate distance should be avoided.

Reynolds number has less significant impact of heat flux and Nusselt number distributions than it has on inverted flames. Increasing of *Re* shifts values higher,

due to increased turbulence that causes temperatures, however the gain is marginal due to temperatures in the region that are already at very high levels.

Thermal efficiency of partially-inverted flames is in the range of 30 – 51%. It increases with smaller nozzle-to-plate ratios and decreases with higher values of *Re*. Thermal efficiency is generally lower in partially-inverted flames than in inverted flames.

Comparison of partially-inverted flames with inverted flames reveals that the presence of outer reaction zone is more significant in further nozzle-to-plate distances as it further elongates plateaus with high heat flux and *Nu*. For optimal uniform heat flux and *Nu* distribution, nozzle-to-plate ratio is higher for partially-inverted flames than for inverted flames.

In comparison with regular Bunsen flame and Bunsen flame with induced swirl, partially-inverted flames present very uniform heat flux distribution, in contrast with regular Bunsen flames, which drawback is significant drop in heat flux at stagnation region.

Empirical correlations

Empirical heat transfer correlations for impinging inverted and partially-inverted flames have been determined by multiple regression method. Correlations are presented in form of non-dimensional parameters: $Nu = Nu(Pr, Re, H, \phi)$. Total 14 correlations have been deduced, representing local and area-averaged distributions.

All presented models have a good reliability with 95% confidence and can be used for future design purposes.

Correlations for impinging inverted flames used *Re*, *H*, B_R and B_T as independent input parameters. The effect of rod protrusion B_R has been found to be negligible thus the parameter was excluded from correlations. The effect of *H* has generally negative effect on *Nu* distributions. Both *Re* and B_T are more significant than *H*. All parameters have less significant impact on area-averaged *Nu*.

Correlations for impinging partially-inverted flames used *Re*, *H* as independent input parameters. In comparison with inverted flames, the effect of *H* is less profound. The effect of *Re* is more significant than *H*. The positive effect of *Re* on *Nu* is at stagnation point, impingement and wall-jet regions.

8.2. Recommendations

The presented research study is the first of its kind in the field of impinging premixed rod-stabilized flames. Such fact implies that there are many possible research topics arising. Looking at the extensive research that has been done for regular (Bunsen) impinging flames, clearly, several similar topics can be selected. There could be two fundamental approaches in further research: innovative and conservative approach. Despite wording, both of them could significantly contribute the research area.

Conservative approach would include:

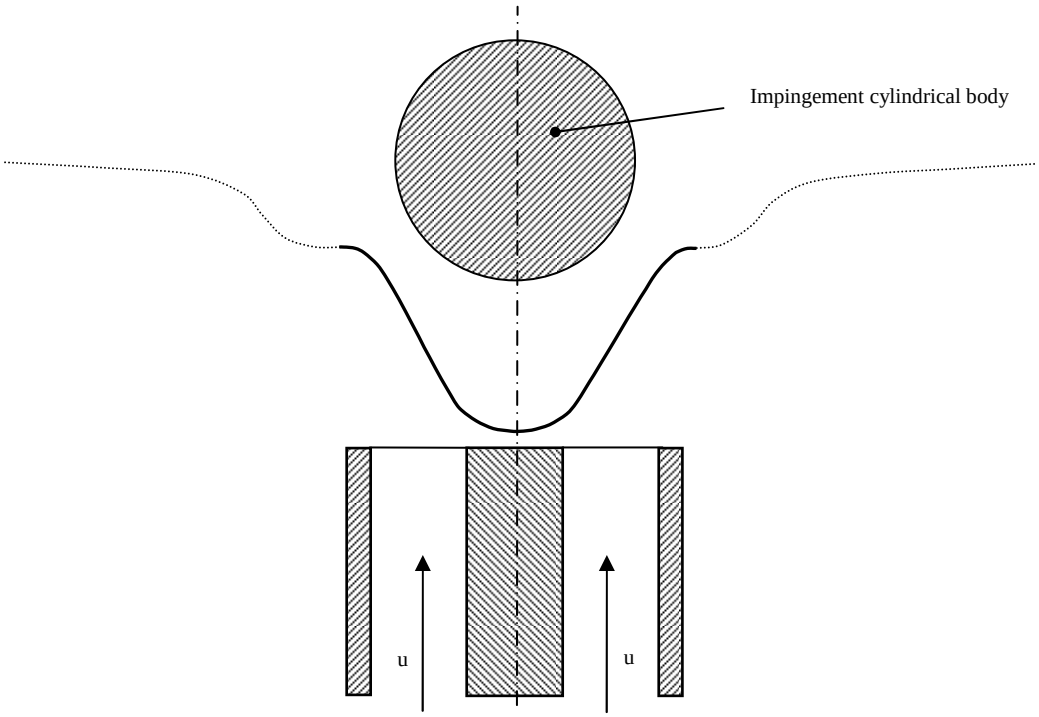

Figure 8.1. Inverted flame impinging onto the cylindrical body.

1) Further investigation of the effects of basic geometrical parameters defined in this study, e.g. rod protrusion, rod-to-tube ratio, etc.

2) Investigation of fundamental heat transfer mechanisms associated with rod-stabilized flames, e.g. determination of radiation fraction, or investigation of thermochemical heat release, etc.

3) Numerical study of impinging rod-stabilized flames or isothermal jets.

Innovative approach would deal with:

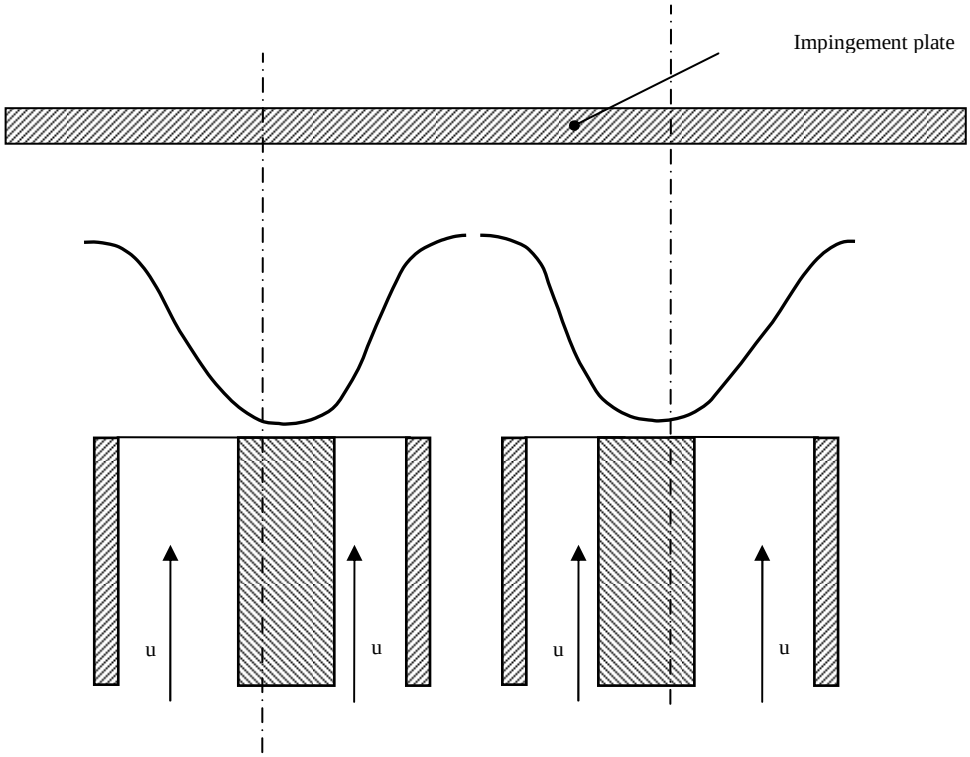

Figure 8.2. Array of two nozzles with asymmetrically mounted rods.

1) Investigation of impinging rod-stabilized flames onto cylindrical body.

2) Study of multiple jets with asymmetrically arranged rods.

ad1) due to convex shape of the inverted and premixed flames and presence of wide central core of burned gas with high temperatures, rapid forced convection heat transfer to the cylindrical body might produce promising results in terms of heat transfer uniformity. Figure 8.1 shows an example of inverted flame, impinging onto cylindrical body.

ad2) the rod can be mounted asymmetrically, producing asymmetric flow and flame shape. While such setup can be investigated on a single jet, it might be very useful in the array of two or more jets, where nozzles on the sides would be with asymmetrically mounted rod, while the inside one would be with axially-mounted rod. Such concept could increase the overall efficiency of an array by decreasing the inside spacing while at the same time extending heat transfer distribution on the sides. In fact there is an analogy with variation of rod-to-tube ratio (rod diameters), where smaller rod diameter is associated with wider spread angle γ and better heat transfer over a large area. Figure 8.2 shows an array of two nozzles with asymmetrically mounted rods, producing inverted flames. The rods are mounted in the way that inner sides of the nozzles produce steeper flame cones (narrow spread angle γ), while at the outer space is filled with wider flame cones (wide spread angle γ).

Other feasible research topics include investigation of impingement heat transfer of combination of slot tube with round rod, or slot rod with round tube, etc. Possibilities are infinite.

REFERENCES

Baukal C. E. and Gebhart B. (1995) A Review of Flame Impingement Heat Transfer Studies – Part 1, Experimental Conditions, *Combustion Science and Technology*, Vol. 104, pp. 339-357.

Baukal C. E. and Gebhart B. (1995) A Review of Flame Impingement Heat Transfer Studies - Part 2, Measurements, *Combustion Science and Technology*, Vol. 104, pp. 339-357.

Baukal C.E. and Gebhart B. (1995) A Review of Semi-Analytical Solutions for Flame Impingement Heat Transfer, *International Journal of Heat and Mass Transfer*, Vol. 39, pp. 2989-3002.

Baukal, C.E. (1996) Heat Transfer from Flame Impingement Normal to a Plane Surface, Ph.D. Thesis, University of Pennsylvania.

Baukal, C.E., Farmer, L.K., Gebhart, B., and Chan, I., (1996) Heat Transfer Mechanisms in Flame Impingement Heating. *1995 International Gas Research Conference*, pp. 2277-2287.

Baukal, C.E. and Gebhart, Jr B., (1996) A Review of Empirical Flame Impingement Heat Transfer Correlations. *International Journal of Heat and Fluid Flow,* Vol.17, pp. 386-396.

Baukal, C.E. and Gebhart, B., (1997) Surface Condition Effects on Flame Impingement Heat Transfer. *Experimental Thermal and Fluid Science,* Vol. 15, pp. 323-335.

Baukal, C.E. and Gebhart, B., (1998) Oxygen-Enhanced / Natural Gas flame Radiation. *International Journal of Heat Mass Transfe,r* Vol. 44, pp. 2539-2547.

Beer, J.M. and Chigier, N.A. (1974) Combustion Aerodynamics, *Applied Science Publishers Ltd.*.

Beer, J.M. and Chigier, N.A. (1968) Impinging Jet Flames, *Combustion and Flame,* Vol. 12, pp. 575-586.

Birbaud A.L., Ducruix S., Durox D. and Candel S. (2008) The Nonlinear response of inverted "V" flames to equivalence ratio nonuniformities, *Combustion and Flame*, Vol. 154, pp. 356-367.

Choi W. and Puri I. K. (2003) Response of Flame Speed to Positively and Negatively Curved Premixed Flames, *Combustion Theory Modelling*, Vol. 7, pp. 205-220.

Choi W. and Puri I. K. (2001) Contribution of Curvature to Flame-Stretch Effects on Premixed Flames, *Combustion and Flame*, Vol. 126, pp. 1640-1654.

Coghe, A., .Solero, G. and Brunello, G. (2000) Multiple V-flame Burner: Investigation on Flame Interaction, *Open Meeting on Combustion*.

Dong, L. L., (2002) Studies of Single and Multiple Impinging Hydrocarbon Flame Jets, Ph.D. Dissertation, The Hong Kong Polytechnic University.

Dong, L. L., Cheung, C. S. and Leung, C. W. (2003) Heat Transfer of a Row of Three Butane/air Flame Jets Impinging on a Flat Plate, *International Journal of Heat and Mass Transfer*, Vol. 46, pp. 113-125.

Dong, L. L., Cheung, C. S. and Leung, C. W. (2002) Heat Transfer from an Impinging Premixed butane/air slot flame jet, *International Journal of Heat and Mass Transfer*, Vol. 45, pp. 979-992.

Dong, L. L., Cheung, C. S. and Leung, C. W. (2001) Heat Transfer Characteristics of an Impinging Butane/air Slot Jet of Low Reynolds Numbers, *Experimental Heat Transfer*, Vol. 14, pp. 265-282.

Edmondson H. and Heap M. P. (1970) The Correlation of Burning Velocity and Blow-off Data by the Flame Stretch Concept, *Combustion and Flame*, Vol. 15, pp. 179-187.

Friedman R. (1953) Measurement of the Temperature Profile in a Laminar Flame, *Fourth Symposium on Combustion*, pp. 259.

Fristrom R. M. and Westenberg A. A. (1965) Flame Structure, McGraw-Hill Book Company; New York.

Gardon, R. and Akfirat, J.C., (1996) Heat Transfer Characteristics of Impinging Two-Dimensional Air Jets, *Journal of Heat Transfer* Vol. 88, pp. 101-108.

Gardon, R. and Cobonpue, J., (1961) Heat Transfer between a Flat Plate and Jets of Air Impinging on It, *International Development in Heat Transfer Part 2*, pp. 1-60.

Gaydon G. and Wolfhard H. G. (1979) Flames – Their Structure, Radiation and Temperature, 4th edition, Chapman and Hall, London.

Goldstein, R. J. and Timmers J. F., (1982) Visualization of Heat Transfer from Arrays of Impinging Jets, *International Journal of Heat and Mass Transfer*, Vol. 25, pp. 1857-1868.

Hargrave, G. K., Fairweather, M. and Kilham, J. K. (1987) Forced Convective Heat Transfer from Premixed Flames –Part 1L Flame Structure, *International Journal of Heat and Fluid Flow*, Vol. 8, pp. 132-138.

Hargrave, G. K. and Kilham, J. K. (1984) The Effect of Turbulence Intensity on Convective Heat Transfer from premixed Methane-Air Flames, *Institute of Chemical Engineering Symposium Series 2*, pp. 1025-1034.

Hrycak, P. (1983) Heat Transfer from Round Impinging Jets to a Flat Plate, *International Journal of Heat and Mass Transfer*, Vol. 26, pp. 1857-1865.

Hrycak, P. (1981) Heat Transfer from a Row of Impinging Jets to Concave Cylindrical Surfaces, *International Journal of Heat and Mass Transfer*, Vol. 24, pp. 407-419.

Huang, X. Q., (2006) Heat Transfer Characteristics of Impinging Premixed Flame Jet with Induced Swirl, MEng. thesis, The Hong Kong Polytechnic University.

Huber, A. M. (1993) Heat Transfer with Impinging Gaseous Jet Systems, Ph.D. Thesis, Purdue University.

Kataoka, K. (1985) Optimal Nozzle-to-Plate Spacing for Convective Heat Transfer in Nonisothermal, Variable-Density Impinging Jets, *Drying Technology,* Vol. 3, pp. 235-254.

Kataoka, K., (1985) Shundoh, H., and Matsuo, H., (1984). Convective Heat Transfer between a Flat Plate and a Jet of Hot Gas Impinging on It, *Drying '84,* pp. 218-227.

Karlovitz, B., Denniston D. W., Jr., Knapschaefer D. H. and Wells F. E. (1953) Studies on Turbulent Flames, A. Flame Propagation across Velocity Gradients; B. Turbulence Measurement in Flames, *4th Symp. (Int.) on Combustion*, pp. 613-620.

Kilham, J. K. and Purvis, M. R. I. (1971) Heat Transfer From Hydrocarbon-Oxygen Flames, *Combustion and Flame,* Vol. 16, pp. 47-54.

Kilham, J. K. and Purvis, M. R. I. (1978) Heat Transfer From Normally Impinging Flames, *Combustion Science and Technology*, Vol. 18 (3-4), pp. 81-90.

Kilham, J. and Kirmani, N, (1978) The Effect of Turbulence on Premixed Flame Noise, *17th Symposium on Combustion,* The Combustion Institute, pp. 327-336.

Kline, S. J. and McClintock, F. A., (1953) Describing Uncertainties in Single Sample Experiments, *Mechanical Engineering*, Vol. 75, pp3-8.

Kwok, L. C., Leung, C. W. and Cheung, C. S. (2003) Heat Transfer Characteristics of Slot and Round Premixed Impinging Flame Jets, *Experimental Heat Transfer*, Vol. 16, pp. 111-137.

Kwok, L. C., (2003) Studies of the Premixed Butane / Air Impinging Flame Jets, MEng. thesis, The Hong Kong Polytechnic University.

Kwok, L. C., Leung, C. W. and Cheung, C. S. (2005) Heat Transfer Characteristics of an Array of Impinging Pre-mixed Slot Flame Jets, *International Journal of Heat and Mass Transfer*, Vol. 48, pp. 1727-1738.

Law, C. K. and Sung, C. J. (2000) Structure, Aerodynamics, and Geometry of Premixed Flamelets, Progress in Energy and Combustion Science, Vol. 26, pp. 459-505.

Lewis, B. and Von Elbe G. (1987) Combustion, Flames and Explosions of Gases, Academic Press, New York.

Lewis, B. and Von Elbe G. (1942) Stability and Structure of Burner Flames, *Journal of Chemical Physics*, Vol. 11, pp. 75-97.

Lytle, D. and Webb, B. W. (1994), Air jet impingement heat transfer at low nozzle-plate spacings, *International Journal of Heat and Mass Transfer*, Vol. 37, pp. 1687-1697.

Milson, A. and Chigier, N.A., (1973) Studies of Methane and Methane-Air Flames Impinging on a Cold Plate, *Combustion and Flame*, Vol.21, pp. 295-305.

Moffat R. J. (1988) Describing the Uncertainties in Experimental Results, *Experimental Thermal and Fluid Science*, Vol. 1, pp. 3-17.

Mohr, J. W., Seyed-Yagoobi, J., and Page, R. H., (1997) heat Transfer Characteristics of A Radial Jet Reattachment Flame, *Journal of Heat Transfer,* Vol. 119, pp. 258-264.

Mohr, J. W., Seyed-Yagoobi, J., and Page, R. H., (1997) Heat Transfer from a Pair of Radial Jet Reattachment Flames. *Journal of Heat Transfer,* Vol. 119, pp. 633-635.

Popiel, Cz. O., Van der Meer, Th.H. and Hoogendoorn, C. J., (1980) Convective Heat Transfer on A Plate in an Impinging Round Hot Gas Jet of Low Reynolds Number, *International Journal of Heat and Mass Transfer,* Vol. 23, pp.1055-1068.

Posillico, C. J. and Lederman, S. (1989) Laser Diagnostics of Reacting Stagnation Point Flow, *AIAA Journal*, Vol. 27, pp. 67-78.

Reed, S. B. (1967) Flame Stretch – A connecting Principle for Blow-off Data, *Combustion and Flame,* Vol. 11, pp. 177-189.

Riggby, J. R. and Webb, B. W., (1995) An Experimental Investigation of Diffusion Flame Jet Impinging Heat Transfer, *Proceedings of the ASME/JSME Thermal Engineering Joint Conference,* Vol. 3, pp.117-126.

Schulte, E. M. (1972) Impingement Heat Transfer Rates from Torch Flames, *J. Heat transfer*, Vol. 94, pp. 231-233.

Sibulkin, M., (1952) Heat Transfer Near the Forward Stagnation Point at a Body of Revolution. *Journal of Aeronautic Science*, Vol. 19, pp. 570-571.

Sze, L. K., Cheung, C. S. and Leung, C. W. (2004) Temperature Distribution and Heat Transfer Characteristics of an Inverse Diffusion Flame with Circumferentially Arranged Fuel Ports, *International Journal of Heat and Mass Transfer*, Vol. 47, pp. 3119-3129.

Trimis, D., Durst, F., Pickenacker, O. and Pickenacker, K. (1999) Porous medium combustor versus combustion systems with free flames.

Tuttle, S. G. Characterization of local, time-averaged and time-resolved heat transfer from an impinging flame jet, MSc Thesis, Brigham Young University.

Tuttle, S. G., Webb, B. W. and McQuay, M. Q. (2005) Convective heat transfer from a partially premixed impinging flame jet. Part I: Time-averaged results, International Journal of Heat and Mass Transfer, Vol. 48, pp. 1236-1251.

Tuttle, S. G., Webb, B. W. and McQuay, M. Q. (2005) Convective heat transfer from a partially premixed impinging flame jet. Part II: Time-resolved results, International Journal of Heat and Mass Transfer, Vol. 48, pp. 1252-1266.

Van der Meer T. H. (1987) Heat Transfer from Impinging Flama Jets, Ph.D. Thesis, Delft University of Technology, Netherland.

Van der Meer, Th.H., (1991) Stagnation Point Heat Transfer from Turbulent Low Reynolds Number Jets and Flame Jets. *Experimental Thermal and Fluid Science,* Vol. 4, pp. 115-126.

Viskanta R. (1996) Convective and Radiative Flame Jet Impingement Heat Transfer, *The Ninth International Symposium on Transport Phenomena in Thermal-Fluids Engineering,* pp. 46-60.

Viskanta R. (1993) Heat Transfer to Impinging Isothermal Gas and Flame Jets, *Experimental Thermal and Fluid Science,* Vol. 6, pp. 111-134.

Viskanta R. (1991) Enhancement of Heat Transfer in Industrial Combustion Systems: Problems and Future Challenges, *ASME/JSME Thermal Engineering Proceedings,* Vol. 5, pp. 161-173.

Viskanta, R. and Mengus, M. P., (1987) Radiation Heat Transfer in Combustion Systems, *Progress in Energy and Combustion Science,* Vol. 13, pp. 97-160.

Zhao, Z., Wong, T. T. and Leung, C. W. (2004) Impinging premixed butane/air circular laminar flame jet—influence of impingement plate on heat transfer characteristics, International Journal of Heat and Mass Transfer, Vol. 47, pp. 5021-5031.

APPENDIX A. ADIABATIC FLAME TEMPERATURE

When a combustion process is assumed to be an adiabatic, e.g. heat losses to the surroundings are zero and combustion is complete, the flame temperature could be referred to as the adiabatic flame temperature. It is the maximum temperature that can be achieved for given air / mixture. It occurs at stoichiometric ratio.

It might be possible to use the constant adiabatic flame temperature for given equivalence ratio to calculate Nu instead of local flame temperatures that were obtained experimentally.

For example, inverted flames are lean flames, with equivalence ratio being less than unity. Assuming only propane as the main component in LPG / air mixture, the chemical reaction is:

$$bC_3H_8 + 5(0_2 + a\ N_2) \Rightarrow 3\phi CO_2 + 4\phi H_2O + 2(1-\phi)O_2 + 5aN_2 \quad \text{(A.1)}$$

Where $\phi = b$.

The enthalpy of reactants H_1 must be equal to the enthalpy of products H_2. By integrating and assuming that constant heat capacities are constant, it can be obtained:

$$\begin{aligned}&(3\cdot\phi\cdot C_{pk}^{m}\cdot(CO_2)+4\cdot\phi\cdot C_{pk}^{m}\cdot(H_2O)+5\cdot a\cdot C_{pk}^{m}\cdot(N_2)+2\cdot(1-\phi)\cdot C_p\cdot(O_2))\cdot(T_2-T_0)=\\&(\phi\cdot C_{pk}^{m}\cdot(C_3H_8)+5\cdot C_{pk}^{m}\cdot(O_2)+5\cdot a\cdot C_{pk}^{m}\cdot(N_2))\cdot(T_1-T_0)+\phi\cdot Q_m\end{aligned} \quad \text{(A.2)}$$

Where Q_m is molar heat of reaction (J), C_p is heat capacity (J/moleK), T_0 is the reference temperature (T_0 = 298.15 K), T_1 is reactant temperature (K) and T_2 is

flame temperature. A = 3.76 moles of N_2 for one mole of O_2 in air. Consequently, adiabatic flame temperature can be calculated from Eq. A.2 as:

$$T_2 = \frac{(50 \cdot \phi + 683) \cdot (T_1 - T_0) + Q_m \cdot \phi}{207 \cdot \phi + 683} \tag{A.3}$$

In our case, ϕ = 0.9, for T_1 = 300 K and Q_m = 2073 kJ, adiabatic flame temperature T_2 = 2148 K (= 1850^0C). By modifying equation for Nusselt number calculation (Eq. 2.12), it can be written as:

$$Nu_{adb} = \frac{\dot{q} \cdot d_e}{(T_2 - T_s) k(\tilde{T})} \tag{A.4}$$

Figures A.1 – A.3 compare Nusselt number distributions at adiabatic flame temperature, with Nusselt numbers obtained from experimental data. It is evident that the use of adiabatic flame temperature (as the reference flame temperature) shifts the whole range of Nu numbers by a factor ½.

In case of radial Nu distributions, the adiabatic Nusselt numbers are more flattened in comparison with the experimental values at both ends. Adiabatic Nu distributions at stagnation point, stagnation circle and maximum values show similar patterns as the experimental Nu distributions. The same applies to area-averaged Nu distributions.

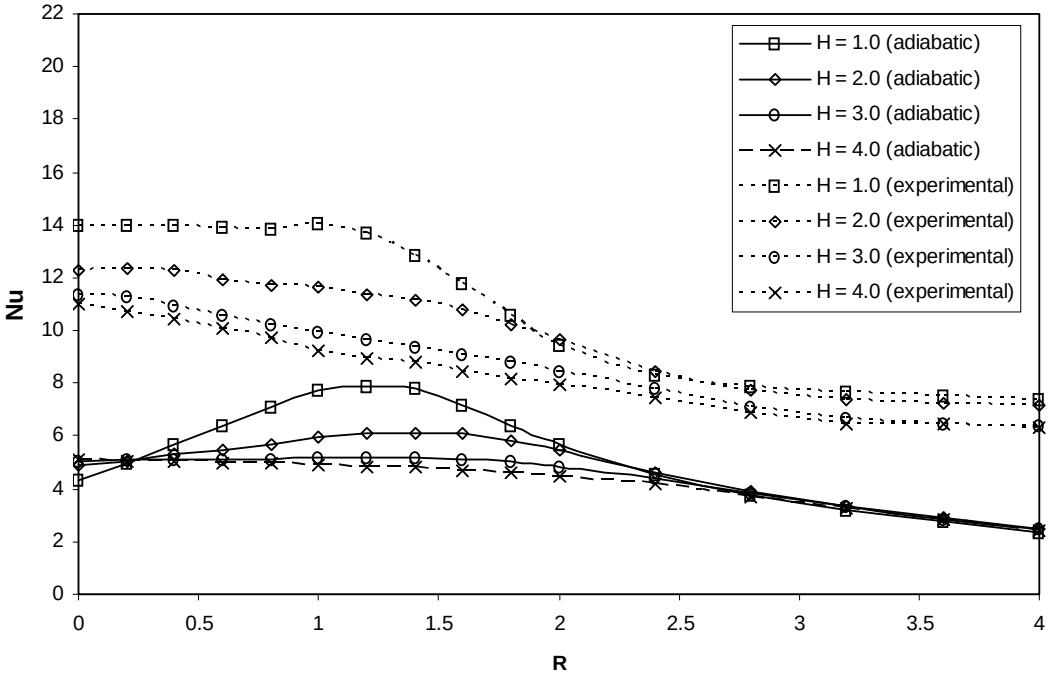

Figure A.1. Comparison of radial *Nu* distributions with experimental and adiabatic flame temperatures for various *H* at $\Phi = 0.9$, $Re = 2000$, $B_R = 0$, $B_T = 0.51$.

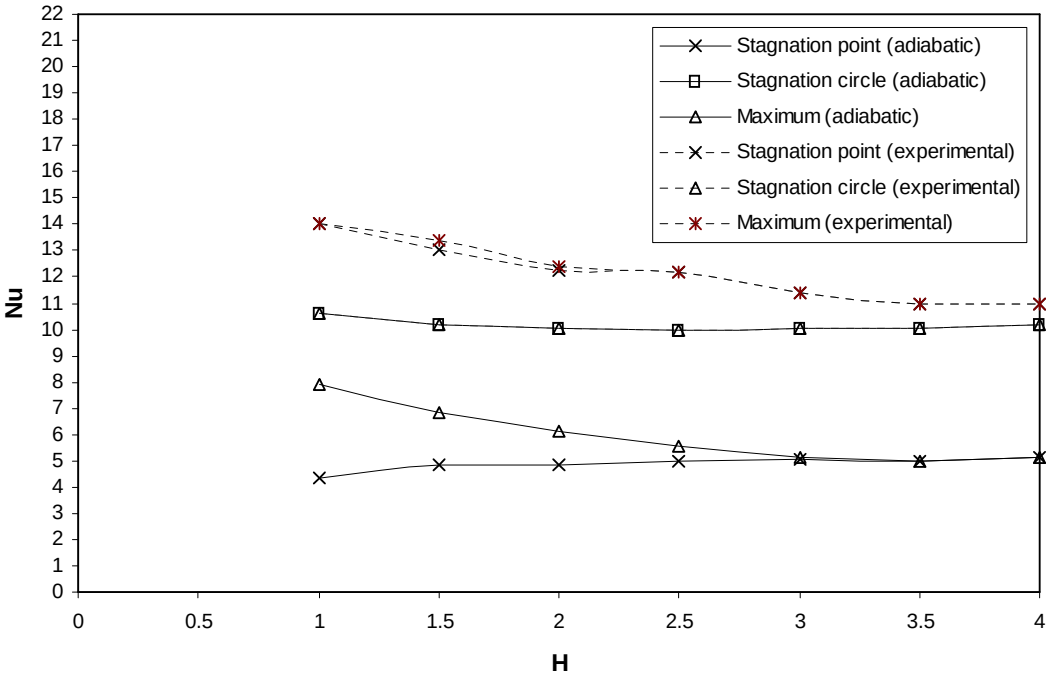

Figure A.2. Comparison of *Nu* distributions with experimental and adiabatic flame temperatures for various *H* at stagnation point, stagnation circle and maximum *Nu* at $\Phi = 0.9$, $Re = 2000$, $B_R = 0$, $B_T = 0.51$.

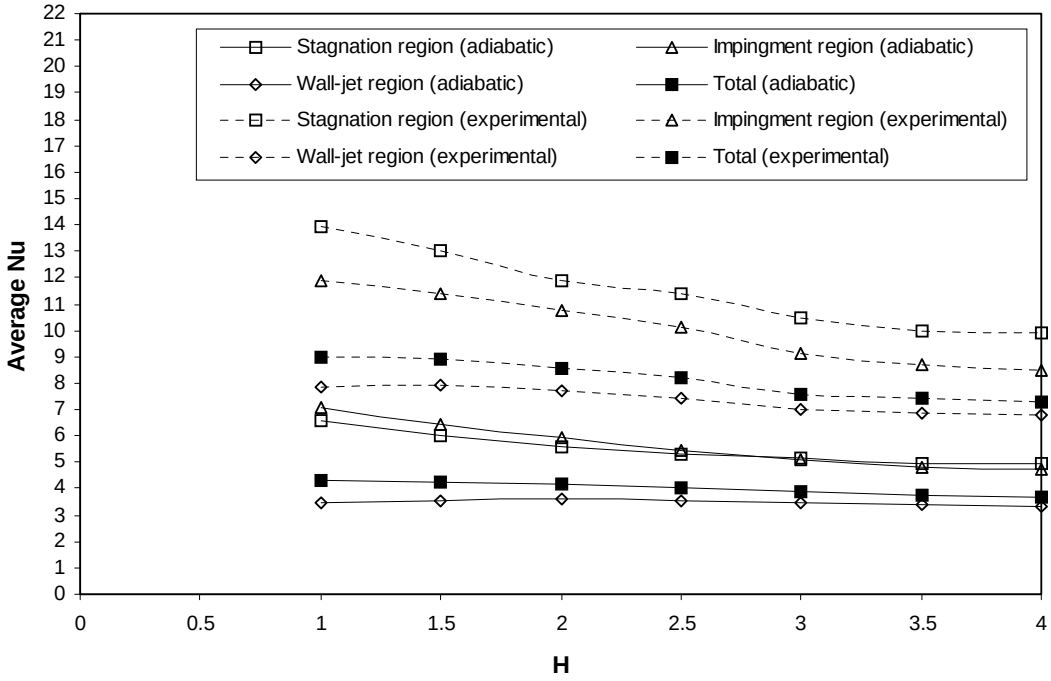

Figure A.3. Comparison of average *Nu* distributions with experimental and adiabatic flame temperatures for various *H* at different impingement regions at $\Phi = 0.9$, $Re = 2000$, $B_R = 0$, $B_T = 0.51$.

APPENDIX B. EMPIRICAL HEAT TRANSFER CORRELATIONS FIGURES

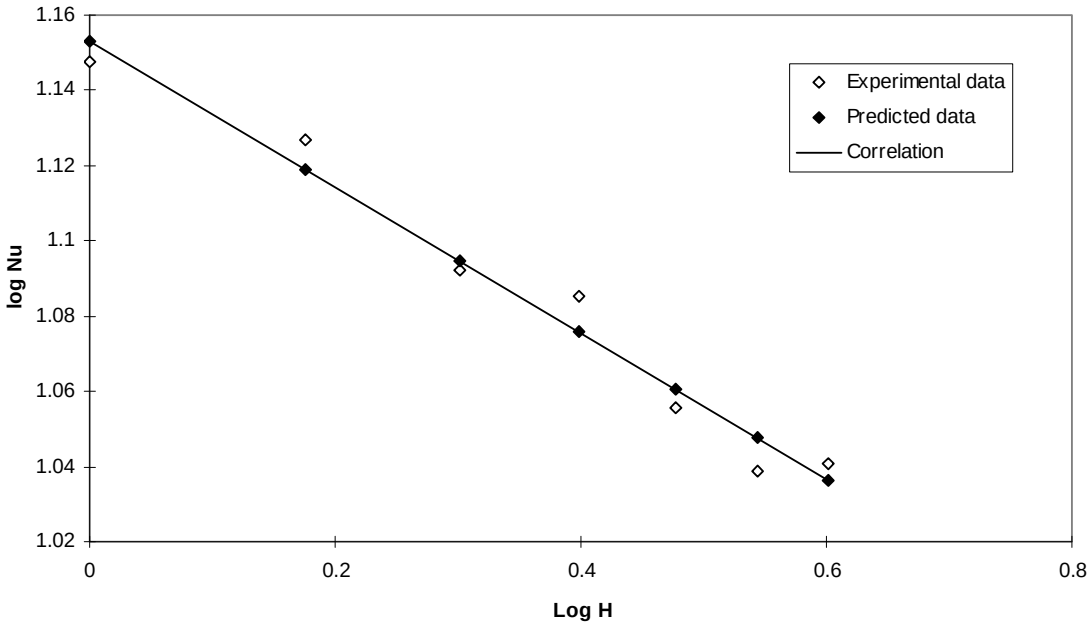

Figure 7.1. Maximum Nu prediction for inverted flames: correlation of H.

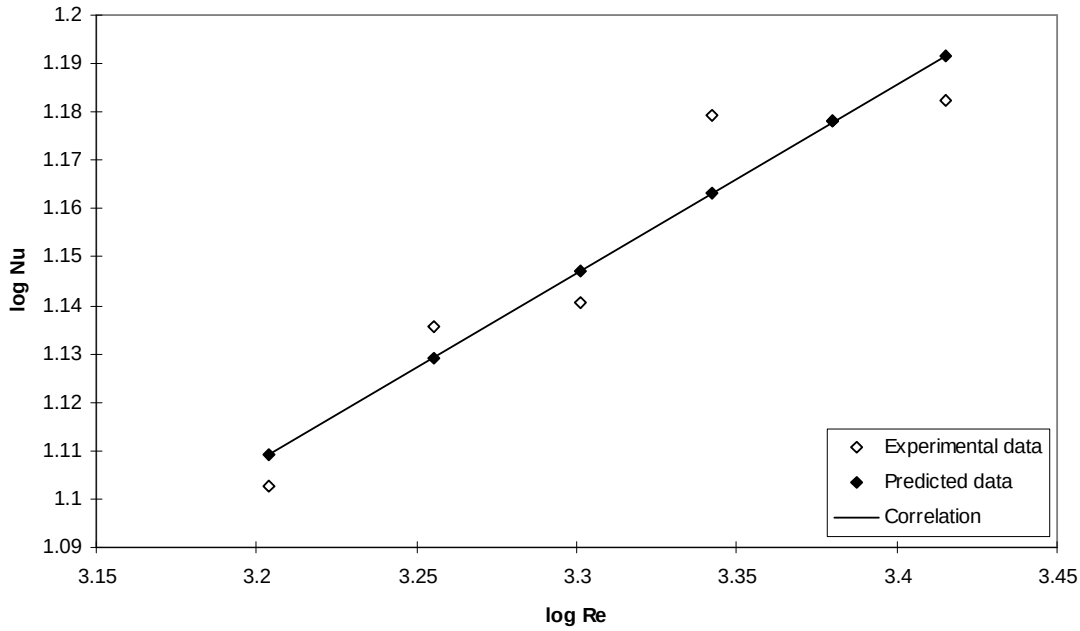

Figure 7.2. Maximum Nu prediction for inverted flames: correlation of Re.

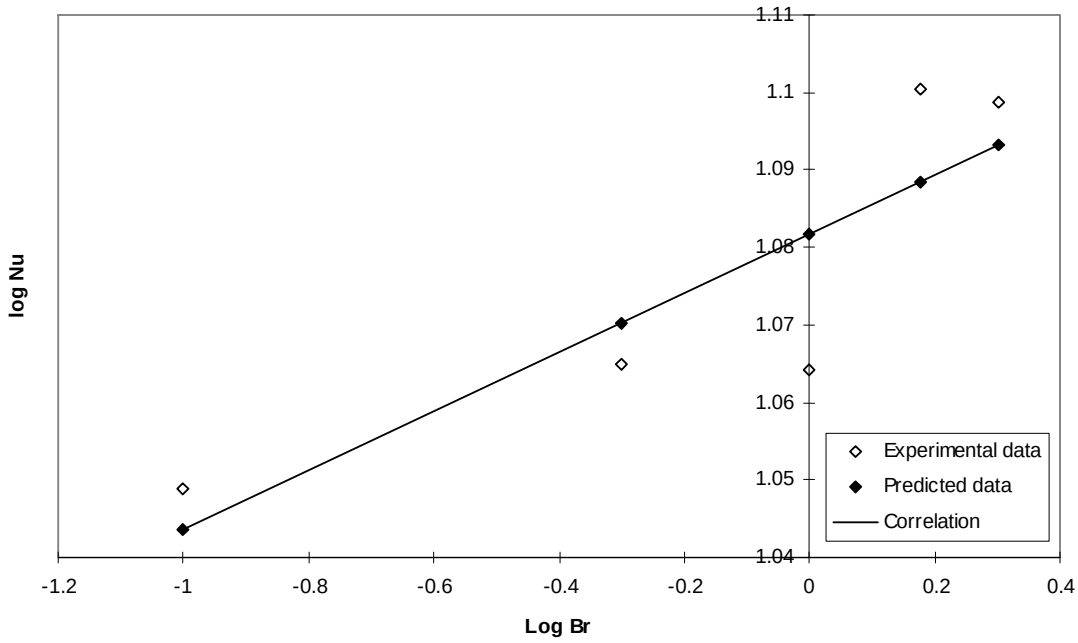

Figure 7.3. Maximum Nu prediction for inverted flames: correlation of B_R.

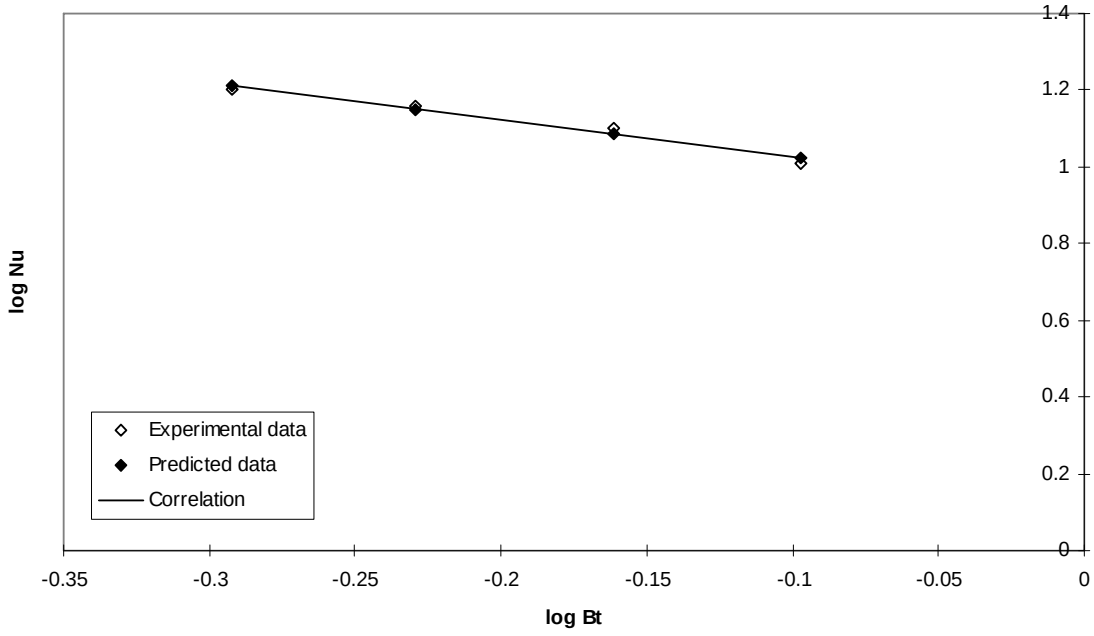

Figure 7.4. Maximum Nu prediction for inverted flames: correlation of B_T.

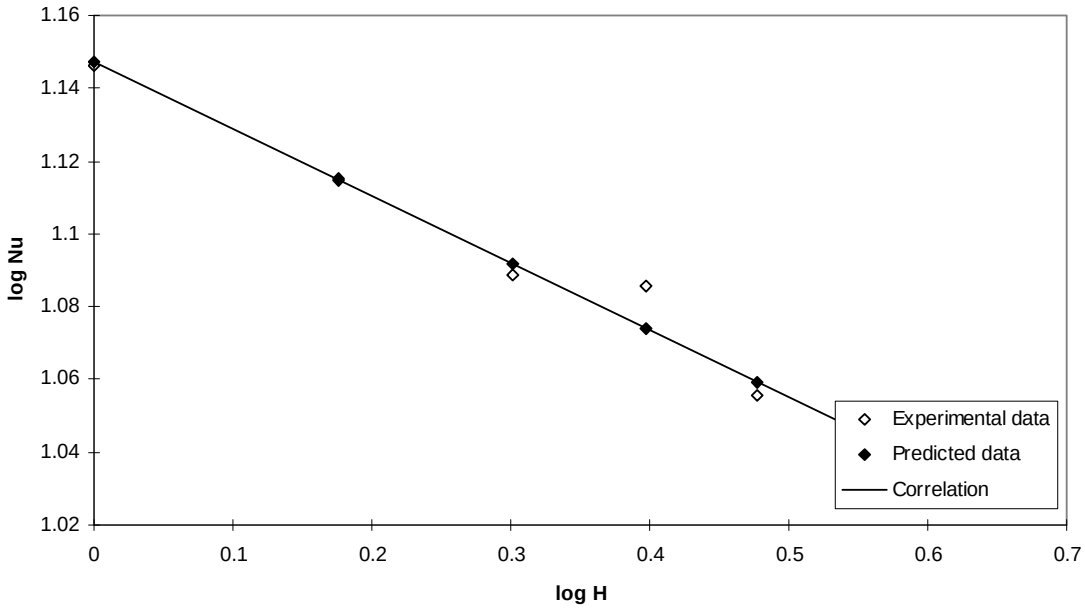

Figure 7.5. Stagnation point Nu prediction for inverted flames: correlation of H.

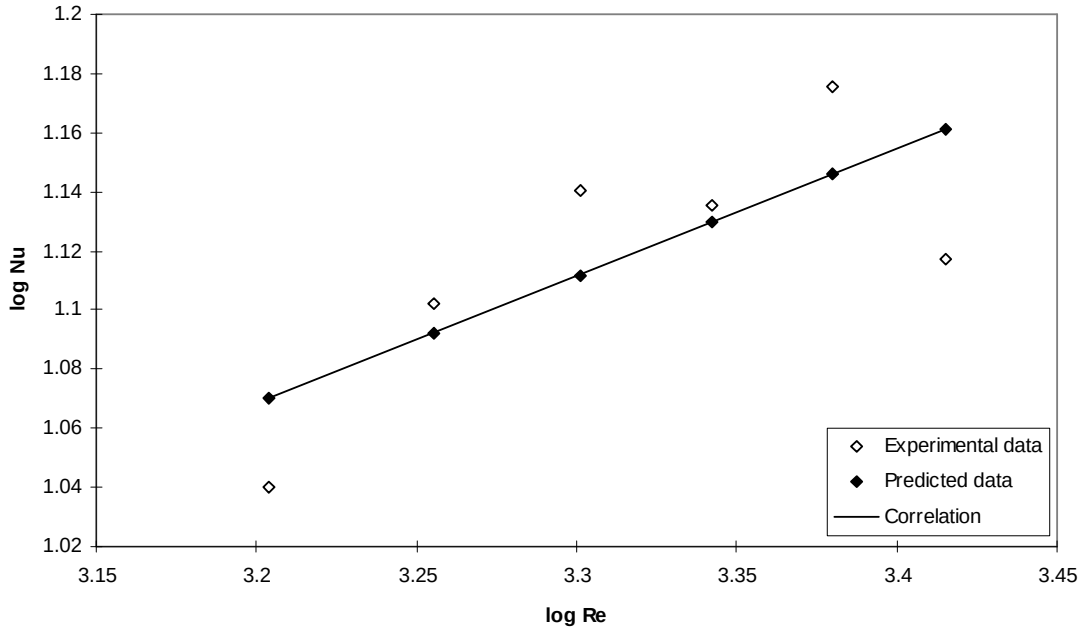

Figure 7.6. . Stagnation point Nu prediction for inverted flames: correlation of Re.

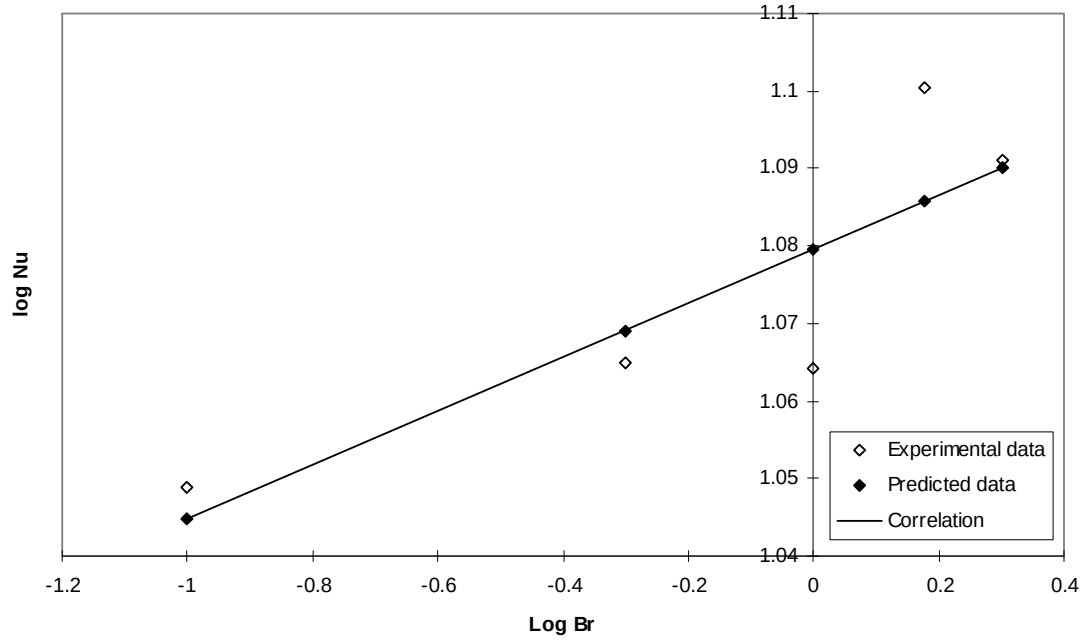

Figure 7.7. Stagnation point Nu prediction for inverted flames: correlation of B_R.

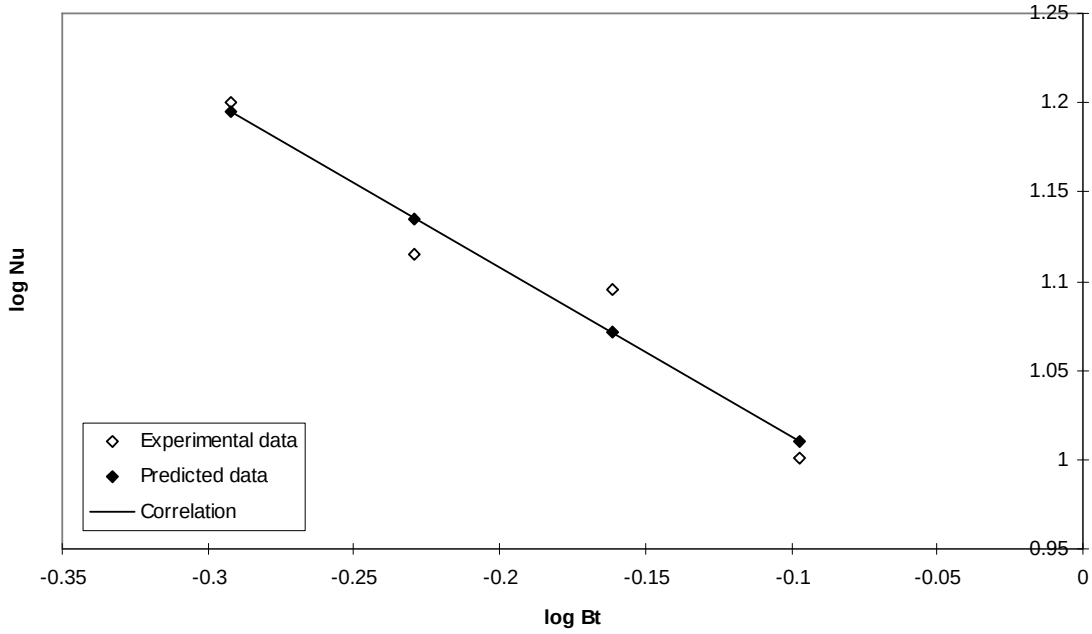

Figure 7.8. Stagnation point Nu prediction for inverted flames: correlation of B_T.

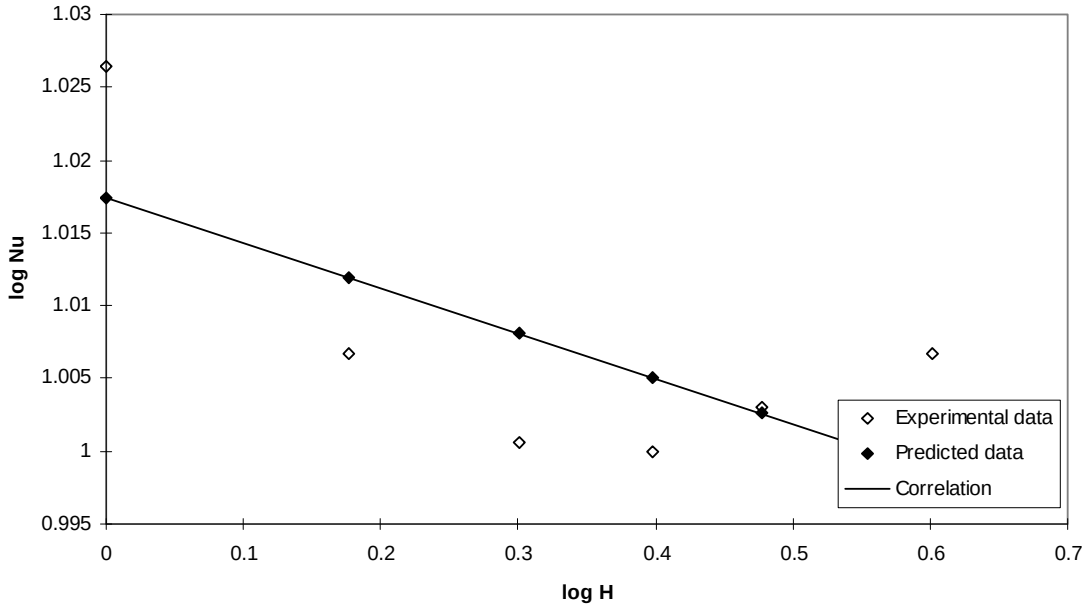

Figure 7.9. Stagnation circle Nu prediction for inverted flames: correlation of H.

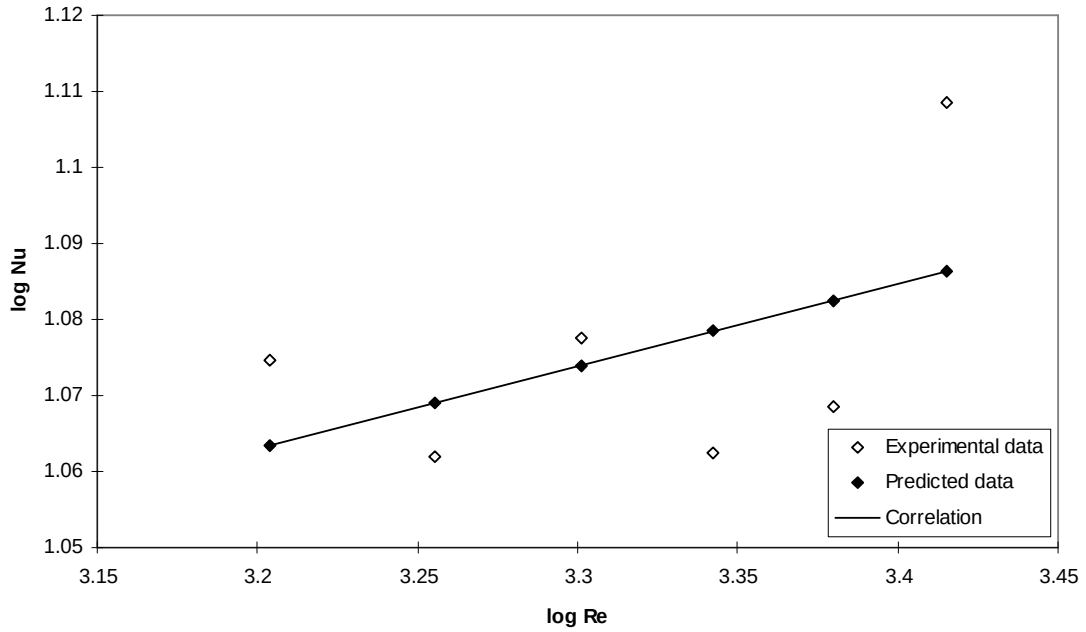

Figure 7.10. Stagnation circle Nu prediction for inverted flames: correlation of Re.

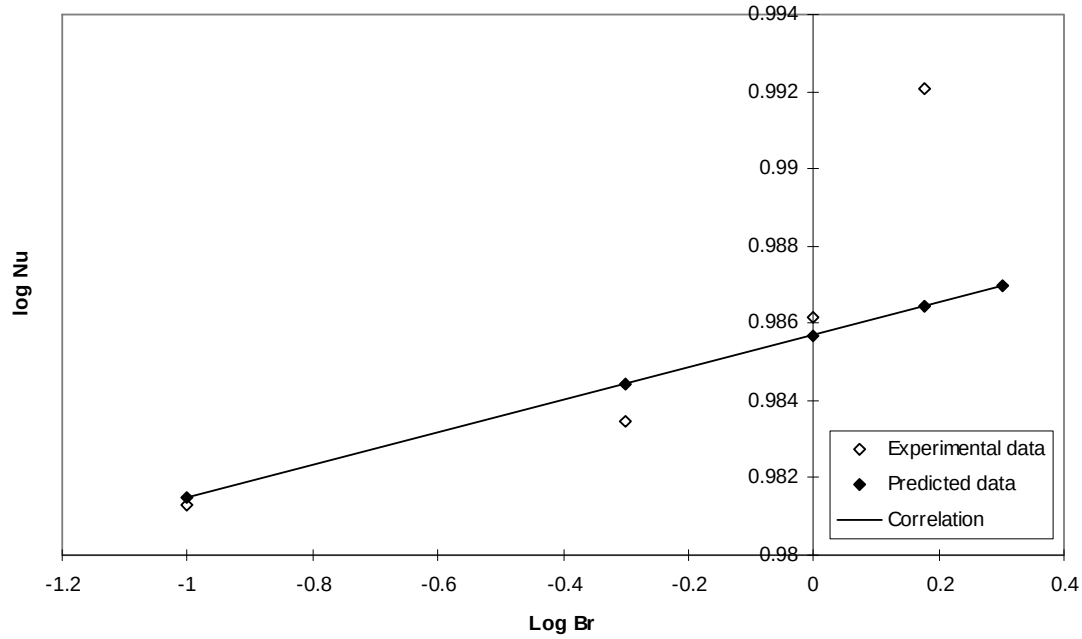

Figure 7.11. Stagnation circle Nu prediction for inverted flames: correlation of B_R.

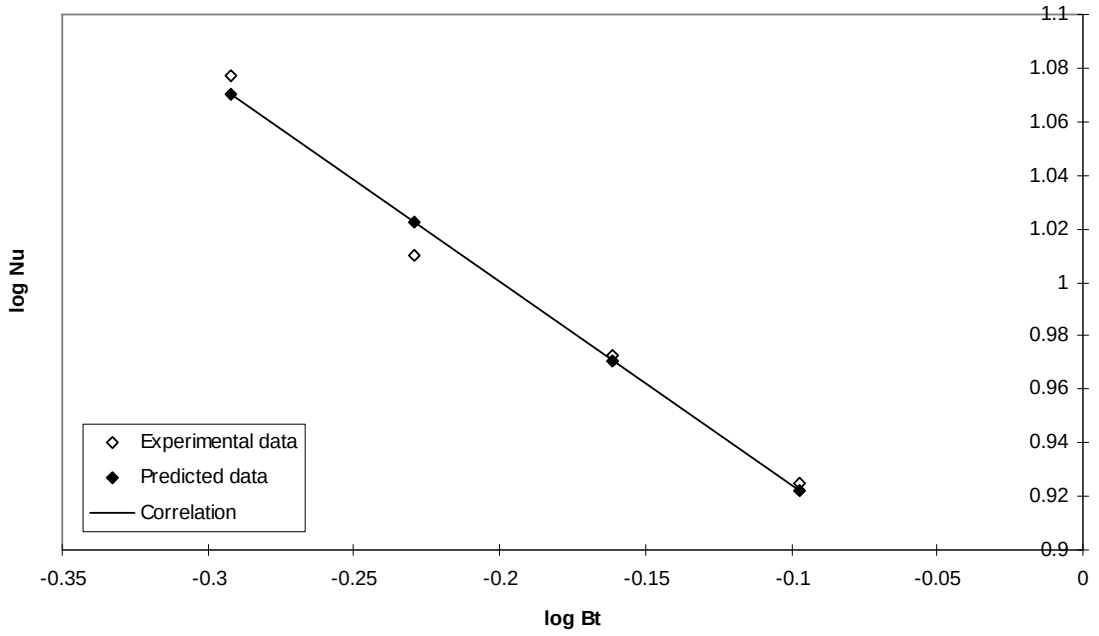

Figure 7.12. Stagnation circle Nu prediction for inverted flames: correlation of B_T.

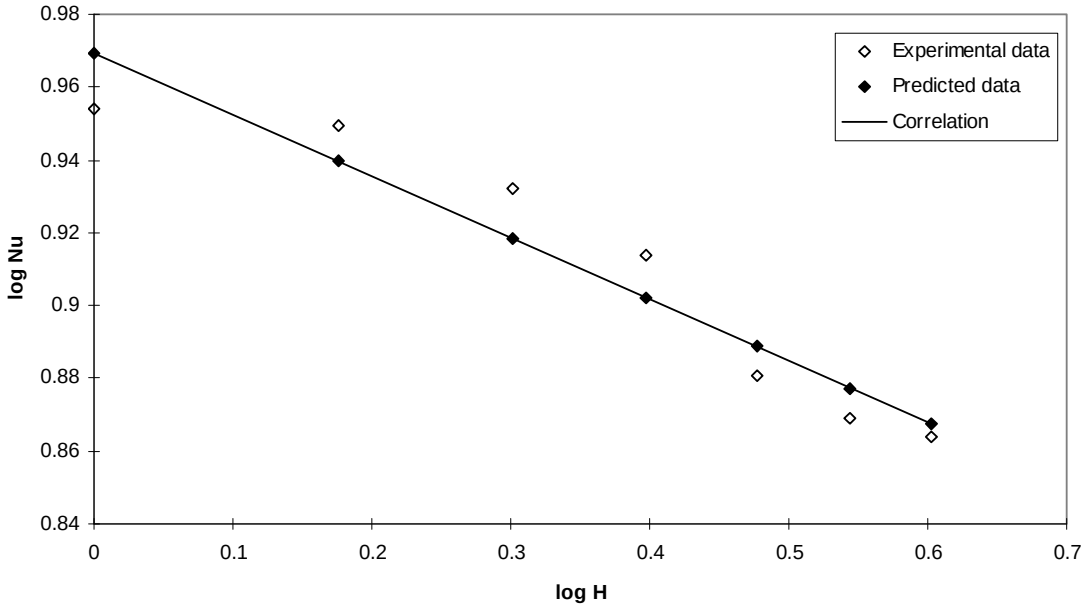

Figure 7.13. Total area-averaged Nu prediction for inverted flames: correlation of H.

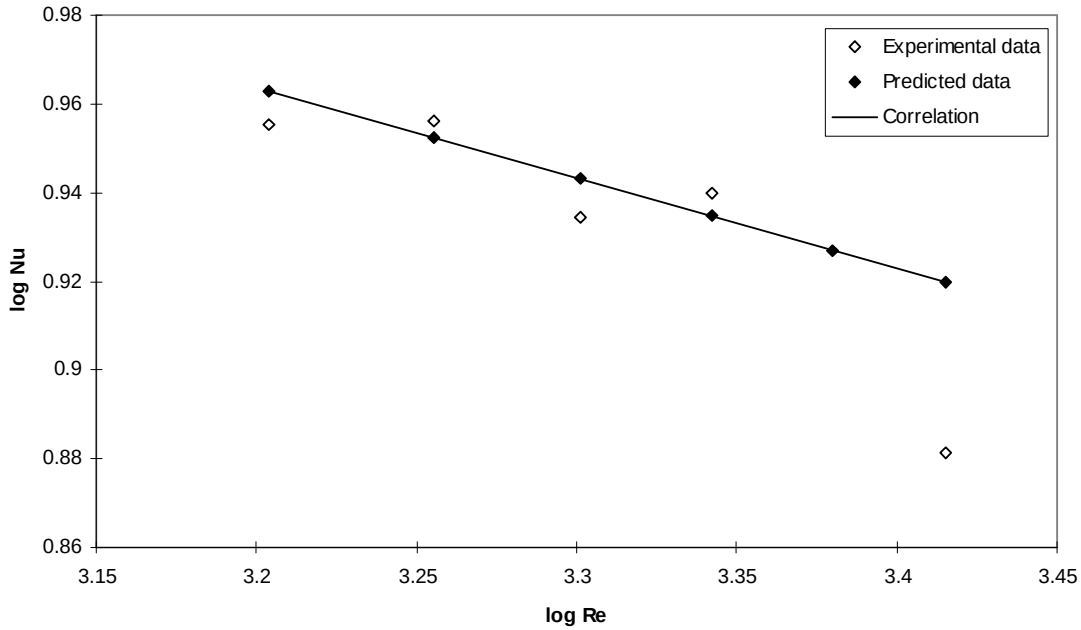

Figure 7.14. Total area-averaged Nu prediction for inverted flames: correlation of Re.

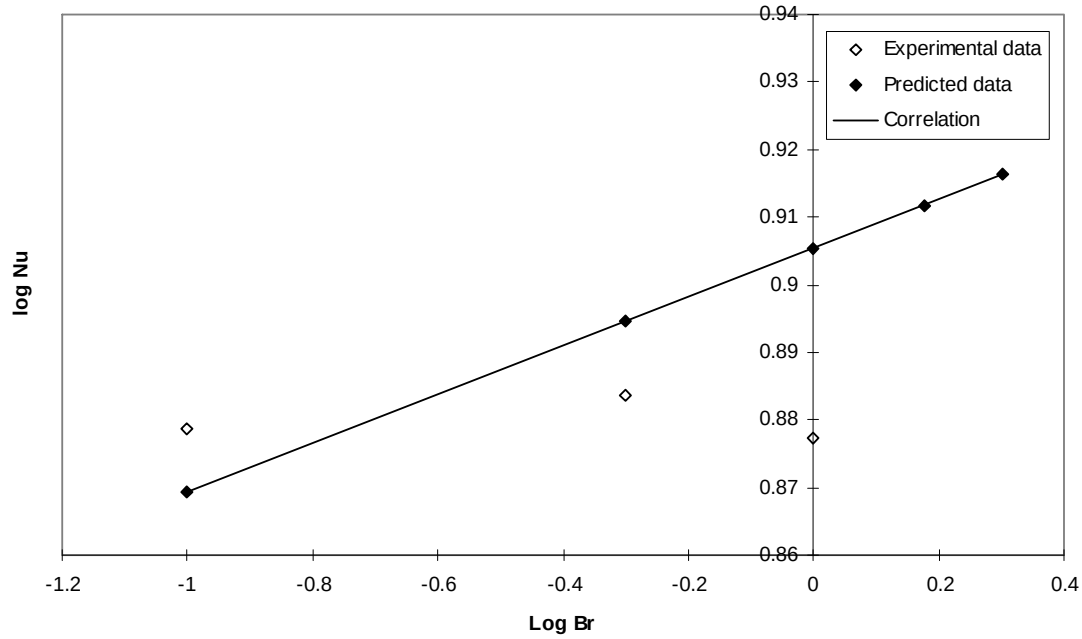

Figure 7.15. Total area-averaged Nu prediction for inverted flames: correlation of B_R.

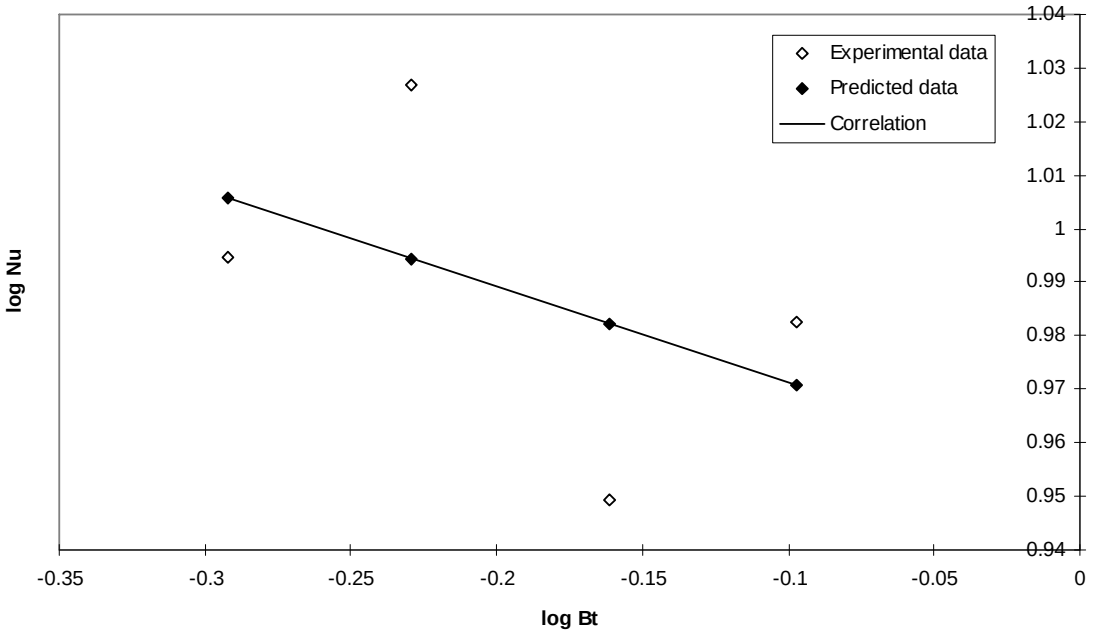

Figure 7.16. Total area-averaged Nu prediction for inverted flames: correlation of B_T.

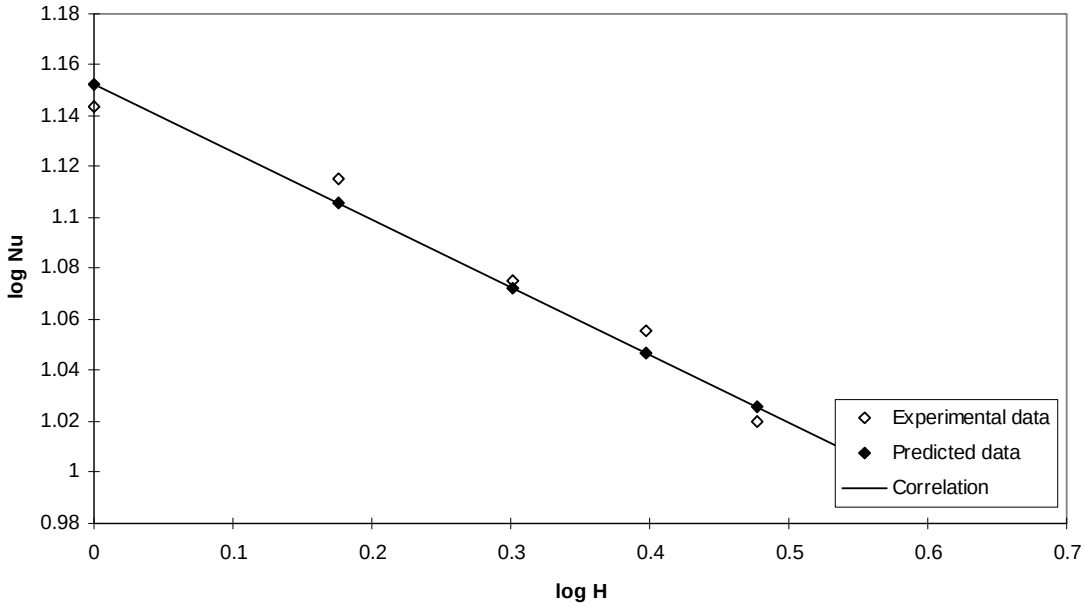

Figure 7.17. Stagnation region area-averaged Nu prediction for inverted flames: correlation of H.

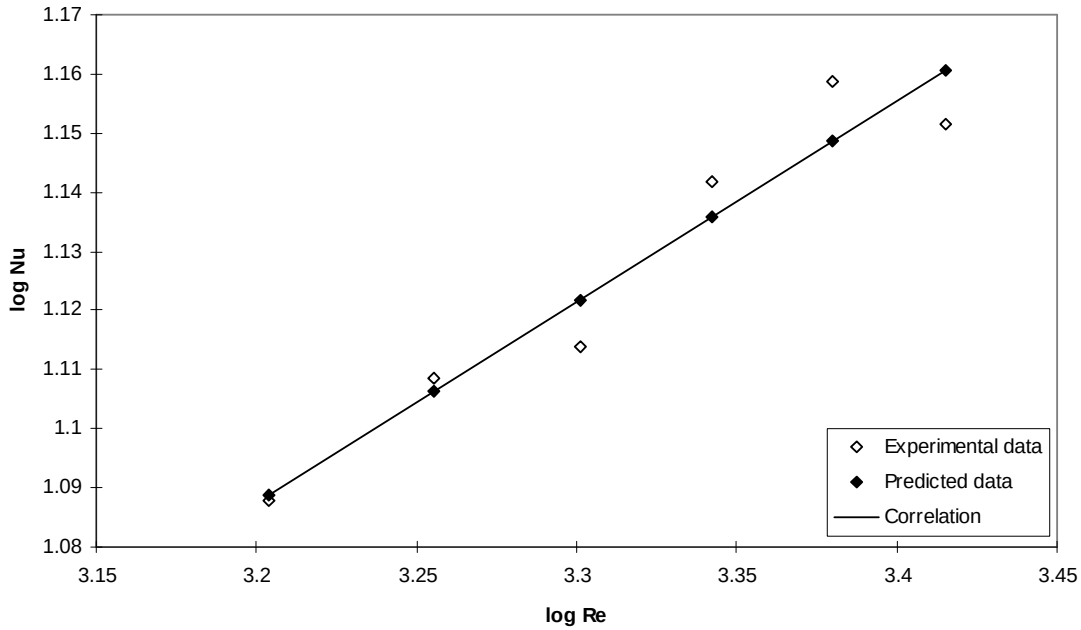

Figure 7.18. Stagnation region area-averaged Nu prediction for inverted flames: correlation of Re.

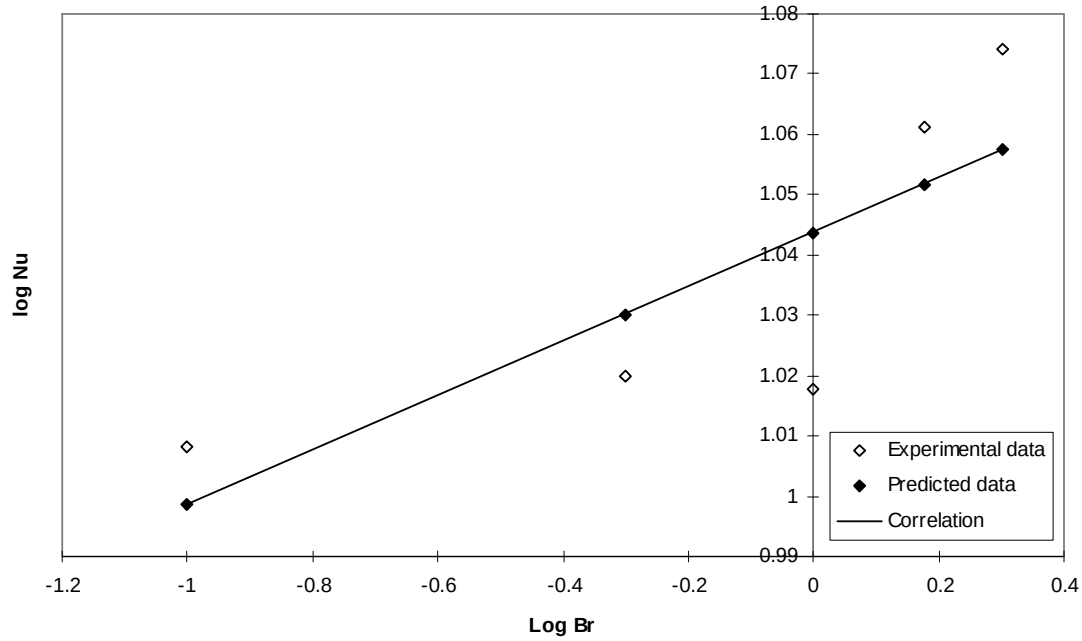

Figure 7.19. Stagnation region area-averaged Nu prediction for inverted flames: correlation of B_R.

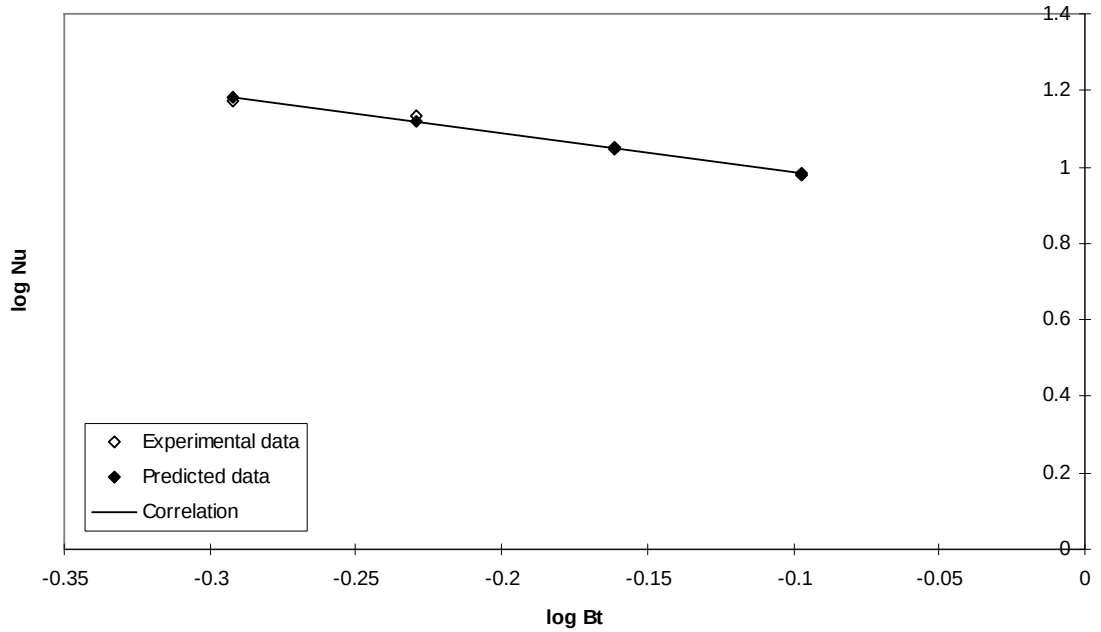

Figure 7.20. Stagnation region area-averaged Nu prediction for inverted flames: correlation of B_T.

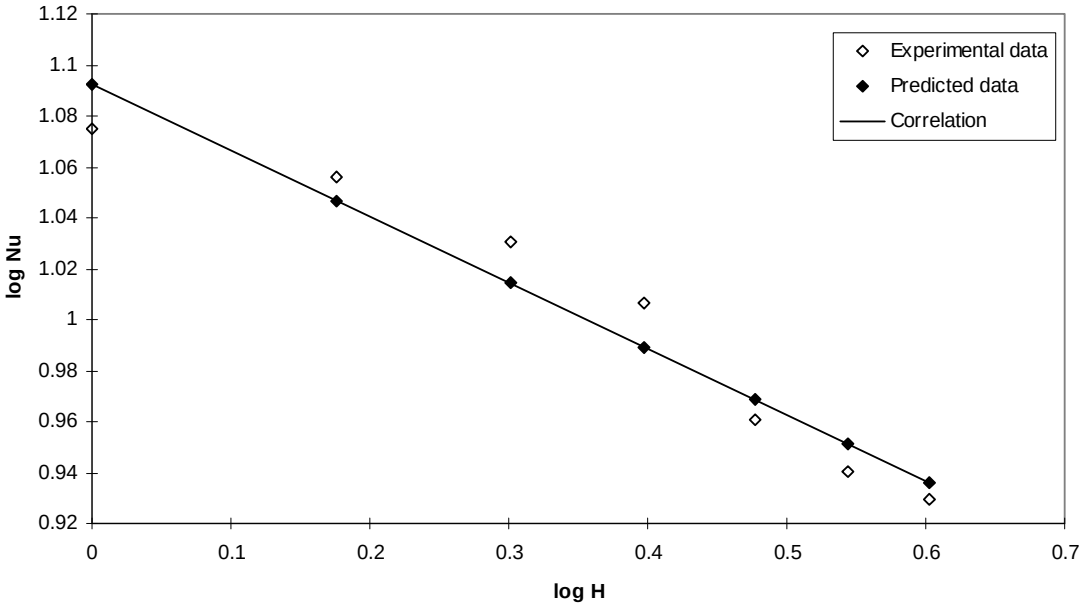

Figure 7.21. Impingement region area-averaged Nu prediction for inverted flames: correlation of H.

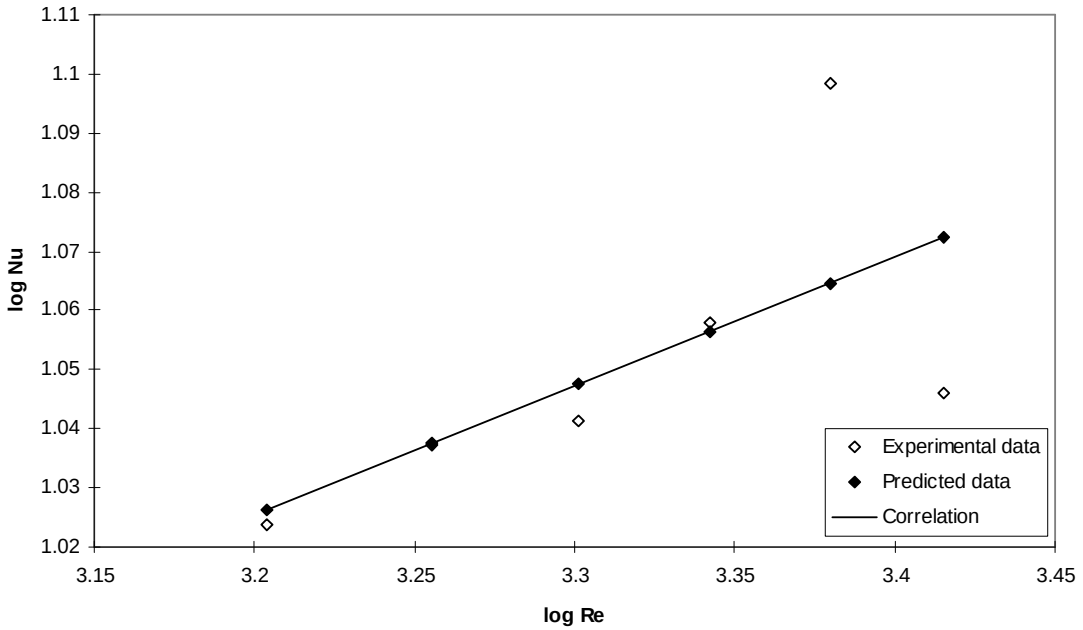

Figure 7.22. Impingement region area-averaged Nu prediction for inverted flames: correlation of Re.

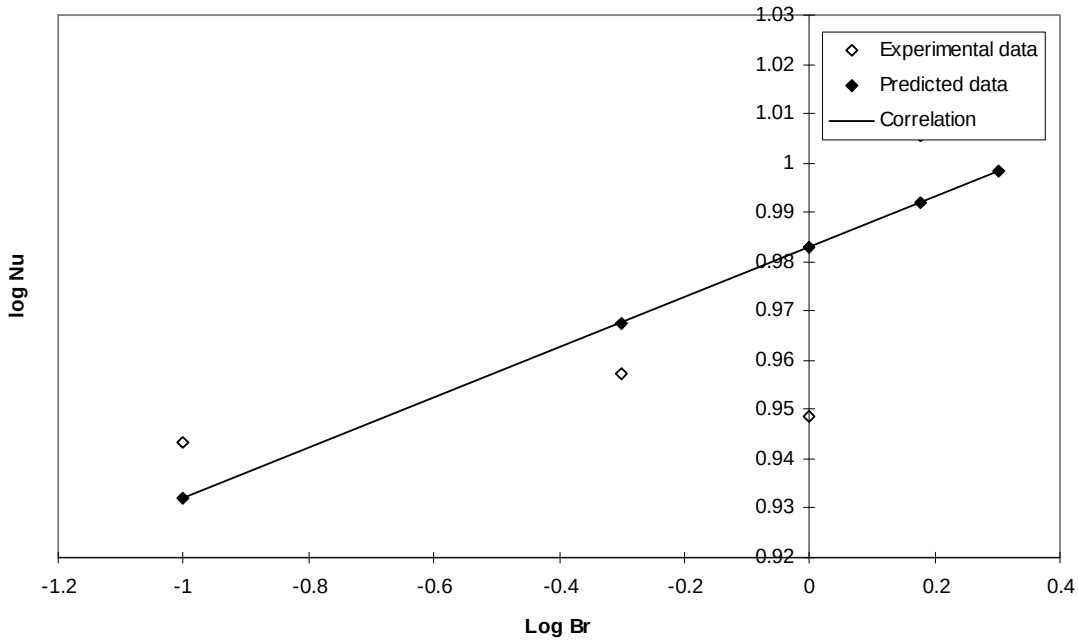

Figure 7.23. Impingement region area-averaged Nu prediction for inverted flames: correlation of B_R.

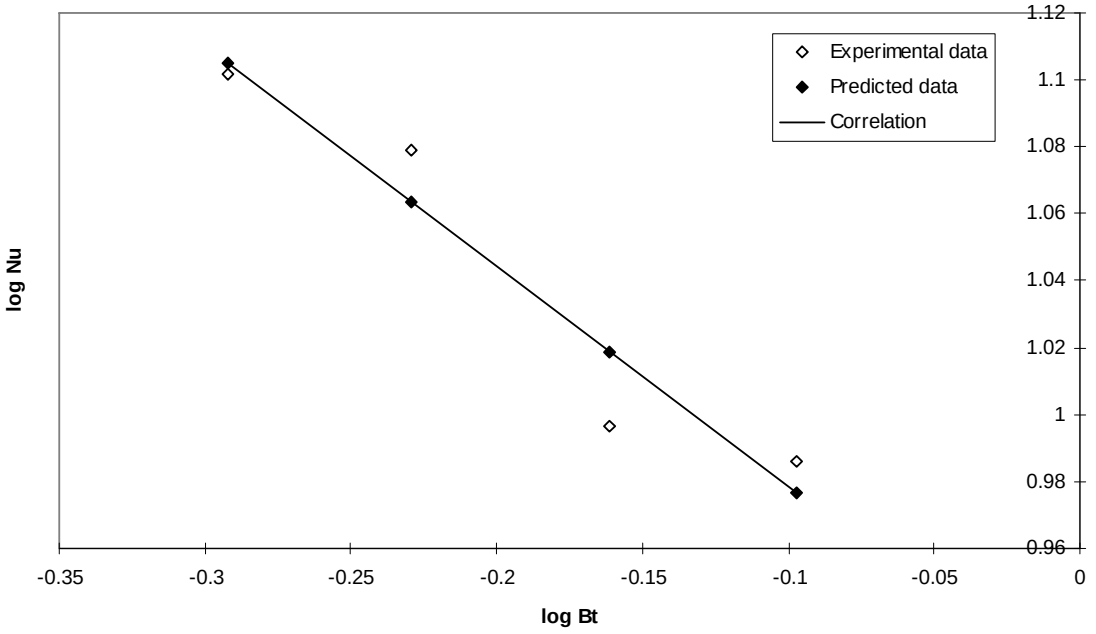

Figure 7.24. Impingement region area-averaged Nu prediction for inverted flames: correlation of B_T.

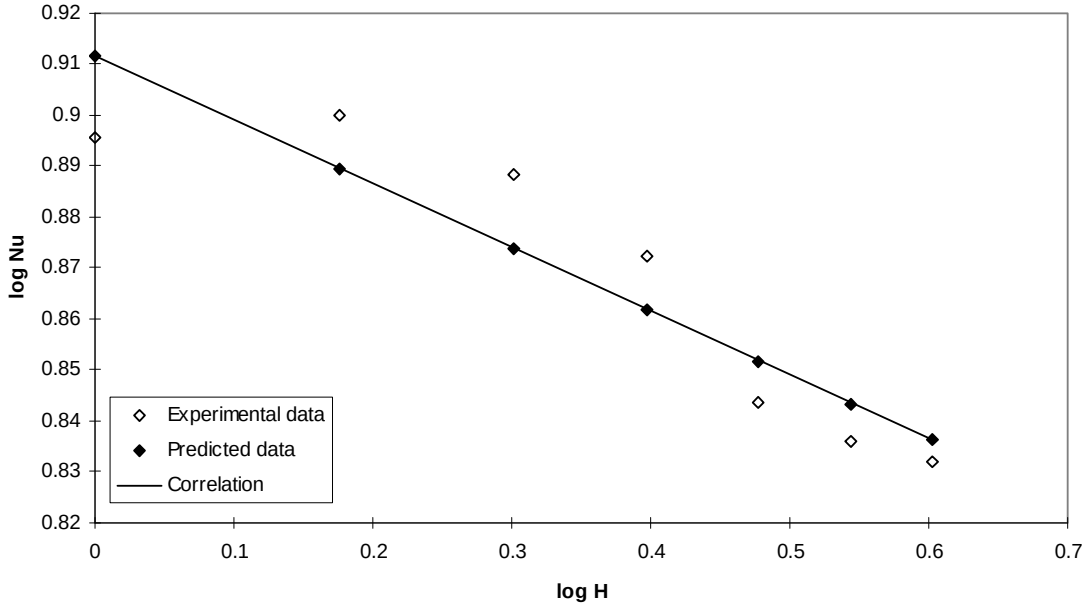

Figure 7.25. Wall-jet region area-averaged Nu prediction for inverted flames: correlation of H.

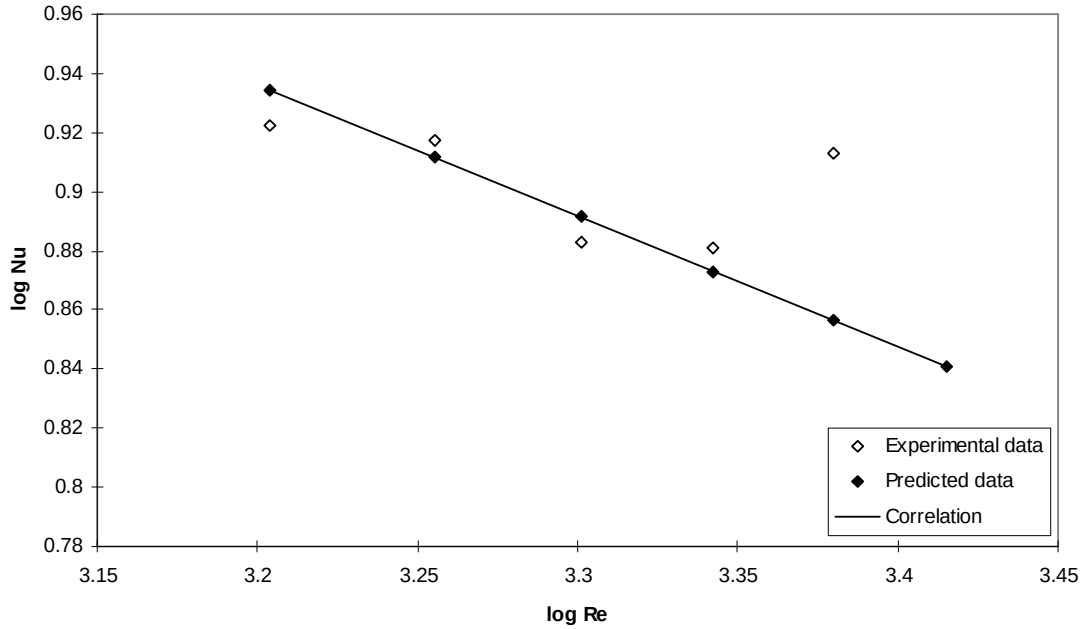

Figure 7.26. Wall-jet region area-averaged Nu prediction for inverted flames: correlation of Re.

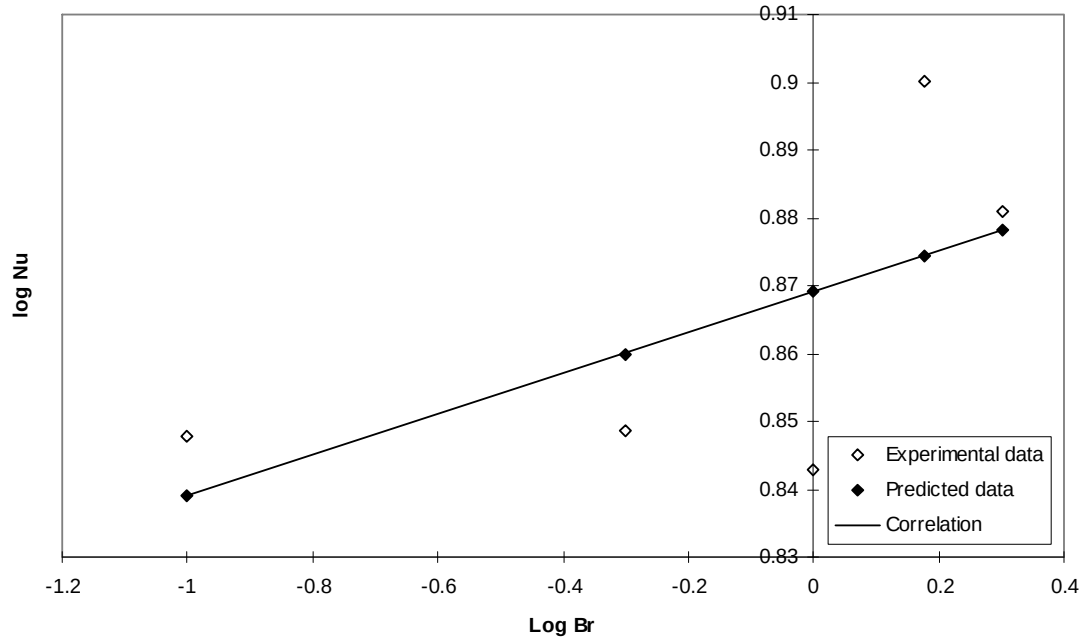

Figure 7.27. Wall-jet region area-averaged Nu prediction for inverted flames: correlation of B_R.

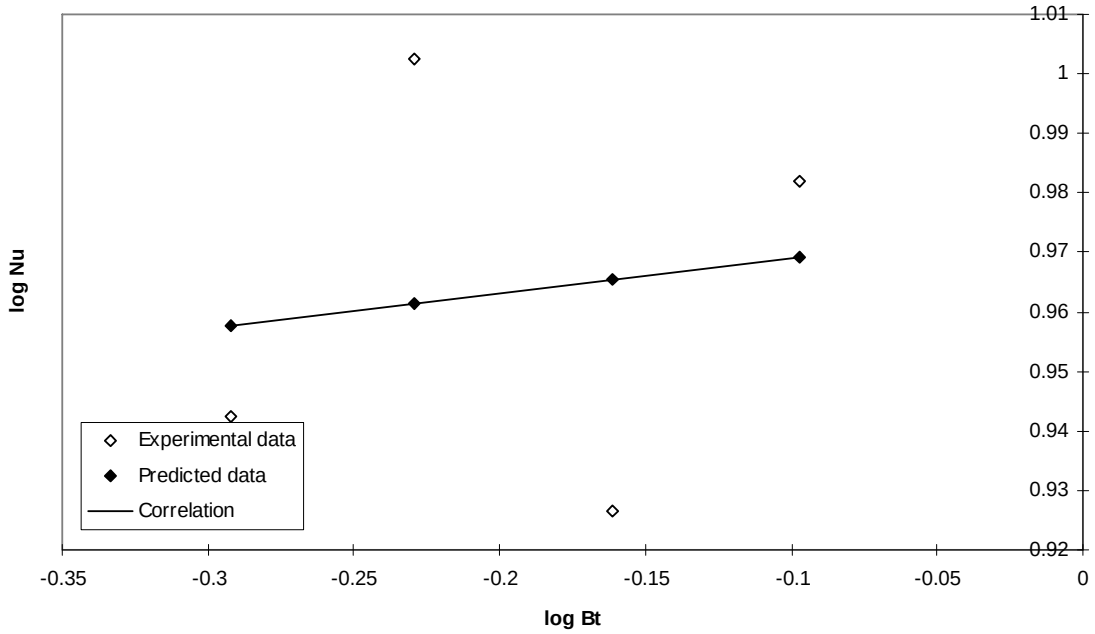

Figure 7.28. Wall-jet region area-averaged Nu prediction for inverted flames: correlation of B_T.

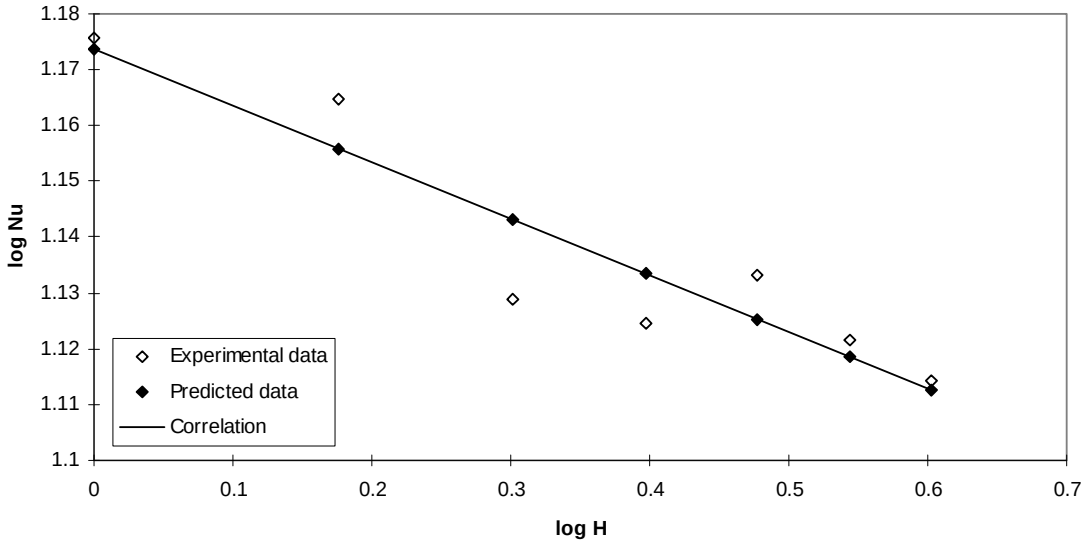

Figure 7.29. Maximum Nu prediction for partially-inverted flames: correlation of H.

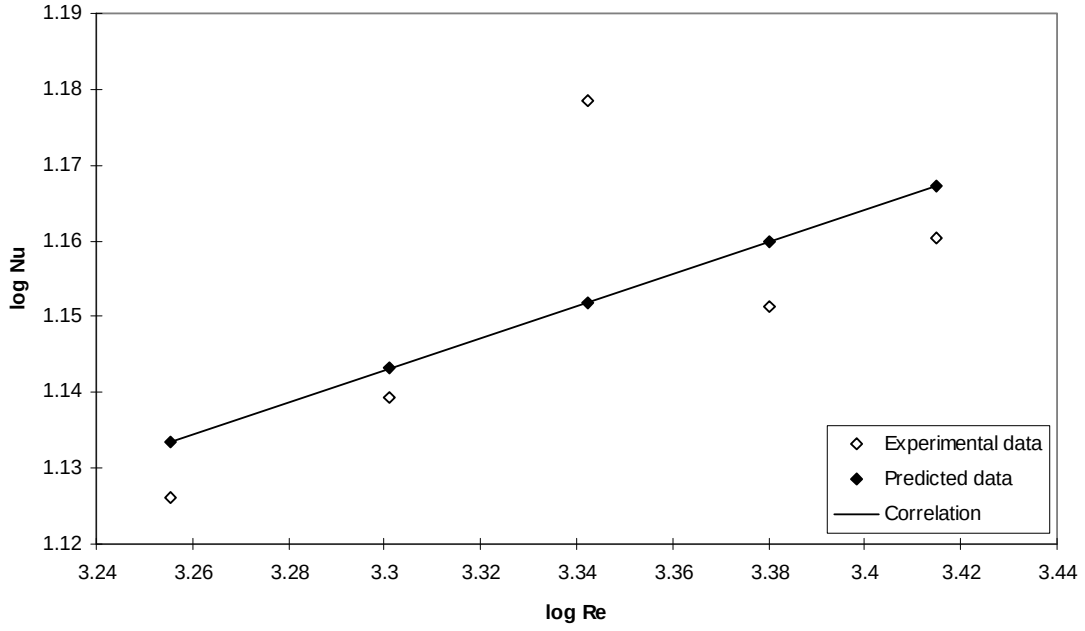

Figure 7.30. Maximum Nu prediction for partially-inverted flames: correlation of Re.

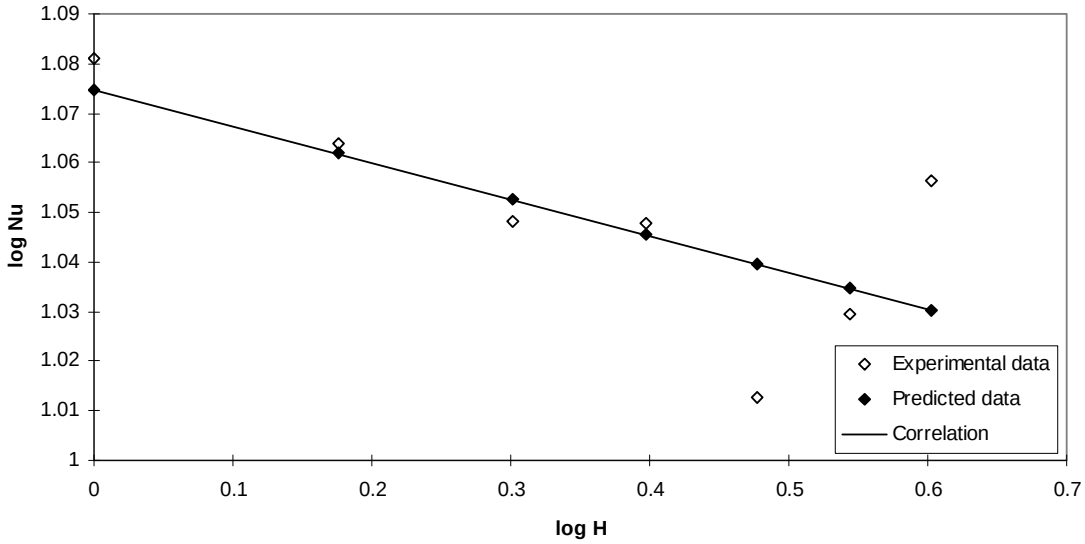

Figure 7.31. Stagnation point Nu prediction for partially-inverted flames: correlation of H.

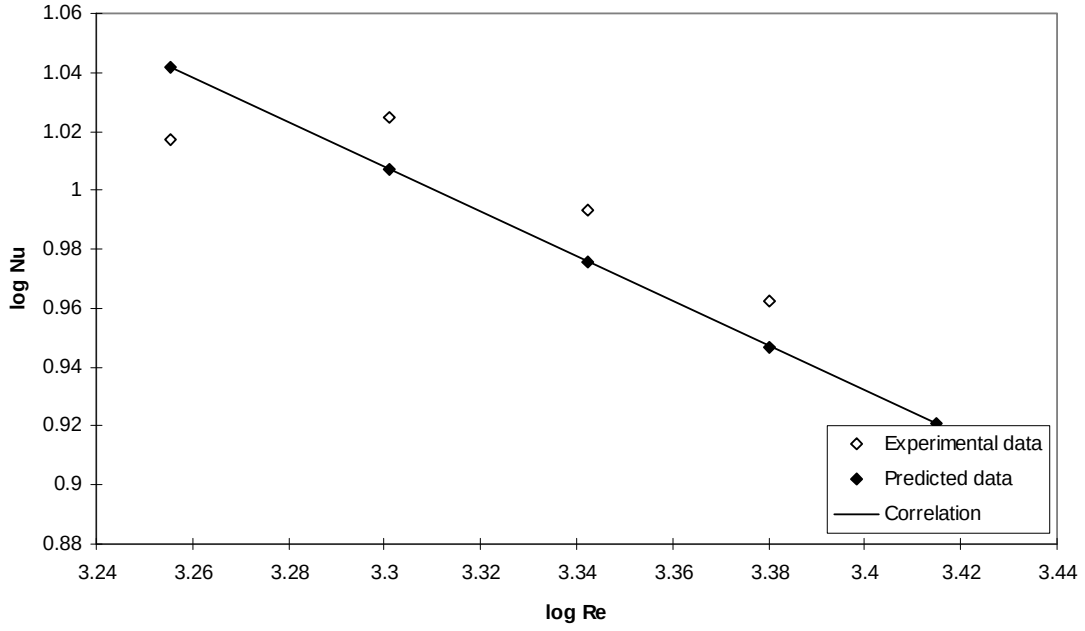

Figure 7.32. Stagnation point Nu prediction for partially-inverted flames: correlation of Re.

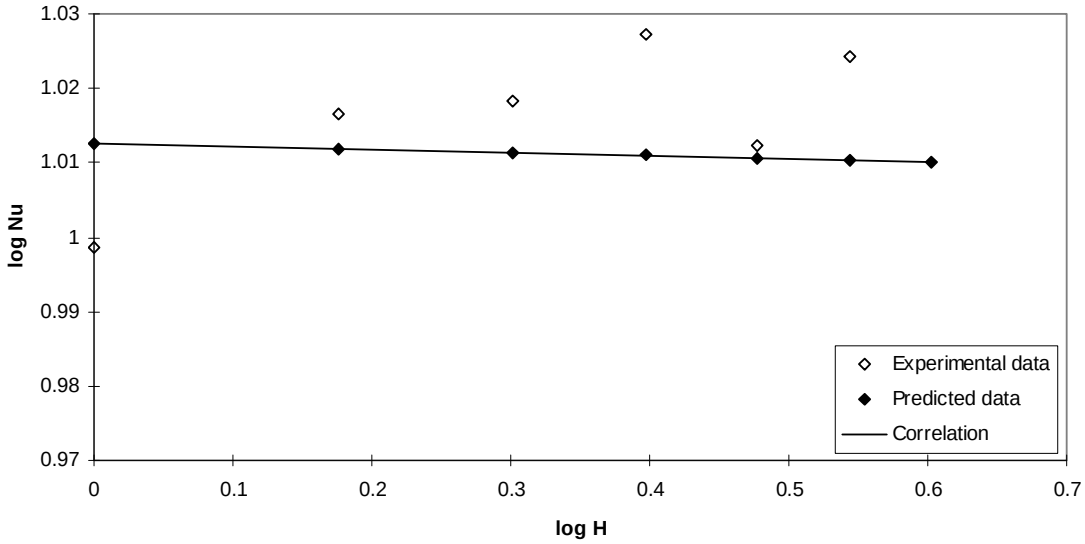

Figure 7.33. Stagnation circle Nu prediction for partially-inverted flames: correlation of H.

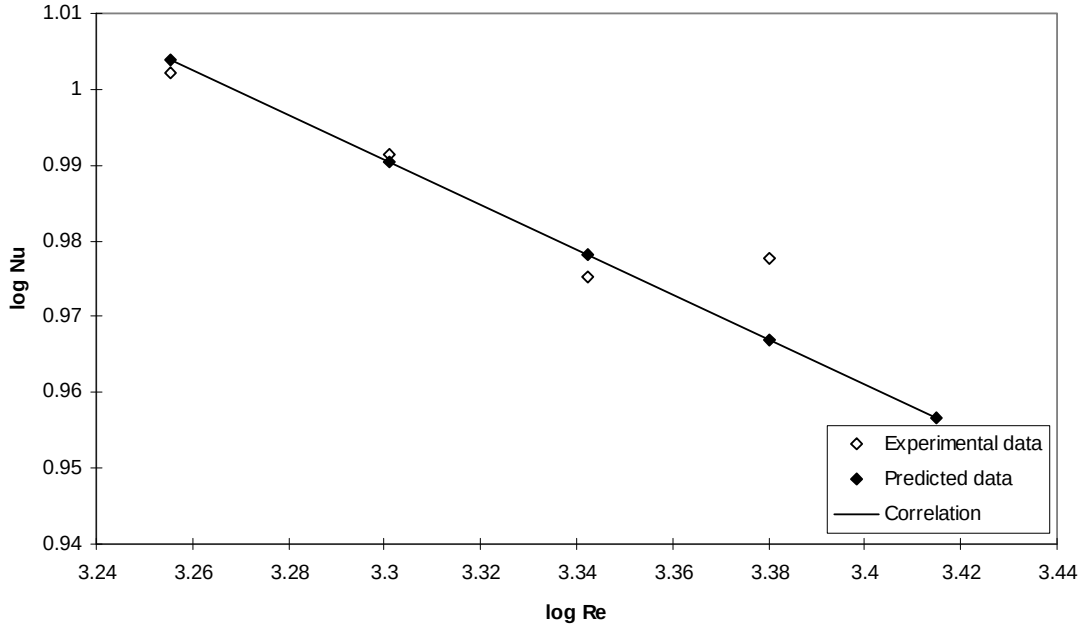

Figure 7.34. Stagnation circle Nu prediction for partially-inverted flames: correlation of Re.

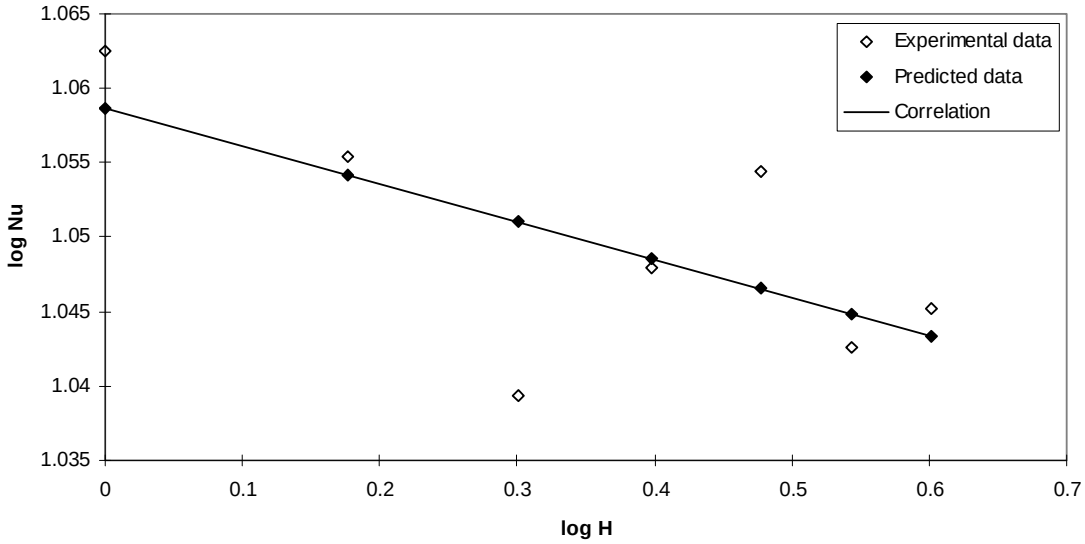

Figure 7.35. Total area-averaged Nu prediction for partially-inverted flames: correlation of H.

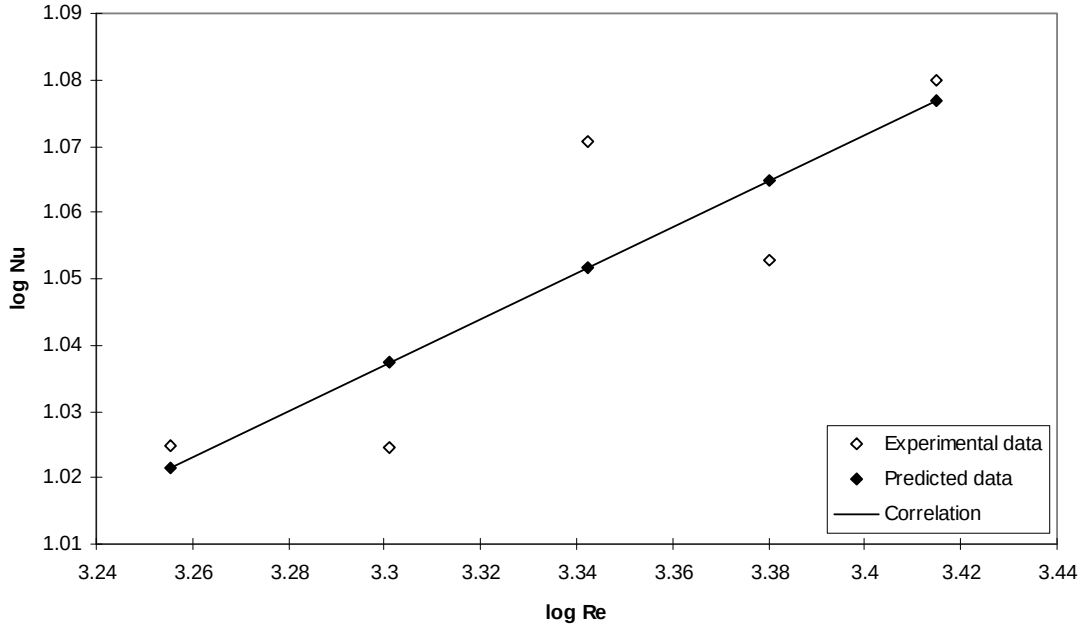

Figure 7.36. Total area-averaged Nu prediction for partially-inverted flames: correlation of Re.

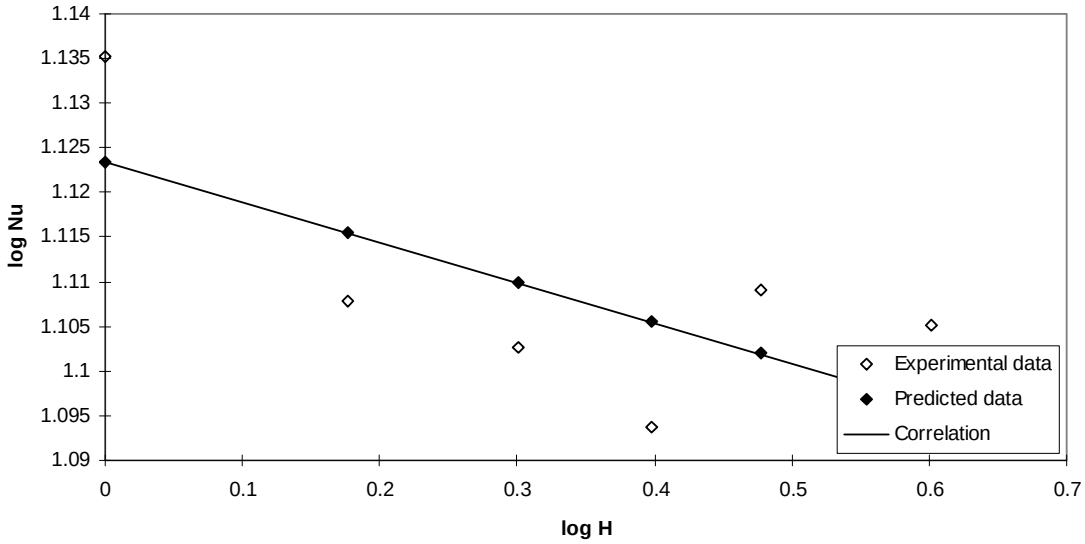

Figure 7.37. Stagnation region area-averaged Nu prediction for partially-inverted flames: correlation of H.

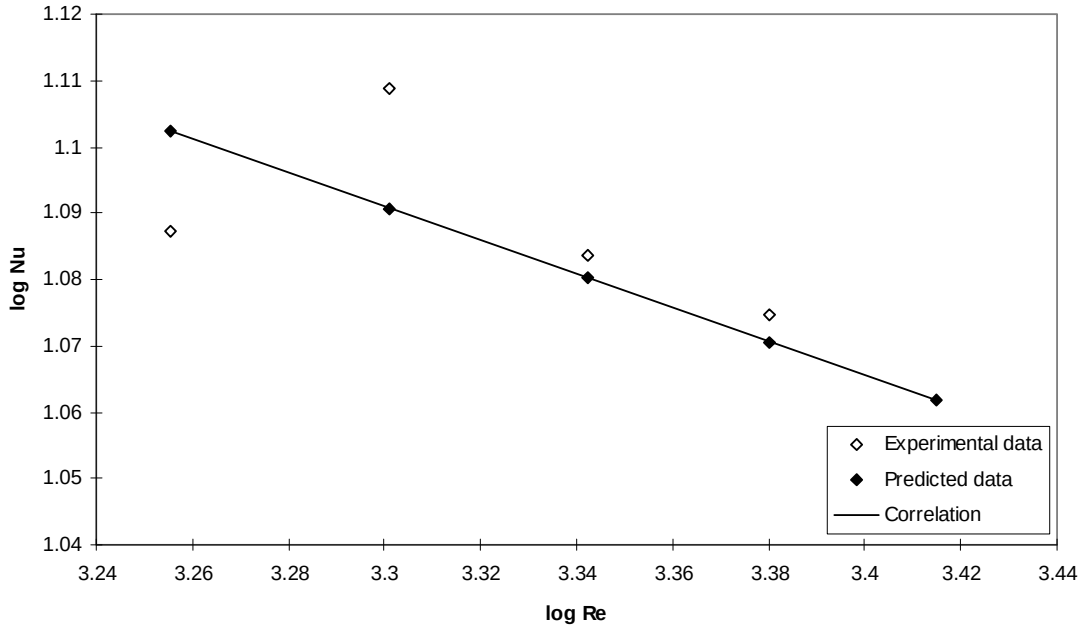

Figure 7.38. Stagnation region area-averaged Nu prediction for partially-inverted flames: correlation of Re.

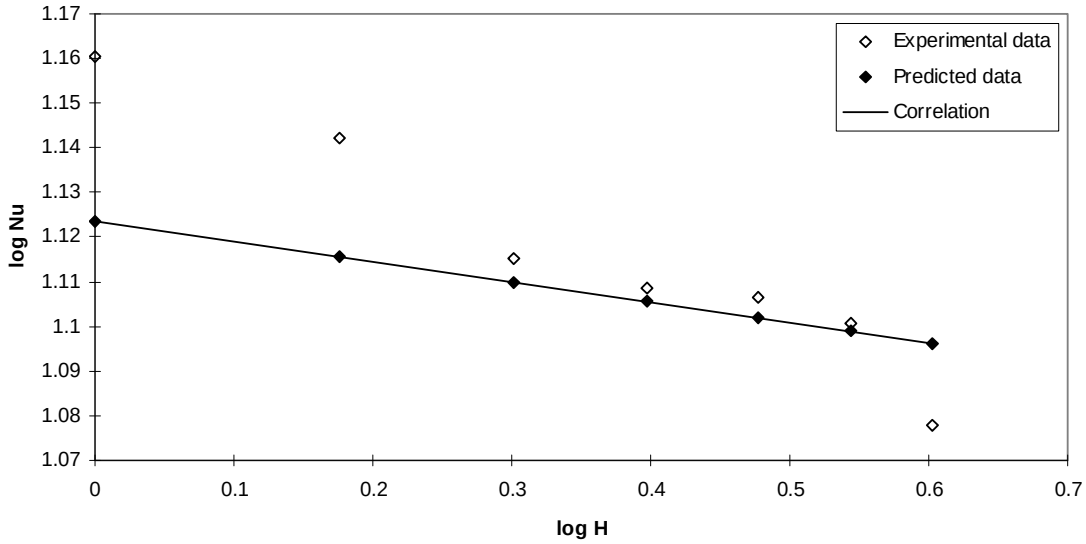

Figure 7.39. Impingement region area-averaged Nu prediction for partially-inverted flames: correlation of H.

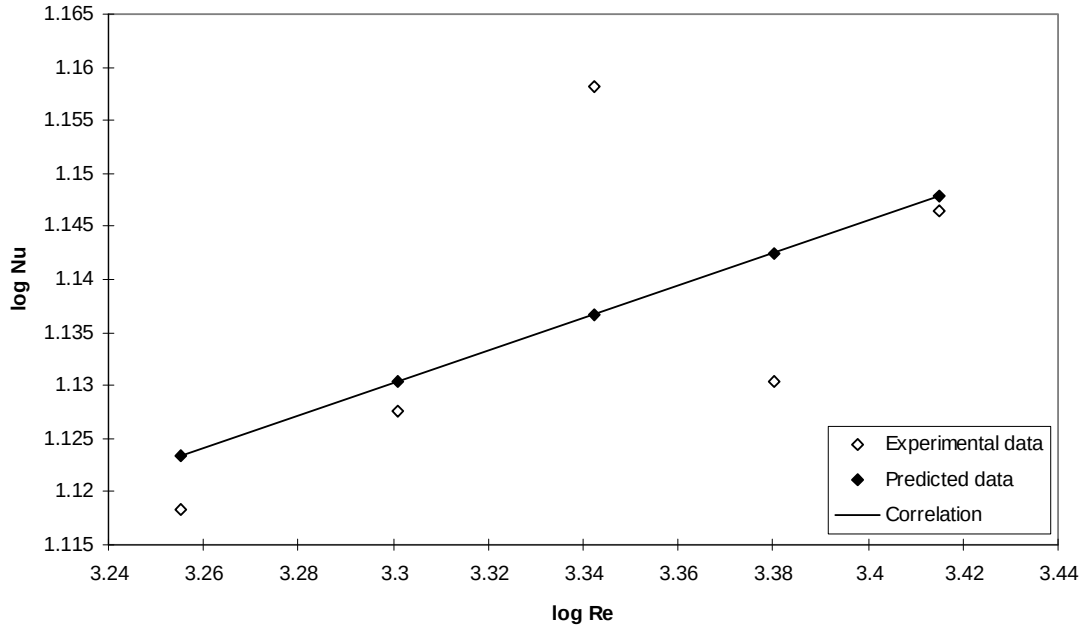

Figure 7.40. Impingement region area-averaged Nu prediction for partially-inverted flames: correlation of Re.

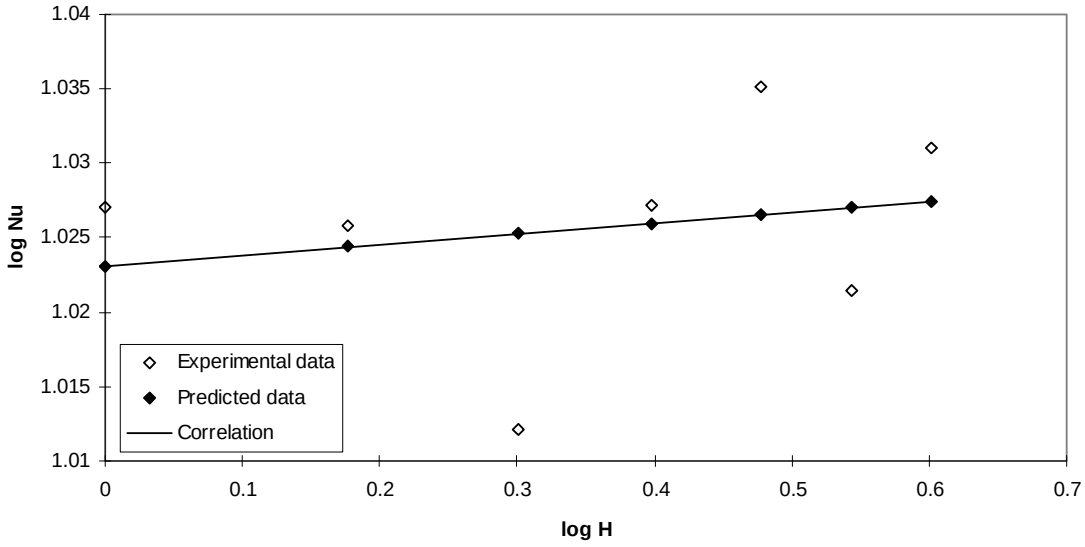

Figure 7.41. Wall-jet region area-averaged Nu prediction for partially-inverted flames: correlation of H.

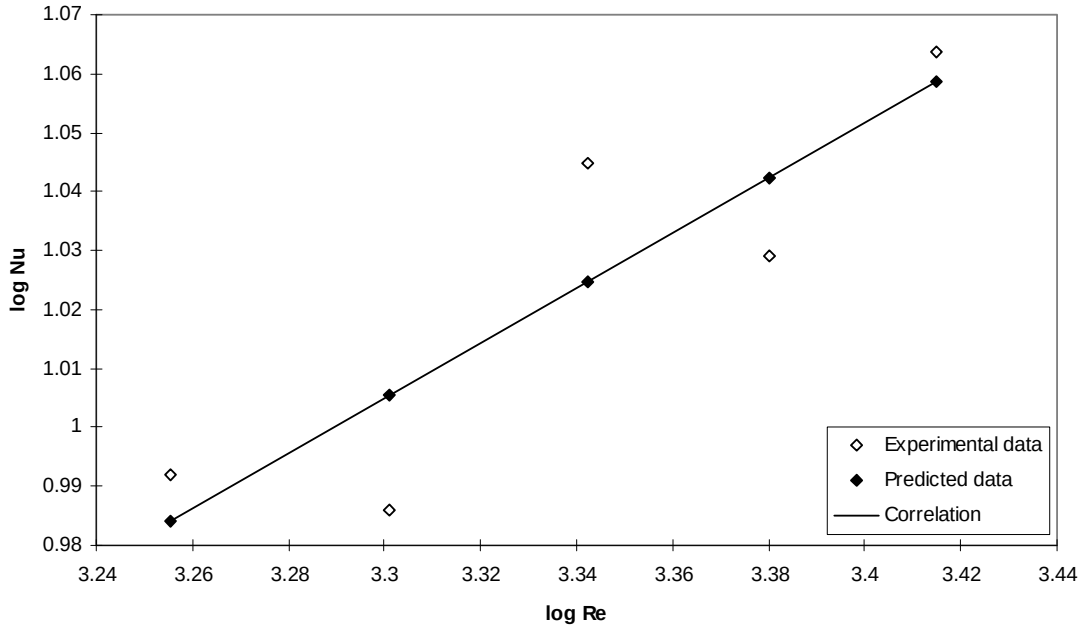

Figure 7.42. Wall-jet region area-averaged Nu prediction for partially-inverted flames: correlation of Re.